
THE UNIVERSITY
*of* EDINBURGH

# An assessment of a nearshore modular flap-type wave energy converter


Laurie Fletcher Wilkinson

A thesis submitted in partial fulfilment of the requirements for the award on an Engineering Doctorate

University of Edinburgh

College of Science & Engineering

2018

# IDCORE

This thesis is submitted in partial fulfilment of the requirements for the award of an Engineering Doctorate, jointly awarded by the University of Edinburgh, the University of Exeter and the University of Strathclyde. The work presented has been conducted under the industrial supervision of Aquamarine Power Ltd and Queen's University Belfast, as a project within the Industrial Doctoral Centre for Offshore Renewable Energy.





## Abstract

This thesis presents an assessment of a modular flap-type wave energy converter. Comparisons are made to an equivalent width rigid device. All quoted relative difference results here use the rigid device as the reference point. The variables that are evaluated are the power capture and surge and yaw foundation loads. The power capture is evaluated at both module and device level, while the foundation loads are assessed just at the device level. The investigation is carried out through testing of a $30^{th}$ scale physical model in a wave tank.

A key output from the work is the development of the physical model. The model consists of six flap modules, mounted on a common base structure. Each module contains a highly controllable and compact power take off system.

The devices are tested in a range of conditions, primarily consisting of regular waves of different period and direction. The damping strategy employed is the simplest approach available, setting the achievable damping level on each module to be the same.

For the modular device in head-on regular waves, the results show that the power capture increases significantly moving from the outer to the central modules. On average, the central pair of modules produce 68 % of the total mean power, the inner modules 25 % and the outer modules only 7 %.

Between the devices, it is shown that the power captures in head-on waves are similar, with a mean relative difference of -3 %, with +/-5 % uncertainty. Thus, no statistically significant change in power capture is shown. In off-angle waves, the mean relative difference is –1 %, with +/-4 % uncertainty. However, for the highest wave direction that was tested in, 27.5 degrees, the modular device outperforms the rigid flap, by 10 %, with uncertainty of +/-1 %.

The surge foundation loads are shown to be very similar for the two devices - in head-on waves, the mean relative difference is +2 %. Depending on the level

of applied damping, however, significant differences in the yaw foundation loads are shown. Using damping where the power capture is maximised, the yaw loads increase by a mean of 10 %; using damping where the power to load ratio is instead maximised, the modular yaw loads are 26 % lower.

Finally, the economics of the power production is estimated through division of the power capture with a cost metric, the foundation loads. While this does not provide a full techno-economic assessment, it effectively captures the interdependency of the power capture and foundation loads for the devices.

The mean relative differences in the power per load ratios of the devices are found to be similar across the wave conditions. In the head-on waves, the differences are between –8 and –0.4 %, depending on damping strategy; in the off-angle waves, the differences are between –6 and +10 %. For both sets of wave conditions, the modular flap performs better when the damping is set to maximise the ratio of power capture to foundation loads.

The work concludes that the modular and rigid devices produce power and experience foundation loads at similar levels in head-on waves. Given the high power capture efficiency, nearshore location, simple mode of operation and high survivability of the flap-type WEC, this suggests that the modular device is a viable stand-alone concept. The work also finds that in off-angle waves, some benefits can be achieved with an appropriately damped modular system, notably in improved power capture and reduced yaw foundation loads. These could reduce the sensitivity that flap-type devices have in off-angle waves and allow expansion of the width and hence capacity of machines.

Further work should extend the wave conditions tested in, by using more irregular and directional waves, and investigate more damping strategies and geometries. Economic assessment should also be carried out.

## Lay Summary

This thesis presents an assessment of a modular flap-type wave energy converter. Comparisons are made to an equivalent width rigid device. All quoted relative difference results here use the rigid device as the reference point. The variables that are evaluated are the power capture and foundation loads, which are measures of the revenue generated by and cost of a device, respectively. The investigation is carried out through testing of a scale physical model in a wave tank.

A key output from the work is the development of the physical model. The model consists of six flap modules, mounted on a common base structure. Each module contains a highly controllable and compact generator simulating system.

Between the devices, it is shown that the power captures in head-on waves are similar, with a mean relative difference of -3 %, with +/-5 % uncertainty. Thus, no significant change in power capture is shown. In off-angle waves, the mean relative difference is –1 %, with +/-4 % uncertainty. However, for the highest wave direction that was tested in, 27.5 degrees, the modular device outperforms the rigid flap, by 10 %, with uncertainty of +/-1 %.

The head-on foundation loads are shown to be very similar for the two devices, with the mean relative difference being +2 %. Depending on the level of applied damping, however, significant differences in the off-angle foundation loads are shown. Using damping where the power capture is maximised, the off-angle loads increase by a mean of 10 %; using damping where the power to load ratio is instead maximised, the modular yaw loads are 26 % lower.

The work concludes that the modular and rigid devices produce power and experience foundation loads at similar levels in head-on waves. Given the high power capture efficiency, nearshore location, simple mode of operation and high survivability of the flap-type WEC, this suggests that the modular device is a viable stand-alone concept. The work also finds that in off-angle waves,

some benefits can be achieved with an appropriately damped modular system, notably in improved power capture and reduced yaw foundation loads. These could reduce the sensitivity that flap-type devices have in off-angle waves and allow expansion of the width and hence capacity of machines.

**Acknowledgements**

Funding from the Energy Technologies Institute (ETI) and the RCUK Energy Programme for the Industrial Doctoral Centre for Offshore Renewable Energy (Grant number EP/J500847/1) is gratefully acknowledged.

Thank you to the sponsors of this project, Aquamarine Power Ltd and Queen's University Belfast (QUB), for guidance, encouragement and financial support.

Thank you to the technicians at QUB, for their advice, patience and skills during the creation and testing of the physical model featured in this thesis.

Thanks to my friends and colleagues in the QUB Marine Research Group (MRG) and department, for making the last four years an altogether enriching experience. Highlights include tag rugby, cake Fridays and being surrounded by people of similar levels of marine nerdiness! Special thanks to Ken, Aidan, Paul and Louise for technical and literary advice over the course of the research.

Thanks to my supervisors, Trevor, Philipp, Sandy and David, for advice and encouragement.

Finally, thanks to Megan, especially for support during the physical modelling campaign, and to my parents for motivation, particularly during the write up.

## Declaration

I declare that this thesis was composed by myself and that the majority of the material presented is my own work. Any significant contributions by others, such as members of the Queen's University Belfast and Aquamarine Power Ltd Marine Research Group, have been clearly stated. I declare that the work has not been submitted for consideration as part of any other degree or professional qualification. Furthermore, the following journal and conference papers, presented in Appendix 16, are also my own work, with contributing authors specified in the references section:

- Wave Loads on The Foundation of a Bottom-Hinged Modular Flap Structure (Wilkinson *et al.*, 2014)
- Modelling of a Modular Flap Type Wave Energy Converter (Wilkinson *et al.*, 2015)
- The Power-Capture of a Nearshore, Modular, Flap-Type Wave Energy Converter in Regular Waves (Wilkinson *et al.*, 2017)

Signed:

Laurie Wilkinson, 23/05/18

## List of Figures

## List of Tables

## Nomenclature

| | |
|---|---|
| $CF$ | capture factor of a device |
| $\rho$ | density of water (kg/m$^3$) |
| $W$ | device width (m) |
| $F$ | foundation load force (MN) |
| $M$ | foundation load moment (MNm) |
| $P_{inc}$ | incident power per metre of crest (kW/m) |
| $\dot{\theta}_n$ | instantaneous angular velocity of nth module (deg/s) |
| $Tc_n$ | instantaneous damping torque for nth module (MNm) |
| $P_n$ | instantaneous power-capture of nth module (kW) |
| $\theta_n$ | instantaneous rotation of nth module (deg) |
| $i$ | instantaneous signal index |
| $P_T$ | instantaneous total power-capture of device (kW) |
| $Tw_n$ | instantaneous wave excitation torque on nth module (MNm) |
| $\bar{P}_{T,max}$ | maximum total mean power-capture of a device (kW) |
| $\bar{P}_{T,max}$ | maximum total mean power-capture of device for single wave condition (kW) |
| $\overline{\lvert\dot{\theta}_n\rvert}$ | mean absolute angular velocity of nth module (deg/s) |
| $\bar{P}_n$ | mean power-capture of nth module (kW) |
| $\overline{\Delta CF'}$ | mean relative difference in capture factor between modular and rigid devices, with reference to rigid device, for a set of wave |

| | |
|---|---|
| | conditions |
| $T_{01}$ | mean wave period (s) |
| $n$ | module number |
| $M$ | number of modules |
| $a_{pk}$ | peak wave amplitude (m) |
| $T$ | regular wave period (s) |
| $\Delta CF'$ | relative difference in capture factor between modular and rigid devices, with reference to rigid device |
| $Tc_{n,RMS}$ | RMS of instantaneous damping torque of nth module (MNm) |
| $Tw_{n,RMS}$ | RMS of wave excitation torque on nth module (MNm) |
| $H_{m0}$ | significant wave height (m) |
| $S_P$ | smoothness of power-capture of device (%) |
| $Su_{ELR}$ | surge foundation effective load range |
| $t$ | time (s) |
| $\overline{\lvert\dot{\theta}_T\rvert}$ | total mean angular velocity of device (deg/s) |
| $\bar{P}_T$ | total mean power-capture of device (kW) |
| $Tc_{RMS,T}$ | total RMS damping torque of a device |
| $Tc_{RMS,T}$ | total RMS of instantaneous damping torque of device (MNm) |
| $V$ | value of power (kW/£) |
| $a$ | wave amplitude (m) |
| $D$ | wave direction angle (degrees) |

| | |
|---|---|
| $Y_{ELR}$ | yaw foundation effective load range |

## Abbreviations

| | |
|---|---|
| *AMTI* | Advanced Mechanical Technology, Inc |
| *$CO_2$* | carbon dioxide |
| *CFD* | computational fluid dynamics |
| *CAD* | computer aided design |
| *DAQ* | data acquisition |
| *DoF* | degree of freedom |
| *DC* | direct current |
| *EMEC* | European Marine Energy Centre |
| *EU* | European Union |
| *GHG* | greenhouse gases |
| *IP67* | International Protection 67 |
| *ITTC* | International Towing Tank Conference |
| *LED* | light-emitting diode |
| *MPB* | magnetic particle brake |
| *NI* | National Instruments |
| *PVC* | polyvinyl chloride |
| *PTO* | power take off |
| *PCB* | printed circuit board |
| *QUB* | Queen's University Belfast |
| *RMS* | root-mean-square |

| | |
|---|---|
| *TTF* | tank transfer function |
| *WEC* | wave energy converter |

# 1. Introduction

This chapter provides the reader with the background and motivation for the work contained in this thesis. The research questions posed are detailed and subsequent aims and objectives of the research established. The chapter concludes with a brief outline of the thesis structure for the benefit of the reader.

## 1.1 Background

### 1.1.1 Renewable Electricity

There is strong evidence that warming of the Earth's surface, atmosphere and oceans has occurred since the 19$^{th}$ century. These rises in temperature have been largest since the mid-20$^{th}$ century. There is a strong link between this warming and an increase in adverse effects such as sea level rise, reduction in summer sea-ice extent, ocean acidification and an increase in extreme weather conditions (Intergovernmental Panel on Climate Change, 2013b).

It has been shown, with 95 % certainty, that human activity has been the dominant driver for global warming (Intergovernmental Panel on Climate Change, 2013a), with greenhouse gases (GHG) the principal source (Intergovernmental Panel on Climate Change, 2013b). As a result of this, international bodies have set GHG emission reduction targets. The European Union (EU), for example, aims to reduce emissions by at least 80 %, compared to 1990 levels, by 2050 (European Commission, 2016a).

Energy use represents by far the greatest source of GHG emissions, at 68 % of total releases (International Energy Agency, 2015a). Carbon dioxide, $CO_2$, is the highest contributing gas, making up 90 % of the emissions related to energy use. The use of fossil fuels, such as coal, oil and gas, for energy production, has been one of the key contributors to the rise in global $CO_2$ emissions. In 2013, fossil fuels made up 82 % of world primary energy supply (International Energy Agency, 2015a).

There is a great need to reduce our reliance on fossil fuels as a source of energy supply. Of the targeted areas, the electrical power sector has the largest potential for reduction, with an aim for almost total elimination of $CO_2$ emissions by 2050 in the EU. This will be due to an increase in contributions from low-carbon sources, such as renewable electricity (European Commission, 2016b). The increased use of renewable electricity would also improve the energy security of nations that currently heavily rely on imported fossil fuels. Renewable electricity has been traditionally derived from sources such as hydro, wind and solar power. Wave energy is another form, which is discussed in the following section.

### 1.1.2 Wave Energy Resource

Waves are generated in the ocean by mechanisms such as wind forces, earthquakes and tides. The most energetic, and of greatest importance to wave energy extraction, are wind generated waves. These are created through interaction of winds with the surface of the ocean. This initially causes ripples which, if the wind blows strongly and long enough, develop into waves.

The basic parameters used to describe a wave, such as the height, period and wavelength, are defined in Figure 1.

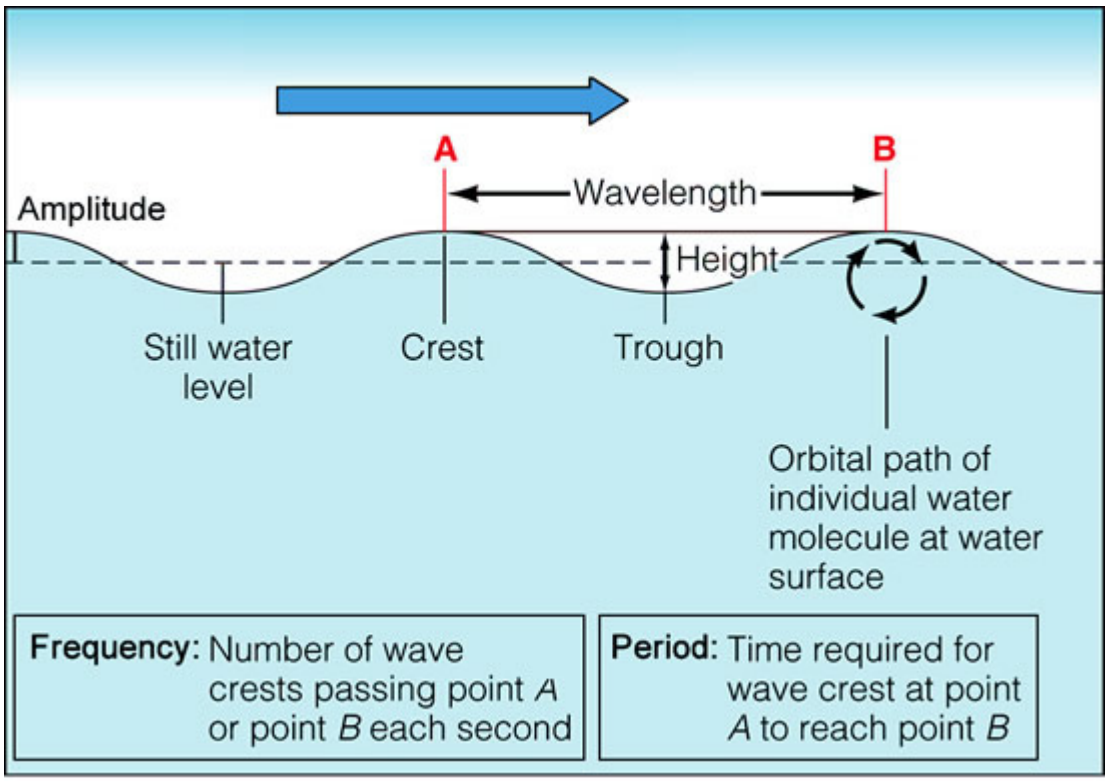


**Figure 1. Diagram providing definition of basic ocean wave parameters (passyworldofmathematics.com, 2013).**

Swell and local wind waves typically have periods of 1-25 s (Massel, 1996). In deep water, the wave height is primarily determined by the wind's speed, duration and fetch (European Marine Energy Centre, 2016a). A deep-water wave is defined as one that occurs in depths that are more than half the wavelength of the wave.

As waves move into shallower water, they transform due to the presence of the seabed. The wave transformation processes are namely: shoaling, wave breaking, refraction, diffraction and reflection (Massel, 1996).

Shoaling is the slowing down and steepening of the wave. The wave period stays the same but the wavelength reduces. For non-breaking waves, the energy-flux is maintained and so the reduction in velocity is compensated for by an increase in energy density. This manifests itself through an increase in the wave height. This causes the crest to shorten and the trough to widen. The water particle motion in the wave changes from circular to elliptical. The effect

of this is that the surge motion is amplified. The particle motion also extends down to the seabed, which maximises the available power per unit depth.

The increase in wave height due to shoaling is limited by the water depth. When the height is typically around 80 % of the depth, the waves break and dissipate their energy (Coastal Wiki, 2008). The transition and transformation of waves from deep to shallow water and classification of water depths is illustrated in Figure 2.

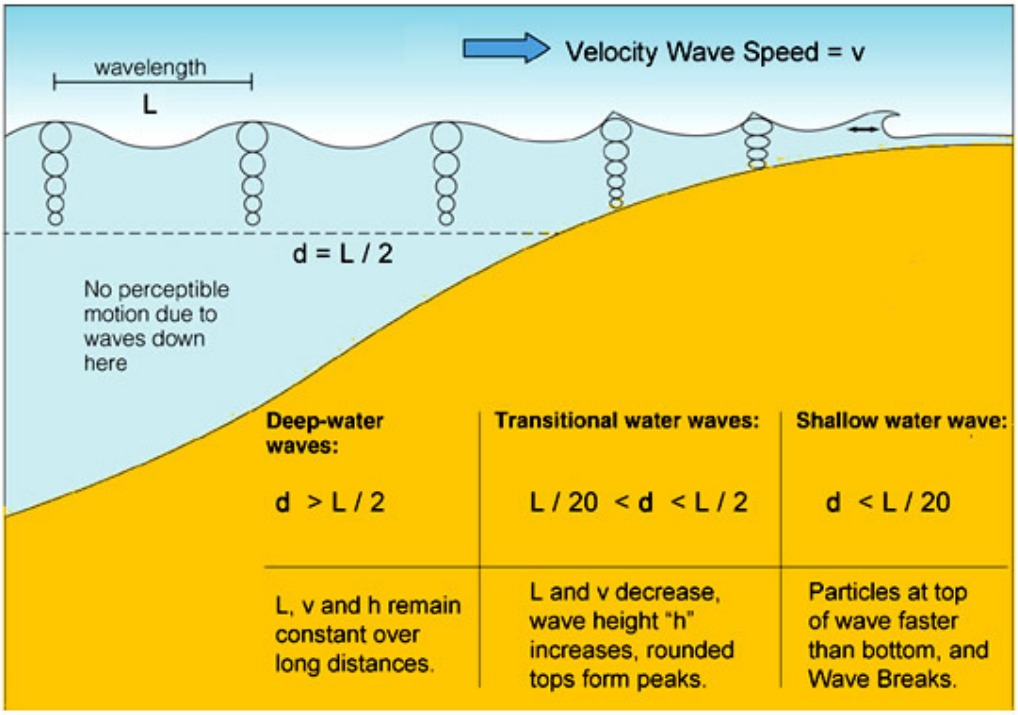


**Figure 2. Transition and transformation of waves moving from deep to shallow water and water depth classification (passyworldofmathematics.com, 2013).**

Of the depth ranges shown in Figure 2, the one that is most relevant for this thesis is the 'transitional' zone. The depth range that is of most interest within this is 10-20 m, which is termed as the 'nearshore' (Whittaker, T. and Folley, 2012).

It has often been perceived that the deep water resource is greatly superior to the nearshore, due to energy dissipation resulting from seabed friction and wave breaking. However, this perception is associated with the 'gross'

available power. By resolving the available power to the orientation of a wave farm and by setting maximum powers for economic extraction, the more useful 'exploitable' resource can be defined. It has been shown that, typically, the exploitable resource reduces by only 10-20 %, moving from 50 m to 10 m water depths. Hence, advantages of the nearshore, discussed now, can be exploited without significantly compromising the available incident wave power (Whittaker, T. and Folley, 2012).

Refraction, which is the aligning of waves to the direction that is orthogonal to the seabed contours, causes directional variation to reduce in the nearshore (Whittaker, T. and Folley, 2012). This is an advantage as it reduces costly torsional loads on an offshore structure and concentrates the available wave power into a smaller directional band. Additionally, wave breaking in nearshore depths naturally filters out the largest and most destructive waves, increasing the survivability of a wave energy device (Whittaker, T. and Folley, 2012). Finally, the nearshore environment is closer to the shore, reducing costs for transmitting electricity and vessel journeys, for installation, maintenance and decommissioning. The proximity also makes placing power conversion equipment on the shore feasible, which eases access to the plant (Henry et al., 2010). Hence, the nearshore environment is an attractive, and largely unexploited, zone for wave energy development (Whittaker, T. and Folley, 2012).

The global theoretical wave power resource is vast, being estimated by Gunn and Stock-Williams (2012) as 2.1 TW +/-0.05 TW. Using an example device and array configuration, the same authors estimated that 5 % of this available resource could be practicably exploited, giving an output of 0.10 TW. However, the array that was used was sparse and not tuned to each location (Gunn, K. and Stock-Williams, 2012). Hence, it is reasonable that this yield estimate could be increased to 10 %, giving an output of 0.21 TW. Based on the total energy consumed over the year, a recent estimate for the average global electricity demand was 2.7 TW (International Energy Agency, 2015b).

Therefore, a wave power output of 0.21 TW represents an 8 % contribution to global electricity demand. This shows that wave power has significant global market potential and could be a key part of the energy supply mix.

To focus development, it is also important to note that the available resource is particularly high on the western coasts of the land masses. In locations such as the west coast of Europe, the southwest coast of South America and the northwest coast of North America, annual mean power densities of 70-120+ kw/m have been estimated (Gunn, K. and Stock-Williams, 2012).

### 1.1.3 Wave Energy Converters

The movement of water particles in ocean waves results in pressure acting on a body placed in the water. The pressure results in a force, which, if the body is not externally damped, causes it to oscillate. When a force is applied to these motions by a 'damper', using a power take off (PTO) mechanism, useful power can be extracted (Henry, 2008). These systems are known as 'wave energy converters' (WECs).

The first recorded patent for a WEC was submitted by Monsieur Girard in 1799. Activity has been most significant since the early 1970s, however, with a huge variety of WECs being developed (Whittaker, W. and Folley, 2005). These machines have been designed to be placed either on the shoreline, in the nearshore region or in deep water (Henry et al., 2010). The range of operational principles is even larger, with devices attenuating, or moving in heave or pitch, for example (European Marine Energy Centre, 2016b). A few full scale WECs, of individual capacities of up to 2 MW, but typically much lower, have been installed (International Renewable Energy Agency, 2014). The early wave energy devices were largely 'oscillating water columns' (OWCs). These devices extract power using a turbine placed in an airflow generated due to compression and decompression of air in a chamber open to waves. One of the first grid-connected, commercial scale wave energy devices, for example, was a shoreline based OWC in Toftestallen, Norway. The device was rated at 500

kW and installed in 1985, operating until 1988, when it was destroyed by a storm (Falcão and Henriques, 2016). Since then, different types of devices have been installed, such as a number of flat-type WECs, discussed in section 1.1.4 (O'Boyle *et al.*, 2015; European Marine Energy Centre, 2016b). However, installations remain at the single device or small array stage and so wave power is not yet a commercial industry. This relatively slow progress has partly been due to the very challenging conditions that the machines are subjected to, such as extreme forces and high rates of corrosion.

### 1.1.4 Flap-Type WECs

The WEC category that this thesis focuses on is the bottom-hinged flap-type device, otherwise known as an 'oscillating wave surge converter'. These devices are particularly designed to absorb the energy contained in the horizontal, or 'surge', motion of the particles in ocean waves.

The use of a hinge at the bottom of the flap converts the surge force into a torque and grants freedom for oscillation in the pitch mode of motion. The hinge is typically mounted on the seabed, which provides the reaction to the wave forces. The flap is buoyant, to provide a restoring force. The size of the body varies, but typically the width and/or height are significantly larger than the thickness. The top of the body also either pierces the water surface or sits below it (Folley, Whittaker and van't Hoff, 2007).

Flap-type WECs typically use a hydraulic system as the primary stage of their PTO. The hydraulic energy is then converted into electricity by means of a device such as a hydro-electric turbine or hydraulic motor (Folley, Whittaker and van't Hoff, 2007; Henry et al., 2010).

Along with its nearshore location, the flap-type WEC offers several important advantages, making it an attractive device for research. One such advantage is their natural survival mechanism of decoupling from waves as they grow larger (Whittaker, T. and Folley, 2012). They are also simple in operation, moving only in pitch. This owes itself well to improved mechanical reliability. Both of

these features provide the potential for cost savings, by lowering structural and maintenance costs, respectively. The flap-type device also possesses high power conversion efficiency, thus providing the potential for significant revenue generation (Babarit *et al.*, 2012; Babarit, 2015). Combined with reduced costs, this offers the opportunity for a low price of energy, the benchmark metric for device assessment (de Andres *et al.*, 2016).

As a result of its advantages, the device type has received significant commercial focus, with a number of large scale devices deployed, such as Aquamarine Power Ltd's Oyster machines and AW-Energy's WaveRoller (Henry et al., 2010; AW-Energy, 2012; Whittaker, T. and Folley, 2012). To visualise the key components of such a device, a schematic of the surface-piercing Oyster machine is shown in Figure 3.

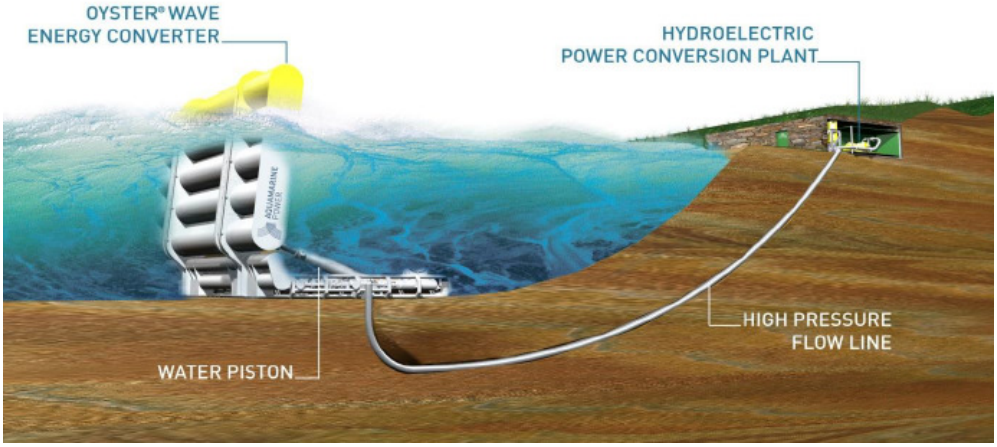


**Figure 3. Schematic of flap-type WEC example, the Oyster, showing water piston PTO, pipeline and onshore plant. Not to scale (Álvarez, 2015).**

As with other WECs, it is envisaged that the wide scale deployment of flap-type devices will be in farms, or 'arrays', of multiple machines (Sarkar, Renzi and Dias, 2014). This will likely result in savings, for example through the sharing of maintenance and electrical connection costs (Child, 2011). It is also likely that each of these arrays will be formed as a line of devices, to minimise energy shadowing (Whittaker, T. and Folley, 2012).

## 1.2 Motivation

This section presents the motivation for the research. Firstly, there is a general need to improve the economic viability of WECs, for them to compete in the energy market. Design solutions must be found that have high energy yields, whilst offering manageable manufacturing, installation, maintenance and decommissioning costs. One of the key design challenges is that machines must be built that are efficient in the smaller, frequent sea states, but simultaneously able to withstand the forces generated in extreme, infrequent wave conditions (Lamont-Kane *et al.*, 2015).

Most flap-type devices employ a single body for their rotating section (Folley, Whittaker and van't Hoff, 2007). If this is large, for example 26 m in width like the Oyster 800 device, then asymmetric pressure across the flap, for example in directional waves, will generate torsion in the structure and its foundation (Henry et al., 2010). Loads drive the design of a foundation, which are a key component in the capital costs of a WEC (Whittaker, W. and Folley, 2005). Additionally, the power capture of a wide flap is sensitive to the direction of the incident wave, typically reducing with greater than the square of the wave direction angle (Henry, 2008). Even in nearshore sites, directional variation and spreading can be prominent (Herbers, Elgar and Guza, 1999; Wilkinson *et al.*, 2014). Finally, the use of a single wide unit like this can also necessitate the use of large, expensive installation vessels (Aquamarine Power Ltd, 2009).

This thesis assesses the potential of a variation of the flap-type WEC. This could reduce the magnitudes of the discussed shortcomings related to the size of the concept. Formed by splitting the rotating body into several mechanically independent modules, mounted on a common foundation, the concept variation is referred to here as the 'Modular Flap'. Due to the independence and size of the modules, this design change could provide several improvements. These could be, for example, increased power production in directional waves, reduced foundation loads and lower manufacturing and installation costs. There could also be operational advantages such as increased availability. This would

be achieved by isolating the effects of component failures to single modules, as opposed to flaps with multi-module capacities. Additionally, a modular formation would make the scaling up of devices, in terms of overall width, arguably more feasible. This would likely provide economies of scale, for example by concentrating offshore maintenance activities, and increase the market for the flap-type WEC through heightened packing density on the seabed. The Modular Flap therefore represents a promising concept, worthy of investigation.

## 1.3 Aim and Objectives

This section first presents the key research questions that have been posed in this thesis. These are then used to form the aim and objectives of the research. To first pose the questions, it is necessary to define the scope of the project.

In this work, a Modular Flap is assessed and compared to a benchmark single unit with an equivalent total width, referred to as the 'Rigid Flap'. Renderings of examples of the two devices are shown in Figure 4.

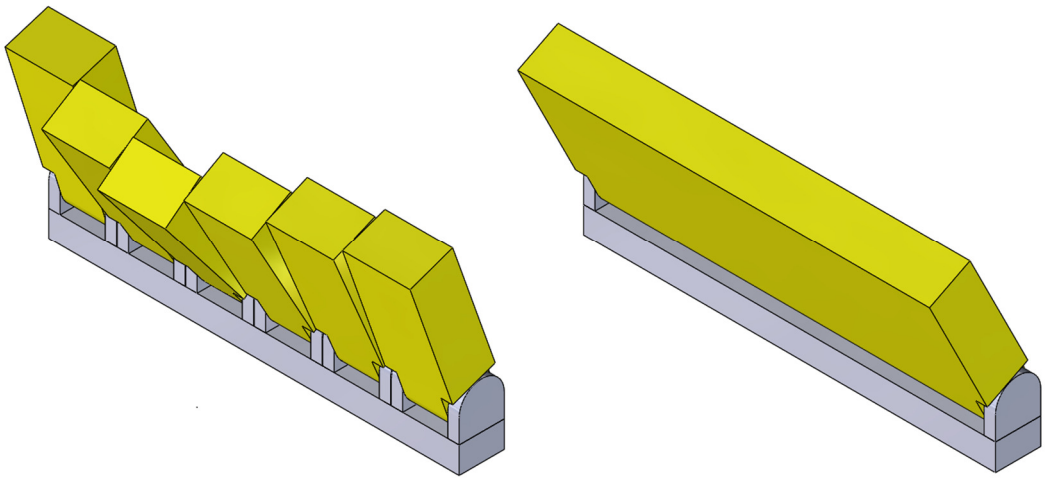

**Figure 4. Computer aided design (CAD) renderings of Modular Flap (left) and Rigid Flap (right) concepts.**

The dimensions of the concept that has been studied in this thesis were similar to the Oyster 800 machine. This device was operational at the European

Marine Energy Centre (EMEC) at the time of this research commencing and therefore represented an industrially relevant benchmark to use (O'Boyle *et al.*, 2015). To provide the reader with some perspective, the principle device dimensions that were used for guidance were: 26 m width, 2 m thickness, 4 m hinge height, 13 m water depth and 3 m freeboard (Babarit *et al.*, 2012).

As an initial step in evaluating the feasibility of the modular flap-type WEC, the hydrodynamic power capture and foundation loads experienced by the device were assessed. These variables are key indicators of economic viability, the first indicative of revenue potential and the second of structural cost (Folley, Whittaker and van't Hoff, 2007; Babarit *et al.*, 2012).

To assess the power capture of the devices, it was necessary to measure and then sum the power production of each flap module. For the device foundation loads, on the other hand, it was assumed that the modules would be mounted on a common base structure and hence it was sufficient to measure loads at a single point. It would have been useful to also measure the loads acting on each flap module, for further design information. However, the device loads were prioritised due to their greater general importance and the practicality of measuring them being higher. Hence, individual module load measurement was deemed outside the scope of the thesis.

It is important to assess foundation loads in both commonly occurring and rare, extreme sea states. This is because results from testing in common sea states can be used in fatigue analysis of an offshore structure, while extreme loads are used to determine the maximum expected stresses (Brown, A and Paasch, 2014). The majority of the energy generated by a WEC over its lifetime is typically produced in the commonly occurring sea states (Hiles, Beatty and de Andres, 2016). Hence, a focus on commonly occurring sea states in this thesis provided the opportunity to simultaneously evaluate the power capture and fatigue conditions for a modular flap-type WEC. The decision to not assess extreme loads was also made due to the fact that a study such as this, also using physical modelling, already existed (Wilkinson *et al.*, 2014).

Identification of these areas of investigation therefore lead to formation of the key research questions, being:

1. What are the magnitudes of the power capture and foundation loads for a Modular Flap, for a range of commonly occurring wave conditions?
2. How do the above compare to those measured for a non-modular device, such as the Rigid Flap?
3. What are the differences in power capture between individual flap modules?

The posing of these questions leads to the single aim of the thesis being formed:

*To assess the local and global power capture and foundation loads of a modular flap-type WEC, in commonly occurring wave conditions, and, where applicable, compare them to those for an equivalent rigid device.*

A range of modelling methods, including numerical and physical techniques, was available to carry out this assessment. Numerical modelling is typically faster than physical modelling, but the former also has its disadvantages (Day *et al.*, 2015). Numerical approaches are generally defined by the balance between accuracy, time and computational requirements. At the lower-resource side are methods based on linear potential flow theory. While these allow rapid parametric assessments, they typically do not include nonlinear and viscous effects, which can play a major role in the hydrodynamics of flap-type WECs (Folley, Whittaker and van't Hoff, 2007; Sarkar, Doherty and Dias, 2016). At the other end is computational fluid dynamics (CFD), which can be fully viscous and non-linear (Schmitt, 2013). However, the use of CFD is often limited to a small number of wave cycles due to its high computational requirements (Bourdier *et al.*, 2013). While it can be more expensive, the use of scale physical modelling can address the drawbacks of numerical modelling. It does this by firstly working in a real, viscous fluid. It also provides reasonably fast generation of data time-series that are long enough for

computing the reliable statistics that are desired for the type of assessment carried out in this thesis (Bourdier *et al.*, 2013). Physical modelling in a wave tank is therefore used here to carry out the assessment. Based on these considerations, the following were the key objectives of the research project, in chronological order:

- To develop an instrumented and damped physical model that allows measurement of power capture and foundation loads of modular and rigid flap devices;
- To verify the functionality of the physical model through testing;
- To develop an appropriate physical modelling test plan to answer the research questions;
- To calibrate appropriate wave conditions;
- To use the physical model to produce high quality results, for focused qualitative and quantitative analysis.

## 1.4 Thesis Structure

This section provides a description of the thesis structure to help guide the reader. In Chapter 2, a literature review is carried out, to learn from previous work and highlight the research gap. In Chapters 3, 4 and 5, the modelling methodologies are presented. These provide details of the physical model, the sensor calibration and model testing methodologies and the data analysis methods that were employed, respectively. Chapters 6 and 7 then present the key power capture and foundation load results from the study, respectively. Finally, Chapters 8, 9 and 10 provide discussion of the impact of the work on the wider context, suggestions for further work and overall conclusions, respectively. To aid the reader, this structure is illustrated in Figure 5.

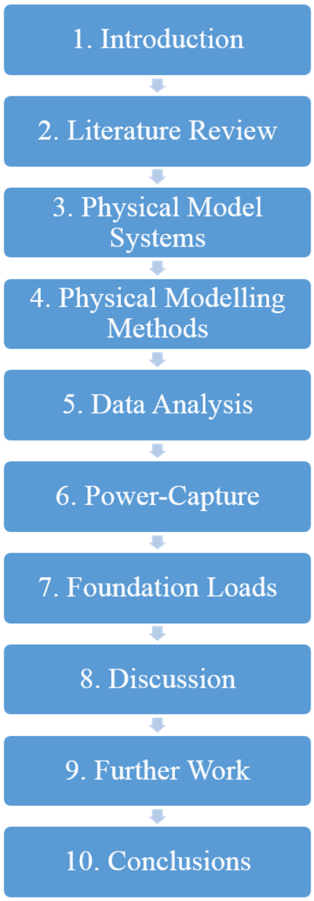


**Figure 5. Flow chart showing thesis chapter structure.**

# 2. Literature Review

## 2.1 Introduction

Historically, most research on WECs has focused on deep water devices, principally operating in heave motion (Child, 2011; O'Boyle, 2013; P. Lamont-Kane, 2015a). Research on flap-type WECs in the nearshore is less extensive, perhaps due to the perception that the resource there is significantly smaller than that available offshore (Whittaker, T. and Folley, 2012).

As was discussed in section 1.1.2, however, it has been shown that the *exploitable* nearshore resource is similar to that available offshore and that the location offers a number of techno-economic advantages (Whittaker, T. and Folley, 2012).

Additionally, there are now several recognised advantages of the flap-type WEC, as discussed in section 1.1.4. As a result, the device has received a greater amount of literary attention in recent years (Whittaker, T. and Folley, 2012; O'Boyle *et al.*, 2015).

As in this thesis, the behaviour and design space of flap-type WECs has been largely explored through assessment of the variables of power capture and structural loads. A large range of modelling methods have been employed to carry out these assessments. Broadly speaking, these methods can be split into physical and mathematical modelling.

Physical modelling has been used to measure variables by performing tests in wave tanks, at scales of 10-60, followed by the application of scaling laws (Henry, 2008; Clabby, 2013; Dias, F. and Sammarco, 2013).

Mathematical modelling, using hydrodynamic theory, has been applied to predict power-capture and structural loads by solving equations, for example of the motion of a flap. Mathematical modelling can be further broken down into analytical, numerical and CFD approaches.

The most relevant literature are works that study devices that are similar in design and geometry to the Rigid Flap and the Modular Flap concepts studied in this thesis. Hence, these works are reviewed in sections 2.2 and 2.3, respectively. Both sections are structured to first critically review the research methods, followed by summarising the key findings of the works. In section 2.4, the research gaps are highlighted and it is explained how this thesis addresses them.

## 2.2 Rigid Flap-Type WECs

### 2.2.1 Literature Review

This section presents the key methodologies that have been applied for modelling rigid flap-type WECs. The works are grouped into those that use mathematical and physical modelling approaches, respectively.

Up until the 1980s, one of the only works that focused on the flap-type WEC was by Scher (1985). Here, an analytical model was developed to study the effects on power capture of, for example, design parameters, such as device width and deployment depth. Other analytical works, based on linear potential flow theory, have studied the device in both a channel (Renzi and Dias, 2012, 2013) and the open ocean (Renzi and Dias, 2013). These analytical studies provide fast device assessment but are typically carried out in an inviscid fluid, using regular, small amplitude waves (Renzi and Dias, 2013).

Folley et al. (2007), developed a frequency-domain numerical model that included viscous effects and motion constraints. It was shown that these should be included in a model to accurately predict the power capture of this device. The model was developed further by transformation into the time-domain in van ’t Hoff (2009). Operation in the time-domain allows consideration of non-linear effects and control strategies, such as ‘constant’ or ‘Coulomb’ damping. This is where the PTO damping torque has a constant amplitude, independent of the instantaneous velocity. The model achieves the latter by allowing

specification of forces at discrete time steps, instead of as sinuisoidal signals in frequency-domain models.

A mathematical method that considers viscous and non-linear effects is CFD. In Schmitt (2013), CFD was used to study the dynamics of flap-type WECs. Results were compared to physical wave tank tests. Agreement of surface elevation, flap acceleration, surface deformation and flow pattern results, in highly non-linear waves, was very good. Visualisation and quantification of these variables across the fluid provided a valuable insight into the physical processes governing the flap dynamics. An example of flow visualisation in CFD is provided in Figure 6.

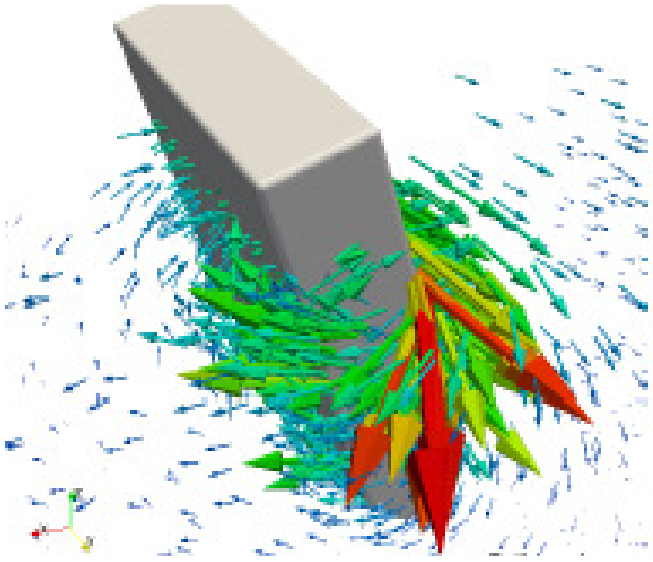

**Figure 6. Flow visualisation around a flap using CFD (Schmitt, 2013).**

The CFD tools were applied to research topics such as scaling, PTO systems and flap shape variations (Schmitt, 2013).

Mathematical models typically require physical data for calibration and validation. This is because physical modelling provides direct consideration of viscous and non-linear effects (van ’t Hoff, 2009; Clabby, 2013).

One of the key parameters that has been assessed using physical modelling is the power capture of flap-type devices (Henry, 2008; Clabby, 2013). This has

necessitated the use of PTO dampers in scale models. A large number of studies have used constant, or 'Coulomb', PTO dampers, using hydraulic systems to replicate the damping in full scale machines (Henry, 2008; O'Boyle *et al.*, 2015). This type of damping is where the magnitude of the damping torque is constant, with the sign changing with the angular velocity, illustrated in an ideal example in Figure 7.

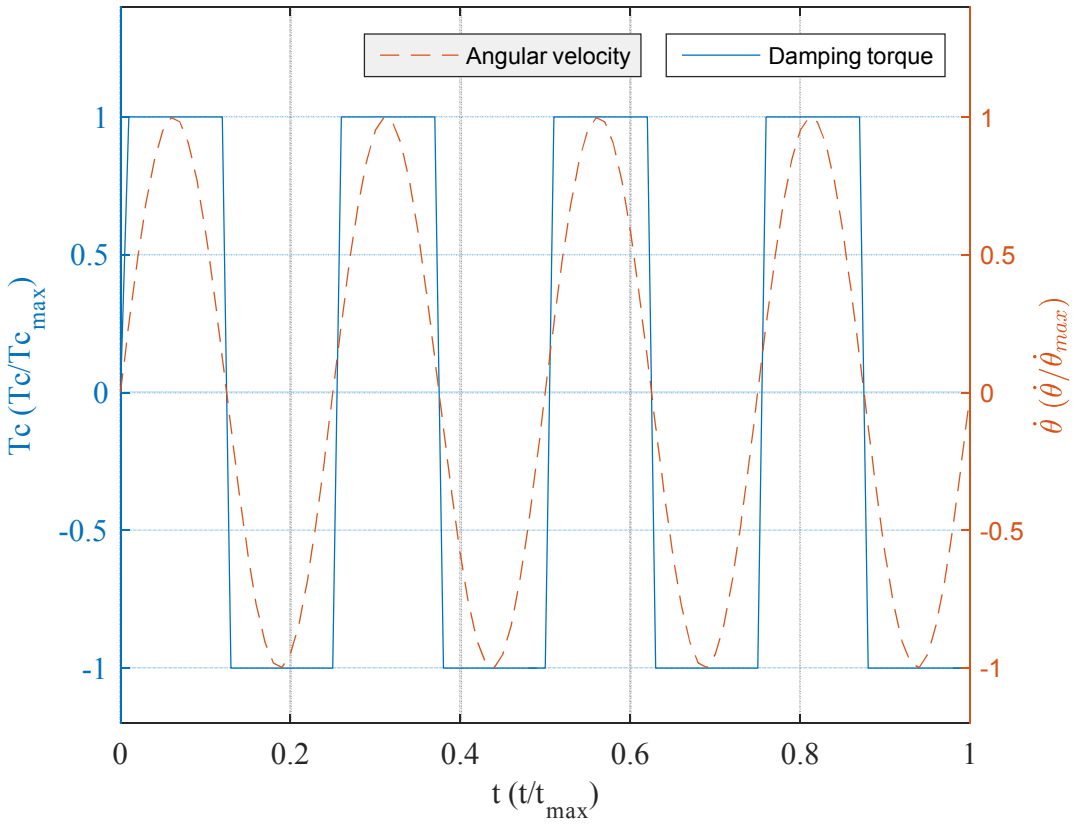


**Figure 7. Example of ideal Coulomb/constant damping torque timeseries, showing variation of damping torque, *Tc*, and angular velocity, $\dot{\theta}$, against time, t, with the results normalised to show general case.**

Due to its common full scale application in flap-type WECs, constant damping torque was also chosen for later use in the physical model in this thesis and hence it should be noted that, from herein on in, 'damping torque' or 'damping' refers to constant damping torque, unless otherwise stated.

A physical modelling campaign of device power capture assessment was carried out in Henry (2008). The flap-type design space was explored through

assessment of the power capture in 40th and 20th scale testing. A picture of a configuration of the 20th scale model is provided in Figure 8.

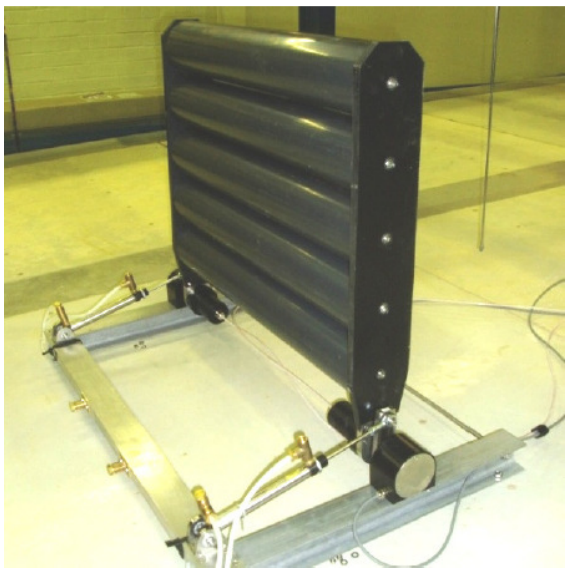

**Figure 8. 20th scale physical model, 12 m wide at full scale, used in Henry (2008).**

A constant damper was simulated in this work using hydraulic cylinders, valves and an accumulator (Henry, 2008). However, the amplitude of the damping torque was found to not be constant. There were also spikes and oscillations in the signal, partly due to flexibility in the pipe work and the inertia of the fluid in the system, with an example damping torque timeseries shown in Figure 9 (Henry, 2008).

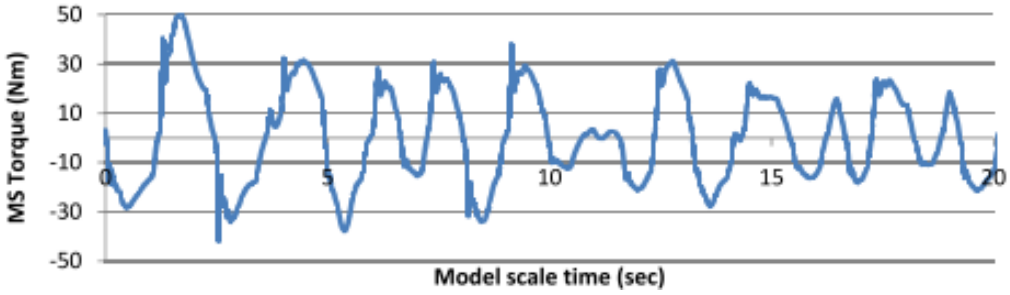


**Figure 9. Example damping torque timeseries using a hydraulic water damper with an accumulator. The graph shows the variation in the amplitude of a desired constant amplitude signal (Henry, 2008).**

Clabby (2013) then alternately used hydraulic cylinders and disc brakes to simulate constant damping in a 20th scale model. The disc brakes are described

further here because a hydraulic system has already been discussed (Henry, 2008). The disc brakes used a calliper to apply friction to a disc attached to the shaft of the flap. A schematic of the disc brakes, showing how they integrated with the flap model hinge is shown in Figure 10.

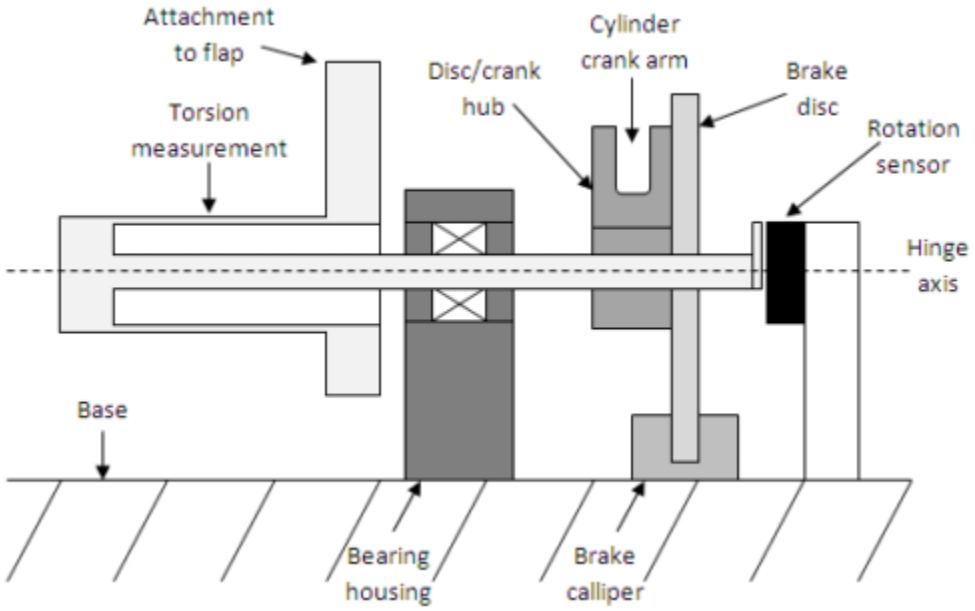


**Figure 10. Schematic of disc brake damper, used in Clabby (2013), showing its integration in the flap model hinge.**

The damping torque applied by the disc brakes was controlled by changing the force generated by the calliper. This was changed using a lever above the water and linked to the calliper via a hydraulic hose. The level was then controlled via a line and pulley to a point outside the wave tank. The suspension of weights on the end of the line allowed one to control the force applied by the calliper (Clabby, 2013). A schematic of this control system is shown in Figure 11.

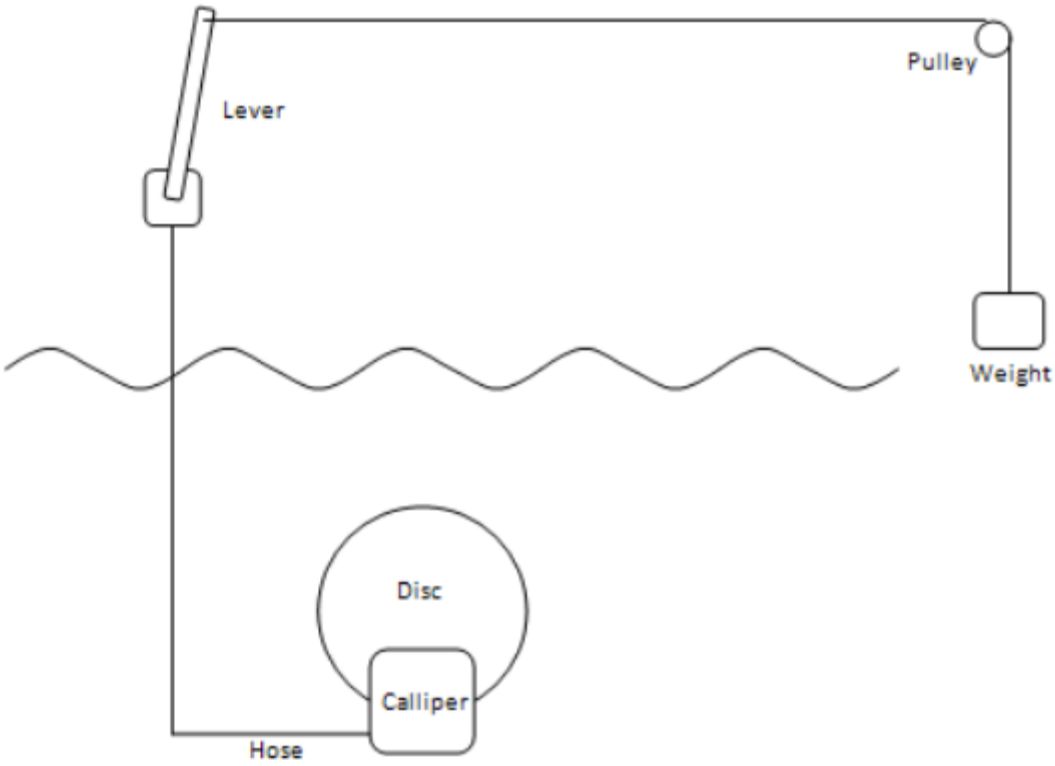


**Figure 11. Schematic of disc brake damper control system, used in Clabby (2013).**

However, like in Henry (2008), the damping amplitude provided by the disc brakes varied, due to the thickness of the disc changing. The hydraulic system and disc brake PTO options may have been relatively low cost. However, it is clear that, through their application, difficulty was found in achieving high damping controllability and consistency (Henry, 2008; Clabby, 2013). This learning was used as input to the damper selection process that was carried out for this thesis, described in section 3.5.

Foundation loads for rigid flap-type WECs have also been physically assessed (Howard, Whittaker and Doherty, 2009; Bourdier *et al.*, 2013; Henry *et al.*, 2014; Mckinley *et al.*, 2014; Lamont-Kane *et al.*, 2015). Studies have been divided between those considering 'pulsating' or 'impulsive' loads. The former are periodic, long-duration loads, caused by variation in the wave surface elevation and water particle motion, while the latter are short-duration and caused by impact events, such as slamming (Lamont-Kane *et al.*, 2015).

In this thesis, pulsating loads in common sea states are of most relevance. However, the focus of pulsating foundation load measurement has been on extreme sea states, with fatigue loading assessment concerned only with deriving pressures on the face of a flap (Howard, Whittaker and Doherty, 2009; Bourdier *et al.*, 2013). Nevertheless, the findings in extreme sea testing are of relevance for this thesis because they reveal differences in the loads in the degrees of freedom, for example.

Extreme pulsating loads were measured using a five degree of freedom load cell on a 40$^{th}$ scale flap model. It was shown that loads in the surge degree of freedom were two times as large as those in the heave axis (Howard, Whittaker and Doherty, 2009). The study also investigated the effect of PTO damping torque on the magnitudes of rotation and foundation loads. It was shown that the difference between the results with and without PTO damping were small. The positive surge load magnitude increased by only 11 %, for example. However, the damping level applied in the study was a single value, derived from tests in *commonly* occurring, production sea states. The wave heights used in the study, 8-10 m, were approximately four times greater than those in common sea states at the site of interest (Howard, Whittaker and Doherty, 2009; O'Boyle *et al.*, 2015). Hence, assuming a degree of linearity between wave torque and height, it can be deduced that the wave torques were also approximately four times greater in these extreme tests than the common seas. As an approximate estimate, the optimum applied damping torque for power production in a sea state is half the wave torque. Assuming this, the damping torque applied in the study was eight times smaller than the wave torque. Hence, it is not surprising that the rotations and foundation loads did not change significantly with applied damping torque. Further work is hence needed to determine the relationship between applied damping and foundation loads, especially in common sea states.

A further limitation of the work and indeed the available literature, is the lack of research on the effects of the wave direction angle on foundation loads of

flap-type WECs (Howard, Whittaker and Doherty, 2009). Work has been completed on this but only the surge, heave and sway forces were measured and, again, the waves were confined to extreme sea states (Mäki, Vuorinen and Mucha, 2014).

### 2.2.2 Summary of State of the Art

The research methods discussed thus far have been used to define the design space that the Rigid Flap studied in this thesis occupies. From the literature, it seems that the maximisation of capture factor, or power capture per displaced volume, has driven this choice of design space (Folley, Whittaker and van't Hoff, 2007; Henry, 2008). This process is summarised here, followed by a discussion of literature on scaling physical modelling results. Finally, a look to the future, with a review of literature on evolution of the concept, is provided.

Using two-dimensional theory, a single degree of freedom device can absorb a maximum of 50 % of the incident wave energy. Half of the remaining energy is then transmitted in the direction of propagation, with the other half reflected. This is what happens for terminator type devices, where the body is wide in relation to the wavelength (Scher, 1985; Henry et al., 2010).

For a point absorber, on the other hand, its principal dimension, such as its width, is small relative to the wavelength. In this case, three-dimensional effects allow the body to extract more than 50 % of the wave energy. Thus, in this case, the power extraction is related to only the wavelength, and not the size of the body (Budar and Falnes, 1975; Newman, 1976; Scher, 1985; Henry et al., 2010).

It has been shown that a flap-type device acts like a point absorber when it is narrow compared to the wavelength, and like a terminator when it is wide (Scher, 1985; van 't Hoff, 2009).

To maximise the power capture of a device, it is beneficial to tune it so that its natural period matches the incident wave period. A way to tune a device,

without the use of complicated PTO control, is through design of its geometry (Folley, Whittaker and van't Hoff, 2007).

Flap type devices tend to have natural periods that are greater than that of the incident waves. This is due to their dynamics being dominated by their added inertia. However, they can be tuned to have a lower natural period, by making them: (1) narrow to reduce the added inertia, and (2) thick to increase their restoring buoyancy (Henry et al., 2010). However, in order to compensate for the resultant reduction in wave force due to decreased width, it has been shown that such a device has to move with large amplitudes of motion, likely beyond the practical restrictions of machinery (Scher, 1985). Folley et al. (2007) also demonstrated that such motions are heavily damped by viscous drag forces. These combined effects limit the power capture gains that are derived through tuning a flap-type WEC device (Scher, 1985; Folley, Whittaker and van't Hoff, 2007).

As an alternative to tuning, it has been shown that maximisation of power capture for a flap-type device can be achieved by maximising the wave torque (Henry, 2008; Renzi and Dias, 2013). This shows that the dynamics of the flap-type WEC are dominated by diffractive processes (Renzi and Dias, 2013).

Increasing the flap width has been used as one way to increase the wave torque. Henry (2008) found that, initially, the wave torque increases with the square of the width. This led to a similar increase in the 'capture factor', which is the ratio of absorbed to incident power across the device width (Henry et al., 2010), as defined in Equation 1.

$$CF = \frac{P_{abs}}{P_{inc} \cos(D)\, W} \qquad \text{Equation 1}$$

Where, $P_{abs}$ is the absorbed power, in kW, $P_{inc}$, is the incident power per metre of crest, in kW/m, $D$ is the wave direction in rad. and $W$ is the device width, in m.

Another benefit of increasing the flap width is that it broadens the range of wave periods within which high capture factors are achieved (Scher, 1985; Renzi and Dias, 2013). Beyond a certain width however, the flap becomes a terminator and the wave force increases linearly with the width. This reduces the rate of increase of power capture per unit width (Henry, 2008).

The average capture factor across a range of wave conditions has been shown to be typically highest for a flap-type device in the range of 20-30 m width (Henry, 2008; Henry et al., 2010). Figure 12, which is taken from Folley et al. (2007), demonstrates this peaking of capture factors. It also shows the reduction in power capture, that occurs when viscous losses and motion constraints are considered.

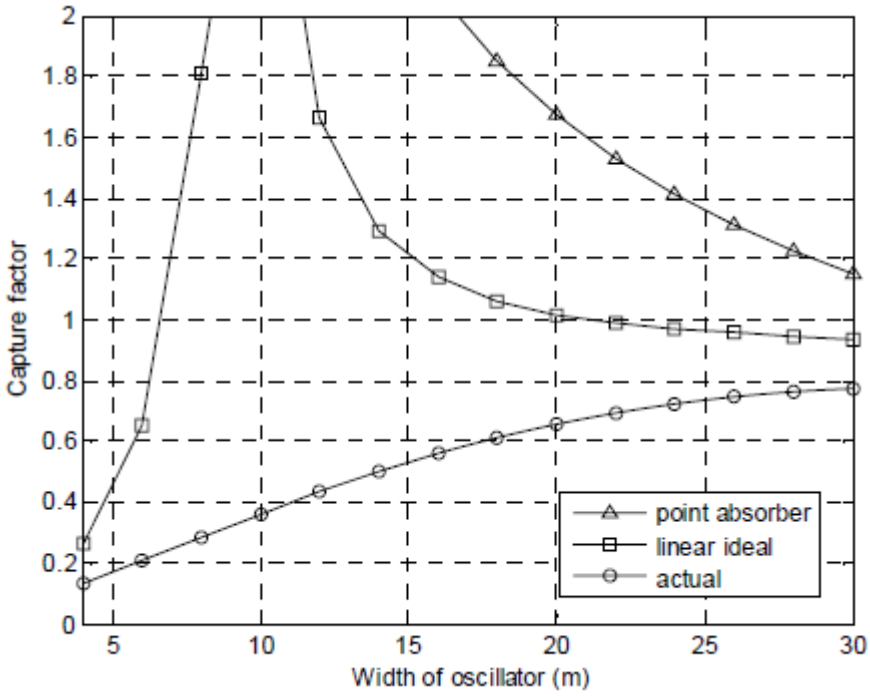


**Figure 12. Graph showing variation of capture factor with width of oscillator from Folley et al. (2007). Results are shown for an ideal point absorber and a numerical model of a flap without and with viscous losses and motion constraints ('linear ideal' and 'actual', respectively). Results were for a flap with a thickness of 2.5 metres, in a water depth of 8.0 metres and in a wave with a period of 12.0 seconds and an amplitude of 1.0 m.**

While an effective converter in head-on seas, the power-capture of a flap-type device has been shown to be sensitive to the incident wave direction (Scher, 1985; Henry, 2008). For an 18 m wide flap, for example, it has been demonstrated that the power capture is proportional to the cosine of the wave direction raised to the power of 2. Higher exponents, and hence rates of reduction, were found for wider flaps (Henry, 2008). In addition to the peaking of capture factors, this is an important limitation for the expansion of the width of the rigid flap concept. It should be noted that the power capture of the modular flap concept, on the other hand, would likely be less sensitive to the direction, due to the independence of the modules. Whether this is the case is shown later in section 6.3.4.

Research has shown that another way to increase wave torque for a flap-type WEC is to design a device that extends through the entire water column. This is achieved by using a hinge point that is close to the seabed, to maximise the lever arm length, and a freeboard, to reduce overtopping (Henry, 2008).

The device should also be placed in shallow water, due to amplification of the surge force experienced there. However, it has been shown that, due to wave breaking, there is a sharp drop off in power beyond a water depth of 10 m. There, a typical tidal range of 3 m can also have a significant negative effect on the dynamics of the flap (Henry et al., 2010).

The observations presented here have led to the definition of the design space for a flap-type WEC for a number of studies and, indeed, for this thesis (Howard, Whittaker and Doherty, 2009; van ’t Hoff, 2009; Renzi and Dias, 2013; O’Boyle *et al.*, 2015). This is a surface piercing flap, approximately 20-30 m wide and approximately 2 m thick, placed in water depths of 10-15 m (Henry, 2008; Henry et al., 2010; Whittaker, T. and Folley, 2012). It has been shown that adoption of these design criteria results in capture factors of 0.5-0.7, which are amongst the highest in WEC literature (Whittaker, T. and Folley, 2012; Babarit, 2015).

Within this design space, two full-scale prototypes have been developed and operated. These are the 315 kW rated, 18 m wide Oyster 1 and the more recent 800 kW rated, 26 m wide Oyster 800 (fugro, 2011). The latter is shown in Figure 13, which gives an impression of the size and mechanical formation of the machine.

**Figure 13. The Oyster 800 prototype being prepared for installation (Hydroworld, 2015).**

The design of these prototypes were informed by results from measurement of power capture and structural loads in scale model testing of flap-type WECs (Henry, 2008; Howard, Whittaker and Doherty, 2009). To convert these data to full scale, typically Froude or Reynolds laws are used. Gravitational forces, such as body weight and wave forces, scale with Froude laws, whereas viscous drag forces, scale with Reynolds laws. Using different laws means that gravitational and viscous drag forces contribute differently at various scales (van 't Hoff, 2009). Froude laws have been historically used to scale up physical model results from flap-type WEC testing (Henry, 2008; Schmitt *et al.*, 2012; Clabby, 2013). Using this method to accurately scale results therefore requires that the contribution of viscous drag forces to the total forces acting on the flap is consistent across scales. Viscous drag forces arise from the combination of form drag, resulting from flow separation, and friction drag, due to shear stress (Clabby, 2013).

A number of studies have compared physical modelling power capture results to full scale prototype recordings (Clabby, 2013; O'Boyle *et al.*, 2015). This exercise determines how accurately scale physical modelling predicts full scale results (O'Boyle *et al.*, 2015). In one of the most dedicated studies, measurements of the power capture of Oyster 1 were compared to those predicted by 20$^{th}$ scale model results (Clabby, 2013). It was estimated that the prototype mean power capture was 12 % greater than that predicted by the model. This was attributed to the prototype velocity being equally greater than the velocity of the model. However, this discrepancy was not attributed to sensor errors or the incorrect scaling of viscous forces. Instead, it was thought that this arose from the greater magnitude of wave excitation torque felt by the prototype due to a more seaward angular equilibrium position.

In Clabby (2013), the inaccurate scaling of viscous forces was assumed to not have a significant impact using a logical argument. Some background theory is presented here before this argument is discussed.

The classical approach to determining the viscous drag force on a body moving in unsteady flow, i.e. waves in this case, is to apply the relevant section of Morison's equation, as defined in Equation 2.

$$F_D = \frac{1}{2}\rho U|U|A_f C_D \qquad \text{Equation 2}$$

Where, $\rho$ is the density of water, $U$ is the velocity of the body relative to the fluid, $A_f$ is the frontal area of the body and $C_D$ is the drag coefficient (Techet, 2004).

Inspecting Equation 2, the terms that may change due to a difference in testing conditions are the density and the drag coefficient.

Scale model testing is usually conducted in freshwater while full scale devices operate in the sea. Freshwater has a density of 1000 kg/m$^3$; seawater has a higher density, due to salinity. This density is a function of the saltwater

content and temperature, which are strongly linked to the water depth. To illustrate the changes in density with depth, a typical ocean profile is provided in Figure 14.

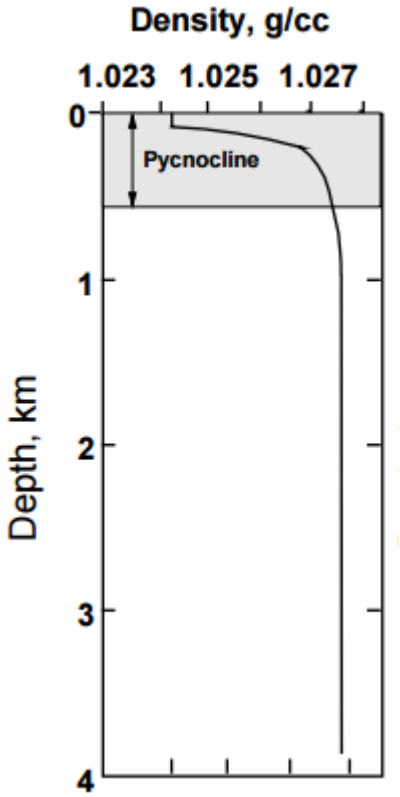


**Figure 14. Typical seawater density-depth profile (Stanford University, no date). Note that the pycnocline is the ocean layer where there is rapid change in density (Rhode Island College, no date).**

It can be seen from Figure 14 that seawater density, in the 10-20 m depth of interest for this study, is typically 1024 kg/m$^3$. This represents an increase over freshwater of only 2.4 %. Hence, it can be assumed that differences in water density do not contribute significantly when scaling drag forces.

Using Froude laws, area and velocity scale by the length factor to the powers of 2 and ½, respectively. Referring back to Equation 2, it can be seen that the product of the length scale factors associated with these terms, $L_{U,A}$, is a cube, as shown in Equation 3.

$$L_{U,A} = L_f^{\frac{1}{2}} L_f^{\frac{1}{2}} L_f^{\,2} = L_f^{\,3}$$ Equation 3

Where $L_f$ is the length scale factor, 30 for this thesis.

Therefore, if the drag coefficient is equal across scales, then the drag force will scale with the length factor cubed. Using Froude scaling, the same rule applies to gravitational and inertial forces, i.e. these forces also scale with the length factor cubed. This means that viscous drag forces would scale in the same way as the gravitational and inertial forces and so no significant deviations between model and full scale results would arise.

To test whether the drag coefficient remained constant across the scales, Clabby (2013) first calculated the corresponding Reynolds numbers. These calculations used the peak flap velocities measured in free decay tests using a 20$^{th}$ scale model. The scaling analysis also required the assumption that a rigid flap can be approximated as a flat plate. Given the high ratio of device width and height to the thickness, this is a fair assumption. For a flat plate orientated perpendicular to the flow, it was shown that, over the quoted range of Reynolds numbers, the drag coefficient was constant. This implies that the scaled drag forces and full scale values should be the same for a rigid flap.

Given these arguments, it was reasonable to assume that viscous drag forces did not significantly negatively impact the accuracy of scaling of physical model results of a rigid flap-type WECs using Froude laws (Clabby, 2013). For a modular flap-type WEC, no similar set of studies on the scaling of viscous forces on single devices has been completed (Schmitt *et al.*, 2012; Clabby, 2013; Wei *et al.*, 2015). Further discussion of the applicability of Froude scaling to the Modular Flap physical model results is therefore explored further in section 5.3.7.

Even with the development of full scale prototypes, fundamental research on the flap-type concept continues to this day. This includes, for example, further investigation of wave slamming and validation of a numerical model, as well

as further large scale prototype development (AW-Energy, 2015; Lamont-Kane *et al.*, 2015; Crooks, 2016).

The literature discussed thus far has solely consisted of work investigating flap-type WECs with a single, continuous body as their prime movers. To finish the review of rigid flap-type WEC literature, work on a design evolution of this concept in Tom et al. (2016) is discussed. Here, a flap with controllable geometry was investigated. Up to four rotatable, horizontal plates were used to alter the frontal area of the flap over time. A rendering of the flap is shown in Figure 15.

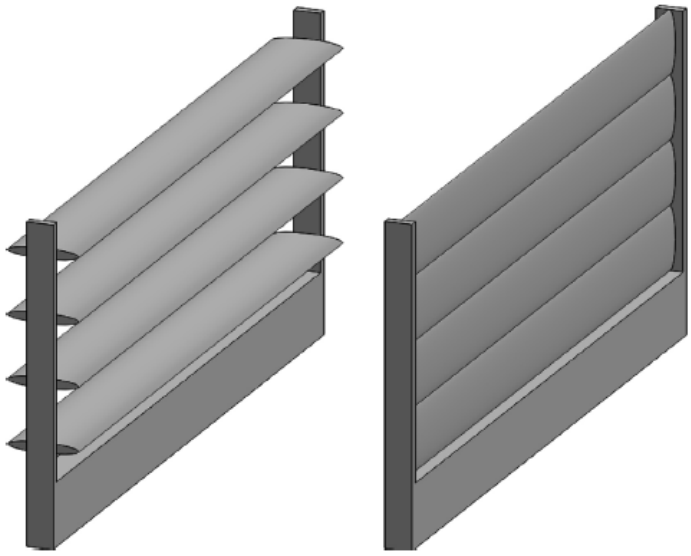

**Figure 15. Rendering of flap with controllable geometry, with plates open (left) and closed (right), from Tom et al. (2016).**

The power capture and structural loads were predicted. An approximately linear reduction in power capture was shown with each additional plate opened. However, the loading reduced faster than the rate of power decrease. This implied that loads could be shed in the most energetic sea states, whilst maintaining acceptable power capture. As in this thesis, this study represented the seeking of a design solution that reduces structural loads, whilst maintaining high power capture (Tom *et al.*, 2016).

## 2.3 Modular Flap-Type WECs

### 2.3.1 Literature Review

The Modular Flap can be viewed as a closely-packed array of rigid devices, a stand-alone device or an example of a form that could be expanded to large widths. Hence, the literature reviewed here covers all of these perspectives.

The work on devices constructed of closely packed flap modules has been predominately influenced by two applications: the first, as a means of flood protection and the second, as a WEC. While research into the latter has clear relevance here, the former is important too. This is because many of the related studies have assessed the motions of the flood defence modules in response to waves. Hence, findings from these studies can be used to help understand the responses of a modular flap-type WEC.

Research into a modular flap structure for use in flood protection has had its practical routes in a project that is currently underway at the inlets of the Venice Lagoon, in Italy. The primary purpose of the project is to protect Venice against high tides. The project consists of barriers of submersible, closely spaced flaps. The flaps remain horizontal in calm water but float up to an inclined equilibrium position when required (Windsor, 2015a).

The barriers will span the entire inlets of the lagoon, have a total length of 1.6 km and consist of 78 flaps (Dias, F. and Sammarco, 2013). Each flap is 20 m in width, 30 m in height and 5 m in thickness, and weighs 300 tonnes. A photograph of a section of a barrier is shown in Figure 16.

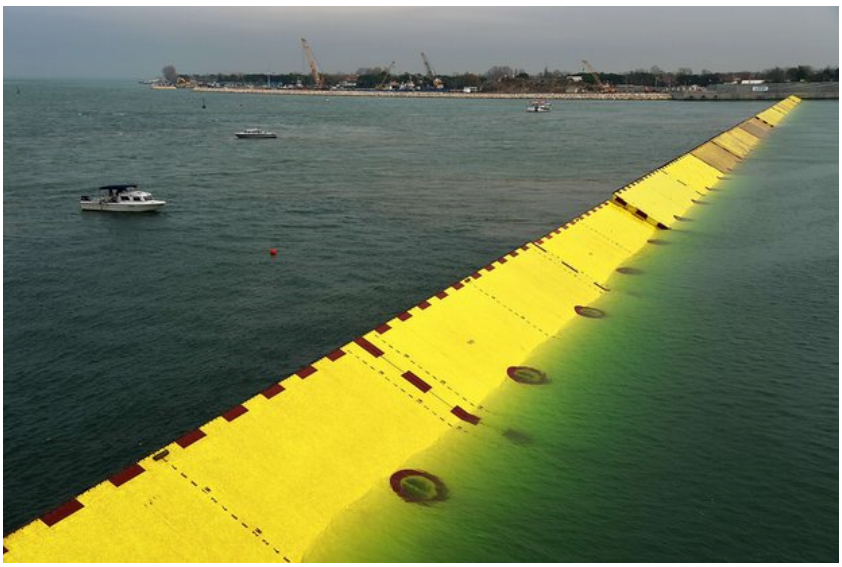

**Figure 16. Venice Lagoon flood protection barrier (Windsor, 2015b).**

The design of the project has been informed by a large body of physical and analytical modelling that dates back to the 1970s (Mei *et al.*, 1994; Adamo, A. and Mei, 2005; Dias, F. and Sammarco, 2013). One of the main purposes of the research was to measure the rotations of the flaps in response to wave action.

Extensive physical modelling campaigns were carried out in the years 1986-2002. The facilities included wave channels and tanks, the number of gates tested ranged from 2-22 and the model scales 10-60 (Dias, F. and Sammarco, 2013). The tests were conducted with models that extended across the full widths of the experimental facilities.

Early analytical work modelled the barriers in channels of infinite length (Mei *et al.*, 1994), followed by Adamo and Mei (2005) extending the theory to allow one side of the barrier to be open to the ocean. This geometry was more like the Venice Lagoon and indeed the device arrangement in this thesis.

Consideration of a modular device for power extraction, instead of flood protection, forms a much more recent body of work. The research has exclusively used mathematical modelling, applying analytical and CFD approaches. The geometries of the devices studied have varied from multiple

barriers in channels to single devices in the open ocean (Michele *et al.*, 2015; Abadie, T. & Dias, 2016; Sarkar, Doherty and Dias, 2016).

Of the analytical works and perhaps amongst all literature, the most relevant piece of work for this thesis is arguably that by Sarkar et al. (2016). In this paper, the power-capture of a modular flap-type WEC was assessed. The fluid was assumed to be inviscid and incompressible and the flow irrotational. The devices were assessed in regular, head-on waves with amplitudes of 0.4 m and periods 5-20 s.

The modular device in this study was made up by six cylindrical modules, with a total width of 24 m and a 0.1 m gap between modules; the rigid device was modelled as a thin plate. The devices operated in a depth of 13 m. These dimensions are therefore similar to those of the devices studied in this thesis. A diagram of the concepts is provided in Figure 17.

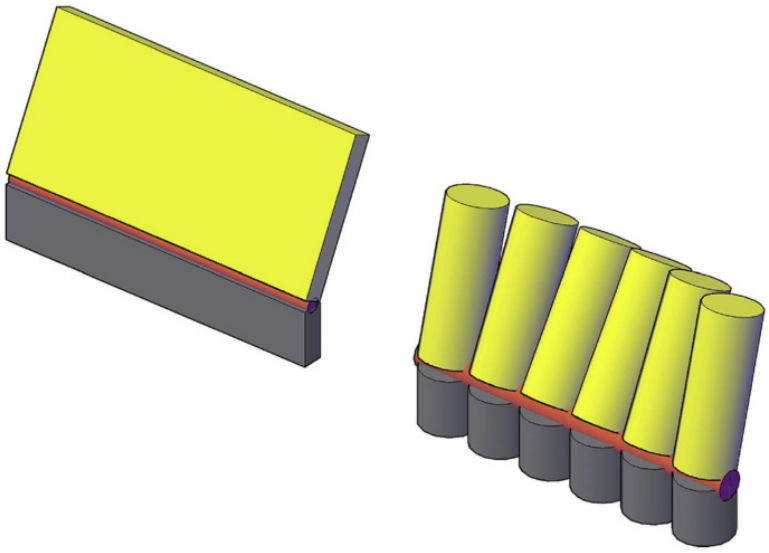

**Figure 17. Renderings of rigid flap (left) and modular flap (right) concepts studied in Sarkar et al. (2016).**

While this study provided an insight into the potential of the device and details on relative module power production, there were limitations of the modelling that was used, such as not considering nonlinear and viscous effects and irregular or directional waves (Sarkar, Doherty and Dias, 2016). This is a

common downside to the analytical studies that have been conducted on a modular flap WEC (Sammarco, Michele and D'Errico, 2013; Michele *et al.*, 2015; Sarkar, Doherty and Dias, 2016). In the real ocean, viscous, nonlinear effects, for example, would alter the behaviour of a device. As was shown in section 2.2.2, this severely reduces any peaks in power-capture that would be expected due to resonance effects (Folley, Whittaker and van't Hoff, 2007).

The need for studies that consider viscous and non-linear effects has partly been satisfied through the use of CFD by Abadie & Dias (2016). This was an investigation on the dynamics of a modular flap, the individual modules and of a single rigid flap.

The study considered the applied pitching moments and the resulting rotations for the individual modules, as well as the total surge and heave loads acting on the structure.

The device was a $30^{th}$ scale model made up of 6 box-shaped modules with dimensions $0.12 \times 0.4 \times 0.18$ m. Regular waves were generated, with periods of 1.5-2.5 s and wave amplitudes ranging from 0.04-0.12 m. Both of these sets of parameters were similar to those used in this thesis. Unlike in this thesis, however, difference values for the spacing between modules were used, of 0-20 % of the total width of the device without gaps (Abadie, T. & Dias, 2016).

This work provided useful insight into the rotations and loading on the modular flap. A key missing part however was that the modules did not have PTO damping applied to them and therefore the power capture was not assessed (Abadie, T. & Dias, 2016).

### 2.3.2 Summary of State of the Art

From the literature reviewed in section 2.3.1, several key findings that are of relevance to this thesis were made. These are summarised here, beginning with those produced in the works related to the Venice Lagoon flood defence.

A key finding from Venice Lagoon work was the identification of a resonance phenomenon in the flap barrier. This was characterised by the amplification of the motion the flap gates and adjacent modules being out of phase with each other. A photo showing this phenomenon, taken during a physical modelling campaign, is provided in Figure 18.

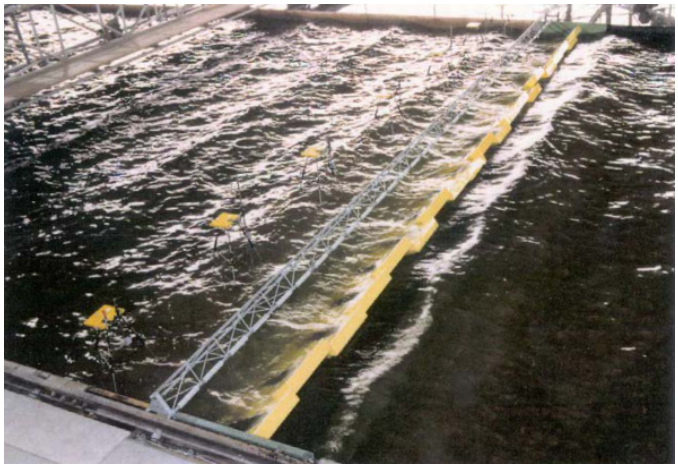

**Figure 18. Photograph showing physical modelling of barrier and fundamental first out of phase mode (Dias, F. and Sammarco, 2013).**

A further characteristic of the resonance phenomenon, when fully developed, was that the motions had a period that was twice that of the incident wave period. Results showing the doubling of the period of oscillation and the increase of amplitude, are shown in Figure 19.

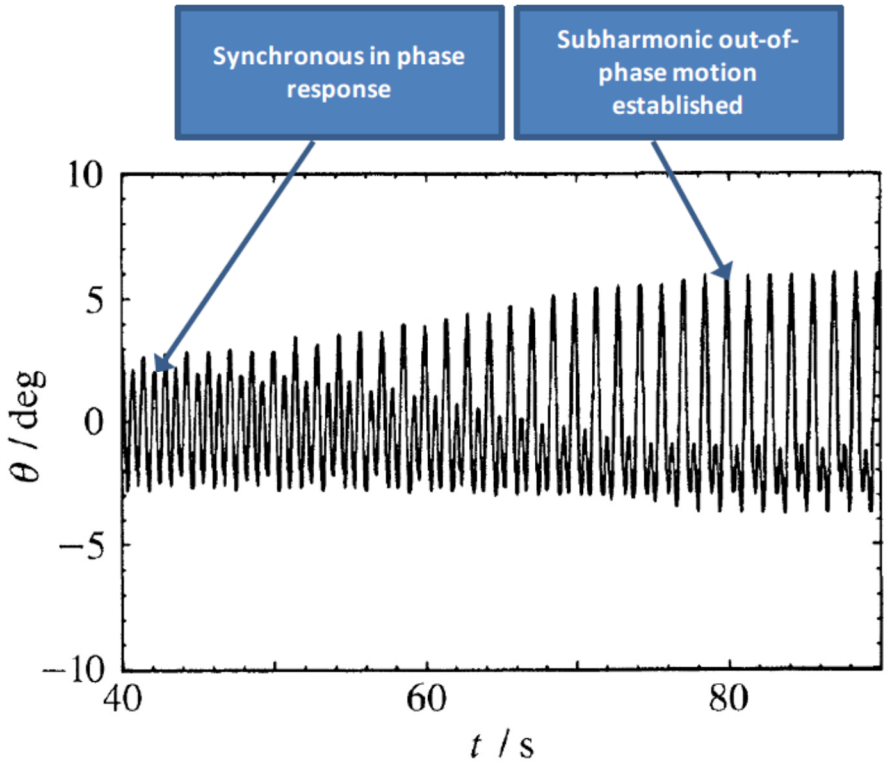


**Figure 19. Out-of-phase resonance of wave barriers from physical model results of two-gate barrier, showing doubling of the period of oscillation and the increase of amplitude. Y-axis is rotation and x-axis is time (Mei *et al.*, 1994).**

Mei et al. (1994) developed analytical theory to help explain the resonance phenomena for a two-gate system. The oscillation of the system was shown to be a natural mode of the barrier and water coupled together. Subharmonic motions occurred when the incident wave period was half the natural period of the system (Mei *et al.*, 1994).

In Adamo and Mei (2005), analytical modelling was used to study a 20 flap barrier in regular waves. The wave periods were varied between 4 and 60 s, covering the vast majority of expected incident periods. The maximum responses of the gates, due to resonance are illustrated in Figure 20.

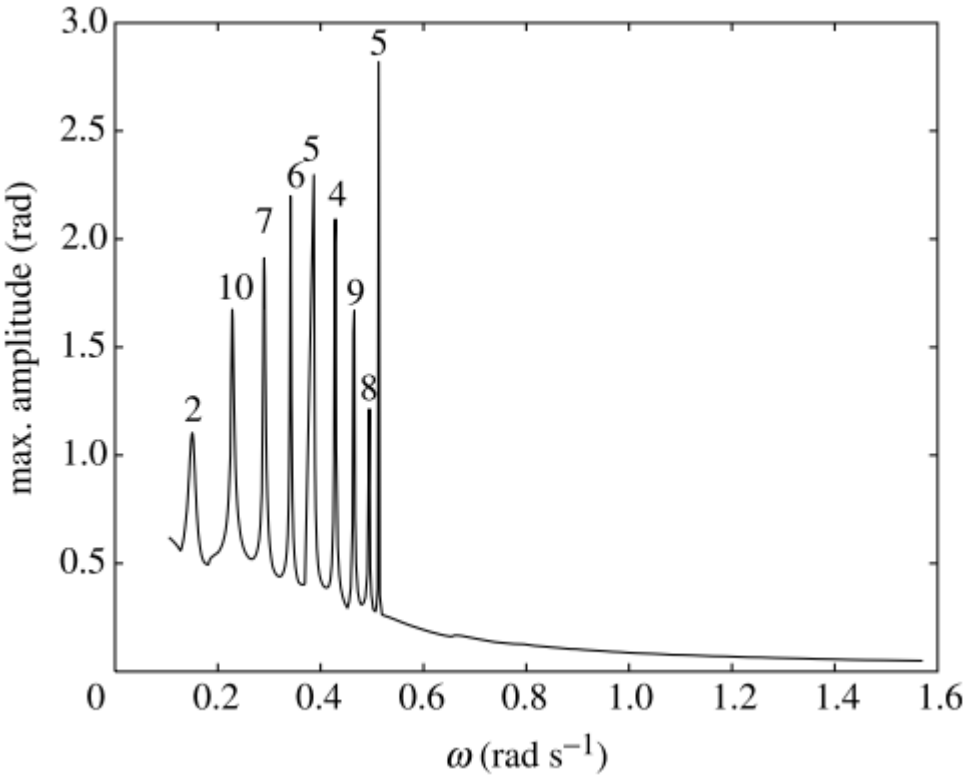


**Figure 20. Maximum amplitude of gate displacement against the frequency of incident wave, $\omega$. The number above the peak identifies the gate which has the maximum amplitude (Adamo, A. and Mei, 2005).**

As shown in Figure 20, the highest motion amplitudes of each gate occurred at incident wave frequencies of less than 0.5 rads$^{-1}$, i.e. greater than wave periods of 12 s. For typical wave energy sites, the majority of wave energy occurs at peak periods of less than 12 s (Babarit *et al.*, 2012). This fact suggests that resonance of a flap gate barrier in a channel of this width may only have a strong effect for sites characterised by wave spectra with energy at periods that are higher than the typical range. The narrowness of each resonance peak in Figure 20 also indicates that contributions by each one to random incident waves with a broad bandwidth would not be significant (Adamo, A. and Mei, 2005). These are positive conclusions for flood defence applications but arguably negative for wave energy extraction. It suggests that this resonance phenomenon would not have a major effect on the power production of a modular flap system.

It has been argued that the amplified motions of flaps may, in fact, be exploited through careful design. For a given relevant wave spectrum, the number of flaps in a barrier could be chosen to have all of their natural periods in the energetic band of the energy spectrum. This would likely result in more energetic motions and therefore high power production (Dias, F. and Sammarco, 2013).

The studies focused on closely spaced flaps discussed thus far have been on undamped devices, i.e. with no power production. While these provide insights into the modular WEC concept, of most relevance for this thesis are studies where damping has been applied (Sammarco, Michele and D'Errico, 2013; Michele *et al.*, 2015; Sarkar, Doherty and Dias, 2016).

The studies found that the power-capture of a modular flap-type WEC was strongly dependent on the PTO damping applied. Michele et al (2015), for example, found that with high PTO damping on a barrier, the efficiency of the system was dominated by the exciting torque due to diffracted waves. This is similar to the behaviour of a single, rigid flap-type WEC (Henry, 2008). With low PTO damping however, the efficiency of the device was dominated by the resonance effects, due to excitation of the natural modes of the system (Michele *et al.*, 2015).

Sarkar et al (2016) extended the literature by investigating the effects of damping the modules differently. Power-capture was compared to an equivalent width rigid flap. With each module damped equally, both devices achieved similar levels of power-capture. However, using different damping on each module, at wave periods greater than 9 s, the modular flap outperformed the rigid flap, due to the occurrence of multiple resonances. These phenomena occurred due to the closely packed nature resulting in strong interactions.

It was also found that the wave excitation torque and, consequently, power-capture increased towards the central modules. At the edge, the difference in

the velocity potential tended to zero resulting in low excitation torque (Sarkar, Doherty and Dias, 2016).

Finally, the work by Abadie and Dias (2016) provided an insight into the effects of spacing on the flap motions and global loads. It was shown that the oscillation pattern of the modules depended on the wave period and module spacing. For 20 % spacing, i.e. with gaps of similar width to that of a module, the flaps appeared to move almost independently. The main difference between the modular and rigid flaps was observed for a spacing of 5 %, which was most similar to the device in this thesis. For this device, surge loads were greater for the modular flap at the shorter wave periods but smaller at the longer periods; heave loads were very similar. The maximum rotation was achieved by different modules for different wave periods. At the shorter wave periods, for example, the maximum rotation was achieved by the outer modules (Abadie, T. & Dias, 2016).

## 2.4 Scope for Knowledge Contribution

There is a considerable body of work on single, bottom-hinged, nearshore, seabed mounted flap-type WECs, using a range of physical and mathematical models. Research topics have included the evaluation of motions, power production and structural loads and have contributed to the knowledge required to design two full scale prototypes (Folley, Whittaker and van't Hoff, 2007; Henry, 2008; Howard, Whittaker and Doherty, 2009; Clabby, 2013; Renzi and Dias, 2013; Schmitt, 2013; O'Boyle *et al.*, 2015).

Research gaps in the rigid flap literature include the provision of a controllable PTO damper for scale modelling. There has also been limited study of the effects on foundation loading of PTO damping torque and the direction of a wave.

The research on large numbers of multiple flap-type devices is less extensive. The majority of the studies have also been on undamped devices, for the

application of flood protection (Mei *et al.*, 1994; Adamo, A. and Mei, 2005; Dias, F. and Sammarco, 2013). The finding of most relevance to this thesis has been the identification of a resonance phenomenon, of amplified motions occurring at twice the period of the incident wave.

Until recently, there has therefore been a research gap for a structure made of closely-spaced flaps for wave energy extraction. A select number of analytical studies have partially addressed this gap (Sammarco, Michele and D'Errico, 2013; Wei *et al.*, 2015; Sarkar, Doherty and Dias, 2016). They have focused on exploitation of the resonance phenomenon. The studies are limited by their use of small amplitude waves and a lack of consideration for viscous and non-linear effects. Abadie and Dias (2016) have partially addressed the latter limitation through the application of CFD. However, this work does not assess the power extraction of the device or the effect of wave direction.

Physical modelling of a modular flap-type WEC is used in this thesis to address these research gaps. The use of this type of modelling accounts for viscous and non-linear effects. It will be used to assess power-capture and foundation loads in a range of conditions, including head-on and off-angle waves. The requirement for controllable damping also necessitates research into improved PTO damping methods.

# 3. Physical Model System

## 3.1 Introduction

Physical modelling of a WEC is the testing of a device, typically to predict full scale measurements, such as power production. This form of analysis is an important step in the assessment of the performance, feasibility, reliability and survivability of a WEC concept on its way to full scale deployment (Sheng, Raymond and Lewis, 2014). Physical modelling is also a crucial step for calibration and validation of mathematical models (van 't Hoff, 2009).

Physical modelling is conducted at a large range of scales and in a number of facility types, for example 1:100 in small flumes to 1:10 in the largest wave tanks (Falcão, 2014). For concept evaluation, as was carried out for this thesis, it is recommended that testing is carried out with a scale in the range 1:25-100 (European Marine Energy Centre, 2009). In this project, 30 was chosen as the testing scale. This decision was made after consideration of many restricting factors, such as the available wave tank facilities and practical PTO damping limits.

This chapter aims to provide the reader with the key technical information on the physical modelling system that was developed for testing. In this case, a system includes the scale model, instrumentation and the facilities in which the model was tested. The design process is presented both to provide information on the key steps that were taken for this thesis and to offer guidance to other physical modellers.

The design process began with definition of the requirements of the system, as described in section 3.2. From these, the testing facility was selected, which is detailed in section 3.3. The core of a physical WEC model, the instrumentation, including the sensors, dampers and data acquisition (DAQ) systems, were then selected and are presented in sections 3.4, 3.5 and 3.6, respectively. Following this, the design of the physical components commenced. This was carried out

in several iterations, with each key stage of the design verified through testing. The final instrumented model is then described in section 3.7. This is followed by an assessment of the costs of the model, providing a financial context, in section 3.8. The chapter is then drawn to a close with a summary in section 3.9.

## 3.2 Physical Model System Requirements

The definition of the key requirements of the physical model system was crucial at the beginning of the design process. This allowed the design to be completed in a holistic way. The key design requirements were as follows:

- Replication of full scale water depth between 10 and 15 m.
- Generation of wave conditions with energy levels typical of sea states at sites of interest for wave energy development, for example with a full scale period range of 5-13 s and amplitude of 1 m (Babarit *et al.*, 2012).
- Generation of head-on and off-angle waves.
- The model was to consist of a bottom-hinged, simplified box-shaped flap with a fixed connection to the wave tank floor.
- The top of the flap, at mean water level, was to pierce the water surface.
- The target flap dimensions, provided in Table 1, were to be similar to the industry benchmark, Aquamarine Power Ltd's Oyster 800.
- The number of constituent flap modules had to be as high as practicably possible, to maximise the difference between the rigid and modular model forms.
- The model had to be safe and practical to install, operate, maintain and remove.
- The model had to be able to extract, at the very least, mechanical power from the waves using a damper.

- The model had to incorporate sensors that allowed measurement of rotation and angular velocity, the damping torque that was applied to the flap and six degree-of-freedom loads acting on the whole structure.
- The sensor measurements had to be recorded using a DAQ system, at a sufficiently high frequency and with a file format that allowed efficient analysis.
- The model had to produce results that were repeatable enough to allow for a small number of tests to be carried out, for each change of variable, to minimise the uncertainty of results.
- The costs of the model had to be within the budget available.

**Table 1. Target dimensions for physical model, based on Oyster 800 machine. Values taken from Babarit et al. (2012).**

| **Dimension** | Width | Seabed to hinge | Hinge to MWL ('draft') | MWL to top of flap ('freeboard') | Thickness |
|---|---|---|---|---|---|
| **Full Scale Value (m)** | 26 | 4.0 | 9.0 | 3.0 | 2.0 |
| **30$^{th}$ Scale Value (m)** | 0.87 | 0.13 | 0.30 | 0.1 | 0.067 |

## 3.3 Wave Tank

This section details the wave tank employed during physical testing of the modular flap type device. The facility was the Queen's University Belfast (QUB) Portaferry wide wave basin, located in Northern Ireland. The tank is rectangular in plan. On one side of the tank are twenty-four 0.5 m wide wave-generating paddles, with the remaining sides featuring wave-absorbing beaches (Queen's University Belfast, 2016). A photograph of the tank in operation is provided in Figure 21.

**Figure 21. Photograph of Portaferry Wave Tank, showing side absorbing beaches and off-angle waves.**

The wave paddles were classified as top-hinged, displacement piston, sector carrier types and were supplied by Edinburgh Designs Ltd. The paddles were made up by ‘piston paddle’ and ‘sector’ parts.

The horizontal motion of this type of paddle is suited to generating shallow water waves, which are characterised by having large horizontal water particle amplitudes of motion. The sector section creates no appreciable wave behind the paddles, therefore achieving high controllability of the generated wave front (Edinburgh Designs Ltd, 2016a). A diagram of such a paddle is provided for reference in Figure 22.

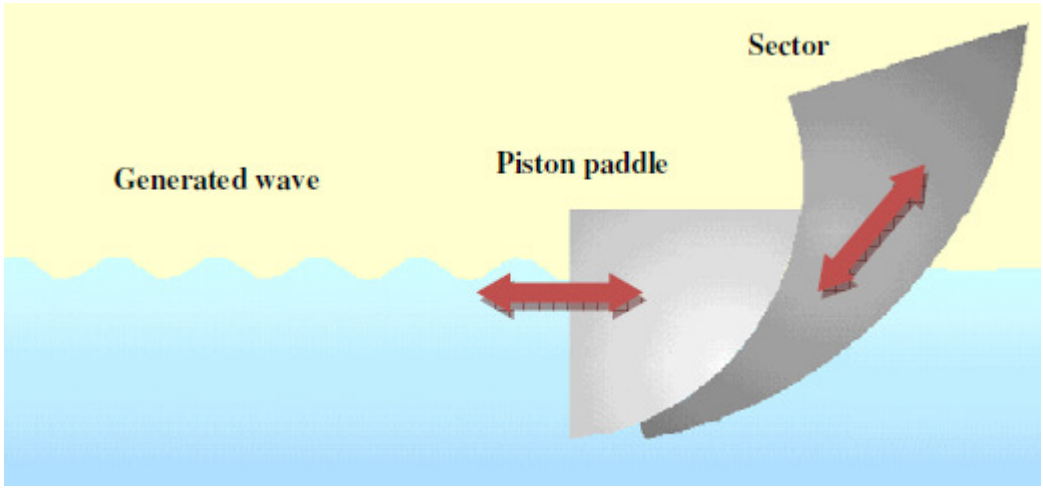


**Figure 22. Diagram of piston type wave paddle (Henry, 2008).**

The paddles were controlled independently using a belt connected to a servo motor. Control of each paddle allowed directional waves to be generated, as is illustrated in Figure 21, through adjustment of the relative phases of motion of the paddles (Henry, 2008).

The tank also has features that minimised the magnitude of wave reflections, thus best simulating the conditions in the open ocean. This was achieved using the wave paddles, which has a force feedback system, and gravel and geotextile beaches on the perimeter. The area in front of the paddles also had parabolic sloped walls, to increase wave height homogeneity (O'Boyle, 2013).

The testing area in the tank consisted of a flat region in front of the paddles, followed by a discontinuous slope constructed with concrete slabs. For an appreciation of all of the key dimensions of the tank, a plan view diagram is provided in Figure 23. Also indicated are the position and relative dimensions of the physical model.

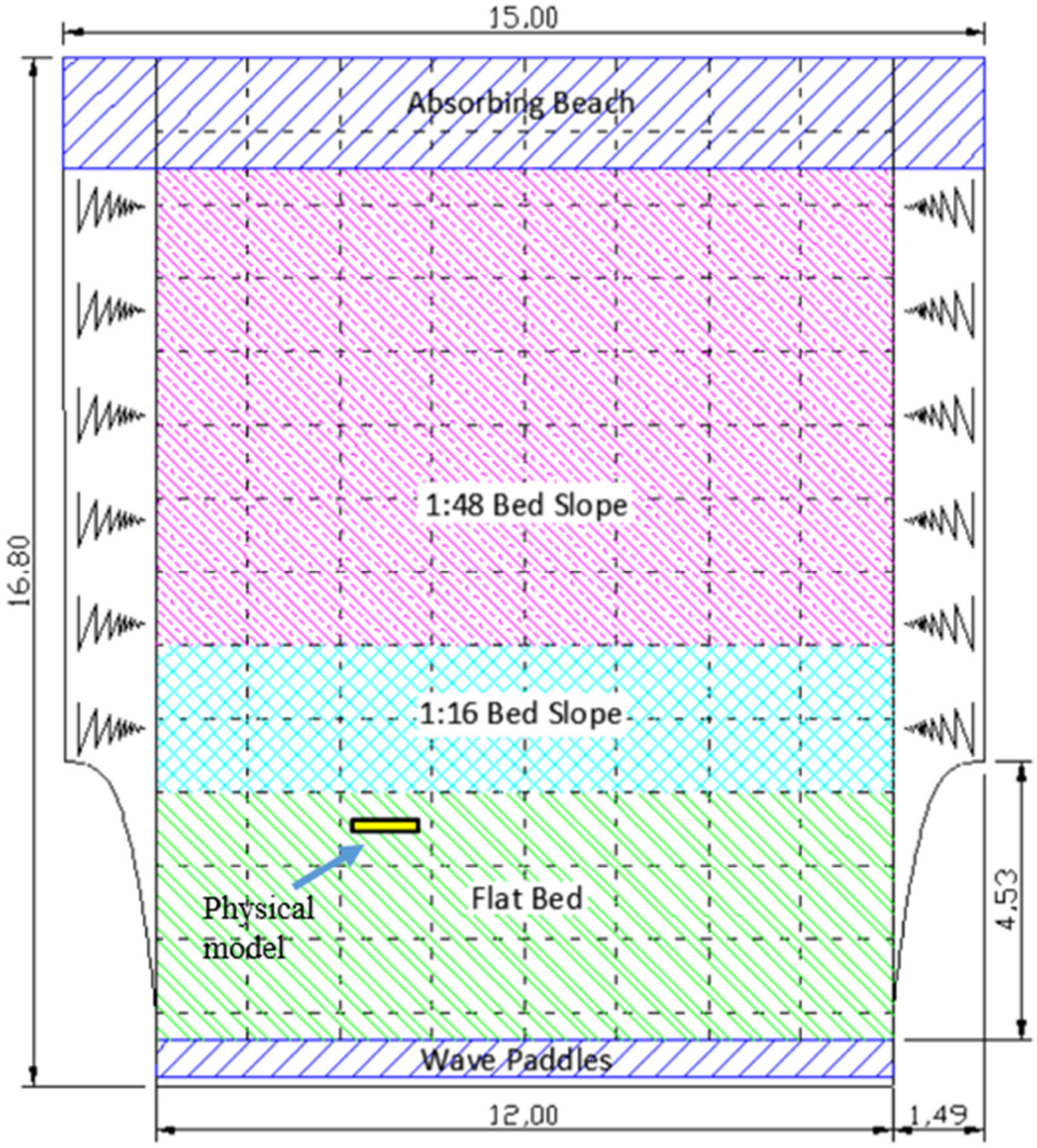


**Figure 23. Plan view of Portaferry wave tank, also showing gradients of slopes. Dimensions are in m (O'Boyle, 2013). Also indicated is position of physical model, with its dimensions approximately to scale.**

One of the key dimensions shown in Figure 23 was the testing area width, 12 m. The width is significant when consideration is given to the variable the 'blockage ratio'. This is the ratio of model to tank width and gives an indication of the level of blockage effects that will be expected in testing. In order for model testing to predict the behaviour of a device in open ocean conditions, it has been recommended that blockage ratios should not be larger

than 0.2 (Renzi and Dias, 2013). Using this guidance, this set the maximum flap model width to be 2.4 m.

Figure 23 shows that the model was positioned close to the back of the flat section of the tank, in between the centreline and one side. It was partly positioned there so that the model would be a reasonable distance away from both the edge of the wave crest and side of the wave tank when generating off-angle waves. It was also placed as far away from the paddles, to allow for minimisation of the effects of evanescent waves (Clabby, 2013). Finally, the position was off-centre to allow for identification of any cross tank reflections (P. Lamont-Kane, 2015a).

It is also important to note that the maximum operational depth of the wave tank was 0.65 m (Queen's University Belfast, 2016). The testing was conducted well within this range, at a depth of 0.463 m, or 13.9 m at full scale.

## 3.4 Sensors

### 3.4.1 Introduction

The physical model system incorporated a range of sensors, for both measuring the applied wave conditions and the dynamics of the model. The latter included the rotation of and damping torque applied to each module and the foundations loads acting on the whole model.

Each of the sensors used an amplifier, to increase the signal to noise ratios of the measurements. However, the details of these amplifiers are out of the scope of this thesis.

The sensors had several requirements, which were as follows:

- High accuracy, for example maximum 3 %;
- High signal quality, with an acceptable noise level and minimum drift;

- Compatibility with available DAQ systems, such as of signal type, cable connectors, etc;
- Relatively easy incorporation into rest of physical model, for example by being compact in physical size;
- For rotation and torque sensors, the mass should not be a large proportion of the total mass of a module, to not have a significant effect on the flap dynamics;
- An ability to be used in water, rated to at least IP67 if required for submergence;
- An expense within budget;
- Ideally, a tried and tested performance.

This section describes any further specific sensor requirements and descriptions of the sensors that were chosen to match these criteria.

### 3.4.2 Wave Measurement

To characterise the wave conditions at the model position in the wave tank, the surface elevation was recorded. This was measured using industry standard sensors, resistance wave probes, which were supplied by Edinburgh Designs Ltd. These probes operate by measuring the resistance of the water between two parallel stainless steel rods. The resistance is proportional to the immersion depth, hence allowing the surface elevation to be measured (Edinburgh Designs Ltd, 2016b). Photographs, of a single wave probe and an array of sensors, is provided in Figure 24 and Figure 25, respectively.

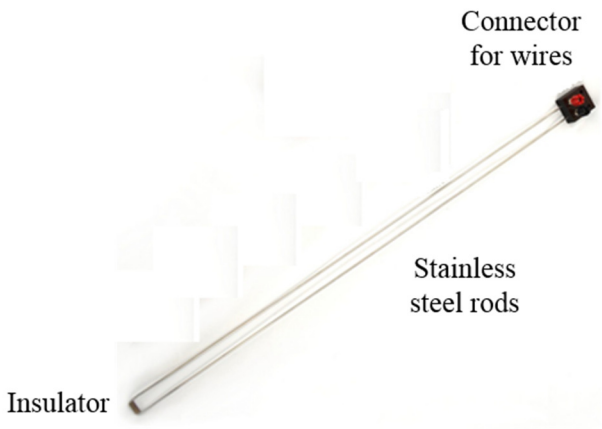


**Figure 24. Photograph of wave probe, showing mechanical construction (Edinburgh Designs Ltd, 2016b).**

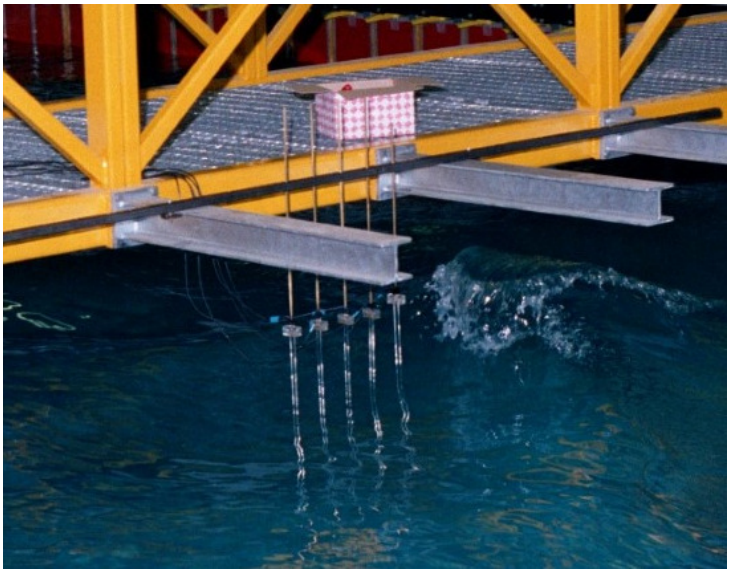

**Figure 25. Photograph of wave probes being used for measuring wave surface elevation (Edinburgh Designs Ltd, 2016b).**

The achievable measurement accuracy of the wave probes was 0.1 % and was therefore not considered to be a significant source of uncertainty in later analyses (Edinburgh Designs Ltd, 2016b).

### 3.4.3 Rotation Measurement

The rotation of each flap module was measured, primarily for use in the power capture calculation process discussed in sections 5.3.3 and 5.3.5.

Considering the requirements specified in section 3.4.1, previous experience within the QUB research group and availability, two rotation sensor types were considered for use.

The first sensor was a Vicon Bonita motion tracking system (Vicon, no date). This used three cameras, each with infra-red LED lights around the lenses. The light from the LEDs was reflected by small, low density target balls placed on the moving objects. From the use of at least three cameras, the position and rotations of the bodies could be calculated.

A key advantage of the sensor was that the reflective target balls could be placed relatively easily on flap modules. This meant that the sensor could be used without significant model design efforts, required for more intrusive sensors.

The accuracy of the sensor for measuring rotation was not available to the author and so was independently assessed. This was carried out by comparing static motion-tracking system results to measurements from an independent sensor, a digital protractor, shown in Figure 26.


**Figure 26. Digital protractor used for providing reference angles for rotation sensor assessment (Mitutoyo, 2012).**

The stated accuracy of the digital protractor was +/-0.2 degrees (Mitutoyo, 2012). For a typical 60-degree rotation range, +/-30 degrees, this represents an accuracy of 0.3 %. The reference sensor was therefore assumed to have negligible uncertainty.

Across eight readings between +/-90 degrees, the mean absolute error between the motion-tracking system and inclinometer was 1.3 degrees. Again using the 60-degree range, this represents an accuracy of 2.2 % (Wilkinson, L. and Pernod, 2014).

The second sensor was an induction-based instrument that measured the position of a rotating metallic activator over 360 degrees. The activator would be attached to the shaft at the hinge of a flap module, with the sensor housed 1.5 mm away. This non-contact method of sensing provided long term reliability. Further advantages of the sensor were its relatively small size, being cylindrical with a 38-mm diameter and 16-mm depth. It was also submersible, being IP67 rated (Gill Sensors and Controls, 2016). The QUB research group also had extensive experience with this sensor, most of which had been positive, which provided verification of its merits (O'Boyle *et al.*, 2015).

The model of the sensor was the 'Blade 360' and hence, to differentiate between the rotation sensors, is referred to here as the 'blade rotation sensor' (Gill Sensors and Controls, 2016). A rendering of the sensor and activator is shown in Figure 27.

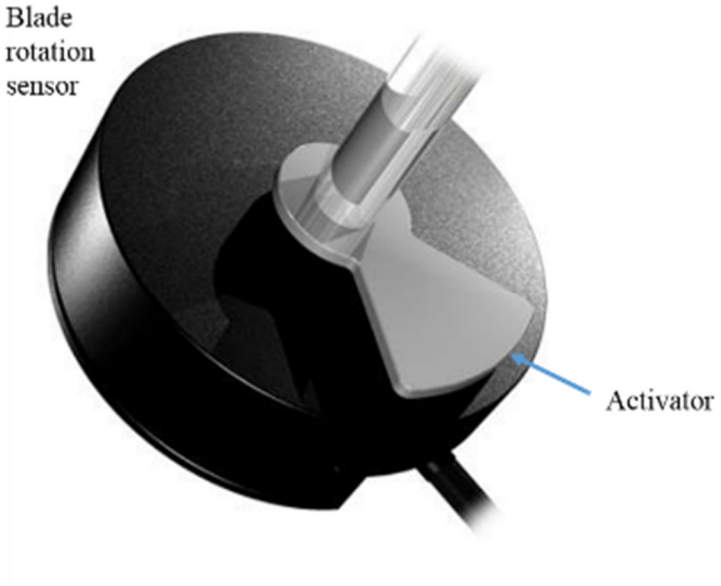


**Figure 27. Rendering of blade rotation sensor and activator (Gill Sensors and Controls, 2016).**

The accuracy of the sensor, quoted by the manufacturer, was 0.5 degrees (Gill Sensors and Controls Ltd, 2015). Again, comparing to the typical rotation range of 60 degrees, this equates to an accuracy of 0.8 %.

An earlier independent study also assessed the sensor accuracy by comparing two blade rotation sensors measuring the motion of the same flap. However, it was found that the accuracy was, in fact, up to 2 degrees, equating to a relative accuracy of 3 % (Perrin, 2012).

The accuracies of the motion-tracking system and blade rotation sensors were found to be similar, both 2-3 %. However, the motion-tracking system would have represented a lower cost option, since the equipment for it was already available to the author. Nonetheless, the crucial advantage for the blade rotation sensor was that it produced uninterrupted data (Wilkinson *et al.*, 2014; Wilkinson, L. and Pernod, 2014). This was an issue for the motion-tracking system due to restricted visibility of the reflective balls in certain testing conditions. This resulted from immersion into water, due to rotation and wave overtopping, and by relative module motion (Wilkinson *et al.*, 2014; Wilkinson, L. and Pernod, 2014). It was for these reasons that the blade rotation sensor was opted for, over the motion-tracking system, for use in the physical model.

### 3.4.4 Torque Measurement

To generate mechanical power, each flap module had to do work against a source of resistive torque. This torque was provided by a damper system and bearings. To determine the mechanical power extracted by each flap module, using the analysis in section 5.3.5, it was necessary to measure this torque.

The sensor chosen to measure the torque had a bespoke design to allow greater flexibility in its specifications, compared to buying an off the shelf component. The overall design originated from guidance from previous physical modelling works where the sensor concept was used with no negative experiences related

to reliability and practicality (Henry, 2008; Perrin, 2012; Clabby, 2013). However, the bespoke nature of the sensor meant that, unlike for some of the other sensors used in this study, the accuracy could not be derived easily from manufacturer technical documents. Nevertheless, a previous study determined the accuracy as approximately 1 %, which was therefore deemed acceptable for this research project (Perrin, 2012).

The sensor consisted of mechanical and electronic components. The mechanical components were designed by the author and machined by technicians in the QUB mechanical workshop, while the acquisition, including specification and assembly, of the electronic components was out-sourced (Vishay, no date; Synectic Electronics, 2016).

The mechanical part of the sensor was machined as two parts, a thin-walled tube with a housing mounting surface and a splined shaft. The parts were then permanently connected using an interference fit. Damping torque applied to the shaft caused the thin-walled tube to twist slightly. This torsion was measured using strain-gauges bonded around the thin-walled tube. The gauges were supplied and bonded by Vishay Measurements Group UK Ltd (Vishay Precision Group Inc, 2015). The strain-gauges were arranged in a full Wheatstone bridge of four gauges, to provide accurate measures of resistance changes. A rendering of a cross-section of the torque sensor sub-assembly is provided in Figure 28.

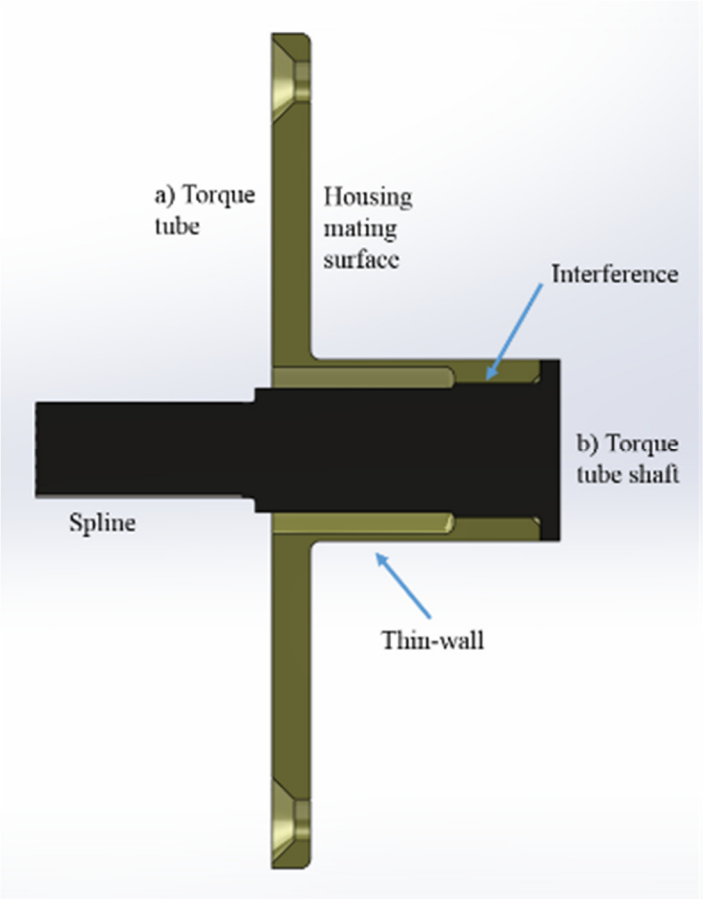


**Figure 28. CAD rendering of cross-section of torque sensor sub-assembly of a) torque tube and b) torque tube shaft, showing key features.**

The dimensions of the mechanical components of the torque sensor were set so that there was sufficient space for the electronic components and that the material stress and strain limits were not exceeded. The principal features that were designed in this way were the thin-wall tube, interference fit and the splined shaft. In the same order, the following text provides the calculation methods that were used for determining the dimensions of these features.

The dimensions of the measuring part of the sensor, the thin-wall tube, were determined to allow for sufficient room for the strain gauges and to ensure that application of the expected torque did not result in exceedance of the stress and strain limits of the stainless steel and the strain gauges. It was also important that the thin-wall was not made too stiff and hence not sensitive enough.

Once the dimensions for providing room for the strain gauges on the thin-wall were determined, its thickness and radius were set. They were chosen to be as low as possible to maximise sensitivity and hence the precision of the measurements. The mechanical restrictions for how low the thickness could be were the strength of the stainless steel and from manufacturing judgement by the QUB technicians. The wall thickness was set at 0.75 mm, with outer, $r_o$, and inner, $r_i$, radii of 9.5 mm and 8.75 mm, respectively. The thin-wall design was deemed to be sufficiently strong by calculation of the torsional factor of safety, *FS*. A relatively high factor of safety, for example greater than 3, was desired, to account for unexpected events, such as dropping of the sensor. *FS* was calculated by first determining the polar moment of inertia, *J*, in $m^4$, using Equation 4.

$$J = \left(\frac{\pi}{2}\right)(r_o{}^4 - r_i{}^4) \qquad \text{Equation 4}$$

Where, $r_o$ and $r_i$ were the outer and inner radii of the thin-wall tube, respectively. Using the stated radii values, *J* was calculated as $3.59 \times 10^{-9}$ $m^4$. The torsional stress per unit of applied torque, $\sigma'$, in Pa/Nm, was then calculated using Equation 5, giving a value of $2.65 \times 10^6$ Pa/Nm.

$$\sigma' = \frac{r_o}{J} \qquad \text{Equation 5}$$

The maximum expected torsional stress, $\sigma_{max}$, in Pa, was then determined using Equation 6.

$$\sigma_{max} = \sigma' Tc_{max} \qquad \text{Equation 6}$$

Where, $Tc_{max}$ was the maximum expected applied damping torque, in Nm. As indicated in section, 3.5.1, this value was approximately 4 Nm at model scale. $\sigma_{max}$ was therefore calculated as $1.08 \times 10^7$ Pa, i.e. 10.8 MPa. *FS* was then calculating using Equation 7.

$$FS = \frac{Y_s}{\sigma_{max}} \qquad \text{Equation 7}$$

Where, $Y_s$ was the yield shear strength of stainless steel. $Y_s$ was determined using the von Mises yield criterion, stated in Equation 8 (University of Florida, 2009).

$$Y_s = \frac{Y_t}{\sqrt{3}} \qquad \text{Equation 8}$$

Where, $Y_t$ was the tensile yield strength, taken as 430 MPa (Azo Materials, 2001). $Y_s$ was hence calculated as 250 MPa. $FS$ was therefore equal to 23.2. This shows that there was very little chance of the tube failing due to torsion.

The maximum expected torsional strain, $\varepsilon_{max}$, was also calculated, using Equation 9, to minimise the chance of the rating of the strain gauges being exceeded, whilst providing sufficient sensitivity.

$$\varepsilon_{max} = \frac{\sigma_{max}}{E} \qquad \text{Equation 9}$$

Where, $E$ was the Young's Modulus of stainless steel, taken as 200 GPa (Azo Materials, 2001). $\varepsilon_{max}$ was hence calculated as 0.005 %. The maximum strain that the typical gauges for measuring torque were rated to measure was 3 % (Vishay Precision Group Inc, 2015). Hence, it was very unlikely that the rating of the gauges would be exceeded. The strain gauges and amplifiers were then chosen by the suppliers Vishay and Synectic, respectively, to match the dimensions of the thin-wall, expected maximum torque and desired voltage range. The gauges were supplied by Vishay Measurements Group UK Ltd and were of the type 'EA-06-062TV-350' (Vishay Precision Group Inc, 2015).

The second stage of the design was to specify the minimum required interference fit between the torque tube and shaft and thin-wall components. The first stage of this calculation was to determine the contact pressure, $P_c$, in Pa, due to the interference, which was carried out using Lame's formula, provided in Equation 10 (University of Washington, 2007).

$$P_c = \frac{E\delta({r_o}^2 - {r_b}^2)}{2{r_o}^2 r_b} \qquad \text{Equation 10}$$

Where $E$ was the Young's Modulus, 200 GPa, $\delta$ was the radial interference, 0.04 mm and $r_b$ was the bore radius, i.e the radius of the hole the shaft was being inserted into, which was 7 mm. $P_c$ was hence calculated as $2.61 \times 10^8$ Pa, i.e. 261 MPa.

The required interference length, $L$, was then calculated. $L$ was set so that the tangential force generated due to the contact pressure, $F_c$, equalled the design tangential force due to the applied damping, $F_t$, as defined in Equation 11 and Equation 12.

$$F_c = 2P_c L\pi r_b \mu \qquad \text{Equation 11}$$

$$F_t = \frac{Tc_d}{r_b} \qquad \text{Equation 12}$$

Where, $\mu$ was the coefficient of friction between the steel surfaces of the interference fit, which was conservatively estimated for a 'greased shrink fit' as 0.08 (Weisz, 2012; Roymech, 2013) and $Tc_d$ was the design damping torque, 20 Nm ($Tc_{max}$ multiplied by a factor of safety of 5). $L$ could then be calculated by equating Equation 11 and Equation 12 and rearranging, to give Equation 13.

$$L = \frac{Tc_d}{2\mu\pi {r_b}^2 P_c} \qquad \text{Equation 13}$$

This resulted in a minimum required contact length of 3.1 mm. Through recommendation from a technician in the QUB mechanical workshop, to account for manufacturing uncertainties, it was decided that 8 mm was used as the final interference length.

The final design feature to specify was the shaft spline. The design of the spline was specified using the ISO 4156 standard, with the code 19z × 0,5m × 45P × 5f. This design was chosen due to the diameter of the shaft and with

guidance from previous work (Weisz, 2012). Each spline was designed to withstand shear, τ, and compressive stresses, $\sigma$, defined using Equation 14 and Equation 15, respectively. The calculations assumed that the stresses were acting on the teeth at the pitch diameter, with a safety factor of 2, assuming that half of the teeth were loaded (Weisz, 2012).

$$\tau = \frac{4Tc_d k_s}{Dzl_e S} \quad \text{Equation 14}$$

$$\sigma = \frac{2Tc_d k_s}{Dzl_e h} \quad \text{Equation 15}$$

Where, $k_s$ was the service factor, D the pitch diameter of the spline joint, 9.5 mm, z the number of teeth, 19, $l_e$ the effective length, 21.5 mm, $S$ the tooth thickness, 0.785 mm and h the spline depth, 0.4 mm. $k_s$ was defined using Equation 16.

$$k_s = \frac{k_a}{k_f} \quad \text{Equation 16}$$

Where $k_a$ was the spline application factor, assumed to be 2 for medium/light intermittent shock and $k_f$ the fatigue life factor, assumed to be 0.4 for 100000 fully reversed cycles (Weisz, 2012). This gave a $k_s$ value of 5. This resulted in values of 131 MPa and 129 MPa for $\tau$ and $\sigma$, respectively. Using a critical shear stress of 186 MPa and critical compressive stress of 170 MPa, this gave acceptable margins of safety of 0.42 and 0.32, respectively (Weisz, 2012).

Finally, the following text describes how each torque sensor interfaced with the rest of the components in the flap modules. Each torque sensor was housed in the central upright of a flap module. The damping torque was measured between the moving flap module and the static damper and bearing. As a result of this mounting arrangement, the torque provided by another bearing was not measured. However, as will be shown in section 5.3.4, this was reasonably well accounted for through data processing. The torque sensor strain-gauges and their amplifier were water-proofed by using an O-ring between the central

upright housing and the mating surface of the torque sensor. The application of torque and the position of the sensor in the model hinge sub-assembly is illustrated in Figure 29.

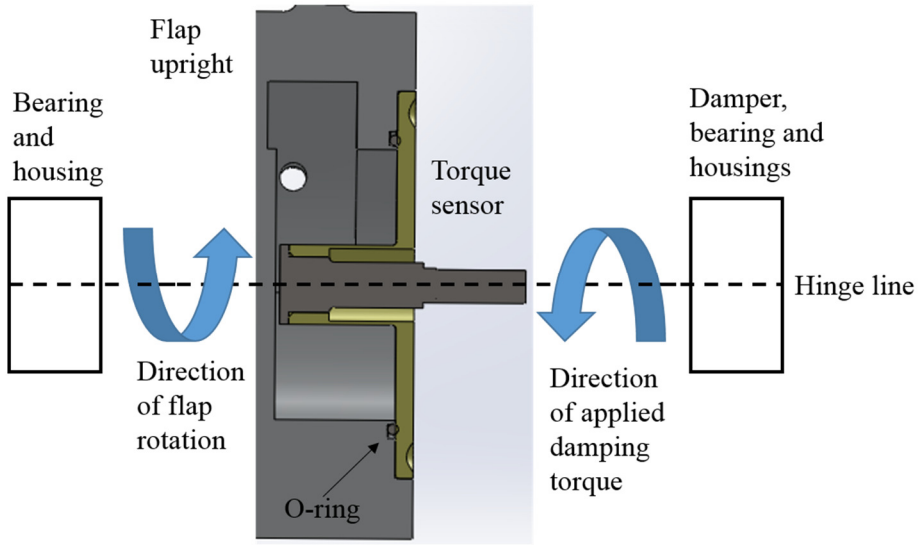


**Figure 29. Diagram illustrating the application of torque and position of the torque sensor in the hinge subassembly.**

### 3.4.5 Foundation Load Measurement

Foundation loads were measured at the connection point between the model and wave tank floor. They were measured in six degrees of-freedom (DoF). It was important to measure all DoF to allow detailed comparison of the loads acting on the modular and rigid devices (Wilkinson *et al.*, 2014). Along the three orthogonal axes, X, Y and Z, were the surge, sway and heave forces, respectively; around these axes were the moments, roll, pitch and yaw, respectively. This reference system is illustrated in Figure 30.

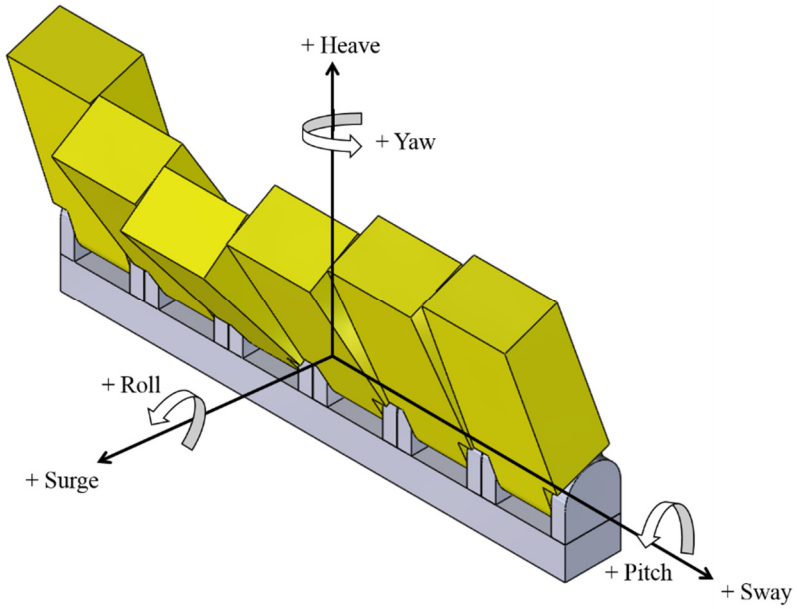


**Figure 30. Diagram illustrating naming and sign convention for the foundation loads.**

The measurement of foundation loads on flap models had been successfully carried out in previous works using a six DoF 'load cell' (Bourdier *et al.*, 2013; Mckinley *et al.*, 2014; Wilkinson *et al.*, 2014). Multiple load cells were also available to the author for use. Hence, the load cell was selected for use, with no significant consideration of other options carried out.

Like the torque sensor, the measuring element of the load cell was a stainless steel, strain-gauged, thin-walled, cylindrical element (Advanced Mechanical Technology Inc, 2012; Mckinley *et al.*, 2014). At both ends of the cylinder were bolt connection points, for fixing to the model and wave tank floor. The cylinder and electronic components were housed in a stainless steel case, providing mechanical protection and sealing from water ingress (Advanced Mechanical Technology Inc, 2012). Each load cell had a maximum diameter and height of 63.5 mm (Advanced Mechanical Technology Inc, 2011). A diagram of a load cell is provided in Figure 31, for illustration of the mechanical construction.

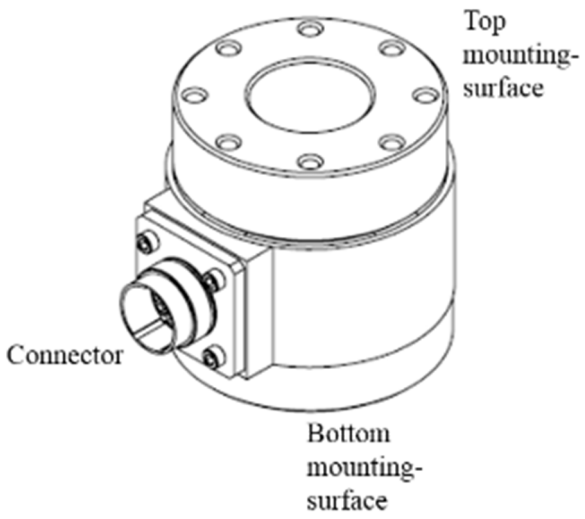


**Figure 31. Drawing of load cell (Advanced Mechanical Technology Inc, 2011).**

The load cells had a different rating for each DoF. A rating was the maximum load that the sensor should be subjected to, using a factor of safety of 3. To not damage the load cells, it was essential that the ratings not be significantly, or ideally ever, exceeded. The ratings were also provided using single DoF loading. It was hence recommended by the manufacturer that simultaneous loading of the axes be kept to within half of the maximum individual loads (Advanced Mechanical Technology Inc, 2012). Due to non-uniform water particle motion, the physical model was very likely to be subjected to simultaneous DoF loading most of the time. Hence, it was sensible to simply use half of the maximum individual loads as the ratings for each DoF, as displayed in Table 2.

**Table 2. Load cell Rating for each degree-of-freedom (DoF), using half of the maximum loads to account for simultaneous DoF loading (AMTI, 2012).**

| ***DoF*** | ***Rating* (N or Nm)** |
|---|---|
| Surge | 2224 |
| Sway | 2224 |
| Heave | 4448 |
| Roll | 113 |
| Pitch | 113 |
| Yaw | 56 |

Foundation loads could be measured either with a single load cell or two load cells coupled together. The choice between these two options was a significant decision that affected the physical model design, sensor calibration and experimental programme. Hence, justification for this decision is provided here. The discussion begins with the consideration of the advantages and disadvantages of using a single load cell.

In previous related works, a flap model was mounted on a single load cell (Bourdier *et al.*, 2013; Mckinley *et al.*, 2014; Wilkinson *et al.*, 2014). The use of a single load cell is convenient for design and calibration and is a more tried and tested approach. However, the use of a single load cell has the following disadvantages:

- It has the highest chance of exceeding the load cell ratings, shown in Table 2;
- The whole model structure is most prone to deflection due to the minimum level of support;
- Wave impact induced structural vibrations due to the elasticity of a single load cell can cause dynamic amplification of loads, distorting results (Mckinley *et al.*, 2014).

The degrees to which these disadvantages were issues for the physical model are now evaluated.

The expected size of the model, shown in Table 1, weight, due to high component concentration, and choice of off-angle wave conditions, meant that there was a concern that the load cell ratings, shown in Table 2, would be in danger of being exceeded if one load cell was used. From the sensor ratings in Table 2 and reasoned judgment, it was likely that the load cell was going to be particularly susceptible to overloading in the surge, yaw, pitch and roll degrees-of-freedom. The sway and heave loads were of lower concern, due to the relatively low cross-sectional area of the model and the high heave load cell rating, respectively.

To avoid exceeding the sensitive load cell ratings, the expected loads that the sensor would be subjected to were estimated and compared to its ratings. The loads included both the static and wave-induced elements. For both cases, the simplifying and reasonable assumption was made that the loads were maximum when the flap was held fixed and upright.

The static loads were the forces and moments due to the weight of the model above the load cell and the buoyancy acting on it. They were estimated using the CAD program, Solidworks. The only DoF that were considered to subject any significant static loads were heave and roll. The heave load was generated due to the difference between the weight, 1254 N, and buoyancy, 532 N, forces. The net heave force was hence -722 N. The roll load was created due to an offset between the model centre and centre of gravity, resulting in a net moment of 6 Nm.

The wave-induced forces were estimated using the wave-structure interaction program, Wamit (WAMIT, 2016). The loads were estimated using the geometry of the Rigid Flap, as it was expected that the forces and moments would be larger for this model configuration than the Modular Flap (Wilkinson *et al.*, 2014). This involved first generating force and moment coefficients at

different wave periods and directions. These were then multiplied with a wave amplitude, to produce the forces and moments. The conditions that were used were the extremes of the regular waves that were expected to be applied in the testing campaign at the time of the analysis. These were: wave periods of 1.1-2.6 s, amplitudes of 0.033-0.066 m and directions of 0-45 degrees.

The total loads were assessed and are grouped as forces and moments, with the results presented in Figure 32 and Figure 33, respectively.

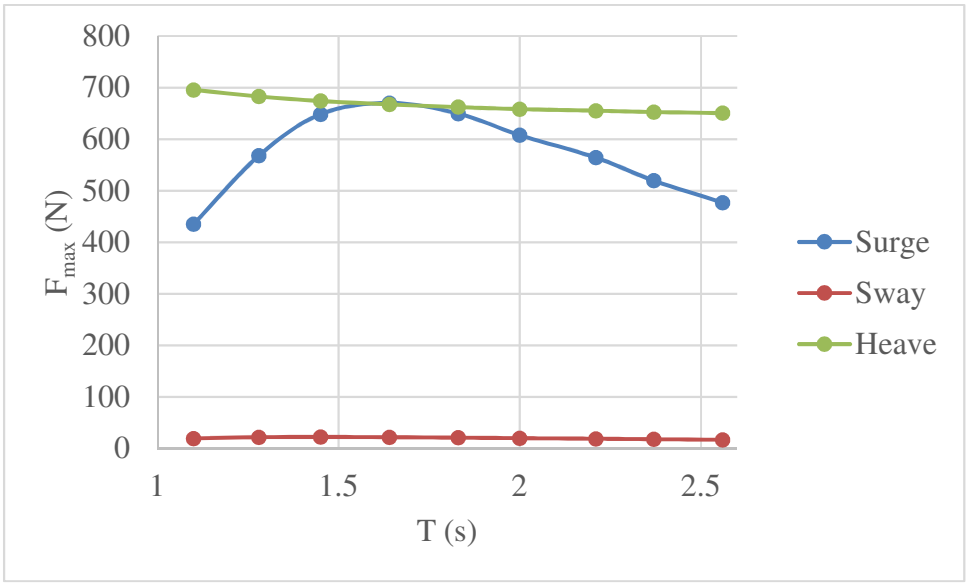


**Figure 32. Maximum expected forces subjected to single load cell, $F_{max}$, against model scale wave period, $T$, on rigid flap physical model.**

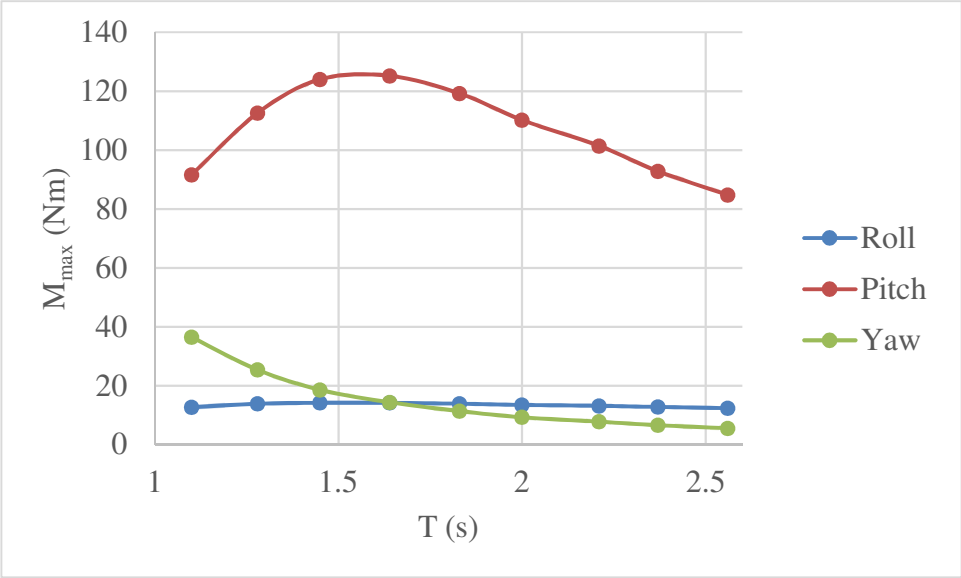


**Figure 33. Maximum expected moments subjected to single load cell, $M_{max}$, against wave period, $T$, on rigid flap physical model.**

The loads shown in Figure 32 and Figure 33 are then put into perspective through comparison to the load cell ratings, shown in Table 2. The maximum load for each DoF was used, with the results shown in Figure 34.

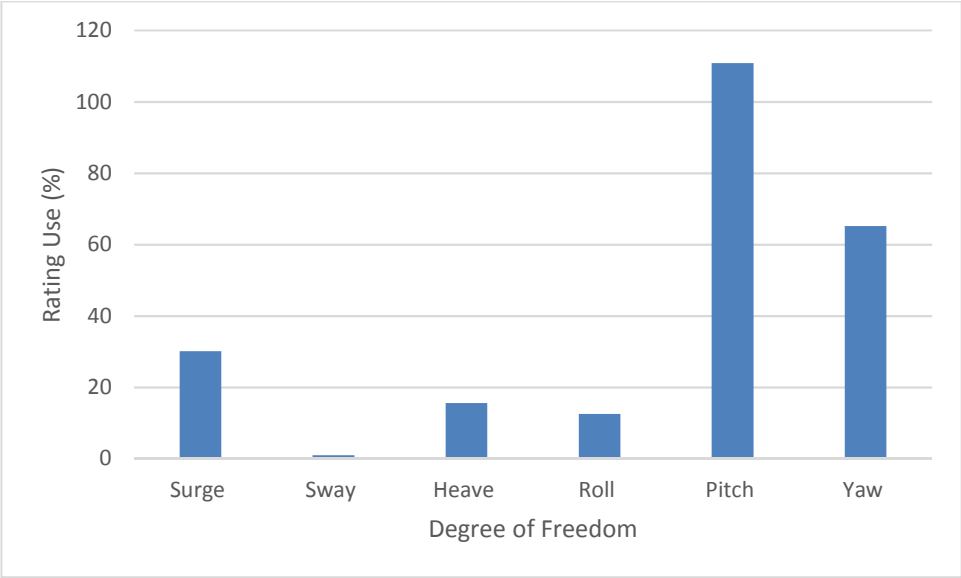


**Figure 34. Graph showing expected maximum loads relative to load cell rating, Rating Use, for each degree of freedom.**

Figure 34 shows that the ratings for the sway, heave, roll and, to a lesser extent, surge DoF were unlikely to be exceeded during the experiments. However, the pitch DoF was expected to be exceeded by 11 %; the yaw DoF, at 65 % rating use, could have had its rating exceeded if the actual loads were approximately 50 % larger than expected, for example. This is conceivable, due to uncertainties in the estimates, from numerical modelling, for example. Hence, there was concern that the pitch and yaw ratings would be exceeded by using a single load cell for the expected test programme.

In addition to load cell rating exceedance, there was concern that the use of one load cell would result in unacceptable deflection of the model cross-beam. Deflection was undesirable as it would result in misalignment in the model, resulting in, for example increased chance of the modules rubbing together.

The cross-beam was the element that connected the flap modules to the load cell and was made of stainless steel, grade 304. To increase the resistance of the beam to deflection, a channel section was chosen over a simpler rectangular section. However, the use of a single load cell would have meant that the cross-beam was still essentially two cantilevers. To determine if this design was acceptable, the maximum deflection of the beam was estimated. This was carried out only based on the weight of the model in the dry. This was because, compared to the buoyancy and the force for the highest expected roll load, shown in Figure 33, the dry weight was expected to be the worst load case.

Calculation of the maximum deflection of the beam, $\delta_{max}$, was carried out using Equation 17 (Talkchannels, 2017). Use of this equation required the reasonable assumption that the weight of the model, 1254 N, was approximately uniformly distributed over the model length which, at that time, was assumed to be 1111 mm.

$$\delta_{max} = \frac{\omega l^4}{8EI} \qquad \text{Equation 17}$$

Where, $\omega$ was the uniformly distributed load, 1.1 $Nmm^{-1}$, $l$ was the cantilever length, 550.5 mm, $E$ was the elastic modulus, 190,000 $Nmm^{-2}$ and $I$ was the second moment of area in the axis of deflection (AZO Materials, 2017).

Of the values required in Equation 17, the only unknown at this point was $I$. This was calculated using the approximate geometry of the beam, using Equation 18 (eFunda, 2017).

$$I = \frac{2sb^3 + ht^3}{3} - A(C_x) \qquad \text{Equation 18}$$

Where $A$ was the area of the cross-section and $C_x$ the vertical distance from the top of the beam to the centre of mass, calculated using Equation 19 and Equation 20, respectively (eFunda, 2017).

$$A = bd - h(b - t) \qquad \text{Equation 19}$$

$$C_x = \frac{2b^2s + ht^2}{2bd - 2h(b - t)} \qquad \text{Equation 20}$$

The variables for Equation 18, Equation 19 and Equation 20 are illustrated in Figure 35.

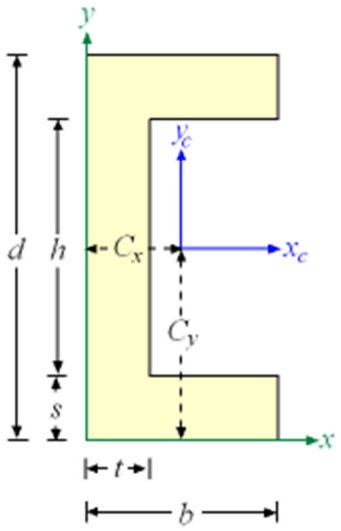


**Figure 35. Dimension variables for cross-section of channel beam (eFunda, 2017).**

The approximate relevant dimensions of the beam were: s = 12 mm, b = 60 mm, h = 94 mm, t = 12 mm and $d$ = 118 m. This resulted in a value for $I$ of 810,000 $mm^4$ and hence a maximum deflection of 0.1 mm. The actual cross-beam had clearance holes on it, for fastening bolts. This will have weakened the beam. Without calculating the effect of this, however, it is unlikely that the weakening would result in the deflection increasing beyond 0.5 mm. Over the length of the cantilever, this deflection is well below the national standard limit, of the length divided by 180, i.e. 3 mm (UK National Annex, 2014). From visual judgement too, this level of deflection was unlikely to have any significant effect on the alignment of the model. Defection of the model structure resulting from the use of one load cell was hence deemed acceptable.

Finally, the issue of structural vibrations was of lower concern for this thesis than in previous work, where extreme wave conditions were used (Mckinley *et al.*, 2014). However, individual high load impact events could have occurred during the test programme in this thesis. While no quantitative assessment was made on this issue, it remained somewhat of a concern.

Of the above issues, the chance for exceeding the load cell ratings in the pitch and yaw DoF was of most concern. The decision was therefore made to avoid the use of a single load cell in the physical model. Instead, the option of using two load cells was selected. This would lower the chance of rating exceedance by distributing the loads between the two sensors. It would also further lower the chance for unacceptable structural deflection by turning the cross-beam into a beam supported at opposite ends, rather than two cantilevers. Finally, this setup would increase the stiffness of the model, hence reducing the chance for structural vibrations. It was also shown that the same level of calibration accuracy, up to 3 %, could be achieved by using one and two load cell setups (P. Lamont-Kane, 2015b). Hence, it was deemed that the lowest risk option, though less convenient, was to use two load cells in the physical model.

The sensor models were partly named with regards to their maximum rating in heave. The ‘2K’ indicated a maximum heave rating of 2000 lb (Advanced

Mechanical Technology Inc, 2012). For the remainder of this thesis, the two load cells that were used will therefore be referred to as 'AMTI2000A' (model number 'MC2.5A-6-2K-6278') and 'AMTI2000B' (model number 'MC2.5D-2K-13487').

## 3.5 Dampers

### 3.5.1 Introduction

Full scale WECs extract energy and convert it into useful output, such as electricity, by employing a PTO mechanism. At model scale, this is simulated through the application of an external force, or torque, by a damper. Hence for this research, the damper was one of the most important components in the physical model. This section summarises the process that was undertaken to choose the damper and provides details on the selected system.

The criteria that were used to choose a damper are provided in 3.5.2. Many options were reviewed against these criteria to inform the selection. Information for the review came from surveying members of the QUB research group and reading literature (Henry, 2008; Clabby, 2013; Wilkinson, L. and Lamont-Kane, 2013). Where information for promising damper systems was not accessible, testing was also carried out for the review. This testing is discussed in a reasonable level of detail in section 3.5.3. The damper review is then summarised in section 3.5.4. Details on the way in which the chosen damper was waterproofed and then controlled are provided in sections 3.5.5 and 3.5.6, respectively.

### 3.5.2 Requirements

The design requirements for the damper system covered attributes such as geometry, controllability and torque rating. Some discussion of these is provided here, before all of the requirements are summarised.

As discussed in section 2.2, the type of damping that it was decided to apply in the physical model was constant, due to being commonly used in full scale flap-type WECs (Henry, 2008; O'Boyle *et al.*, 2015). Hence, a key requirement was that the chosen damper could provide constant damping torque.

The torque rating, i.e. the maximum torque that a damper could supply, was also one of the most important criteria. Based on guidance from previous studies on a model of the flap-type WEC, the Oyster 800, which is 26 m at full scale, it was decided that a target damping level of at least 3.9 Nm RMS torque, at $40^{th}$ scale, would be used (Doherty, 2013; O'Boyle *et al.*, 2015). To take into account the damping profile not being perfectly square though, an instantaneous value of 5 Nm was used instead of the RMS value. Using Froude scaling, this is equivalent to 15.8 Nm at $30^{th}$ scale. This assumes though that the total full scale width of the model would be 26 m, i.e. 0.87 m at model scale. With a target number of modules of six, this would require a model scale width, including gap, of 144 mm for each module. This was seen as too ambitious and so a 25 % larger target width, of 181 mm was used. Optimum damping torque magnitudes typically increase with the square of the flap width (Henry, 2008). Hence, the target total torque level went up to 24.7 Nm. Per module, and hence damper, this gave a requirement of 4.1 Nm. At the other end of the scale, it was desirable that the damper could also supply as close to 0 Nm of torque as possible. This was to allow supplementary testing, such as for free-decay experiments and for numerical model calibration (van 't Hoff, 2009). A bearing, with geometry relevant to this work, typically provides up to 0.05 Nm of torque, as later shown in Figure 85. Hence, an additional torque provided by the damper of 0.1 Nm, i.e. equivalent to the two bearings required for a module, was deemed acceptable.

Further requirements of the damper were that it was practical to integrate within the flap modules, hence needing to be compact, simple in form and ideally rotary. Additionally, accurate and simple controllability was very important. This was because there would be many modules to apply damping

to and it has been shown that the power capture of a modular flap-type WEC is highly dependent on the applied damping strategy (Sarkar, Doherty and Dias, 2016).

In view of the above discussion, the damper design requirements were summarised as follows:

- The damper could apply constant/Coulomb damping torque;
- The torque range of 0.1-4.1 Nm could be supplied.
- The torque level could be accurately and easily controlled;
- The torque level would be highly repeatable;
- The torque would be supplied with minimal backlash;
- The damper would have a maximum cost per unit of approximately £1000;
- The geometry of the damper would allow simple incorporation into the model, ideally being rotary, with a maximum diameter and length of 120 mm;
- The damper would be able to apply torque underwater.

### 3.5.3 Tested Dampers

This section summarises the damper evaluation testing carried out during this research project and the feasibility observations for each tested system. Further information on each damper and the testing can be found in referenced internal reports.

Testing was conducted in dry and wet conditions. Dry testing was performed where wet testing, which allowed greater assessment of the damper feasibility, was not practical or deemed necessary. For the majority of cases, the dampers were tested using bespoke bench rigs, designed and manufactured by QUB technicians and operated by the author. Using these, the damper shaft was manually oscillated with a lever arm, with the damper then providing resistive torque. In all cases, damping torque was measured using a torque sensor,

similar to the one described in section 3.4.4, and rotation measured using a blade rotation sensor, described in section 3.4.3. Results were acquired either using the Belfast QUB Wave Tank data acquisition system or an auxiliary system, described in previous work (Henry, 2008).

Dampers were selected for testing based on review of literature and market research (Aalborg University, 2013; Lamont-Kane, Folley and Whittaker, 2013; Institute for Fluid Power Drives and Controls, 2016). The dampers that were tested were as follows:

- Hydraulic oil system
- Linear motor
- Electrical hysteresis brake
- Magnetic particle brake

The following text summarises the testing and analysis of results, in the same order that the dampers were listed above in.

The hydraulic oil system was commissioned by Aquamarine Power Ltd for model testing and manufactured by the Institute for Fluid Power Drives and Controls, Rwth Aachen University (Institute for Fluid Power Drives and Controls, 2016).

The damper was tested in the Belfast QUB Wave Tank by the author and an Aquamarine Power Ltd colleague (Wilkinson, L. and Nicholson, 2013). The system consisted of a base unit that was installed at the hinge line of a flap and an auxiliary hydraulic circuit outside of the wave tank. Photographs of these sub-assemblies are provided in Figure 36 and Figure 37, respectively.

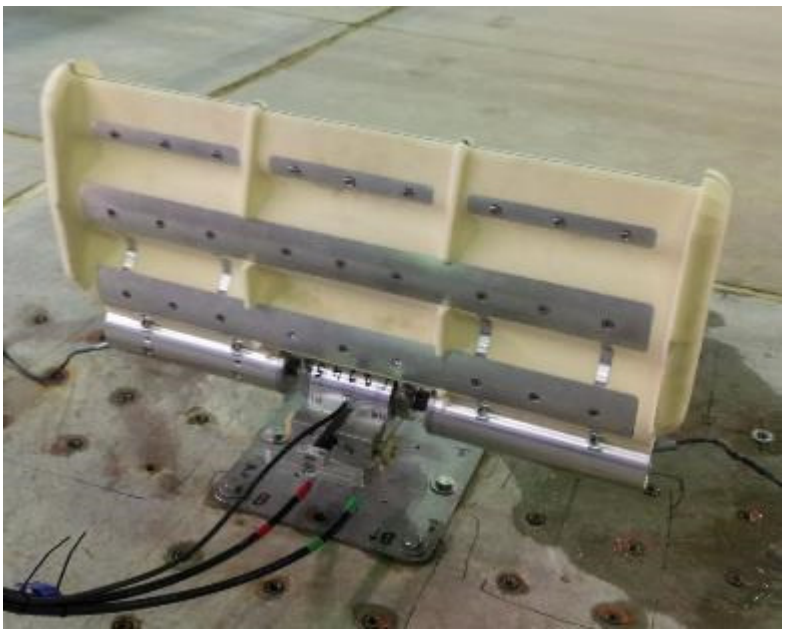

**Figure 36. Photograph of hydraulic-oil damper attached to flap model on wave tank floor.**

**Figure 37. Photograph of auxiliary circuit of hydraulic-oil damper.**

The base unit, pictured in Figure 36, was composed of a wire-wheel drive system and hydraulic cylinders. The wheels rotated with the flap and the wires, wound around the wheels, were attached to the cylinders. This resulted in the rotary motion of the flap being converted into linear motion. The advantage of

this, over a linear lever arm system, was that the applied torque was constant with rotation without dynamic control of the pressure.

The damping level was controlled through adjustment of a high-pressure valve in the auxiliary circuit, shown in Figure 37. The valve was controlled by varying the voltage supplied to it, from 0-10 V, with 0 V providing the minimum damping and 10 V the maximum. A sample of damping torque results from the testing, at 0 and 10 V valve voltage, is provided in Figure 38.

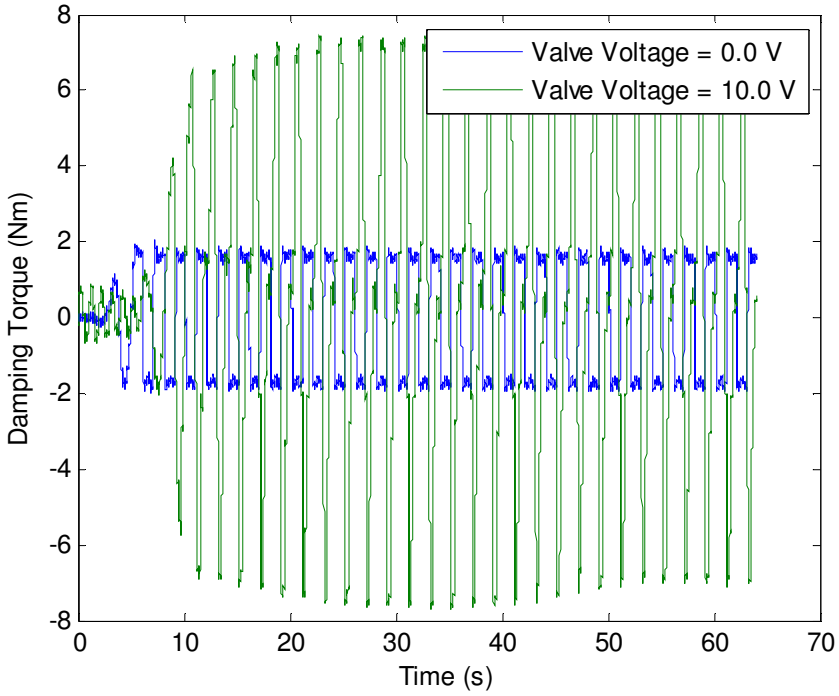


**Figure 38. Plots of variation of damping torque with time for the minimum and maximum valve voltage settings (damping levels). Early part of graph shows build-up of damping as the waves first reached the model (Wilkinson, L. and Nicholson, 2013).**

Figure 38 shows that the damper achieved the target Coulomb damping profile and that the amplitude of damping was reasonably constant. The graph also provides an indication of the minimum and maximum damping levels achieved. Over the course of the testing, it was found that the range of damping magnitudes provided was 1.6-10 Nm. The inability to produce damping close to the target of 0.1 Nm was thought to be because of friction generated by the cylinder seals. So, while the damper achieved the desired damping profile, with

good repeatability and controllability, the minimum torque range was deemed too high for each module in the model. The unit cost of £4,500 was also restrictively expensive.

The second damper that was tested was an electrical linear motor, manufactured by LinMot (Wilkinson, 2013; LinMot, 2018). This was made up by a stationary part – the 'stator' and a moving part – the 'slider'. The stator was an embedded coil, to which current was supplied to control the motor. The slider contained permanent magnets. The magnetic force between the coil and magnets provided the driving force (Wilkinson, 2013). Good experience with this system was found in testing of pitching buoys at Aalborg University and so it was desired that such a system be tested for a flap-type device (Aalborg University, 2013). For this, a demo-kit was acquired from LinMot. The kit was tested in a dry bench rig, shown in Figure 39.

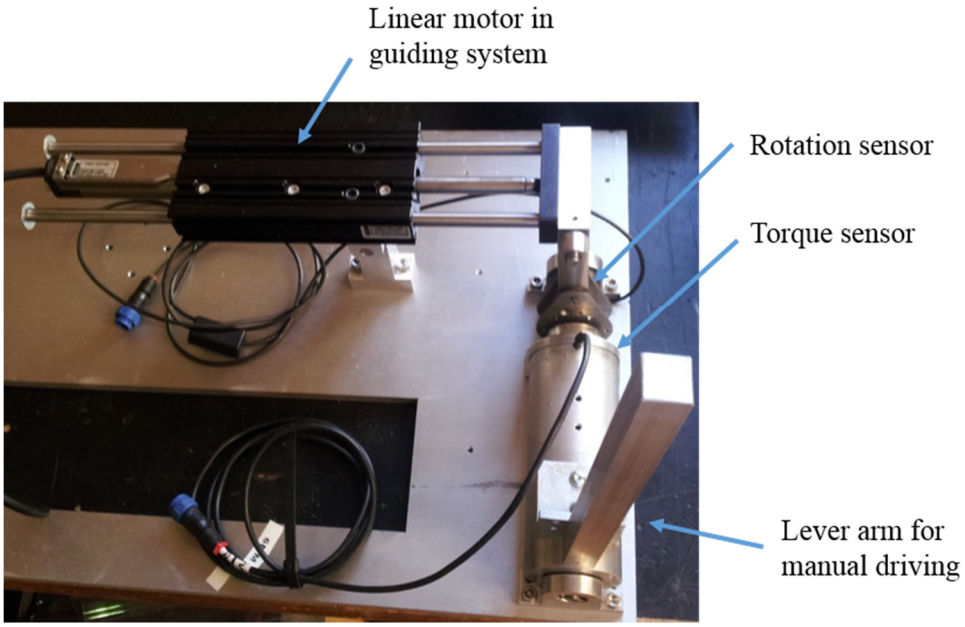


**Figure 39. Rig for bench testing linear motor damper.**

The testing showed that the damping levels were repeatable, with recorded deviations of less than 0.1 Nm for mean torques. The recorded damping torque range was also 0.2-5.2 Nm, showing good suitability for the modular flap model.

For an ideal constant damper, a plot of damping torque against rotation would yield a square shape (Banks, D. and van 't Hoff, 2013). With the linear motor damper in its basic form, it was found that, as one would expect for a linear system without dynamic control, the damping profile was not the desired square shape. It was also found that small oscillations of the damping occurred, likely due to the magnet passing the non-continuous stator coil. A graph illustrating these two observations is shown in Figure 40.

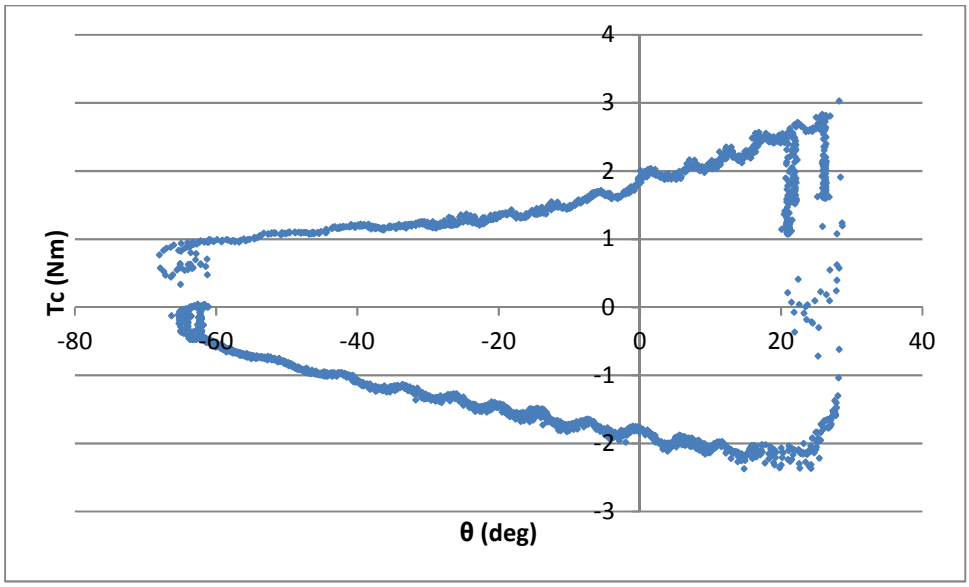


**Figure 40. Typical profile of damping torque, *Tc*, against rotation, *θ*, for tested linear motor damper.**

Furthermore, without dynamic force control, the linear motor was not a passive damper. This was because the damping force was achieved in these tests by running the motor in position control and moving the slider away from the target position. When the stroke was reversed, the target position had to be moved to then apply the damping in the opposite direction (Wilkinson, 2013).

From results produced in testing by another party, it was predicted that the linear motor damper could theoretically provide Coulomb damping (Aalborg University, 2013). However, it would have required an upgrade to the system, using a force control module. This would incorporate a closed-loop measurement and control system for the flap velocity and damping force,

requiring extra hardware and software. Alternatively, for generating constant damping at least, the motor could have used a similar cable-wheel drive system to the one employed in the hydraulic oil damper. Both of these options were feasible but would have required potentially significant design work and additional investigation. Furthermore, the cost of the motor and its control system, around £3000 per unit, were a restrictive aspect for its choice as the damper for the model.

Two further electrical systems, that were both rotary and cheaper than the linear motor, were then investigated. Discussed first is an electrical hysteresis brake (EHB).

The EHB produced a braking torque by exerting magnetic drag on a rotor connected to its shaft. The magnetic field was generated with a coil. The strength of the field, and so the torque level, was proportional to the current. Unlike for the linear motor, the rotary nature of the damper meant that the torque was independent of the rotational velocity or position. This gave the target 'square' wave damping profile.

The purchased damper was manufactured by Mobac GmbH and had a model number of HB-250M-2 (Mobac GmbH, no date). The model had a rated torque of 2.3 Nm, diameter of 112.5 mm and length, with the one-shaft type, of 91.7 mm. A photograph of the damper is provided in Figure 41.


**Figure 41. Photograph of EHB.**

The EHB was tested using a similar experimental rig to the one employed for the linear motor, shown Figure 39. The results showed that the torque matched the desired square profile well, with an example illustrating this in Figure 42.

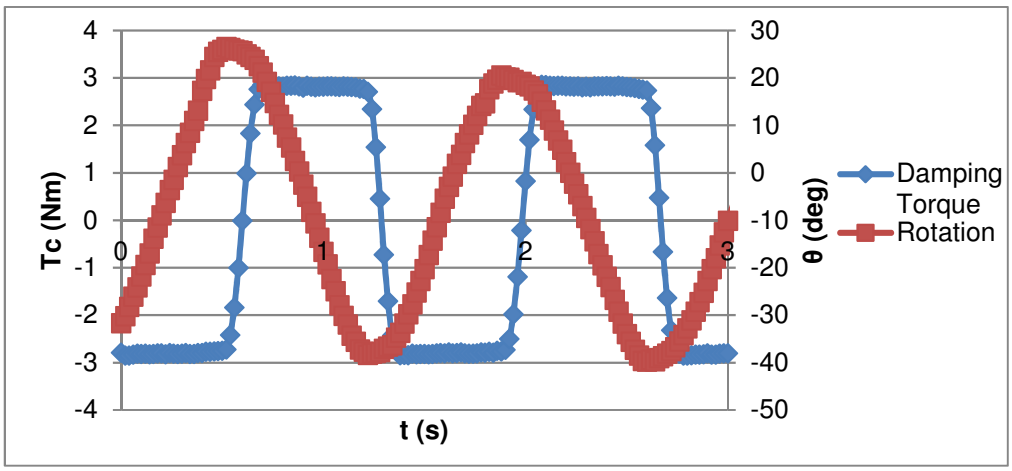


**Figure 42. Example graph for EHB testing, showing variation of damping torque, *Tc*, and rotation, *θ*, against time, *t* (Wilkinson, 2014c).**

The tests also showed very good repeatability of the damping torque levels and a high level of controllability. The downsides for the damper were its relatively high cost and diameter per unit of rated torque.

The second rotary electrical damper that was evaluated was a magnetic particle brake (MPB). This consisted of a stator coil and rotor, with the latter connected to the flap shaft. In between the stator and rotor was a cavity, filled with fine, dry stainless-steel particles. Without a current supplied to the stator coil, the drag applied by the particles was negligible; with current supplied, magnetic field lines were generated between the rotor and stator, linked by the particles. This connection resulted in a resistive torque being applied to the rotor (IBD Wickeltechnik GmbH, no date; Placid Industries, no date a). The friction level, and so damping torque, was controlled by changing the supply current or voltage to the coil (Placid Industries, no date a). The current was approximately linearly proportional to the voltage so control of either had the same effect. A cross-section of the MPB concept, to illustrate its design, is provided in Figure 43 and a diagram to show more details of the magnetic field lines and forces is shown in Figure 44.

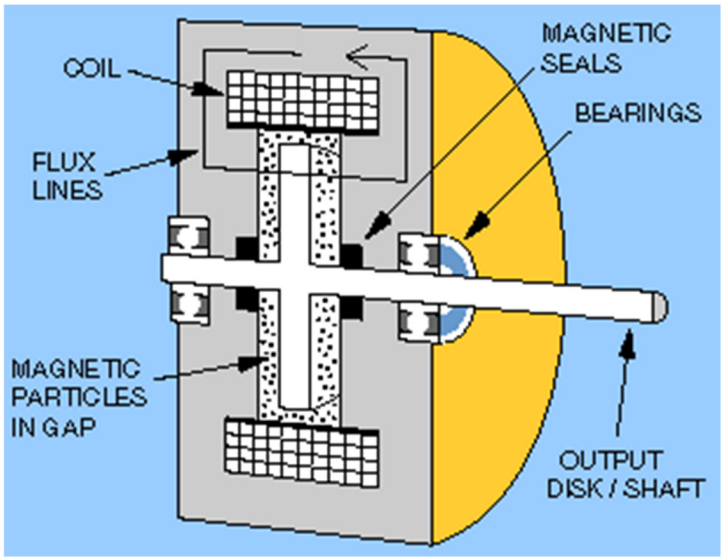


**Figure 43. Cross-section of MPB (Placid Industries, no date a).**

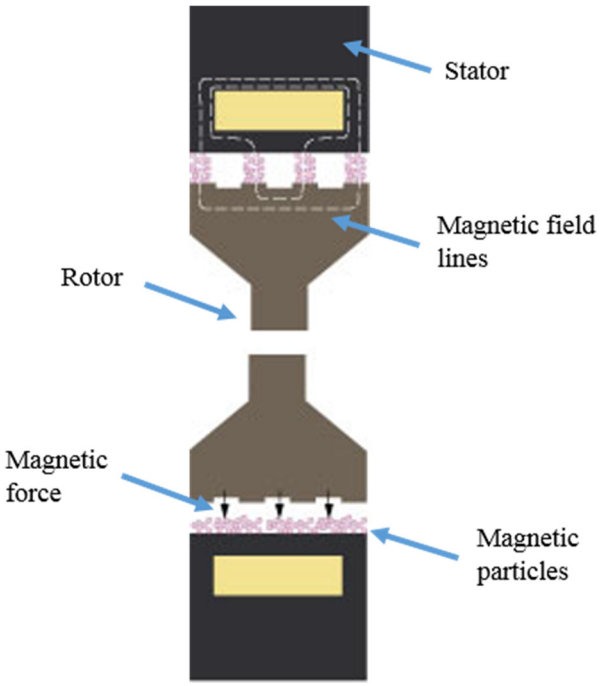


**Figure 44. Diagram showing magnetic field and forces created between rotor and stator in magnetic particle brake (IBD Wickeltechnik GmbH, no date).**

For the feasibility testing presented here, the MPB model B15-1 was used. This had a manufacturer's torque rating of 0.03-1.7 Nm (Placid Industries, no date b). The diameter and total length were 73 mm and 67 mm, respectively.

The damper was tested in a dry bench rig, similar to that used for the linear motor and EHB. The results showed that the damper achieved a relatively constant damping level, independent of speed. An example plot illustrating this is provided in Figure 45.

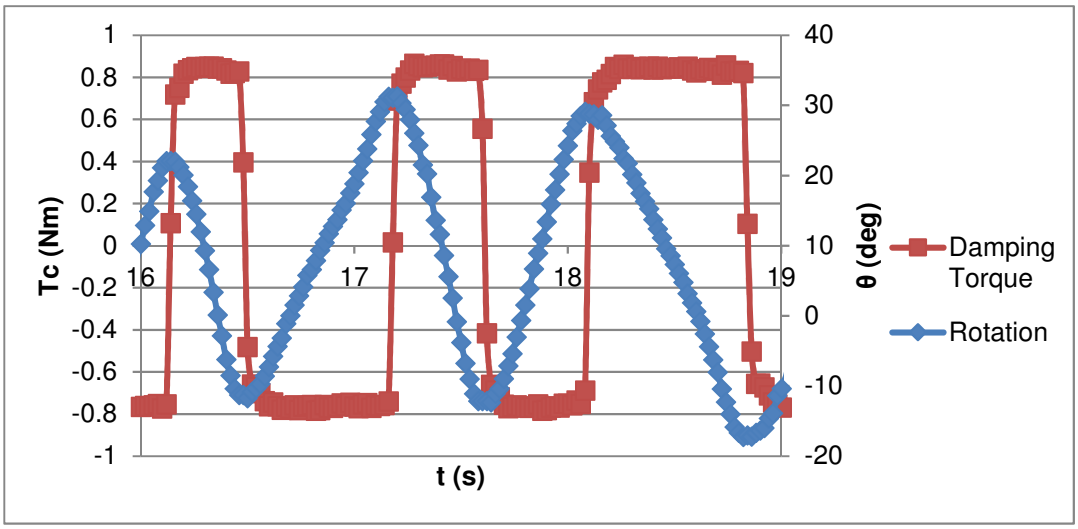


**Figure 45. Example graph for MPB testing, showing variation of damping torque, *Tc*, and rotation, *θ*, against time, *t* (Wilkinson, 2014a).**

Across the supplied voltage range, the measured damping range by the B-15 MPB was 0.05-1.6 Nm. This showed that a very low minimum damping was achieved and the maximum damping was in the right range for the modular flap module requirements. A higher rated model of the brake, the B-35, was also available that had a torque range of 0.1-3.95 Nm and hence better matched the ideal damping range of 0.1-4.1 Nm (Placid Industries, no date c). It was also the right size for the model, being 86 mm and 71 mm in diameter and length, respectively, and hence within the target of 120 mm for both dimensions (Placid Industries, 2014). The cost, of £360/unit, was also well within the target maximum of £1000/unit.

Considering the promising attributes of the MPB system, it was taken to the next stage of testing, in wet conditions. However, a drawback of the MPBs, was that the manufacturer stated that the damper was not waterproof, unlike options like the disc brakes. Hence, a waterproofing solution was sought for a MPB.

It was decided to avoid radial shaft seals as a waterproofing solution, due to the added friction and limited life associated with them. An alternative was to use magnetic couplings. These are magnetic hubs that transmit torque to each other

across an air gap. This non-contact approach avoids using components that wear and hence decline in their ability to waterproof. The couplings can be separated by a non-magnetic 'containment barrier', which would allow isolation of the MPB from water (Magnetic Technologies Ltd, 2015a, 2015b). One hub would be connected to the MPB shaft, with both components then housed in a waterproof box.

Tests were conducted to verify the functionality of the MPB with magnetic couplings (Wilkinson, 2014b). Two types of magnetic coupling were considered for testing: 'disc' and 'co-axial'. In the initial tests, it was the disc-type couplings that were used, not the eventually opted for co-axial type. This was because the decision regarding the choice of coupling type had not yet been made and the disc-type offered simpler mounting. It was assumed that the functionality of both types would be the same and so the testing was deemed to verify the use of the co-axial type too.

The disc magnetic couplings were purchased from Magnetic Technologies. The model was MTD-5, which could transmit a maximum continuous torque of 5 Nm (Magnetic Technologies Ltd, 2015b). The same model of MPB as previously used, the B15-1, was used for the testing. The disc magnetic couplings and MPB were first tested in a dry rig, shown in Figure 46.

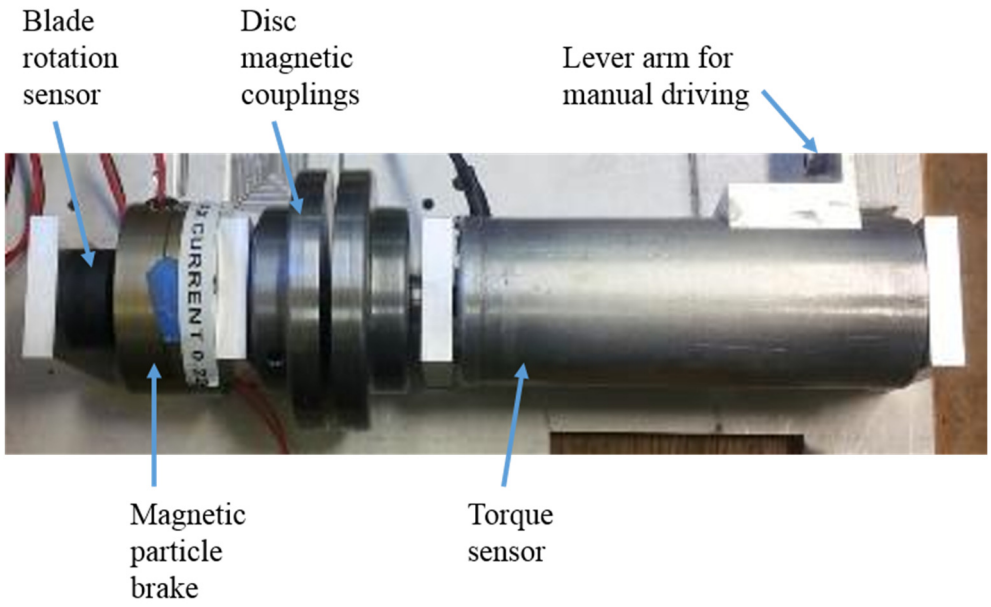


**Figure 46. Blade rotation sensor, magnetic particle brake, magnetic disc couplings and torque sensor in dry bench rig.**

The aim of the experiments was to see if the performance of the MPB was adversely affected by the introduction of the magnetic couplings. The performance was principally measured by evaluation of the achieved damping torque levels at the full range of currents supplied to the MPB. The damping torque level at each current was summarised using the root-mean-square (RMS) of the timeseries, the formula for which is provided in Equation 21.

$$Tc_{RMS} = \sqrt{\frac{\sum_{i=1}^{N} Tc_i{}^2}{N}} \qquad \text{Equation 21}$$

Where $N$ and $i$ were the number of samples and the sample index, respectively, in the time series and $Tc_i$ was the instantaneous applied damping torque.

The recorded torque levels were plotted over the same data acquired for the tests without the magnetic disc couplings, as shown in Figure 47.

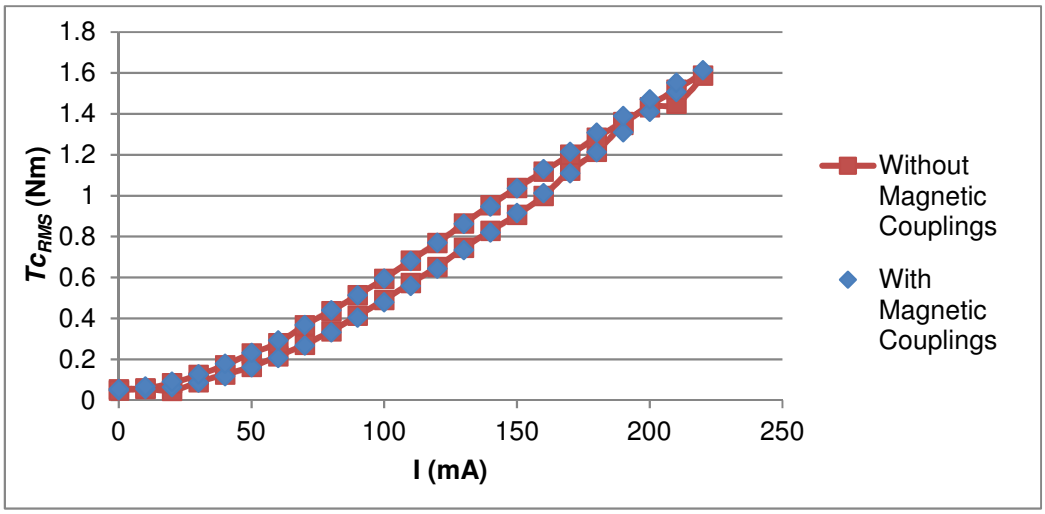


**Figure 47. Comparison of RMS damping torques, $Tc_{RMS}$, recorded at each current setting, $I$, for without and with magnetic disc couplings.**

Figure 47 shows that there was generally very good agreement with the damping torques without and with the magnetic disc couplings, thus proving that the combined system could deliver the required torque levels.

The backlash between the magnetic couplings was also assessed, by measuring the relative angular displacement between the units. During motion in one direction, at all damping levels, there was no detected backlash between the couplings. However, when the shaft changed direction, the couplings only held together well when the damping level was low. At the highest damping level though, there was backlash of around 4 degrees, as illustrated in Figure 48.

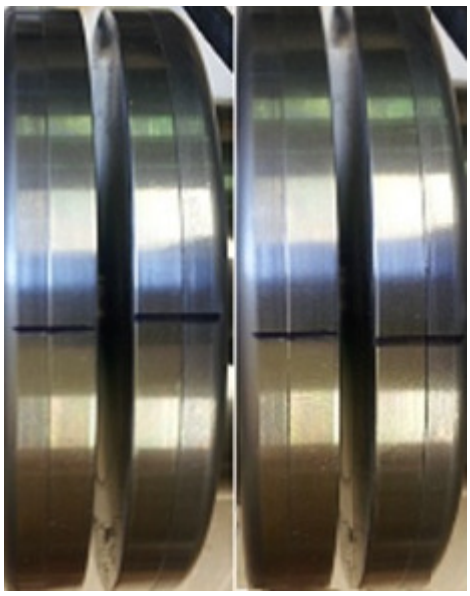

**Figure 48. Photos of magnetic disc couplings, with the disc attached to the magnetic particle brake on the left of each photo, showing angular differences between discs through comparison of the position of the black lines (Wilkinson, 2014b).**

In order to combat the backlash illustrated in Figure 48, the magnetic couplings that were eventually used had a rating much greater than that of the MPB damper.

Finally, the MPB and magnetic couplings were tested in wet conditions. The MPB and one disk coupling were placed in a waterproof box, with the other coupling and other components located outside of the box. The whole rig was submerged in water, with a picture shown in Figure 49.

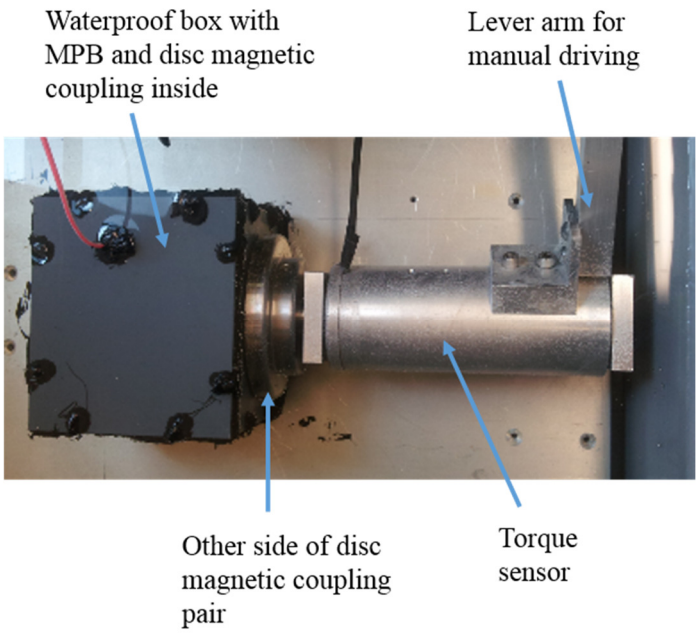


**Figure 49. Rig used for testing magnetic disc couplings, MPB and waterproof box. The whole rig was submersed in a tub of water.**

As expected, the testing showed that there was no noticeable difference in the functionality and damping levels delivered by the MPB and magnetic disc coupling pair when placed in a waterproof box and submerged in water. The components of the waterproofed MPB damper system were therefore fully verified.

### 3.5.4 Review of Damper Options

The information from the survey, literature review and testing was collated into a table that compared the dampers against the requirements. The degree to which the requirements were met by the dampers was measured using a common scoring system with three levels: ‘Poor’, ‘Moderate’ and ‘Good’. As an example, given that a key design requirement was that the dampers were small, a compact damper would be given a score of ‘Good’ for ‘Size’. The results of the review are presented in Table 3.

**Table 3. Coulomb damper selection review (Wilkinson *et al.*, 2015). This is a consolidated version of a larger table, which is provided in the appendix in Table 15.**

| **Damper** | **Criteria** | | | | |
|---|---|---|---|---|---|
| | **Torque Range Suitability** | **Ease of Control** | **Practicality of Integration with Model** | **Relative Size** | **Relative Cost** |
| Braking clutch | Poor | Poor | Good | Good | Good |
| Disc brakes | Good | Poor | Moderate | Good | Good |
| Hydraulic (water) | Unknown | Poor | Poor | Moderate | Moderate |
| Hydraulic (oil) | Moderate | Good | Moderate | Moderate | Poor |
| Linear motor | Good | Moderate | Poor | Moderate | Poor |
| Electro-magnetic clutch | Moderate | Good | Good | Good | Good |
| Magnetic particle brake | Good | Good | Good | Moderate | Moderate |
| Electrical hysteresis brake | Good | Good | Good | Moderate | Poor-Moderate |

The damper chosen from the selection process was the magnetic particle brake. This was because it provided a good approximation to Coulomb damping, was rotary, was relatively compact, offered a suitable damping range and good

repeatability, was relatively inexpensive and was easy to control (Wilkinson *et al.*, 2015).

### 3.5.5 Waterproofing

As discussed in section 3.5.3, the MPB used magnetic couplings to transmit its torque across an air gap and hence allow the damper to be placed in a waterproof box. As was also mentioned, there were two types of coupling considered, the disc and co-axial designs. This section justifies the choice of and describes the coupling that was used.

The co-axial variety was opted for, over the disc type, as they avoided exerting too high of a thrust load on the shaft of the MPB, which could have damaged the latter. It also offered a reduced overall diameter for a similar torque rating. A diagram of the co-axial coupling type, along with a containment barrier for sealing a waterproof box, is shown in Figure 50.

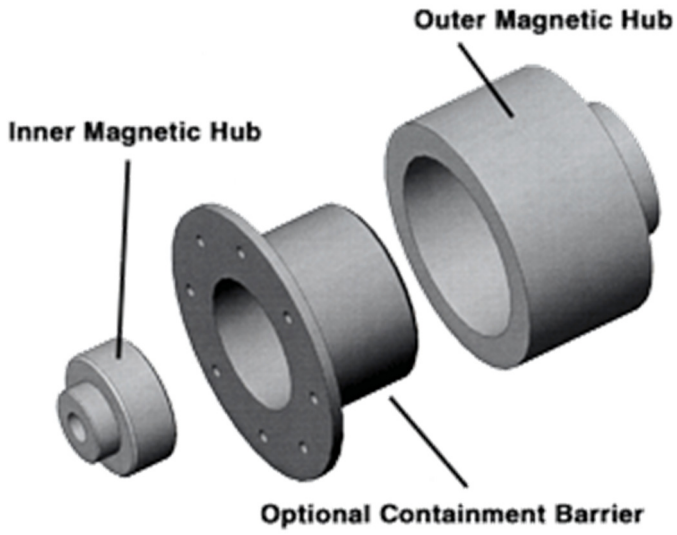


**Figure 50. Magnetic co-axial couplings with containment barrier (Magnetic Technologies Ltd, 2015a).**

The MTC-10 model of co-axial couplings was used, which had a nominal torque rating of 10 Nm (Magnetic Technologies Ltd, 2015a). The couplings were deliberately overrated for the damper to reduce backlash to an acceptable level, as discussed in section 3.5.3 (Wilkinson, 2014b). Although the stiffness

between the couplings would have been a useful parameter for predicting the backlash, it was not available from the manufacturer.

The inner magnetic hub was connected to the MPB damper shaft, using an adaptor plate and bolts. This sub-assembly was then housed in a waterproof box with a plastic containment barrier as the lid; the outer magnetic hub rotated around the inner hub and was connected to the torque sensor shaft, via a spline. The couplings were assembled in a controlled way using a bespoke rig. Further description of the rig is provided in section 3.7.

### 3.5.6 Damper Control

Control of the MPB dampers was required to change the level of torque that they applied to the models. This was to find the damping level that corresponded to the maximum power production for a wave condition. For the multi-body modular flap, it has been shown that its power production is highly dependent on the applied damping strategy (Sarkar, Doherty and Dias, 2016). Hence, it was important to have accurate control over the damping applied to each flap module.

In this thesis, the simplest damping strategy of applying the same achievable torque level to each module was applied. The word ‘achievable’ is used because the actual measured damping torque can only be as high as the wave excitation torque acting on a module. Hence, even with this simple strategy, the damping torques applied to the modules could be different if the wave excitation torques were reached for some of the them. This section provides information on how the dampers were controlled to achieve this strategy.

The magnitude of the torque level provided by each MPB was controlled through variation of the supplied voltage and current. As mentioned in section, 3.5.3, the current drawn by the MPB was proportional to the supplied voltage so either variable could be used for the control. In this project, the voltage was principally used, due to the choice of hardware and software made.

A method of damper control that was sufficiently accurate and practical to use was required. The method chosen and developed to meet this requirement was the use of a distribution box and power supply. The electronic design and assembly of these systems was completed by Kamil Kanas, a technician in QUB, with the mechanical design and assembly carried out by the author and Aidan Flaherty, also a QUB technician.

The outputs of the distribution box and power supply were controlled with a bespoke software program, created by the author, with guidance from previous work by David Crooks, a PhD student at QUB. The purpose of the software program was to convert torques desired by the user to signals received by the power supply. These were then converted to output voltages supplied to the dampers. The software program was written in LabVIEW and allowed simultaneous damper control and data acquisition (DAQ) (National Instruments, 2016a). Further details on the DAQ components are provided in section 3.6. A screenshot, showing the front panel of the software program, is provided in Figure 51.

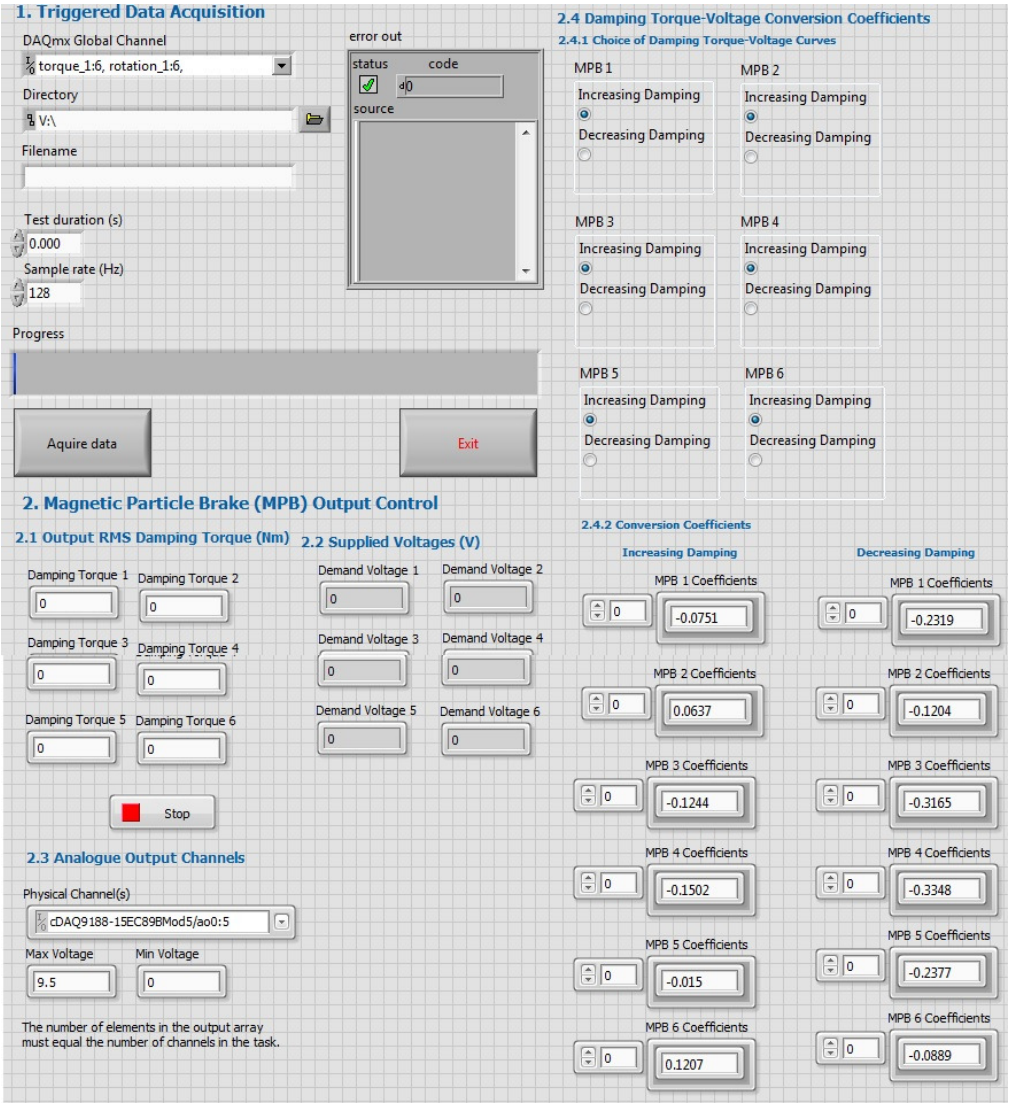


**Figure 51. Screenshot of LabVIEW program, used in physical modelling campaign, for damper control and data acquisition.**

The program received the demand torque, as an RMS level. The program then converted the demand torque level to a voltage, in the range 0-9.5 V, for each damper. The conversion was completed using a polynomial function. The function was characterised by its coefficients, which were input into the program.

The function was derived by measuring the RMS damping torque at a range of voltages. This was carried out by attaching the modules together, to form the Rigid Flap, and exciting the model with waves that were energetic enough to

overcome the resistance of the dampers at all voltage levels. As specified by the manufacturer, a different curve for each MPB was found when the voltages were increased to when they were decreased (Placid Industries, no date c). An example plot showing this, with the functions for the curves provided, is presented in Figure 52.

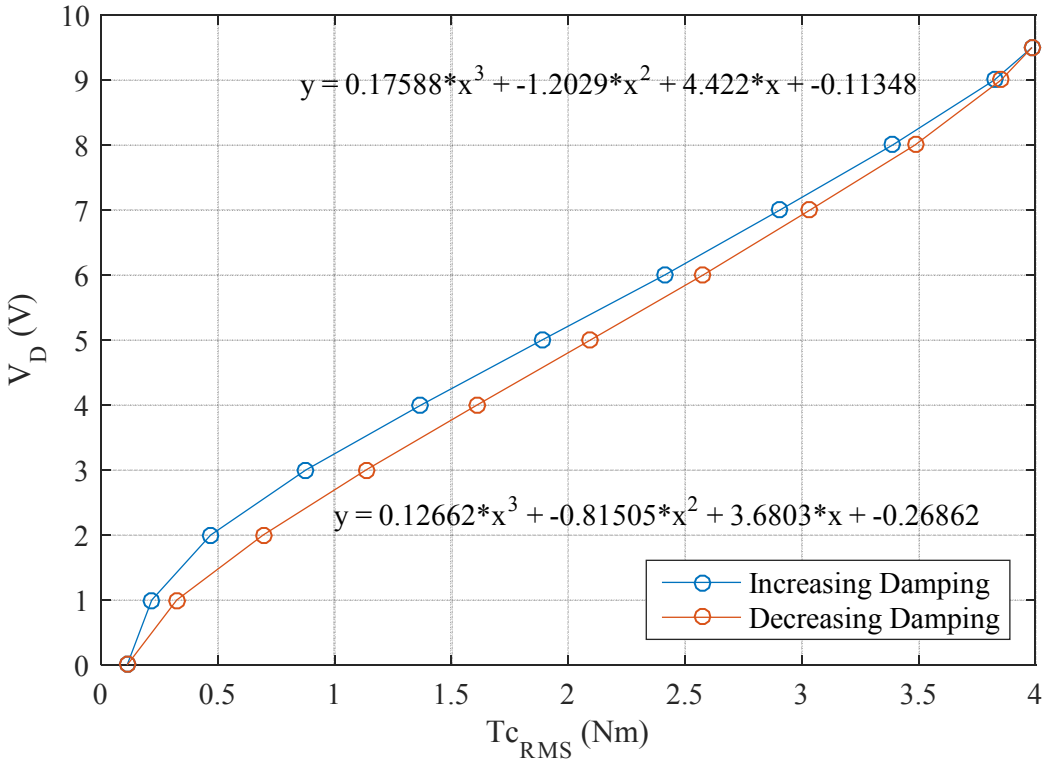


**Figure 52. Example of damping torque-voltage curves for MPB for module 1, with demand voltage, $V_D$,. against RMS damping torque, $Tc_{RMS}$.**

The damping-torque relationships for the different MPBs were slightly different. This resulted in different polynomial coefficients. All coefficients that were used are provided in the Appendix in Table 16.

The voltages computed by the program were received by a National Instruments (NI) CompactDAQ 8-Slot Ethernet chassis, 'NI cDAQ-9188' (National Instruments, 2016c). An analogue voltage output card, 'NI 9264', in the chassis was used to generate the desired voltages (National Instruments, 2009). These voltage signals were received by a printed circuit board (PCB), which routed the paths into BNC connectors. These were then mounted on a

front panel on a portable breakout box. Further details of this box are provided in section 3.6. A cable was then used to send each voltage signal from the breakout box to the distribution box and power supply.

The purpose of the distribution box was to receive the demand voltage signals and convert them to output voltages of suitable magnitudes for the dampers. Like the breakout box, the distribution box also had BNC connectors on its front panel. There, each connector was soldered to a PCB. Each PCB consisted of electronic components that received a voltage signal and converted it, using a gain of approximately 2.5. This meant, for example, that an 8 V signal specified by the LabVIEW program would eventually result in a voltage of 20 V supplied to an MPB. Connection to the resulting power supply for each MPB was via two banana sockets.

The distribution box was powered with a single linear bench power supply. This provided DC power, with a required voltage of above 27 V and a current of at least approximately 0.5 A/damper. A photograph of the distribution box and power supply is provided in Figure 53.

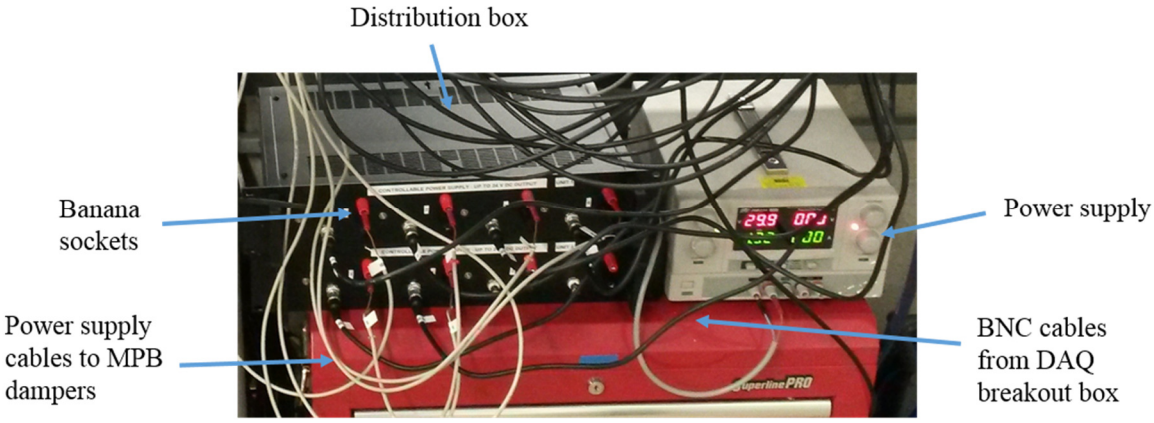


**Figure 53. Photograph of distribution box and power supply for powering MPB dampers, with key components indicated.**

The damper control system did not adjust the damping applied at each moment in time. This meant that, even with the same target RMS torque, instantaneous

variation between the outputs of the dampers was typically up to 15 %, as shown in an example in Figure 54.

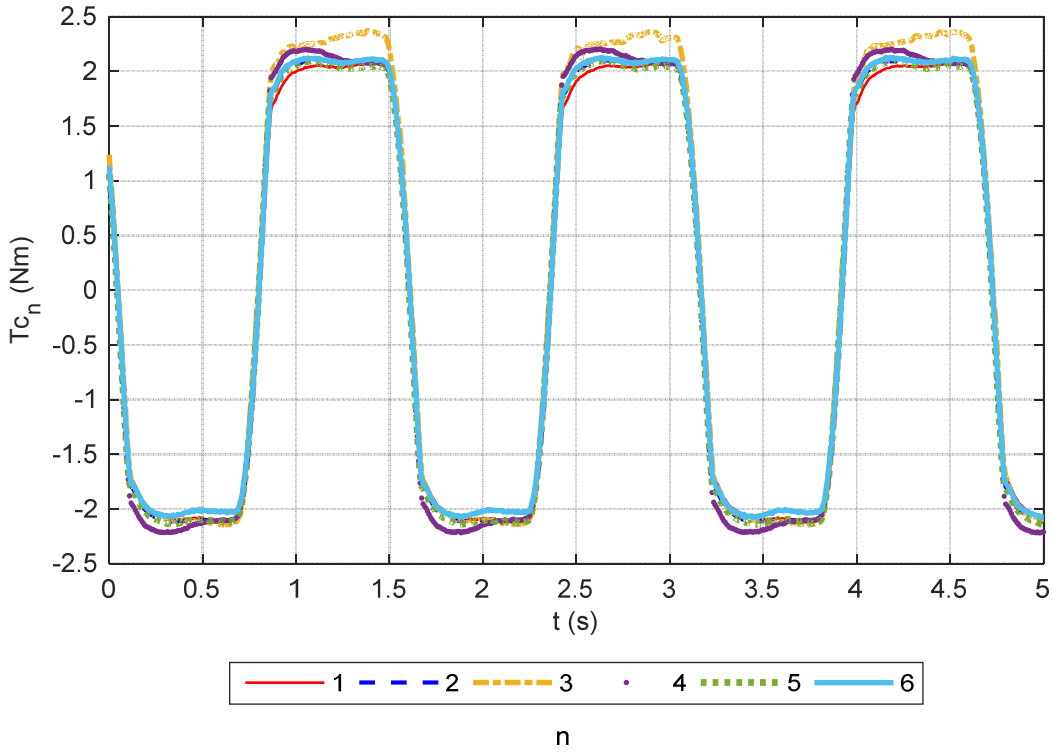


**Figure 54. Example of variation in model scale damping torque, $Tc_n$, with time, $t$, for six modules (n = 1-6) fixed together in the Rigid Flap configuration and damped with the same target RMS torque.**

However, the aim for the control system was to achieve sufficiently high control over the steady-state conditions, as measured with the RMS damping torque. This allowed the differences between the torque applied to each module to be minimised. To illustrate the low level of this variation, the RMS torques, for the same example as used in Figure 54, are shown in Figure 55.

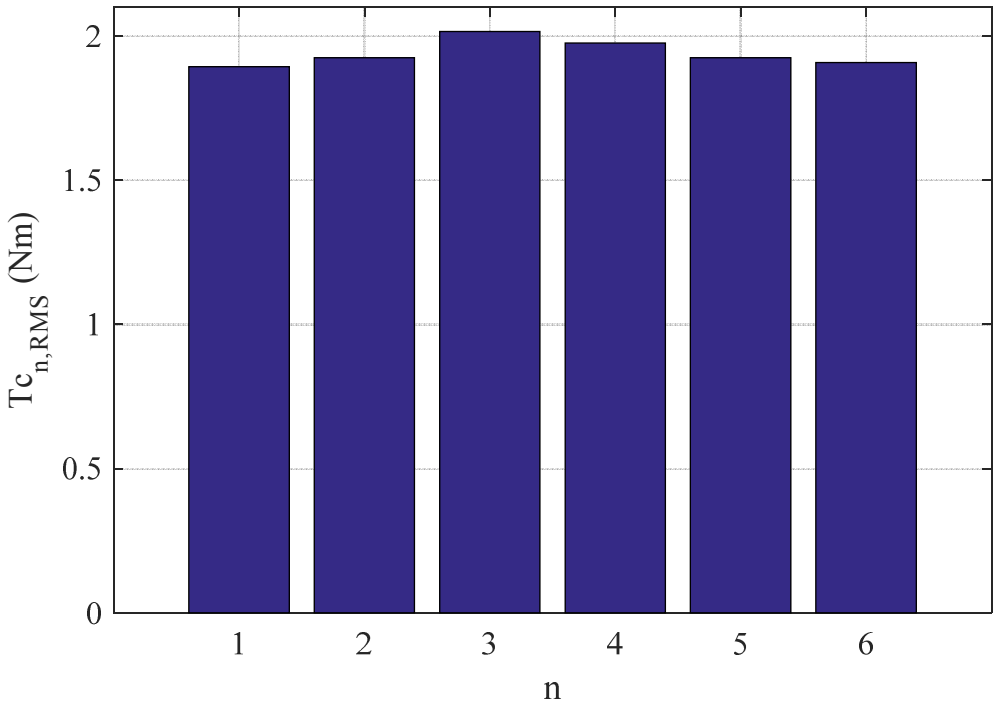


**Figure 55. Example of variation in of RMS damping torque, Tc for six modules (n = 1-6) fixed together in the Rigid Flap configuration.**

The level of variation in RMS damping torques was measured using the standard metric, the coefficient of variation, as calculated with Equation 22.

$$CV_{Tc_{n,RMS}} = \frac{\sigma_{Tc_{n,RMS}}}{\overline{Tc_{n,RMS}}} \qquad \text{Equation 22}$$

Where, $\sigma_{Tc_{n,RMS}}$ and $\overline{Tc_{n,RMS}}$ were the standard deviation and means of $Tc_{n,RMS}$, respectively.

The coefficient of variation for the example shown in Figure 55 was 2 %. This was typical, with the mean, for the tests where the maximum mean Rigid Flap power was recorded, being 3 %. The variation was independent of the damping level too, as shown in Figure 56, which also shows the range of levels of variation.

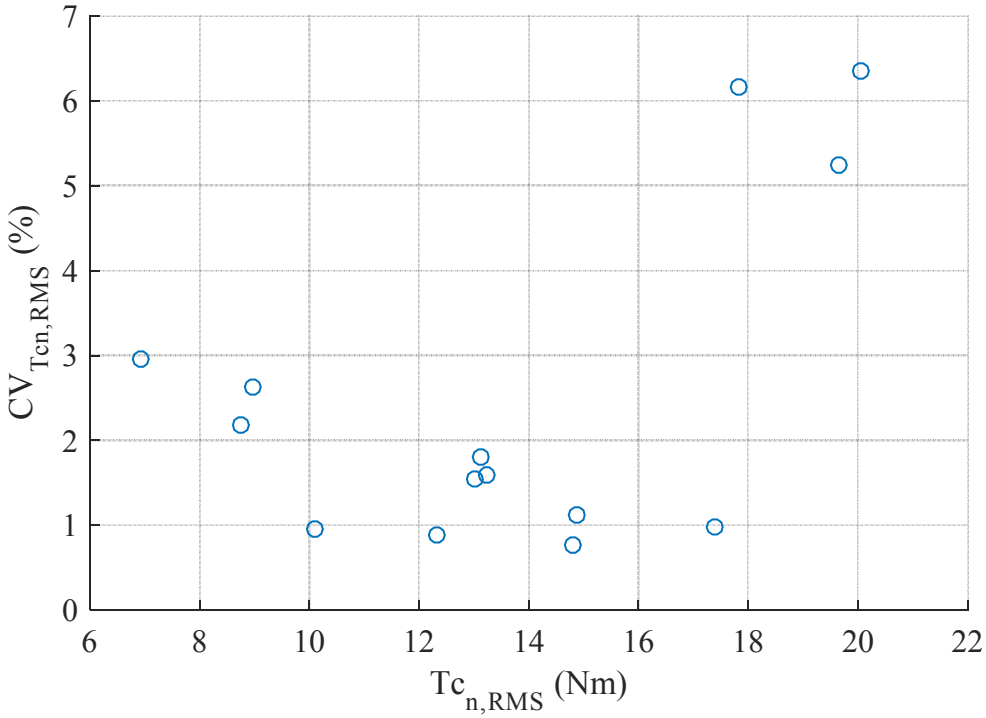


**Figure 56. Coefficient of variation of RMS damping torque for nth module, $CV_{Tc_{n,RMS}}$, against RMS damping torque for nth module for Rigid Flap tests where maximum mean power capture was recorded.**

The damper control system therefore performed to the desired level. This meant that variation in applied module damping was an insignificant source of dispersion in the module powers with the device configured as the Modular Flap.

## 3.6 Data Acquisition

This section provides the reader with information on the data acquisition (DAQ) system used during this project. This was used in both the sensor calibrations and the physical modelling campaign.

The DAQ system served the purpose of recording the measurements from the sensors in the physical model. There is literature already available on the DAQ hardware used for wave probe signal recording and hence this is not discussed here (Edinburgh Designs Ltd, 2016b). The requirements of the DAQ system were as follows:

- To provide connector points for all sensors used in the physical model;
- To measure the sensor signals with no significant time lags;
- To provide adequate grounding to sensors to minimise signal noise generation;
- To not significantly limit the choice of location for testing in the wave tank.
- To be easy to integrate with the damper control system, described in section 3.5.6.

To meet the requirements, a DAQ system was developed during the research project. The system consisted of a steel breakout box with a front panel for the connectors. The connectors were grouped together on PCBs which, where required, also supplied power to the sensors. The PCBs were designed and assembled by Kamil Kanas, a QUB technician, and the mechanical design, manufacture and assembly completed by the author and QUB mechanical technicians.

The input signals were routed on the PCBs to D-sub connectors. Cables were then used to take the signals to a single unit, the NI CompactDAQ 8-Slot Ethernet chassis, 'NI cDAQ-9188' (National Instruments, 2016c). Analogue inputs were recorded using NI 9205 cards and converted into digital signals (National Instruments, 2016b). An Ethernet cable was then used to transmit all signals to a DAQ computer, where they were recorded using the software program shown in Figure 51, section 3.5.6.

Power was supplied to the breakout box via a 24 V DC power supply, with an estimated current consumption of 2 A. The system was triggered with a cable linked to the wave paddles, allowing synchronised DAQ and wave generation. A photograph of the system is provided in Figure 57.


**Figure 57. Photograph of DAQ system.**

## 3.7 Physical Model

This section contains a summary of the physical model, including its design and brief descriptions of procedures for its assembly. The physical model was a collection of sensors, dampers and mechanical components. The latter were the components used to house the sensors and dampers and to provide both the static and moving structure of the flap model. These were principally designed by the author, with guidance from the MRG and QUB technicians, and manufactured in the QUB mechanical workshop.

The model consisted of a set of flap modules mounted on a base structure. Modules were used for power extraction, while the base structure served the purpose of connection to the wave tank floor and for housing the load cells.

The aim of the design of the physical model was to develop it without being exposed to unacceptable project risk. This was achieved by producing the design in several stages. At each of these stages, the design was proven by verification tests, both in the dry and in the wave tank. The tests verified the functionality of the model, including its waterproofing, sensors, dampers, damper control and DAQ systems.

The highest risk element in the model was the set of flap modules. This was because they contained duplicated components, operating together for the first time. Hence, the design process began with the production of a prototype flap module. The module design is summarised in section 3.7.1, followed by the equivalent information for the base structure and whole model, in sections 3.7.2 and 3.7.3, respectively.

### 3.7.1 Module Design

Beyond achieving functionality and high practicality, the primary aim of the module design was to minimise the module width. This was so that the number of modules, and so the degree to which the whole device was modular, could be maximised.

Several design choices were made to minimise the width of each module. One such example was to, where possible, overlap parts. An example of this was using the lower diameter section of the outer magnetic coupling as the direct shaft connection to the torque sensor, as shown in Figure 58.

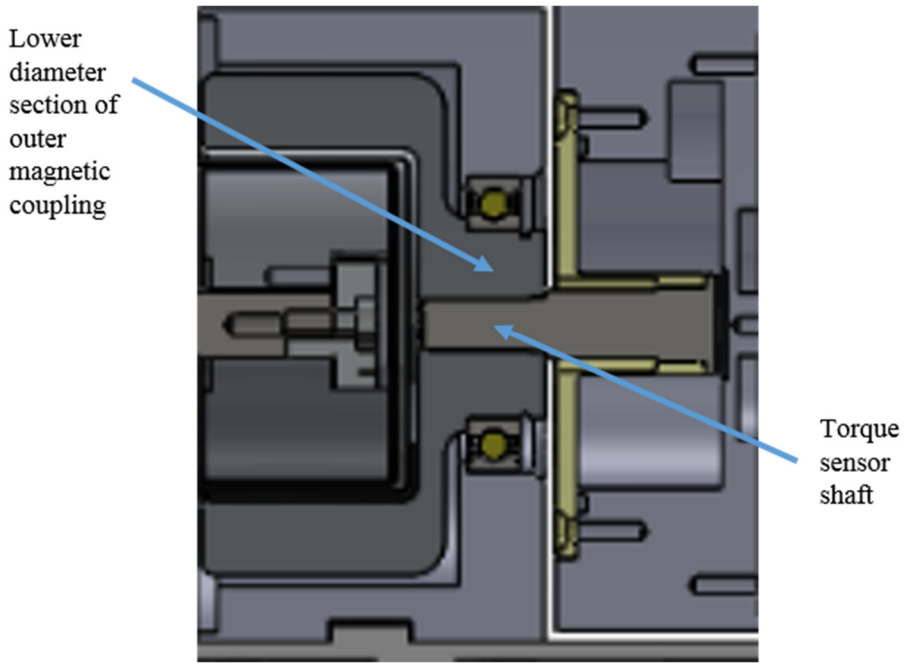


**Figure 58. Cross section of part of module, highlighting using of the lower diameter section of the outer magnetic coupling to directly connect to the shaft of the torque sensor to minimise the contribution of the connection to the flap module width. Please refer to Figure 60 to see the full module.**

Other refinements included requesting bespoke shortened magnetic couplings, minimising the length of the torque sensor, as detailed in section 3.4.4, and using low-head bolts. Applying these refinements, the module width went from approximately 270 mm for the original concept design, to 183 mm, or 5.49 m at full scale for the final design. This transition is shown in Figure 59. This allowed the Modular Flap to consist of a maximum of six modules, close to the target total width, defined in section 3.2, of 1 m at model scale.

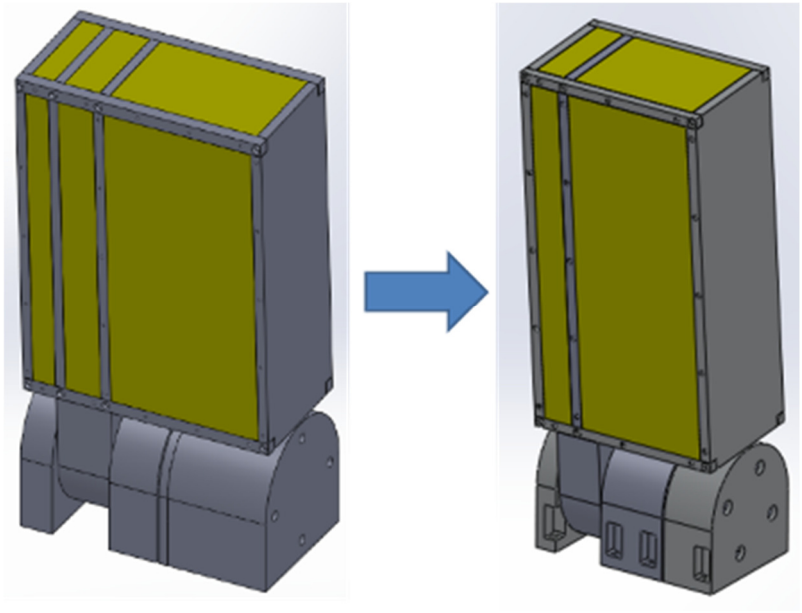

**Figure 59. Reduction in width of flap module, achieved through design refinements (Wilkinson *et al.*, 2015).**

Each flap module consisted of two sub-assemblies, the hinge structure and the prime-mover, i.e. the flap body. At the hinge were the rotation and torque sensors and the damper, as well as their aluminium housings.

The housings were mounted on and located by an aluminium plate. This also served the purpose of keeping the magnetic couplings apart during testing, which was crucial for safety and reliable operation.

The prime-mover sub-assembly was built up from a central upright spine. Around this were two sections of high-density closed cell foam, sandwiched together with aluminium bars (Trident Foams Ltd, no date). A PVC sheet was then fastened to both sides of the prime-mover. These sheets were used to accommodate for model configurations where multiple modules were connected together, for example to form the Rigid Flap. For single modules, the sheets merely served the purpose of maintaining the mass and geometrical properties of the model. A cross-section, indicating the key features of the module, is shown in Figure 60.

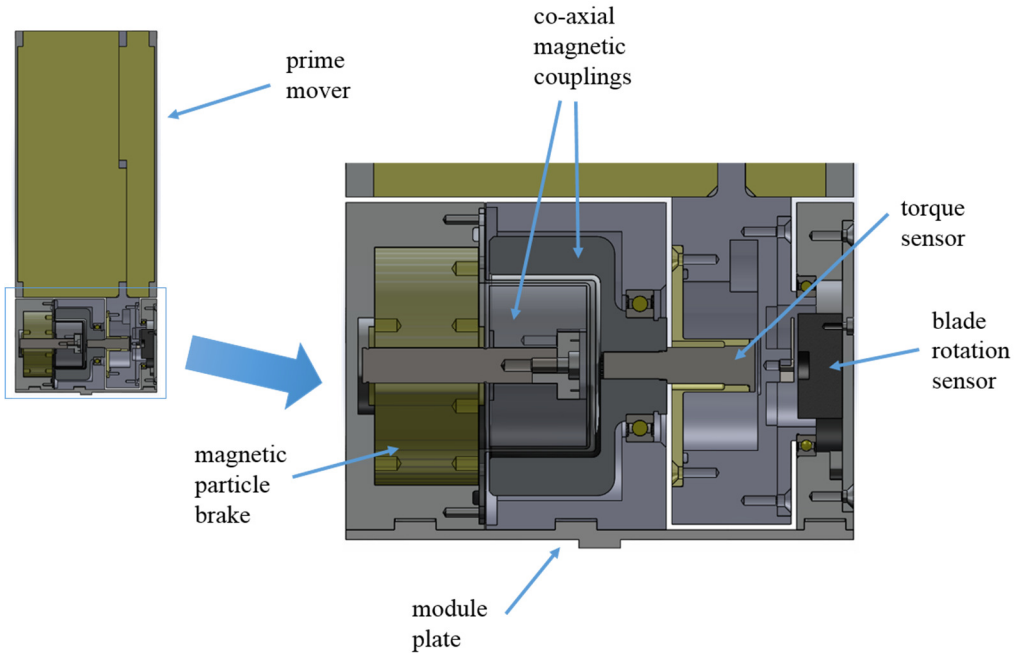


**Figure 60. CAD renderings of cross-section of single module, with key components labelled.**

The most sensitive stage of the assembly of each flap module was the engagement of the magnetic couplings. A high level of control was necessary, to keep the couplings aligned and at their minimum separation distance. This was achieved using a bespoke rig, consisting of linear bearings, guides and threaded bars, connected to the magnetic coupling housings. These allowed the couplings to be wound together. A labelled photograph, illustrating the rig, is shown in Figure 61.

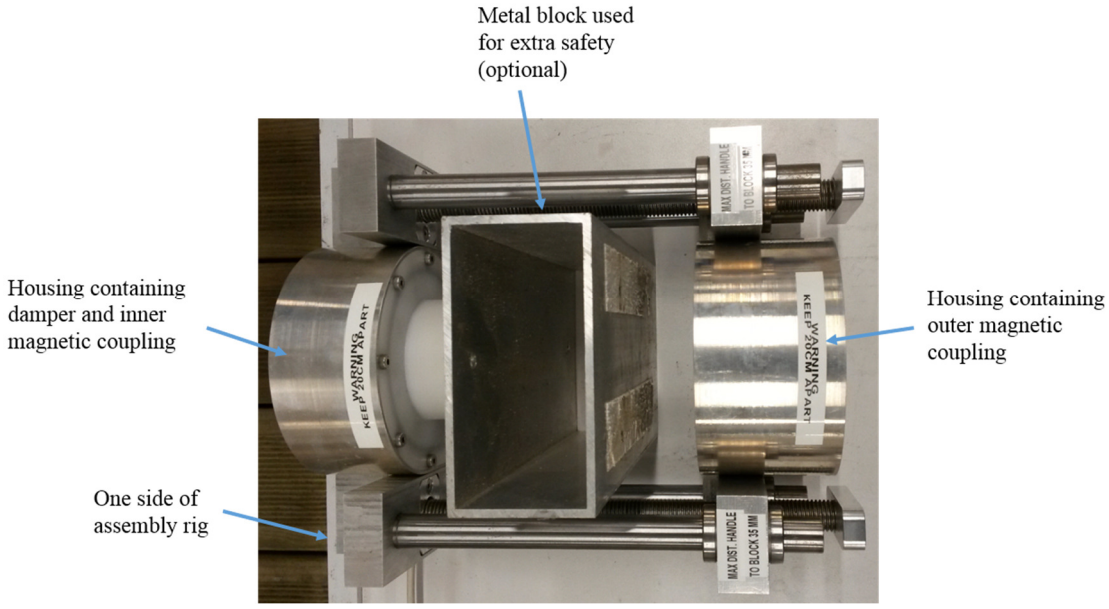


**Figure 61. Photograph showing magnetic coupling assembly rig and housings.**

### 3.7.2 Base Structure Design

The base structure sub-assembly consisted of a stainless-steel cross-beam, two load cells, a stainless-steel base plate and aluminium gap-blockers. The latter were used to minimise the water flowing beneath the model, to maximise power capture (Henry, 2008).

The bottoms of the load cells were fastened to the stainless-steel base plate. The tops of the load cells were then fastened to the stainless-steel cross-beam. The gap-blocking components were fastened to the front and back of the base plate and to each other. A rendering of the base structure is provided in Figure 62.

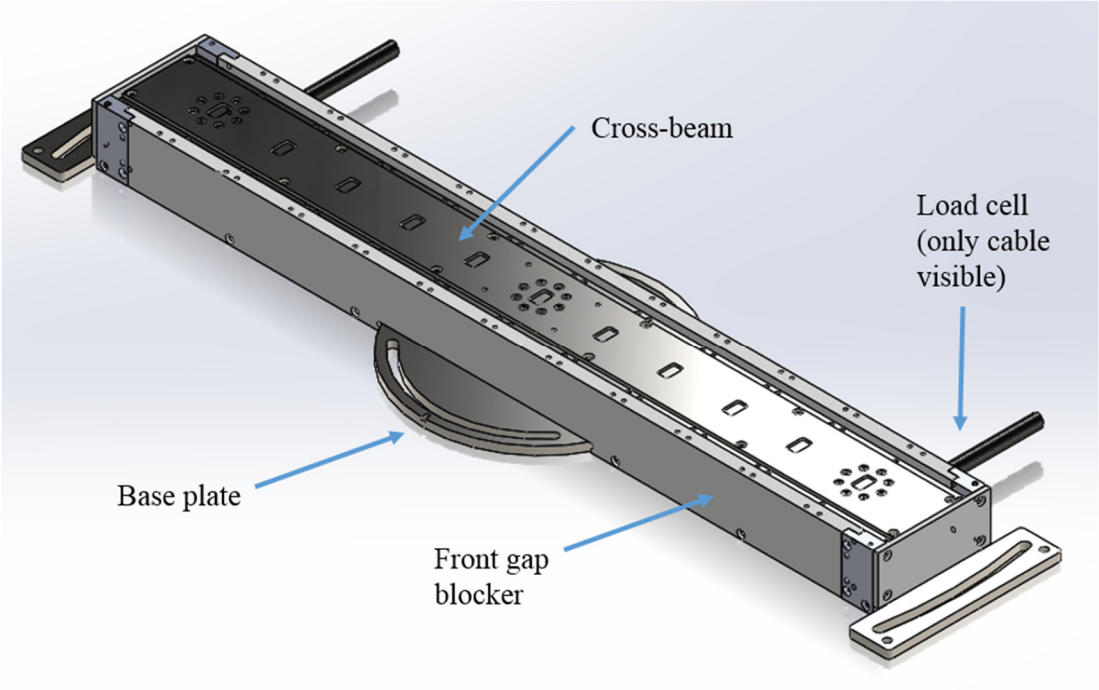


**Figure 62. CAD rendering of base structure sub-assembly.**

### 3.7.3 Whole Model Design

The modules were connected to the base structure via the cross-beam, through bolts fastened into threaded holes in the module housings. A rendering of the whole physical model assembly, in both the modular and rigid configurations, respectively, is shown in Figure 63 and a labelled elevation view of the model, showing the key dimensions, is provided in Figure 64.

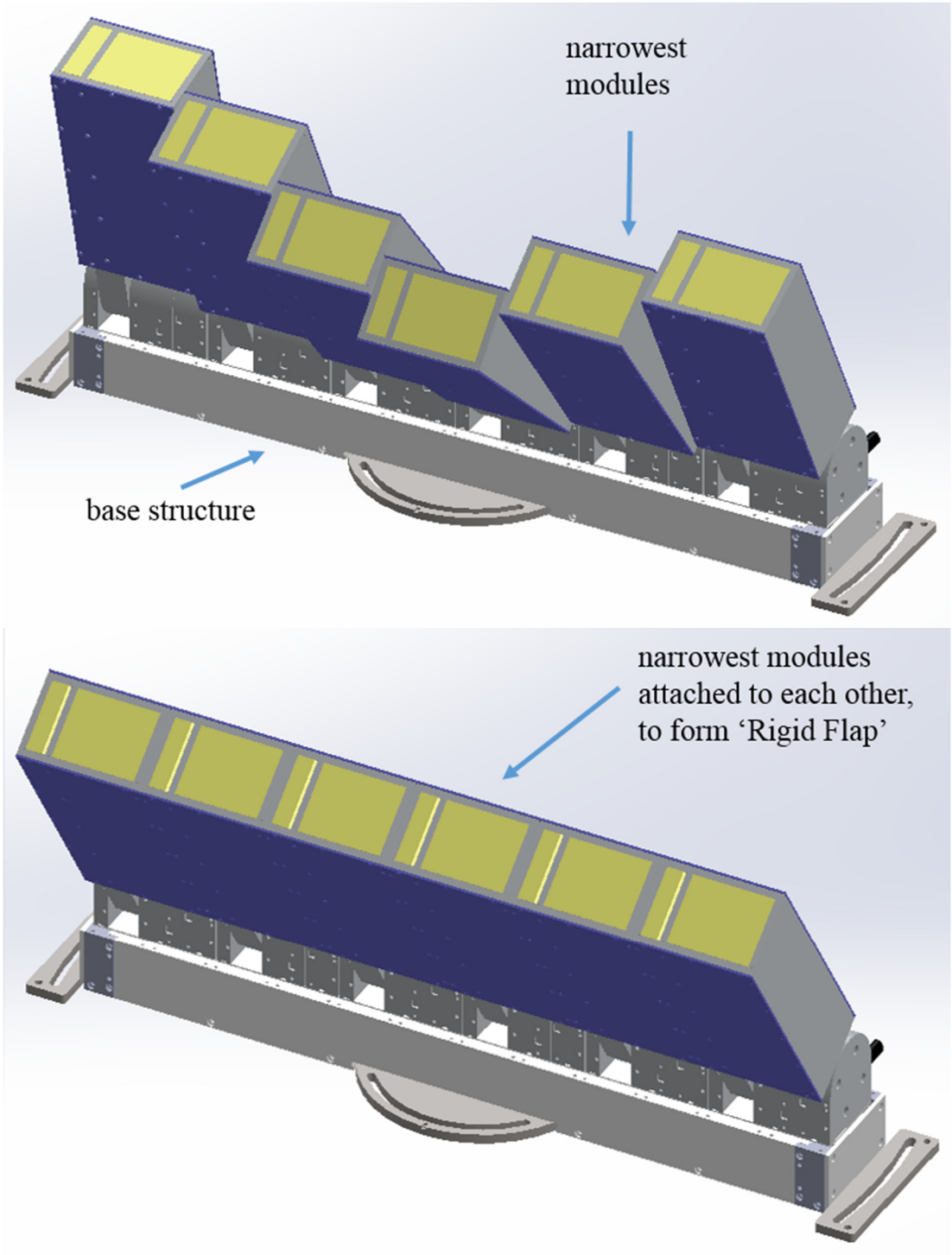


**Figure 63. CAD renderings of Modular Flap (top) and Rigid Flap (bottom).**

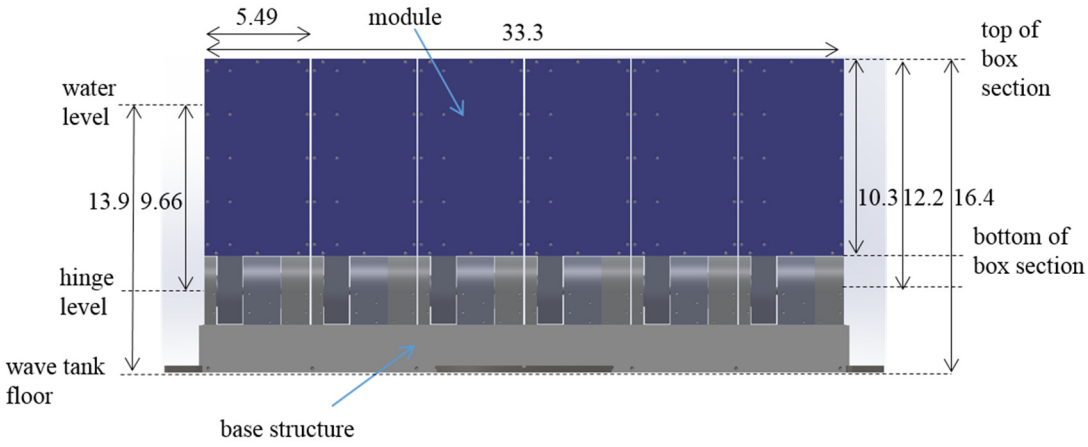


**Figure 64. Physical model device dimensions, in full scale, in m. Note that the thickness of the device was 3.6 m.**

For installing the model in the wave tank, it was first assembled on a temporary table, placed above the model position. The model was then lowered on to the wave tank floor, using a chain block attached to the base plate. For the primary purpose of providing guidance to anyone wishing to further use the physical model, Figure 65 presents a photograph of the whole model on the temporary table and attached to the chain block.

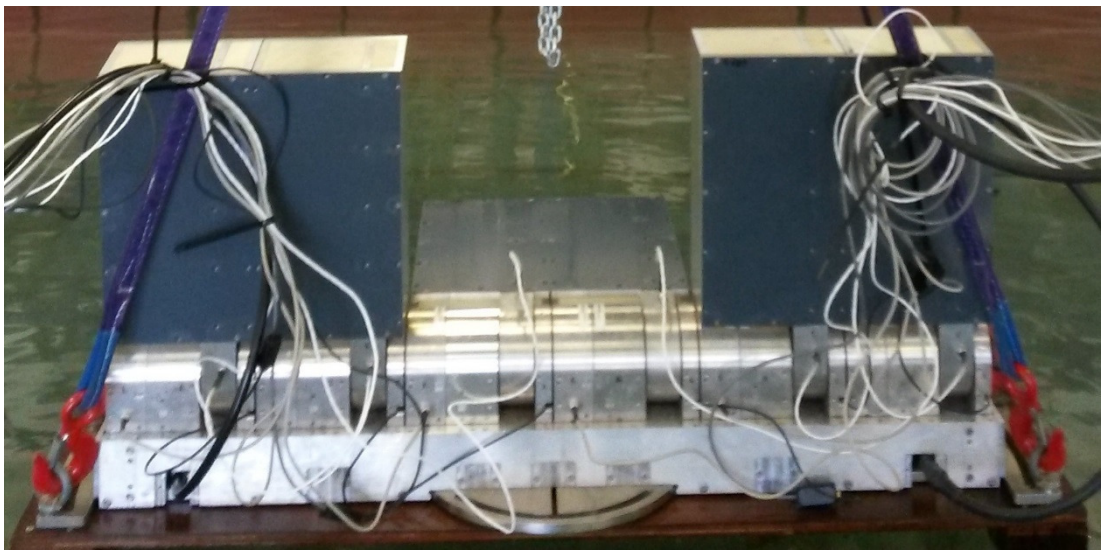

**Figure 65. Photograph of assembled physical model, configured with three modules, with the central module resting horizontally, prior to installation in Portaferry Wave Tank. Note that results from this configuration of the model were not included in the thesis to keep the focus on the six-module device. However, this was the best photo available of the whole model so therefore this picture was used for this purpose.**

The base plate was then fastened to the wave tank floor with bolts inserted into threaded inserts. A photograph of the model, installed and operating in the wave tank is shown in Figure 66.

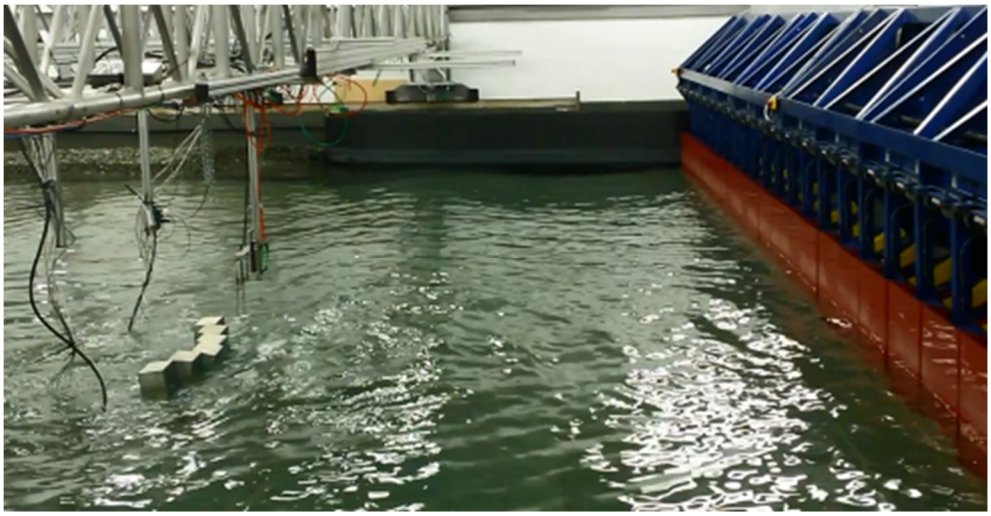

**Figure 66. Photograph of physical model, in its modular configuration, installed and operating in the Portaferry Wave Tank.**

## 3.8 Physical Model System Costs

This section outlines the financial expenditure that was required to produce the physical model system. These are shown to provide the reader with an idea of how much a fully instrumented, multi-body model, with controllable dampers, costs.

The costs included in the analysis were for the physical model and the damper control and DAQ systems. The costs also include spare parts. Parts for seven modules, instead of six, were manufactured, for example. Included also are sensors that were already available to the author, to allow the costs to be most generally applicable.

The assessed costs were for the out-sourcing, in-house design and fabrication of components. The costs are from quotes and best estimates. Only the costs of the main components of the system, such as sensors and the machining of housings, have been included. However, it is estimated that the inclusion of other components would only increase the presented total costs by a maximum of 5 % for this case study.

The costs are inclusive of VAT, at a rate of 20 %. To generalise the calculations, internal costs, for example for QUB technician time, have been treated as external costs, and so VAT has been added.

The summary costs are presented here. A more detailed cost breakdown can be found in the Appendix in Table 17 and all data in an internal spreadsheet (Wilkinson, 2016b).

The total cost of the model was approximately £87,000. These costs were split between those attributed to the 'Physical Model', 'Damper Control' and 'DAQ'. A chart, showing the contributions from each of these sections, is shown in Figure 67.

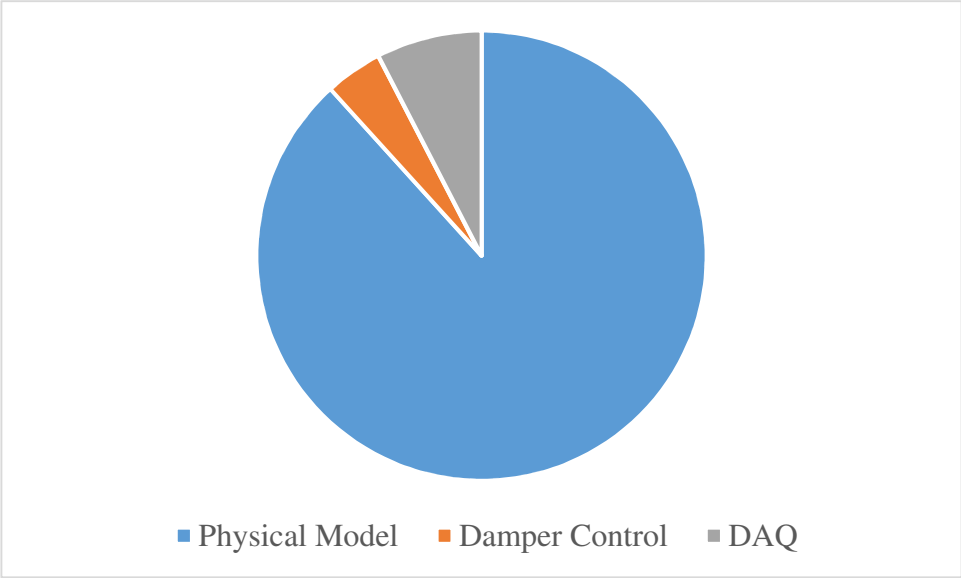


**Figure 67. Pie chart of total cost breakdown for physical model system.**

As Figure 67 shows, at 88 %, by far the largest cost contribution was from the physical model; the damper control and DAQ systems made up 4 % and 8 %, respectively. A breakdown of the costs attributed to the physical model are provided in Figure 68.

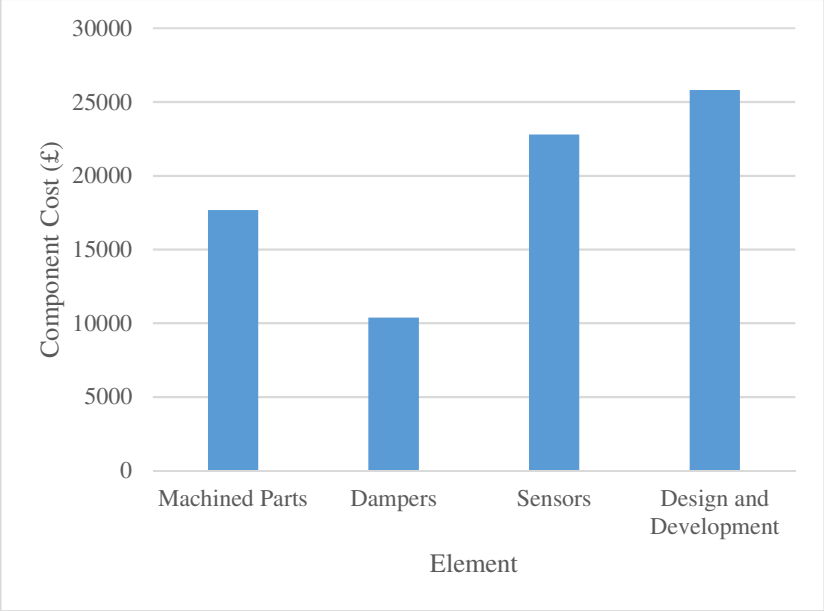


**Figure 68. Bar chart of costs for physical model in fully instrumented physical model system.**

Figure 68 shows that the four sections of the physical model all contributed a significant amount. However, the cost for 'Design and Development' was the greatest, at just over £25,000. This was from the time spent by the author and supporting colleagues for researching, testing and designing components. However, it is likely that, if the design were to be repeated with the experience gained, these costs would be less.

In terms of the tangible, physical items, the sensors were the most expensive element of the physical model. The average cost per item, including all parts, such as the amplifier, was £1425. Of the sensors, the load cells had the highest cost per item, of approximately £8000, but these were already available at the beginning of the research project (Queen's University Belfast, 2015). Of the sensors developed initially for this project, those used for measuring torque were the most expensive, at £659 per unit. The largest component of this was then the costs for machining the parts.

The cost of the machined parts, such as the sensor housings, was the next largest cost. Interestingly, by far the greatest proportion of this was from the actual machining costs. On average, the machining costs were 69 times larger than the material costs. Due to setup time, machining costs were heightened by the number of different operations required to fabricate a part. This suggests that parts should be designed as simply as possible, minimising the number of operations and hence costs.

Finally, the dampers represented the lowest total cost in the physical model. Per unit though, the dampers were slightly more expensive than the sensors, at £1482/unit. Ironically, the largest proportion of the cost of the damper was not from the component itself, but the magnetic couplings used to waterproof them. These proved a very effective waterproofing solution, not creating any appreciable extra friction and avoiding radial seal maintenance. However, they were relatively expensive, costing, for one pair of couplings, £938/unit, not including the extra £113/unit for modification in the QUB workshop. Without attempting to convert the costs to full scale, this use of the magnetic couplings

has highlighted the fact that they may be useful for waterproofing full scale PTOs, if their cost is manageable.

## 3.9 Summary

This chapter has presented a summary of the physical model system, which included the wave tank, instrumentation and the scale physical model that was tested. The instrumentation included sensors, dampers, data acquisition and a damper control system.

The physical model consisted of flap modules, mounted on a base structure. Incorporated in these were the sensors, to measure flap module damping torque and rotations and load cells to measure global foundation loads.

The power extraction of each flap module was simulated using a damper. The chosen damper was a magnetic particle brake (MPB). Each MPB was waterproofed by housing it in a box and transmitting the applied torque using co-axial magnetic couplings.

The torques applied by the dampers were controlled using a multi-port power supply and software program. The chosen damping strategy was to set the achievable damping level on each module as the same. The objective for the control system was hence to minimise the differences between the achievable torques applied to each module. The performance of the system was satisfactory, with average variation of the root-mean-square module damping torques only 3 %.

The cost of the physical model system was assessed for guidance to other designers. The total cost, not including the wave tank and wave measurement facilities, was shown to be £87,000. This shows that there needs to be strong justification for the development of such a model.

# 4. Physical Modelling Methods

## 4.1 Introduction

The aim of this chapter is to present the physical modelling methods that were used to produce the results that will be presented in Chapters 6 and 7. This includes the calibration of sensors, in section 4.2, as well as the generation and calibration of wave conditions, in section 4.3. The experimental setup and tests conducted in the physical model campaign are then presented in section 4.4. Finally, the chapter is summarised in section 4.5.

## 4.2 Sensor Calibration

### 4.2.1 Introduction

The general purpose of each sensor calibration was to produce a calibration function. This was used to convert the sensor raw output, such as voltage, to a usable output in appropriate engineering units, such as Nm for the applied damping torque. Calibration was carried out by applying a known input, such as a known torque, and measuring the output. The output was recorded for a nominal duration, for example 15 s, followed by calculation of the mean. This process was usually repeated for several data points, for example ten. The calibration function, either in the form of a single equation or a matrix, was then derived using the pairs of data points.

### 4.2.2 Wave Probes

An array of wave probes was used for wave elevation measurement. The wave probes for this were calibrated by first recording the raw signals for 15 s. The results were then averaged. This was carried out at two data points.

The calibration points were on the same vertical axis and separated by a known height. The difference in height was measured as a change in surface elevation by the probes. The use of only two data points was assumed to be sufficient

due to the proven linearity of wave probes (Folley, 2010). Folley (2010) carried out an assessment of the linearity of wave probes used in the Portaferry wave tank. The author tested wave probes by measuring the surface elevation for several points. Fourteen probes, from the forty available, were selected at random for these tests. It was found that the $R^2$ measure of linear trend line fit for the probes was always greater than 0.9996, indicating a high degree of linearity (Folley, 2010; P. Lamont-Kane, 2015a).

The difference in height of the two points, at the testing position and at a positive offset, was 100 mm. The probes were raised using a compressed air system. A photograph of a typical array of wave probes in the wave tank, showing the key calibration features, is provided in Figure 69.

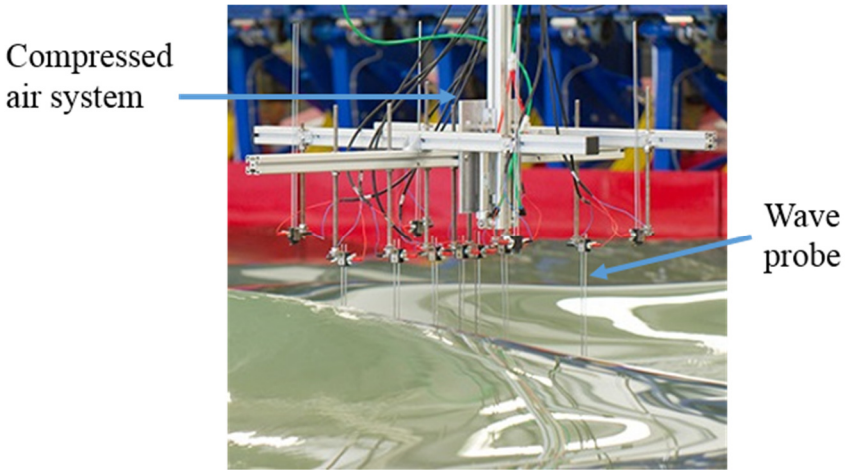


**Figure 69. Photograph of a typical array of wave probes, showing the key calibration features (Queen's University Belfast, 2013).**

The probes were calibrated so that the maximum difference between the values measured by each probe at the operating position was less than 0.5 mm.

The calibration of each the probe was defined with a linear fit, providing a slope and offset. An example of calibration results is shown in Table 4.

**Table 4. Wave probe calibration results example.**

| Position | Height (mm) | Mean Measurement (V) | Slope (mm/V) | Offset (mm) |
|---|---|---|---|---|
| 1 (operating position) | 0 | 0.207 | 1180 | -243 |
| 2 | -100 | 0.122 | | |

### 4.2.3 Rotation Sensor

The rotation sensors were calibrated by recording the signals at several known angles. The reference instrument for determining the known angles was a digital protractor, described in section 3.4.3.

The six rotation sensors, one for each module, were calibrated simultaneously. This was carried out by connecting the modules together with an aluminium bar on each face and rotating the whole assembly. The reference angles were measured on the face of one of the central modules.

The sensors were calibrated in both directions, i.e. ‘seaward’, towards the wave paddles, and ‘landward’, towards the beach at the back of the wave tank. Five points were recorded on each side, with another close to the ‘up right’, or 0° position.

Data was recorded for 10 s at 128 Hz, with the means then taken. An example calibration graph is shown in Figure 70 and a list of the calibration statistics, showing the generally high linearity for all of the sensors, is provided in Table 5.

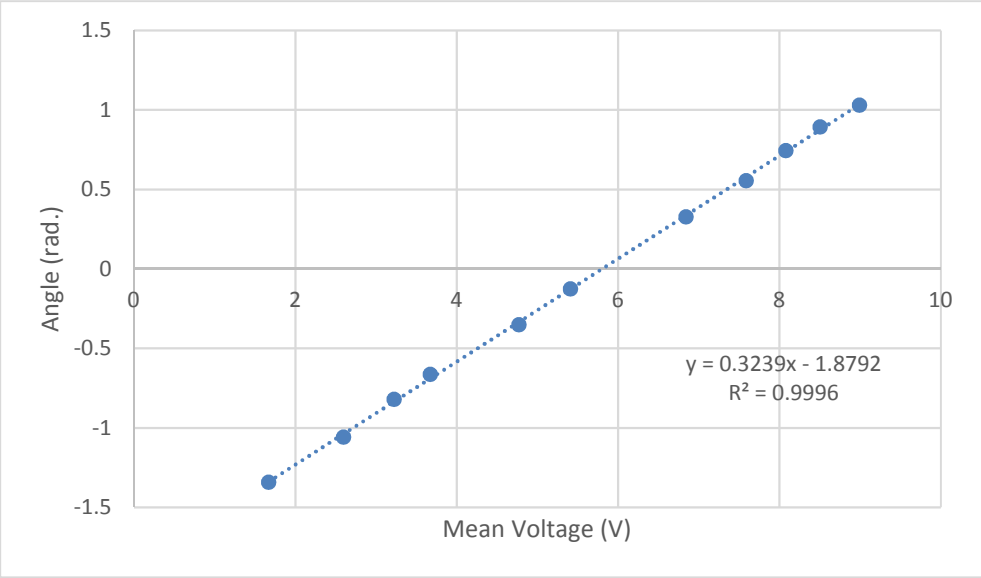


**Figure 70. Blade rotation sensor calibration results example plot.**

**Table 5. Blade rotation sensor calibration statistics.**

| Blade Rotation Sensor No., $n$ | Calibration Slope, $m_\theta$ (rad/V) | Coefficient of Determination of Calibration Data, $R^2_\theta$ |
|---|---|---|
| 1 | 0.3239 | 0.9996 |
| 2 | 0.3309 | 0.9998 |
| 3 | 0.3155 | 0.9994 |
| 4 | 0.3847 | 0.9993 |
| 5 | 0.3836 | 0.9992 |
| 6 | 0.3889 | 0.9986 |

### 4.2.4 Torque Sensors

The torque sensors were calibrated by applying known torques to the sensor shaft and measuring the outputs. The torques were applied by hanging weights

on a lever arm connected to the shaft. The lever arm was at an angle, because of the spline on the shaft, but this was accounted for by measuring the angle using the digital protractor described in section 3.4.3.

Both positive and negative torques were applied, by loading the torque sensor from each side. The measurements were also taken during loading and unloading of the weights, to account for hysteresis.

The torque sensor was held rigid by mounting it in its upright, which was fastened to a table with g-clamps. The shaft of the torque sensor was supported, but allowed to turn, via a bearing and housing. This meant that the shaft was subjected to pure torsion. The calibration apparatus is shown in Figure 71.

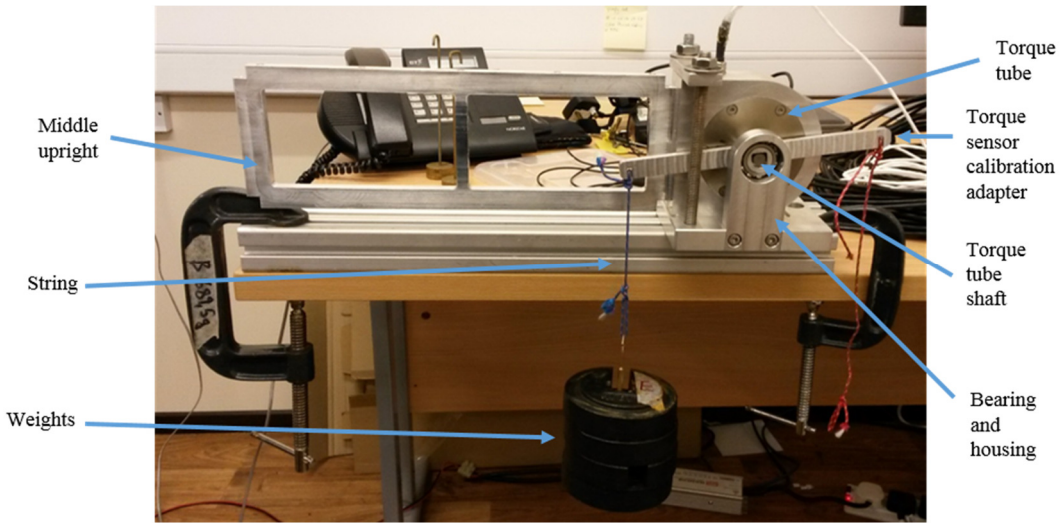


**Figure 71. Torque sensor in calibration rig.**

Data was recorded for 10 s at a frequency of 128 Hz with the means then taken. The mean voltages for each test were plotted against the applied torque. An example of a loading and unloading plot is shown in Figure 72.

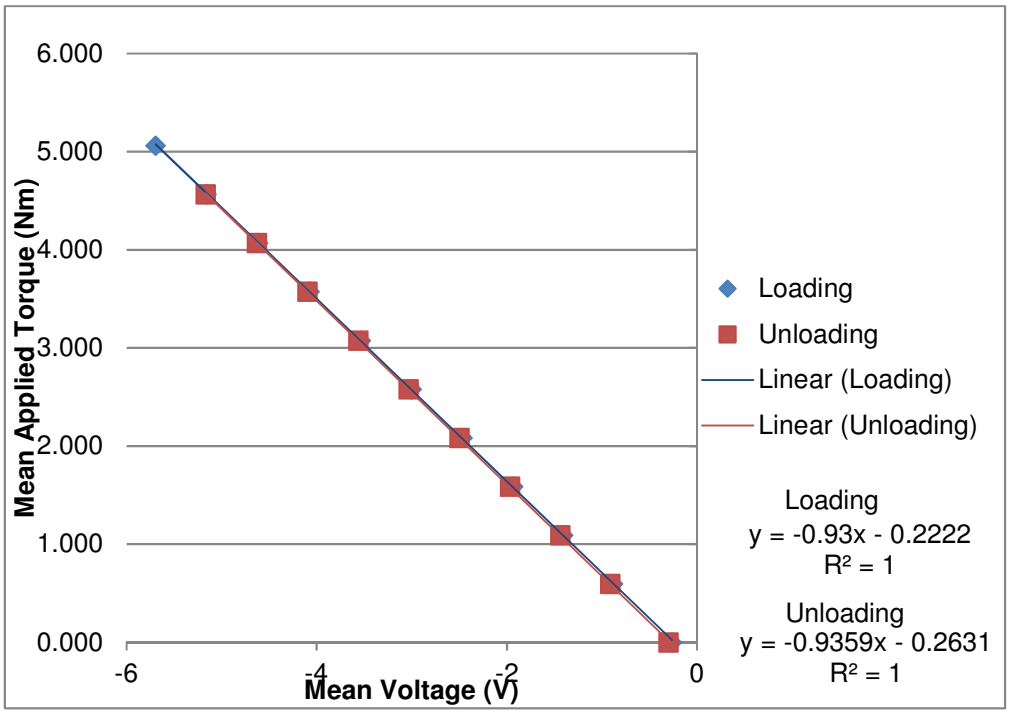


**Figure 72. Torque sensor calibration example plot, showing loading and unloading in positive direction.**

Figure 72 shows that both the loading and unloading results were very linear and that they had similar line equations. This was generally true for the torque sensors.

To define the general calibration equations, a plot was produced for all results for each torque sensor. A linear fit was then put through the data. An example graph is shown in Figure 73.

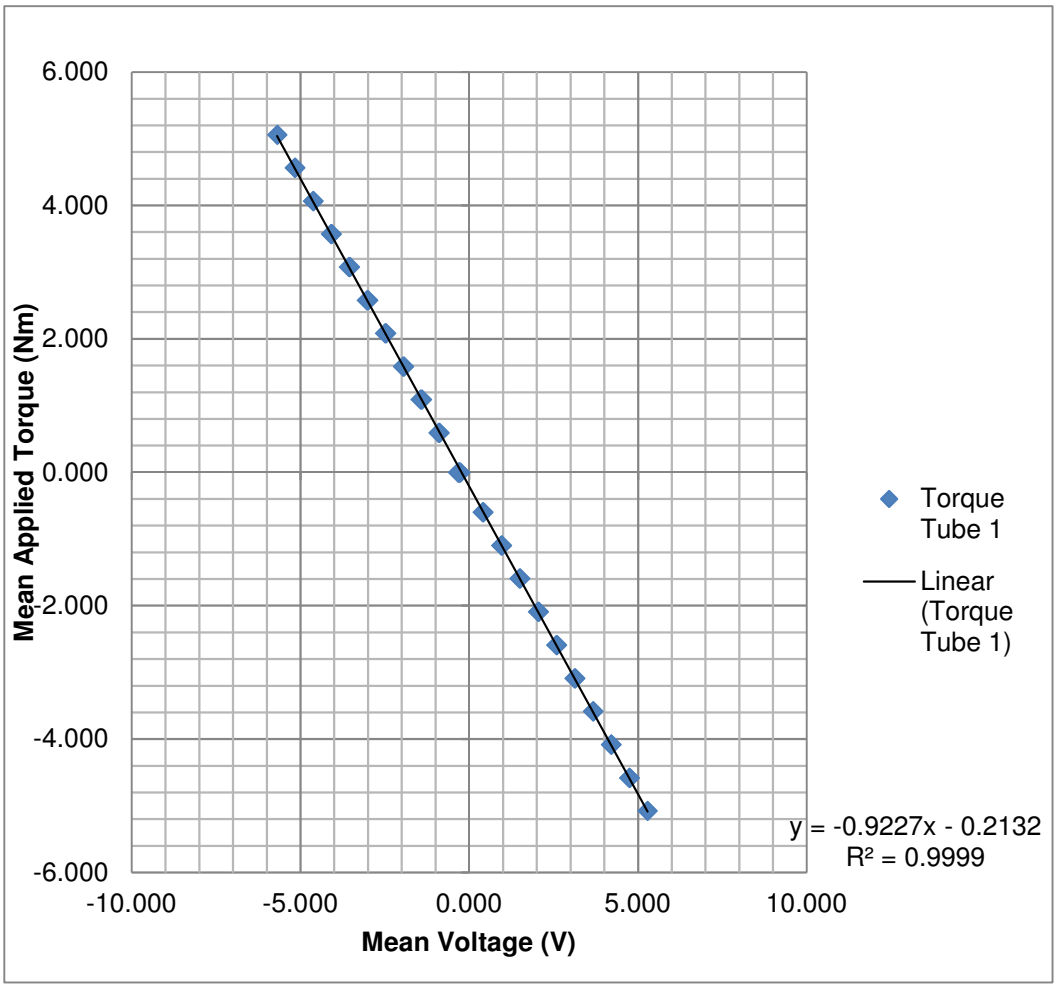


**Figure 73. Torque sensor calibration example plot, showing all results.**

Figure 73 shows that the sensor responded linearly to changes in applied torque. This is implied by the high coefficient of determination, $R^2 = 0.9999$. The summary statistics for all torque sensor calibrations are presented in Table 6.

**Table 6. Summary statistics from torque sensor calibrations.**

| Torque Sensor | Calibration Slope, $m_{Tc}$ (Nm/V) | Calibration Offset (Nm) | Coefficient of Determination, $R^2$ |
|---|---|---|---|
| 1 | -0.9227 | -0.2132 | 0.9999 |
| 2 | -0.8947 | 0.1066 | 1.0000 |
| 3 | -0.8911 | 0.3555 | 0.9999 |
| 4 | -0.9135 | -0.0177 | 1.0000 |
| 5 | -0.8966 | -0.4888 | 1.0000 |
| 6 | -0.8793 | -0.0534 | 0.9994 |

Table 6 shows that all of the torque sensors were calibrated to high degrees of linearity, with $R^2$ values all above 0.9990. The calibration slopes were all also approximately -0.90, suggesting that the electronic and mechanical responses of the sensors were all similar. This consistency of results was desirable as it suggests that the uncertainties associated with the resolution of the measurements will have been similar, making the results between modules more easily comparable.

### 4.2.5 Foundation Load Sensors

The load cells used for measuring foundation loads were calibrated by applying known forces and moments to the sensors and measuring the outputs. All six degrees of freedom, i.e. heave, surge, sway, pitch, roll and yaw, were loaded in the procedure. The reference system for the loads, with respect to the load cells, is provided in Figure 74.

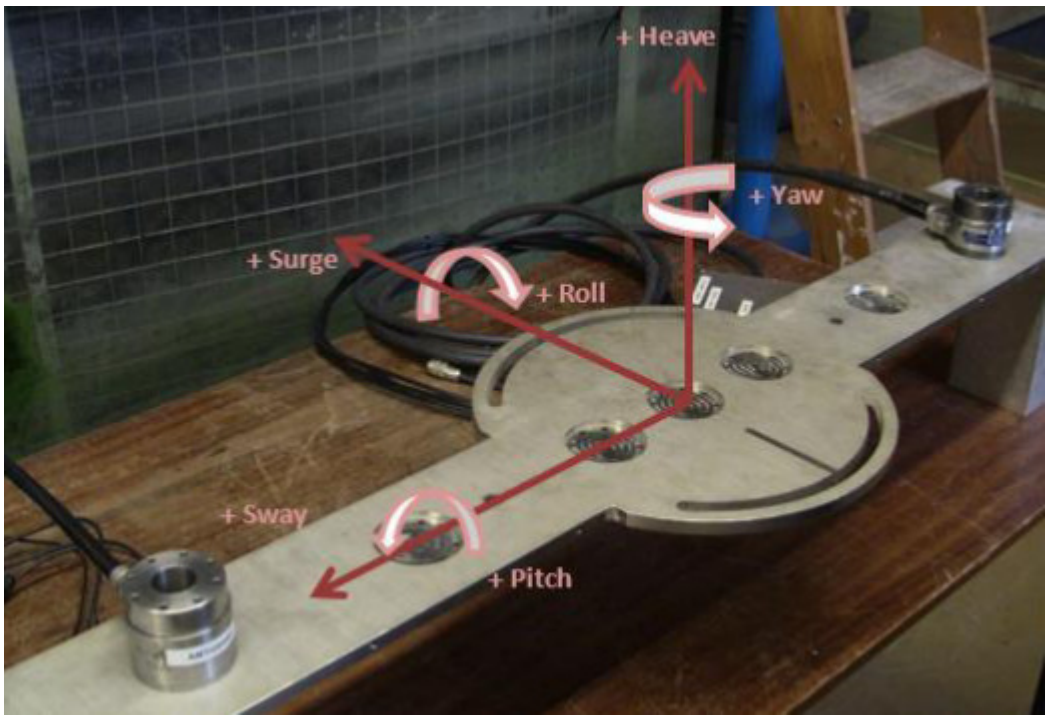


**Figure 74. Foundation load reference system with respect to physical model base plate and load cells (Álvarez, 2015).**

The calibration was conducted using a rig that allowed the model to be configured in various ways, thus allowing different loads to be applied. Forces and moments were applied by hanging weights from lever arms on an adaptor attached to the physical model base structure.

The ranges of weights and lever arm distances were 55-185 N and 75–125 mm, respectively (Álvarez, 2015). Thus, the range of forces and moments was 55-185 N and 4.1-23 Nm, respectively. This represented well the expected ranges of loads acting on the physical model.

A high number, 204, of load cases were applied, to increase the accuracy of the calibration function. In most of these cases, the loads were combined, for example applying loads in the pitch and heave degrees of freedom at the same time. This was to account for the coupling of loads.

The calibration rig was attached to structural beams on the side of the wave tank in the QUB Hydraulics Laboratory in Belfast. The calibration adapter was

placed in the centre of the rig and hence off-axis loading was not considered. However, unpublished testing results for a different flap model showed that applying off-axis loads resulted in a similar level of calibration accuracy to when solely using on-axis loads (Paul Lamont-Kane, 2015). A CAD rendering of the calibration rig is shown in Figure 75.

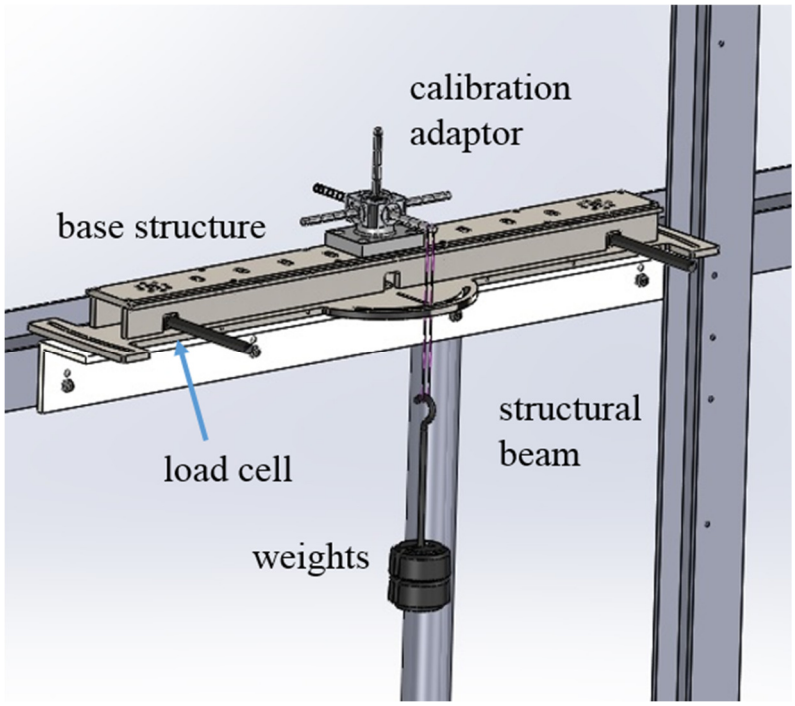


**Figure 75. Two load cells and base structure in calibration rig. Load application shown was positive pitch and negative heave.**

A datum file was recorded before each set of tests cases. Loads were recorded for 5 s, at a sampling frequency of 128 Hz, with the means of the signals then taken. The test data sets were then zeroed with the datum means.

To account for any cross talk between channels, a calibration matrix, instead of a single equation, was used to convert the corrected voltage outputs to the applied loads (Advanced Mechanical Technology Inc, 2012). Unfortunately, during the testing campaign, due to an unknown reason, the heave channel on the AMTI2000B load cell only recorded electrical noise. Due to the coupling of the load cells, this meant that it was deemed necessary to remove the heave channels from the calibration matrix. The calibration data was therefore

reprocessed without the heave data. This reduced the calibration matrix to being five by five cells in size. The heave loads were also not measured during the testing campaign. While the roll readings were taken during the testing, given the strong coupling between the heave and roll degrees of freedom, the roll readings were purely used for resolving the results for the other degrees of freedom.

To determine the calibration matrix, $k$, for each load cell setup, Equation 23 was used.

$$k = \frac{LGV_{ex}10^{-6}}{V_m} \qquad \text{Equation 23}$$

Each variable in Equation 23 is a matrix. $L$ was the known applied loads, in N or Nm, $G$ the gains, $V_{ex}$ the excitation voltages, in V, and $V_m$ the mean measured voltages, in V (Advanced Mechanical Technology Inc, 2012), corrected with the datum values. The values that were used for $G$ and $V_{ex}$ can be found in the appendix in section 13.1. The calibration matrix, $k$, is shown in Table 7.

**Table 7. Calibration matrix values for each degree of freedom (DoF) for the two load cells setup.**

| DoF | $V_{Sway,A}$ | $V_{Surge,A}$ | $V_{Pitch,A}$ | $V_{Roll,A}$ | $V_{Yaw,A}$ | $V_{Sway,B}$ | $V_{Surge,B}$ | $V_{Pitch,B}$ | $V_{Roll,B}$ | $V_{Yaw,B}$ |
|---|---|---|---|---|---|---|---|---|---|---|
| $F_{Sway}$ | -2.96 | -0.09 | 0.05 | 0.00 | -0.04 | -2.97 | 0.03 | -0.06 | 0.00 | -0.20 |
| $F_{Surge}$ | 0.01 | -2.80 | -0.15 | -0.01 | 0.28 | 0.03 | -3.15 | 0.14 | -0.01 | 0.24 |
| $F_{Pitch}$ | 0.00 | 0.29 | -0.04 | 0.00 | -0.01 | 0.00 | 0.31 | -0.06 | 0.00 | -0.03 |
| $F_{Roll}$ | -0.09 | 0.73 | -0.60 | 0.20 | 1.11 | 0.02 | -0.76 | 0.61 | 0.17 | 0.98 |
| $F_{Yaw}$ | 0.00 | 1.41 | -0.01 | 0.01 | -0.06 | 0.01 | -1.39 | 0.01 | 0.00 | -0.02 |

The accuracies of the calibration matrices were evaluated by using them to re-calculate the applied loads. These were then compared to the original reference

loads, with the percentage differences calculated. The mean differences were typically less than 1 %, as shown in Table 8.

**Table 8. Results from comparison of measured to applied loads for each degree of freedom from the load cell calibration.**

| Difference | Degree of Freedom, DoF | | | | |
|---|---|---|---|---|---|
| | Sway | Surge | Pitch | Roll | Yaw |
| Max. Overestimation (%) | 1 | 1 | 1 | 5 | 2 |
| Max. Underestimation (%) | -1 | -1 | -1 | -6 | -4 |
| Mean Difference (%) | 0.0 | 0.0 | -0.1 | -0.7 | -0.2 |

## 4.3 Wave Generation and Calibration

### 4.3.1 Generation

Waves were generated in the wave tank using the Ocean software package, provided by Edinburgh Designs Ltd (Rogers and King, 1997). Wave conditions were specified in the language 'wave' in '.wav' files and compiled in Ocean. This produced a '.sea' file for each set of wave conditions, which was then used in a graphical user interface to run the waves.

The characteristics of the desired waves were determined through the specification of sinusoidal waves. Regular waves consisted of a single frequency component, whereas irregular waves were made up of a combination

of components, with random phases separating them. This idea is illustrated in Figure 76.

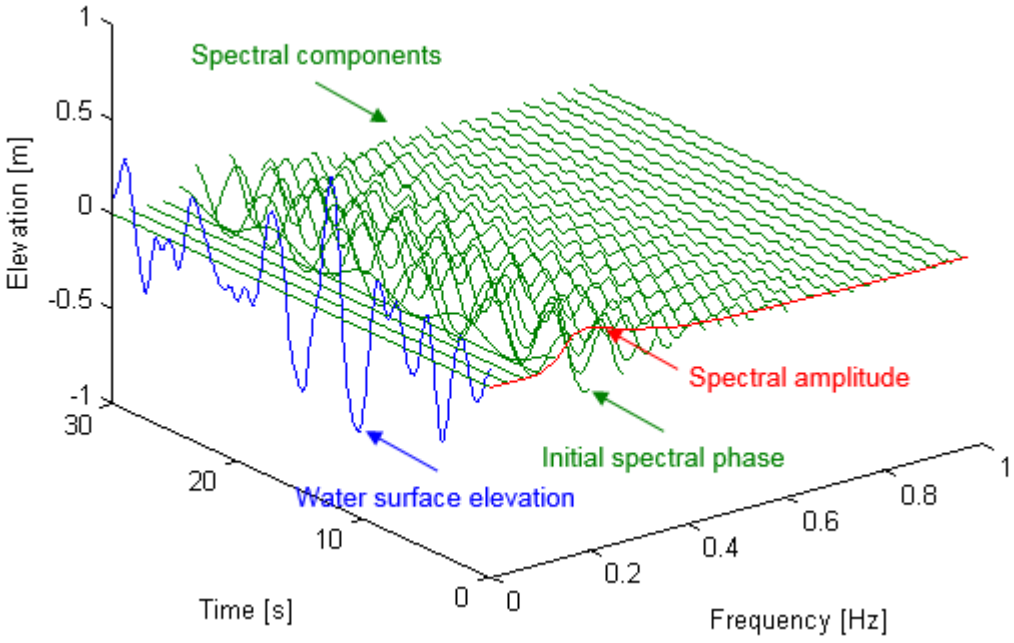


**Figure 76. Graph showing the composition of a time-domain surface elevation through the superposition of individual spectral components (Clabby, 2013).**

The specific frequencies that could be generated in the wave tank was not continuous. Discretisation of the frequency range, $f_\Delta$, in Hz, was determined by the clock rate of the tanks, $CR$, and a run number, $R_{num}$, using Equation 24.

$$f_\Delta = \frac{CR}{2^{R_{num}}} \qquad \text{Equation 24}$$

The clock rate was equal to 32 Hz (O'Boyle, 2013). The frequency of each component, $f$, in Hz, was then determined using Equation 25.

$$f = f_{num} f_\Delta \qquad \text{Equation 25}$$

Where $f_{num}$ was an integer set by the user. Completion of a full cycle of each component occurred within a run time. $R_{num}$ was an integer between 6 and 16 (Lamont-Kane P. and Moore, 2015). As also shown in Equation 24, the larger the $R_{num}$ value, the smaller the frequency discretisation was and so the greater

the number of different frequency components that completed a full cycle in the run time. The $R_{num}$ value was also chosen to provide a repeat time, $RT$, in s, of the wave conditions, as shown in Equation 26.

$$RT = \frac{2^{R_{num}}}{CR} \qquad \text{Equation 26}$$

Only one run of the waves was used for each sea state and so the repeat time was equal to the duration of the tests. As shown in Equation 26, the repeat time was proportional to 2 raised to the power of $R_{num}$. Hence, the available repeat times were between 2 and 2048 s.

For regular waves, the frequency discretisation must be sufficiently high resolution, but only for generating a single component. The required duration for achieving acceptable calibration accuracy is hence lower than for irregular waves. Clabby (2014) showed that the difference between desired and achievable wave periods, for a 7 s wave at full scale, was only 0.3 % for a 64 s model scale testing duration. Hence, this duration was chosen for generating regular waves.

To best represent a realistic irregular sea state, it is desirable to use as continuous a frequency range as possible. This hence leads to the specification of high $R_{num}$ values. This results in long duration seas though, which can be impractical for testing. For fundamental testing, to determine average power capture for example, the industrial standard for the length of an irregular sea state at full scale is 20-30 minutes (European Marine Energy Centre, 2009). These values can be used to determine the test durations at model scale. Using the mean of the range, of 25 minutes, this provides a Froude scaled value of 274 s at 30$^{th}$ scale. The power of 2 value closest to 274 s was 256 s, which was hence the duration used for irregular wave generation.

The amplitude of each sinusoidal component was determined from the product of a tank transfer function (TTF) coefficient and a gain. The TTF was a file that

specified the conversion factor, for each frequency, between the demanded wave amplitude and the force generated by the paddles.

### 4.3.2 Calibration

The wave conditions were calibrated by running and measuring waves in the wave tank without the physical model installed in it. The first stage of the process was compiling target spectra for each sea state. This was a set of gains, one for each frequency component. The waves were then run in the wave tank and the time-series of surface elevation was measured.

The surface elevation signal was converted into the frequency-domain, using a Fast-Fourier-Transform method, presented in Table 24 in appendix section 13.3 (Clabby, D. and Lamont-Kane, 2013). This allowed the individual frequency components to be identified and hence their amplitudes measured.

The ratios of the measured to target amplitudes were then used to adjust the gains of the frequency components. This individual adjustment of the gains allowed detailed control over the shape of the wave amplitude spectrum. Notwithstanding this, the control over the amplitudes of the components was not perfect and the calibration was hence an iterative process. The procedure was repeated until the measured waves were sufficiently close to the target conditions (Clabby, 2014).

The criteria for the regular waves was that the amplitudes were within 2 % of the target values; for the irregular waves, the significant wave height and mean wave period had to be within 5 % of the target values.

The waves were measured with an array of wave probes. The probes were arranged in a cross-shape, with the axes parallel to the x and y axes in the wave tank. The x-axis was in the direction of normal wave propagation and the y-axis parallel to the crest and model hinge. The origin was set above the centre of the model installation area.

On the x-axis line were seven wave probes, with the fifth probe at the origin; on the y-axis were nine probes, with the centre probe at the origin. A further two probes, on a separate compressed air system, were placed on the y-axis, at approximately - 1 m. These were left there during both the wave calibration and model testing in order to have results for checking the wave conditions during testing. A photograph of both wave probe arrays, with the axes shown, is provided in Figure 77. The positions of the probes on the calibration array on the x and y axes are presented in Table 9 and Table 10, respectively.

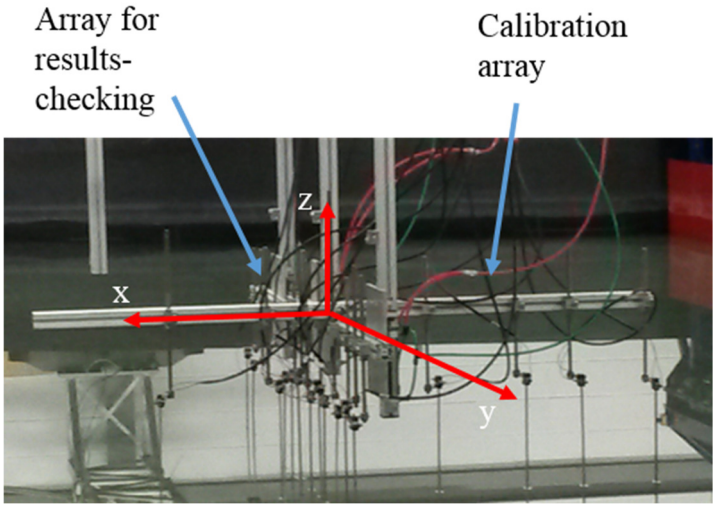


**Figure 77. Wave probe arrays that were used for wave calibration and for results-checking during tests. Also shown are the reference axes.**

**Table 9. Spacing of wave probes on the x-axis.**

| **Probe No.** | 1 | 2 | 3 | 4 | 5 | 6 | 7 |
|---|---|---|---|---|---|---|---|
| **X position (m)** | -0.844 | -0.659 | -0.515 | -0.298 | 0.000 | 0.089 | 0.380 |

**Table 10. Spacing of wave probes on the y-axis.**

| **Probe No.** | 1 | 2 | 3 | 4 | 5 | 6 | 7 | 8 | 9 |
|---|---|---|---|---|---|---|---|---|---|
| **Y position (m)** | 0.464 | 0.371 | 0.278 | 0.093 | 0.000 | -0.093 | -0.278 | -0.371 | -0.464 |

The calibration method that was used was different for head-on and off-angle waves. For the head-on waves, which represented the majority of the conditions, reflection analysis was used (Mansard, E. and Funke, 1980). The reflection analysis was used to separate the incident and reflected components. This was used so that the dynamics of the devices could be better understood and to allow for more accurate representation of the conditions during future numerical modelling.

The reflection analysis technique was largely based on the methodology employed by Clabby (2014), which uses a published method (Mansard, E. and Funke, 1980). The combinations of probes used for the reflection analyses for the head-on regular and irregular waves are provided in the appendix in section 13.2. The reflection analysis was performed using the function 'threeproberef_DJC' (Folley, Clabby and Crooks, 2015), which is shown in Table 22, in appendix section 13.3. This outputs a spectrum of incident and reflected wave amplitudes. An illustration of this, for an example regular wave, with a target period of 13.5 s and amplitude of 1.0 m, is shown in Figure 78.

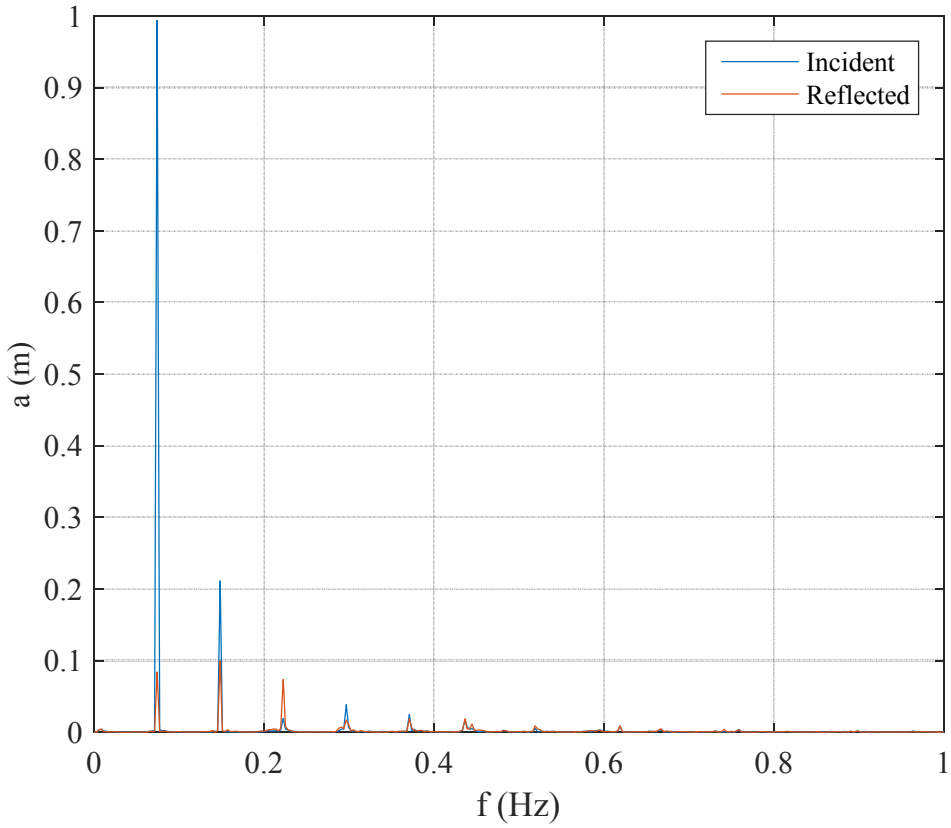


**Figure 78. Example full-scale spectrum of incident and reflected wave amplitudes, *a*, against wave frequency, *f*. Example wave had a target incident amplitude of 1 m and frequency of 0.074 Hz (13.5 s period).**

For the regular waves, the peak incident wave amplitude, i.e. the maximum value, was used to represent the measured wave. As shown in Figure 78, the peak incident wave amplitude was very close to the target value of 1 m.

Figure 78 also shows that the peak reflected wave amplitude was approximately 0.1 m. Reflection coefficients, the ratios of reflected to incident wave amplitudes, measure the level of wave reflection (O'Boyle, 2013). This means that, in this case, the reflection coefficient was 0.1. The energy content of a reflected wave, relative to the incident energy, is proportional to the reflection coefficient squared (O'Boyle, 2013). Hence, the relative reflected energy content was only 1 %. This was typical across the calibrated head-on regular waves. The reflected energy content could therefore generally be

assumed to have insignificant effect on the total energy available for a given wave condition.

The target irregular wave conditions were defined using a Bretschneider wave spectrum, the standard recommended by the International Towing Tank Conference (Techet, 2005). The spectrum is defined using the peak enhancement factor, the frequency range, mean wave period, $T_{01}$, and significant wave height, $H_{m0}$. The spectrum was defined using an in-house written function, presented in Table 23 in appendix section 13.3 (Clabby, 2012). An example spectrum, for a sea state with a target $H_{m0}$ of 2.75 m and $T_{01}$ of 6.5 s is shown in Figure 79. This shows the target spectrum, compared to the measured incident, reflected and total spectra.

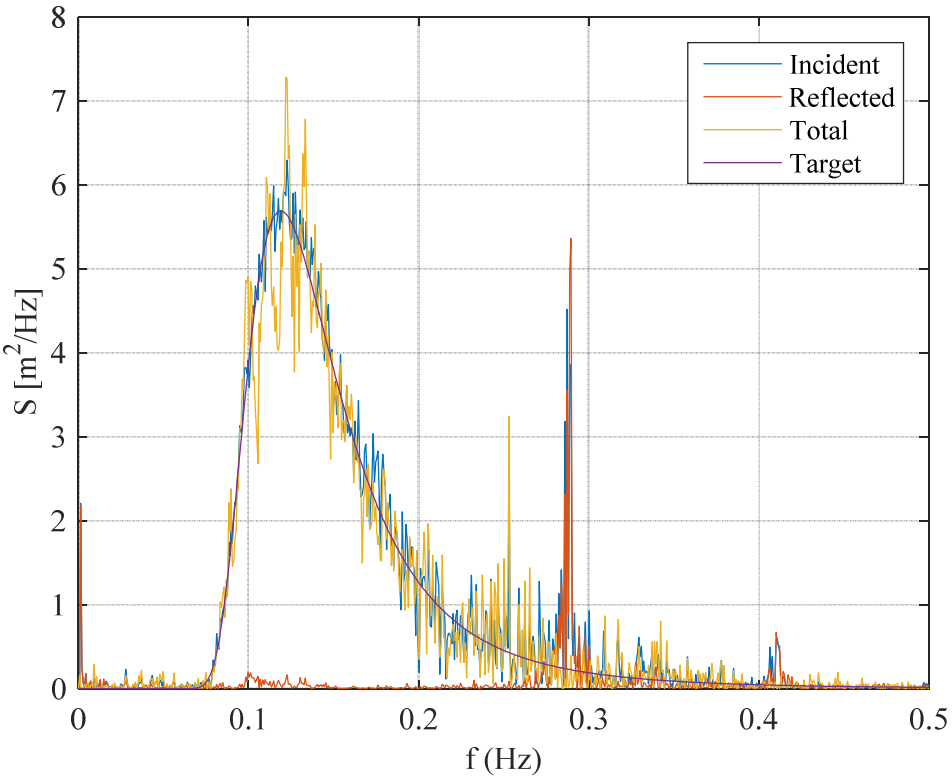


**Figure 79. Example full-scale spectra for calibrated irregular waves, showing spectral energy density, *S*, against frequency, *f*, for measured incident, reflected and total surface elevation, compared to the target components.**

The spectra example in Figure 79 shows that the incident spectrum matched the target one very well. The reflected frequency components were also generally

low in magnitude, apart from in a spike at around 0.3 Hz frequency, or 1.6 Hz at model scale. The spike was also present in the incident spectra. The narrow band of the spike and its relatively high frequency suggests that this was not actually wave reflection. The high amplitude indicates that it may have instead been a wave tank resonance effect. Resonance occurs when a body is excited at a frequency, in this case by waves, that is close to its natural frequency. In order to ascertain if the wave tank was indeed experiencing resonance, its natural frequency, $f_n$, was calculated using Equation 27 (Truong, 2012).

$$f_n = \frac{1}{2\pi}\sqrt{\frac{\pi g}{L}\tanh(\frac{\pi h_z}{L})} \qquad \text{Equation 27}$$

Where, $L$ was the length of the wave tank, taken as 15 m, and $h_z$ was the depth of water. As the wave tank is sloped, $h_z$ was set as the value of the estimated mean depth, calculated using the slopes and dimensions shown in Figure 23 as 0.3 m. Hence, $f_n$ was calculated as 0.6 Hz. This was far away from the frequency of the spike in Figure 79, 1.6 Hz at model scale. Hence, it was unlikely that the spike was a result of resonance. The likely cause was actually the reflection analysis that was applied. One of the limitations of the Mansard and Funke method is that certain probe spacings should be avoided. When the spacing between the probes is equal to half of the product of the wavelength and any integer, the equations used in the method have singularities meaning that the reflected components cannot be determined (Mansard, E. and Funke, 1980). Whether or not this was the case here can be established. The spacings between the probes, referring to Table 9 and Table 21 for information, were 9.87, 27.99 and 18.12 m, at full scale. The spike in Figure 79 was at approximately 0.285 Hz. Using the dispersion theorem, defined in Equation 32, to determine the wave number, $k$, the wavelength, $L$, was then calculated by dividing $k$ by $2\pi$, giving a value for $L$ of 19.2 m. Values of $nL/2$ for $n$ of 1, 2 and 3, for example, were therefore 9.6, 19.2 and 28.8 m, respectively. These values were very close to the probe spacings. Hence, it is likely that the spike

was actually a product of the reflection analysis. This is reinforced by the fact that the 'total' spectrum shown in Figure 79 does not have the spike that appears in the 'incident' and 'reflected' spectra. Therefore, the only effect of the presence of the spike was that it reduced the accuracy of the measured significant wave height, $H_{m0}$. However, the inherent narrow thickness of the spike meant that the change will have been relatively small and could be neglected.

Calibration of the off-angle waves was performed without the reflection analysis. This was because the reflection analysis method that was used for the head-on waves required the wave probes to be on a line parallel to the direction of propagation (Mansard, E. and Funke, 1980). For practical simplicity, the direction of the line of probes was not changed to match the incident wave direction for each angle change. Instead, just the total surface elevation was used, i.e. without splitting the incident and reflected components.

Although they were not measured, the reflection coefficients for off-angle waves were likely similar to those for head-on waves. This is because, as discussed in section 3.3, the Portaferry Wave Tank was surrounded with absorbing beaches. The maximum reflection coefficient for head-on waves was 0.17. This can therefore be assumed to be the maximum coefficient for the off-angle waves too. Hence, use of the total surface elevation, instead of separating the incident and reflected components, would result in the uncertainty on the incident wave amplitude being 17 %. This is not within the previously stated target accuracy of the regular wave calibration of 2 %. However, it is acceptable for this study due to its principal aim being measurement of relative results between the modular and rigid devices.

When regular waves are generated at an angle, the consistency of the amplitude of the crest is not as high as when the waves are head-on (O'Boyle, 2013). To measure this inconsistency and partly mitigate it, the mean amplitude of nine probes was used. These probes were positioned along the y-axis of the calibration array, with their positions provided in Table 10.

A spectrum of amplitudes was recorded for each position, using the analysis script presented in Table 24. The wave was represented then by the mean of the peak amplitudes. An example showing the typical range of peak amplitudes recorded is shown in Figure 80. This shows that there was typically up to 10 % variation in the peak amplitude across the testing area. However, the primary aim was to measure the results associated with the whole devices. Hence, this level of variation at points across the device were acceptable.

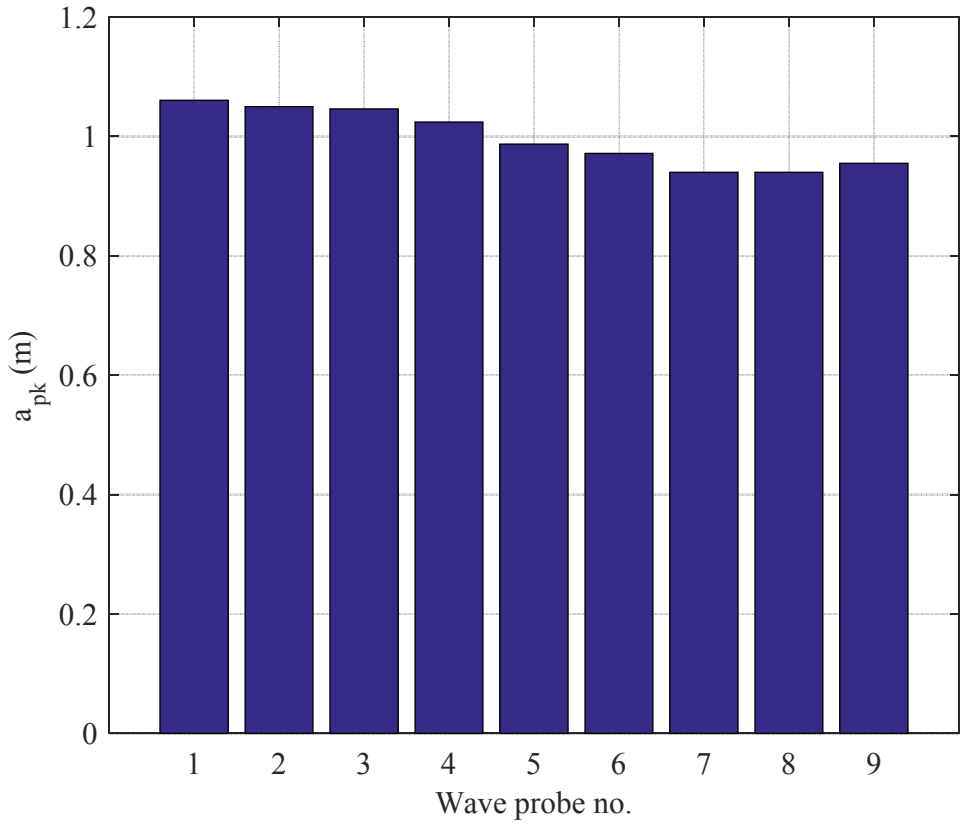


**Figure 80. Peak wave amplitude, $a_{pk}$, against probe number, $n$, showing variation in amplitudes for off-angle wave. Example was for a wave with a full scale period of 8.5 s, nominal amplitude of 1 m and direction of 27.5 degrees.**

## 4.4 Testing Campaign

### 4.4.1 Introduction

This section presents the key information on the experimental setup and the tests that were conducted for the physical modelling campaign. The tests were

conducted to compare the power capture and foundation loads experienced by modular and rigid flaps. These tests were hence performed to answer the key research questions of the thesis, stated in section 1.3. The model configurations were each tested in a range of wave conditions, summarised in section 4.4.2. For each wave condition, a set of damping levels was applied to the model, presented in section 4.4.3.

### 4.4.2 Wave Conditions

The primary variables for wave conditions are the characteristic amplitude, period and direction. The waves can also be regular or irregular and, in the same way, be uni or multi-directional. The degree to which these variables should be changed depends upon the aim of the testing programme and limitations in time and other resources.

As this study was the first of its kind, the primary aim was to assess the fundamental behaviour of the modular device. Hence, the majority of the wave conditions were idealised and simplified by being regular. The conditions were also characteristic, in terms of energy levels, of typical sea states for common power production (Babarit *et al.*, 2012).

For the regular waves, the period and direction were varied. The period was varied because the response of a WEC is generally dependent on it, even for a fairly broad-banded device like a flap-type device (Clabby *et al.*, 2012; Whittaker, T. and Folley, 2012). Eight wave periods were used, approximately evenly spaced between 5.5 s and 13.5 s at full scale. These limits represent the typical range for peak periods at a wave energy site (Babarit *et al.*, 2012). As discussed in section 2.2, the power-capture of a rigid flap-type WEC is also sensitive to the wave direction, typically decreasing by cosine squared of the angle (Henry, 2008). Testing in directional waves can also result in a rigid device being subjected to significant yaw loads (Wilkinson *et al.*, 2014). Hence, the wave direction was varied to determine if employment of the modular device in directional seas could provide an improvement over the rigid

device. Wave direction angles of 0, 7.5, 17.5 and 27.5 degrees were used. These values were chosen to represent a large section of the range of directions that could be expected at a nearshore wave energy site (Wilkinson *et al.*, 2014).

The regular wave amplitude was not varied because, according to linear wave theory, the response of a device to a changing amplitude is predictable and linear, within the limits of small amplitudes of motion. A nominal wave amplitude, of 1 m, at full scale, was used. This value was chosen to represent a typical wave height where significant annual energy can be expected to be available at a site (Babarit *et al.*, 2012).

A small set of three unidirectional, head-on irregular wave sea states, defined using the Bretschneider spectrum, was also used. This was applied to test the model in realistic conditions, to increase the practical significance of the results dataset. The nominal significant wave height, $H_{m0}$, was set at 2.75 m. This value was chosen so that it had the same incident wave power as the 1 m amplitude regular waves, to allow fair comparison between the regular and irregular wave results (Clabby *et al.*, 2012). The mean wave period, $T_{01}$, was set at 6.5, 8.5 and 10.5 s, to cover a reasonable section of the typical wave period range (Babarit *et al.*, 2012). The period range was also chosen through numerical modelling of the Rigid Flap device using the model described in section 15.1 and in Wilkinson *et al.* (2015). The Rigid Flap was chosen to simplify the modelling and analysis. The modelling estimated the mean power capture for head-on irregular sea states across an occurrence table. The occurrence table was derived by averaging the occurrences from two sites of interest for wave energy development on the west coast of Scotland (Aquamarine Power Ltd, 2011, 2012). The power capture and occurrences were then multiplied in order to get expected annual energy generations for the seas states. The energy productions were then normalised with the total annual energy production from all of the sea states. Three sea states were then chosen for physical modelling that had relatively large contributions to the total energy production, had the desired significant wave height of 2.75 m and were spread

well across the period range. The chosen sea states positions in the energy contributions table are shown in Figure 81.

| | Energy contributions (%) | | | | | | | | | | | | | | |
|---|---|---|---|---|---|---|---|---|---|---|---|---|---|---|---|
| | $T_{01}$ (s) | | | | | | | | | | | | | | |
| Hs (m) | 3.5 | 4.5 | 5.5 | 6.5 | 7.5 | 8.5 | 9.5 | 10.5 | 11.5 | 12.5 | 13.5 | 14.5 | 15.5 | 16.5 | 17.5 |
| 0.25 | 0.00 | 0.00 | 0.00 | 0.00 | 0.00 | 0.00 | 0.00 | 0.00 | 0.00 | 0.00 | 0.00 | 0.00 | 0.00 | 0.00 | 0.00 |
| 0.75 | 0.00 | 0.09 | 0.35 | 0.57 | 0.52 | 0.33 | 0.17 | 0.07 | 0.01 | 0.00 | 0.00 | 0.00 | 0.00 | 0.00 | 0.00 |
| 1.25 | 0.00 | 0.14 | 0.76 | 1.43 | 1.61 | 1.07 | 0.60 | 0.28 | 0.09 | 0.02 | 0.01 | 0.00 | 0.00 | 0.00 | 0.00 |
| 1.75 | 0.00 | 0.04 | 0.86 | 2.14 | 2.53 | 2.10 | 1.09 | 0.49 | 0.20 | 0.08 | 0.03 | 0.01 | 0.00 | 0.00 | 0.00 |
| 2.25 | 0.00 | 0.00 | 0.38 | 2.23 | 3.19 | 2.88 | 1.68 | 0.73 | 0.29 | 0.10 | 0.03 | 0.01 | 0.00 | 0.00 | 0.00 |
| 2.75 | 0.00 | 0.00 | 0.06 | 1.54 | 3.51 | 3.38 | 2.28 | 0.97 | 0.35 | 0.09 | 0.02 | 0.00 | 0.00 | 0.00 | 0.00 |
| 3.25 | 0.00 | 0.00 | 0.00 | 0.62 | 3.13 | 3.59 | 2.05 | 1.29 | 0.49 | 0.15 | 0.02 | 0.00 | 0.00 | 0.00 | 0.00 |
| 3.75 | 0.00 | 0.00 | 0.00 | 0.15 | 2.19 | 3.79 | 1.83 | 1.35 | 0.76 | 0.13 | 0.05 | 0.00 | 0.00 | 0.00 | 0.00 |
| 4.25 | 0.00 | 0.00 | 0.00 | 0.03 | 1.25 | 3.10 | 2.10 | 1.48 | 0.75 | 0.21 | 0.04 | 0.00 | 0.00 | 0.00 | 0.00 |
| 4.75 | 0.00 | 0.00 | 0.00 | 0.00 | 0.46 | 2.36 | 2.23 | 1.66 | 0.89 | 0.24 | 0.04 | 0.00 | 0.00 | 0.00 | 0.00 |
| 5.25 | 0.00 | 0.00 | 0.00 | 0.00 | 0.10 | 1.15 | 2.78 | 2.25 | 1.14 | 0.43 | 0.01 | 0.00 | 0.00 | 0.00 | 0.00 |
| 5.75 | 0.00 | 0.00 | 0.00 | 0.00 | 0.02 | 0.40 | 1.08 | 2.35 | 2.22 | 0.90 | 0.05 | 0.00 | 0.00 | 0.00 | 0.00 |
| 6.25 | 0.00 | 0.00 | 0.00 | 0.00 | 0.00 | 0.09 | 0.16 | 1.16 | 1.93 | 0.85 | 0.06 | 0.00 | 0.00 | 0.00 | 0.00 |
| 6.75 | 0.00 | 0.00 | 0.00 | 0.00 | 0.00 | 0.08 | 0.07 | 0.06 | 0.60 | 0.57 | 0.02 | 0.00 | 0.00 | 0.00 | 0.00 |
| 7.25 | 0.00 | 0.00 | 0.00 | 0.00 | 0.00 | 0.01 | 0.01 | 0.00 | 0.00 | 0.03 | 0.01 | 0.00 | 0.00 | 0.00 | 0.00 |
| 7.75 | 0.00 | 0.00 | 0.00 | 0.00 | 0.00 | 0.00 | 0.02 | 0.01 | 0.00 | 0.00 | 0.00 | 0.00 | 0.00 | 0.00 | 0.00 |
| 8.25 | 0.00 | 0.00 | 0.00 | 0.00 | 0.00 | 0.00 | 0.00 | 0.00 | 0.00 | 0.00 | 0.00 | 0.00 | 0.00 | 0.00 | 0.00 |
| 8.75 | 0.00 | 0.00 | 0.00 | 0.00 | 0.00 | 0.00 | 0.00 | 0.00 | 0.00 | 0.00 | 0.00 | 0.00 | 0.00 | 0.00 | 0.00 |

**Figure 81. Table of contributions to total annual energy production from numerical modelling of Rigid Flap at typical wave energy sites in western Scotland (Aquamarine Power Ltd, 2011, 2012; Wilkinson *et al.*, 2015). The sea states are defined using the significant wave height, Hs, and the mean wave period, $T_{01}$.**

The incident power available per metre crest of the waves, $P_{inc}$, was also an important parameter to determine for each wave condition. For the regular waves, $P_{inc}$ was calculated using standard formula, starting in Equation 28 (United States Naval Academy, no date).

$$P_{inc} = EC_G \qquad \text{Equation 28}$$

Where, $E$ was the energy per unit surface area of the wave, calculated using Equation 29 and $C_G$ was the wave group velocity, calculated using Equation 30.

$$E = \frac{1}{2}\rho g a^2 \qquad \text{Equation 29}$$

Where, $a$ was the wave amplitude and $\rho$ was water density, assumed to be 1025 kgm$^{-3}$.

$$C_G = \frac{C}{2}\left(1 + \frac{2kd}{\sinh(2kd)}\right) \qquad \text{Equation 30}$$

Where, $C$ was the wave celerity, calculated using Equation 31, $k$ was the wave number, calculated iteratively using the dispersion theorem, provided in Equation 32, and $d$ was the water depth, 13.9 m.

$$C = \frac{gT}{2\pi}\tanh(kd) \quad \text{Equation 31}$$

Where $T$ is the wave period.

$$\frac{2\pi}{T} = \sqrt{gk\tanh(kd)} \quad \text{Equation 32}$$

For irregular waves, $P_{inc}$ was calculated by summing the powers available in the frequency components of the spectra.

For clarity, tables of the full range of regular and irregular wave conditions are finally provided in Table 11 and Table 12, respectively.

**Table 11. Full scale measured regular wave conditions.**

| Wave No. | Wave Amplitude, $a$ (m) | Wave Period, $T$ (s) | Incident Wave Power, $P_{inc}$ (kW/m) | Direction, D (deg) |
|---|---|---|---|---|
| 1 | 0.99 | 13.5 | 48.4 | 0 |
| 2 | 0.99 | 12.5 | 46.5 | 0 |
| 3 | 1.00 | 10.6 | 44.6 | 0 |
| 4 | 0.98 | 9.5 | 40.3 | 0 |
| 5 | 1.01 | 8.5 | 39.3 | 0 |
| 6 | 1.00 | 7.5 | 34.6 | 0 |
| 7 | 1.00 | 6.5 | 29.3 | 0 |
| 8 | 1.00 | 5.5 | 23.3 | 0 |
| 9 | 1.01 | 8.6 | 39.5 | 7.5 |
| 10 | 0.99 | 8.6 | 36.2 | 17.5 |
| 11 | 1.00 | 8.6 | 34.1 | 27.5 |

**Table 12. Full scale measured irregular wave conditions.**

| Wave No. | Mean Wave Period, $T_{01}$ (s) | Significant Wave Height, $H_{m0}$ (m) | Incident Wave Power, $P_{inc}$ (kW/m) | Direction, D (deg) |
|---|---|---|---|---|
| 1 | 6.2 | 2.9 | 31.6 | 0 |
| 2 | 8.3 | 2.8 | 38.4 | 0 |
| 3 | 10.3 | 2.8 | 43.3 | 0 |

### 4.4.3 Damping Levels

A set of standard achievable damping levels was used for testing. The term 'achievable' is used because, as explained in section 3.5.6, the actual damping torque applied to a model was sometimes lower than the target value. This occurred when the wave excitation torque was lower than the achievable torque applied by a damper on a module. The use of a standard set of torques allowed for direct comparison between damping levels in different tests and for streamlining of the experiments. The damping levels that were used are provided in Table 13.

**Table 13. Standard achievable damping levels applied to each module, at model and full scales, that were used in the physical modelling campaign.**

| Damping Level Number | Target RMS Damping Torque | |
|---|---|---|
| | $30^{th}$ Scale (Nm) | Full Scale (MNm) |
| 1 | 0 | 0.0 |
| 2 | 1 | 0.8 |
| 3 | 1.9 | 1.5 |
| 4 | 2.9 | 2.4 |
| 5 | 3.8 | 3.1 |

An additional damping level, as close to the optimum damping level for power production, was then applied if none any of the previously applied standard levels were sufficiently close to the estimated optimum level. This was carried out by fitting a curve to the initial power-damping pairs. The additional damping level was then the value that corresponded to the maximum mean device power capture using the initial curve. Further explanation for this method for estimating the maximum mean power capture is provided in section 5.6.3.

## 4.5 Summary

This chapter has presented the key methodologies that were applied for generating the results presented in Chapters 6 and 7. The methods used to calibrate the sensors, with the resulting calibration functions, were first presented. This was followed by the techniques used to generate and, subsequently, calibrate wave conditions in the wave tank. The range of wave conditions and damping levels that were applied in the physical modelling campaign were then summarised. The waves were primarily regular, with the

variables being wave period and direction. A set of standard achievable damping torques was applied for each wave condition.

# 5. Data Analysis

## 5.1 Introduction

This chapter presents the analysis methods used to convert instantaneous sensor data into statistical results. At both stages, results were generated for individual modules and whole devices. The latter is the combination of all modules sharing a foundation. For the damping torque and power capture, the device results were the sum of the module values; for rotation results, the device values were the mean rotations of the modules; finally, the device foundation loads were the total global loads. When required to differentiate between module and device results, the subscripts $n$ and $T$ are used, respectively.

The aim of the analysis process was to calculate sets of statistics that were representative of each sea state. This allowed comparison of results, for example between the Modular and Rigid Flaps, across the sea states. Finally, statistics were summarised for a set of sea states, to allow comparison of mean results for the device configurations.

Section 5.2 provides the reader with the reference system used for data interpretation. Presented in section 5.3 are the ways in which the instantaneous data was pre-processed from raw to physical data. Sections, 5.4, 5.5 and 5.6 demonstrate how the key statistics for the angular velocity, damping torque and power capture, respectively, were generated. Section 5.7 provides a summary of evaluating the uncertainties on the power capture. This latter type of analysis was only completed for the power results due to time restraints and to demonstrate the typical quality of the physical modelling methodology. Section 5.8 summarises how the foundation load statistics were generated. The calculation process for computing relative differences in the statistics is then presented in section 5.9. Finally, section 5.9 provides a summary of the chapter.

## 5.2 Reference System

The reference systems for the module numbers and wave directions, necessary for interpretation of the results, are shown in Figure 82.

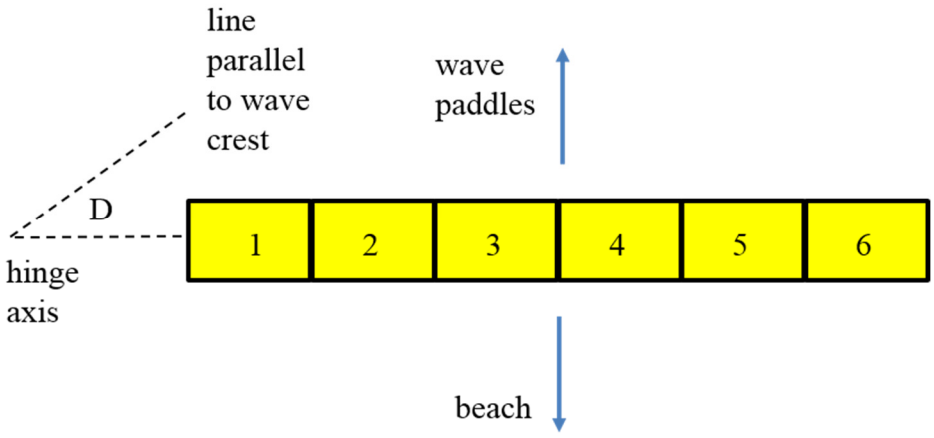


**Figure 82. Plan view of device in modular configuration, showing module numbering and wave direction reference systems.**

## 5.3 Pre-Processing of Instantaneous Data

This section details the conversion of instantaneous sensor voltage data to outputs with engineering units. The sensors in question include the rotation, torque and load sensors, described in Chapter 3. The processes used to convert these signals to new variables, for example angular velocity, are also shown.

### 5.3.1 Signal conditioning

The sensor signals generally required conditioning, to remove synthetic effects, such as electrical noise. The first stage of the process was the zeroing of data with wet datum recordings. A wet datum file contained data with the model installed in still water. The purpose of the recording was to allow the removal of any effects that significantly changed the means of the raw signals from 0 V, i.e. introduced an ‘offset’. For the load cell sensors, for example, an offset could be caused by static buoyancy, which was of less interest than the wave

loads. Without removing these offsets, the statistics of the signals, for example the means, would be distorted. The datum test duration was 10 s, with the mean then evaluated. The means of the signals were then subtracted from the raw signals.

Using analysis software, low pass filtering was used to remove high frequency electrical noise from the signals. All frequencies of the signal were passed between 0 Hz and a specified cut-off frequency (MathWorks, 2016). The rotation signals and most of the foundation load signals were filtered with a 5 Hz cut-off frequency; a 10 Hz limit was applied to the damping torque and pitch foundation load signals. The increased frequency band was granted for the latter case as the 5 Hz cut-off generated synthetic high frequency oscillations on these signals, which closely resembled square-waves. An example, to illustrate the effect of filtering on a signal, is shown in Figure 83.

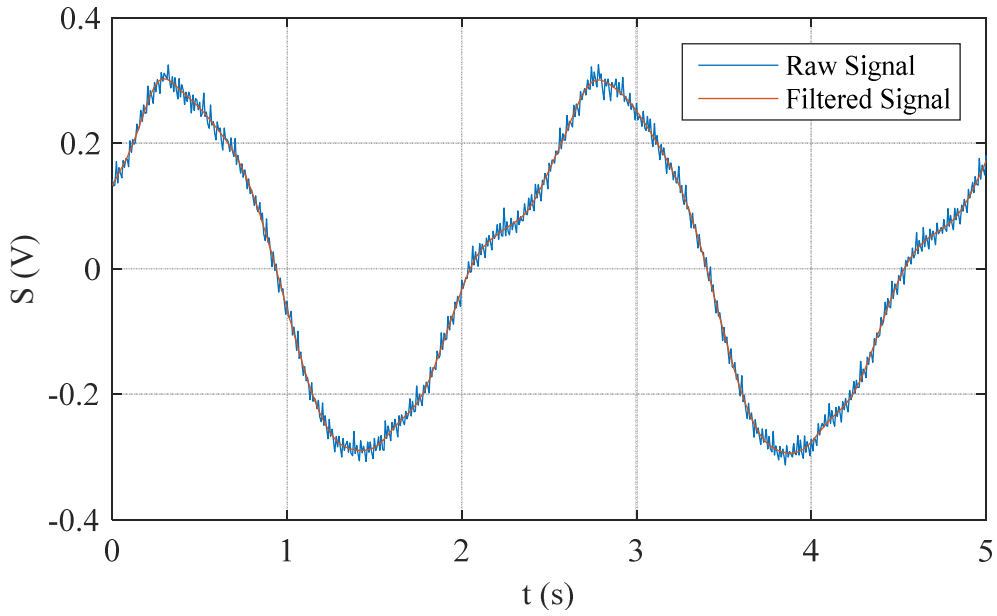


**Figure 83. Example of graph of raw and filtered signals, *S*, against time, *t*, comparing unfiltered and filtered data. Example taken from AMTI2000A surge data.**

### 5.3.2 Rotation

The rotation signals for each module, θ, were generated by multiplying the raw rotation sensor signals with their corresponding calibration coefficients, displayed in Table 5, as shown in Equation 33.

$$\theta = m_\theta V_\theta \qquad \text{Equation 33}$$

Where, $m_\theta$ was the calibration coefficient and $V_\theta$ was the voltage recorded by the rotation sensor.

### 5.3.3 Angular Velocity

The angular velocity was calculated by differentiating the rotation signal with respect to time, as shown in Equation 34. The code used to perform this analysis is shown in Table 26 in appendix section 14.2.

$$\dot{\theta} = \frac{d\theta}{dt} \qquad \text{Equation 34}$$

### 5.3.4 Damping Torque

The damping torque applied to each module was the combination of resistance generated by a damper and the two bearings supporting the prime mover. As was shown in Figure 29, the position of the torque sensor in the module hinge assembly meant that the torque applied by the damper and one bearing was measured. However, the damping torque related to the friction in the other bearing was not measured. While this likely represented a very small component of the total damping torque applied, some account of this torque was taken to increase the accuracy of the total torque values.

The measured torque, $Tc_m$, was first calculated using Equation 35.

$$Tc_m = m_{Tc} V_{Tc}$$ Equation 35

Where, $m_{Tc}$ was the calibration coefficient for a torque sensor and $V_{Tc}$ was the voltage recorded by a torque sensor. The values for $m_{Tc}$ were displayed in Table 6.

To account for the unmeasured bearing damping torque, a synthetic signal was generated to represent it. The damping torque generated by a bearing is from friction. This has a theoretically constant magnitude assuming a constant frictional resistance of the bearing surface, independent of velocity. Hence, the signal was assumed to be a square wave. The synthetic signal was created using the *tanh* function and the angular velocity of the module. This approximated a square-wave damping profile (Wilkinson *et al.*, 2015). The formula for the synthetic bearing damping torque signal for a given module, $Tc_b$, is shown in Equation 36. Note that the subscript *b* has been used to differentiate the bearing damping torque term from that measured using the torque sensor, which was principally generated by the damper.

$$Tc_b = a\, tanh(b\dot{\theta})$$ Equation 36

Where, *a*, was the bearing damping coefficient in Nm, *b* was the bearing slope coefficient, in s, and $\dot{\theta}$ the angular velocity, in deg/s. *a* sets the amplitude of the damping torque signal, while b sets the slope of the rise between the points where the torque is rising and the plateau. An example plot showing this, for a generic damping torque signal, is presented in Figure 84.

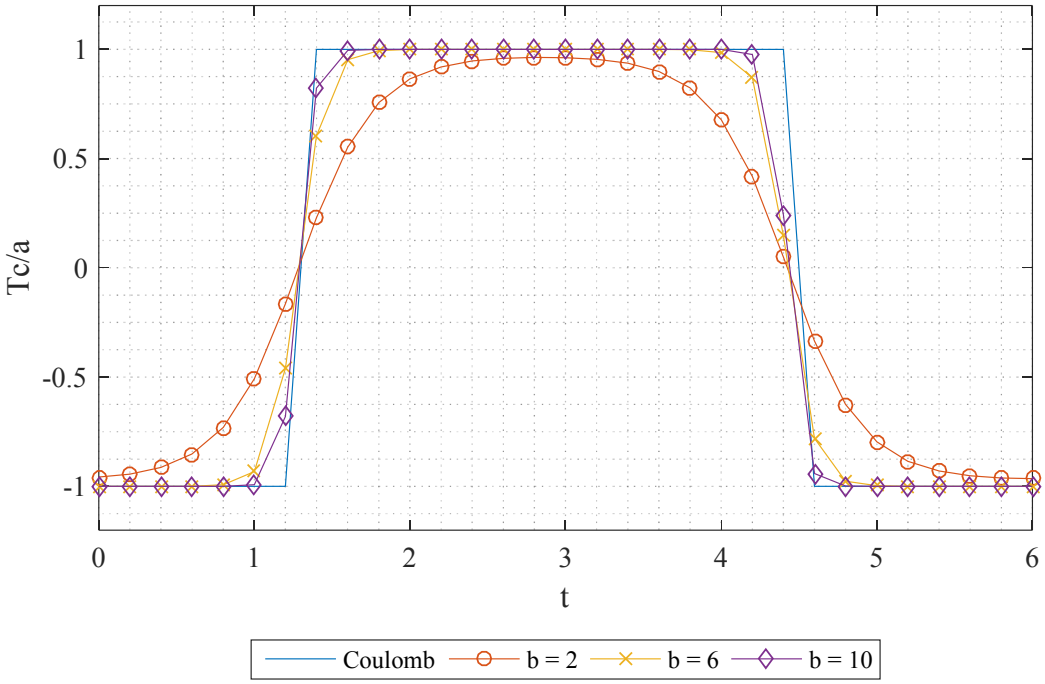


**Figure 84. Demonstration of effect of using different values of *b* for generating synthetic damping torque, Tc, signal. Value of signal amplitude, *a* was 1. Angular velocity was sine function of time (Wilkinson *et al.*, 2015).**

To determine coefficients that approximated the bearing torque well, a bench test was completed to measure the torque applied by a single bearing. The bearing had similar geometry to the one used in the physical model. Sample results from this study are shown in Figure 85. From this study, values of 0.05 and 2 for *a* and *b*, respectively, were chosen as their application resulted in the best fit between the synthetically generated torque and the measured torque.

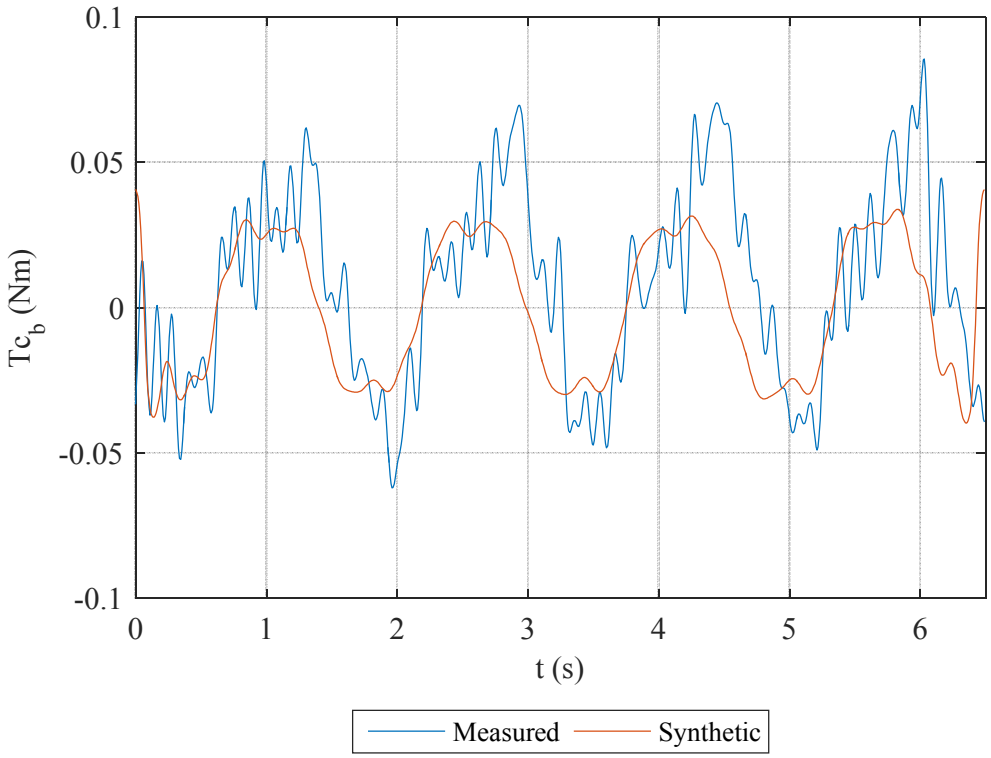


**Figure 85. Comparison of measured and synthetic instantaneous bearing torque, $Tc_b$, against time, $t$, for bench test.**

To then evaluate the total damping torque for a single module, $Tc$, Equation 37 was used.

$$Tc = Tc_m + Tc_b \qquad \text{Equation 37}$$

The uncertainty of the unmeasured bearing torque, relative to its own magnitude, was likely up to 100 %, as an estimate from experience. However, the degree to which this contributed to the uncertainty on the total damping torque was the key metric. This was determined by assessing the contribution of the bearing torque to the total torque. This contribution can be partly comprehended through visual inspection of the relevant time-series, an example for which is provided in Figure 86. The target damping torque level in the example was set at 2.9 Nm for the model scale RMS value and the results are for a central module in the Modular Flap. This hence represented a typical

damping torque level for maximum device power generation across the test range.

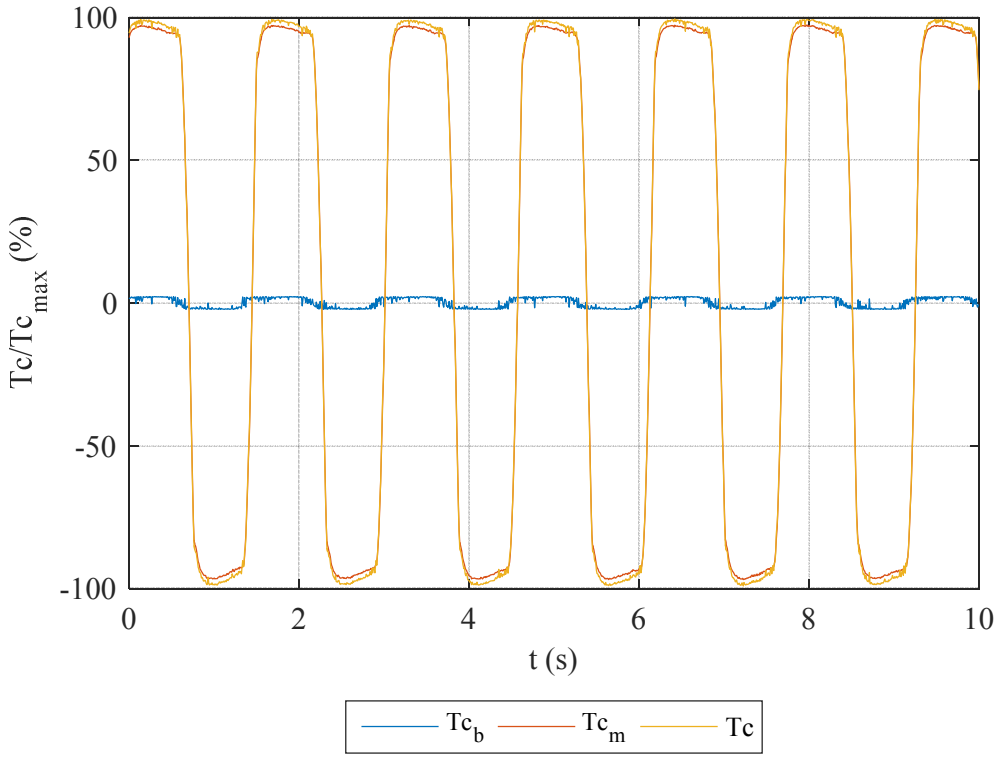


**Figure 86. Components of total module damping torque, *Tc*, showing small contribution of synthetic bearing torque, $Tc_b$, compared to that from the measured damping torque, $Tc_m$. Values have been normalised against the maximum value of *Tc*. The test was using the Modular Flap, with the results shown for the third module. The damping level was set to damping level 4, 2.9 Nm RMS torque at model scale. The results are presented at model scale.**

Figure 86 shows that the contribution of the unmeasured bearing torque appeared to be low. However, it was important to quantify this contribution. This was carried out by first evaluating the total of the root-mean-square (RMS) values of the corresponding torques. The formula for finding the RMS value of a generic variable, *y*, is provided in Equation 38.

$$y_{RMS} = \sqrt{\frac{\sum_{i=1}^{N} {y_i}^2}{N}} \qquad \text{Equation 38}$$

Where *N* and *i* were the number of samples and the sample index, respectively, in the time series.

The contribution of the unmeasured bearing torque was the percentage ratio of the RMS torques. This was evaluated across the operational range of damping torques, using the six-module Modular Flap as the example device, with the results shown in Figure 87.

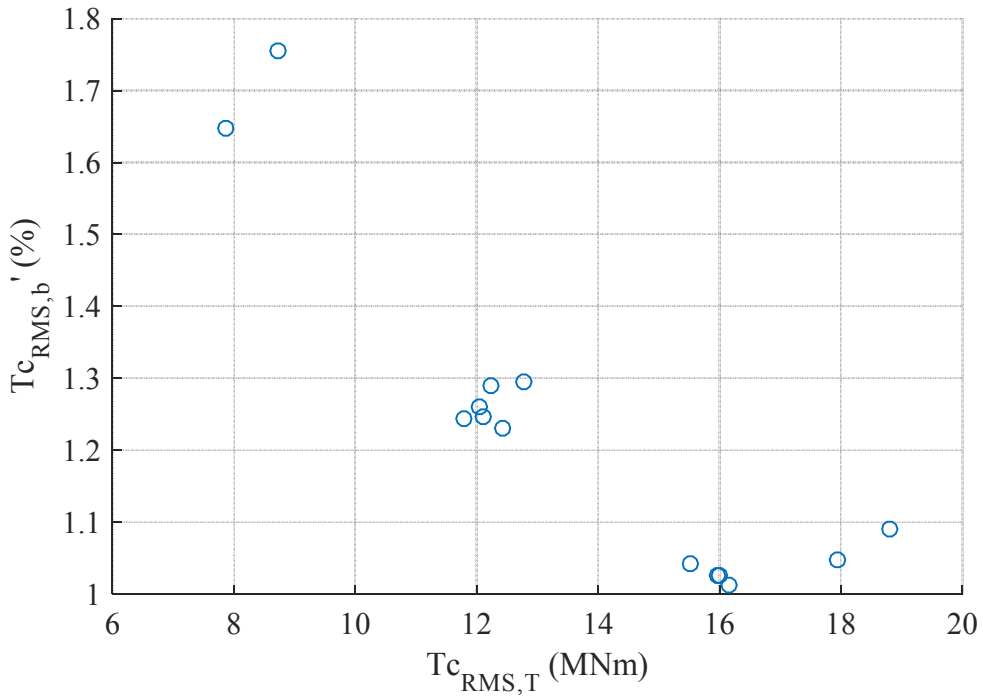


**Figure 87. Graph of relative contributions by RMS synthetic unmeasured damping torque, $Tc_{RMS,b}$' to total damping torque, Total RMS damping torque, $Tc_{RMS,T}$.**

Figure 87 shows that, across the operational range, the range of relative contributions of the synthetic unmeasured damping torque was only 1-1.8 %. The average value was only 1.2 %. This means that, assuming relative uncertainty on this value of 100 %, the maximum average contribution to the total torque uncertainty was only 1.2 %. This suggests that the relative contribution of the unmeasured bearing torque to the uncertainty of the total damping torque was low and could be neglected from the analyses conducted in section 5.7.

### 5.3.5 Power Capture

The instantaneous mechanical power capture for each module was calculated as the product of applied damping torque and angular velocity, as shown in Equation 39.

$$P = \dot{\theta} T_C \qquad \text{Equation 39}$$

The instantaneous total power for the whole device, $P_T$, was calculated using Equation 40

$$P_T = \sum_{n=1}^{M} P_n \qquad \text{Equation 40}$$

Where $P_n$ was the power for the $n$th module and $M$ was the total number of modules, for example 6.

### 5.3.6 Foundation Loads

The foundation loads were converted to physical measurements through application of Equation 41.

$$L = \frac{kV_{fl}10^6}{GV_{ex}} \qquad \text{Equation 41}$$

Where, $L$ was the measured foundation loads, in N or Nm, $k$ was the calibration matrix, shown in Table 7, $V_{fl}$ the measured foundation load voltages, in V, $G$ the gains and $V_{ex}$ the excitation voltages, in V (Advanced Mechanical Technology Inc, 2012). The values for G and Vex are displayed in Table 19 in appendix section 13.1.

### 5.3.7 Scaling

The primary aim for this thesis was to compare results generated by a modular flap to those associated with a rigid flap; the secondary aim was to generate indicative results to inform consideration of the modular concept as a full-scale

WEC. While for the former, percentages were the most appropriate, for the latter, scaling was necessary. The use of full-scale results also allows the reader to comprehend their real-world implications more easily. Hence, the results were converted to full-scale.

Scaling was carried out using Froude scaling laws. The application of this method requires that viscous forces are either insignificant or scale in the same way that inertial and gravitational forces do (Heller, 2012; Clabby, 2013). A strong argument for the satisfaction of this requirement for the Rigid Flap was provided in section 2.2.2; for the Modular Flap, a comprehensive discussion is provided in appendix section 14.3. There, the viscous forces are addressed through analysis of the shear and drag pressure forces. In summary of this discussion, the viscous shear forces are shown to be negligible, while the drag pressure forces are shown to be small (2 %, or less, of the driving surge force) and also reducing towards full scale. The likely result of this is that the power capture and foundation load results would slightly increase at full scale compared to the extrapolated values from the model tests. Without modelling the dynamics of the device at both scales, it is difficult to provide an accurate estimate of the magnitudes of these increases. Based on the analysis in section 14.3 though, it is estimated that, on average, the magnitude increases would only be up to 10 %. Due to the uncertainties around these magnitudes though, they are not applied here and only traditional Froude scaling is applied.

The assumption was made that the difference in the density between fresh water and seawater was negligible in section 2.2.2. This meant that the applied scaling was only based on the length factor, $L$, 30. The scaling was carried out by multiplying the model scale signals by $L$ raised to an exponent, $n$, with the values for $n$ provided in Table 14.

**Table 14. Froude scale exponents, *n*, for different variables that were used in this thesis (Clabby, 2013).**

| Variable | Scale Exponent, n |
|---|---|
| Length | 1 |
| Time | 0.5 |
| Angular velocity | -0.5 |
| Mass | 3 |
| Force | 3 |
| Torque | 4 |
| Power | 3.5 |

### 5.3.8 Verification of Results

To provide verification of the physical model and the analysis methods, some example timeseries results are now presented. The results are assessed for the key outputs of the physical model system, the flap module power generation and the device foundation loads. The verification is carried out by confirming that the profiles and magnitudes of the timeseries match the expected behaviour derived from literature and the author's knowledge (Henry, 2008; Howard, Whittaker and Doherty, 2009).

Results for the Rigid Flap were chosen for verification use to allow greater comparison with previous works and because this eliminated the possibility of alteration of the results due to module interaction. A regular wave condition was chosen to both simplify the inspection of results, observe the system in steady state and because regular waves represented the majority of the test conditions. A regular wave was chosen that represented the range of variables, amplitude, period and direction, well and excited the model in all foundation

loading degrees of freedom. To meet these criteria, a wave with an amplitude of 1 m, period of 8.5 s and direction of 17.5 degrees was used. The damping level was number 3, to represent a mid-range torque.

Verification of the flap module power generation is first carried out. To achieve this, a graph showing the variables that were used in the power calculation is shown in Figure 88.

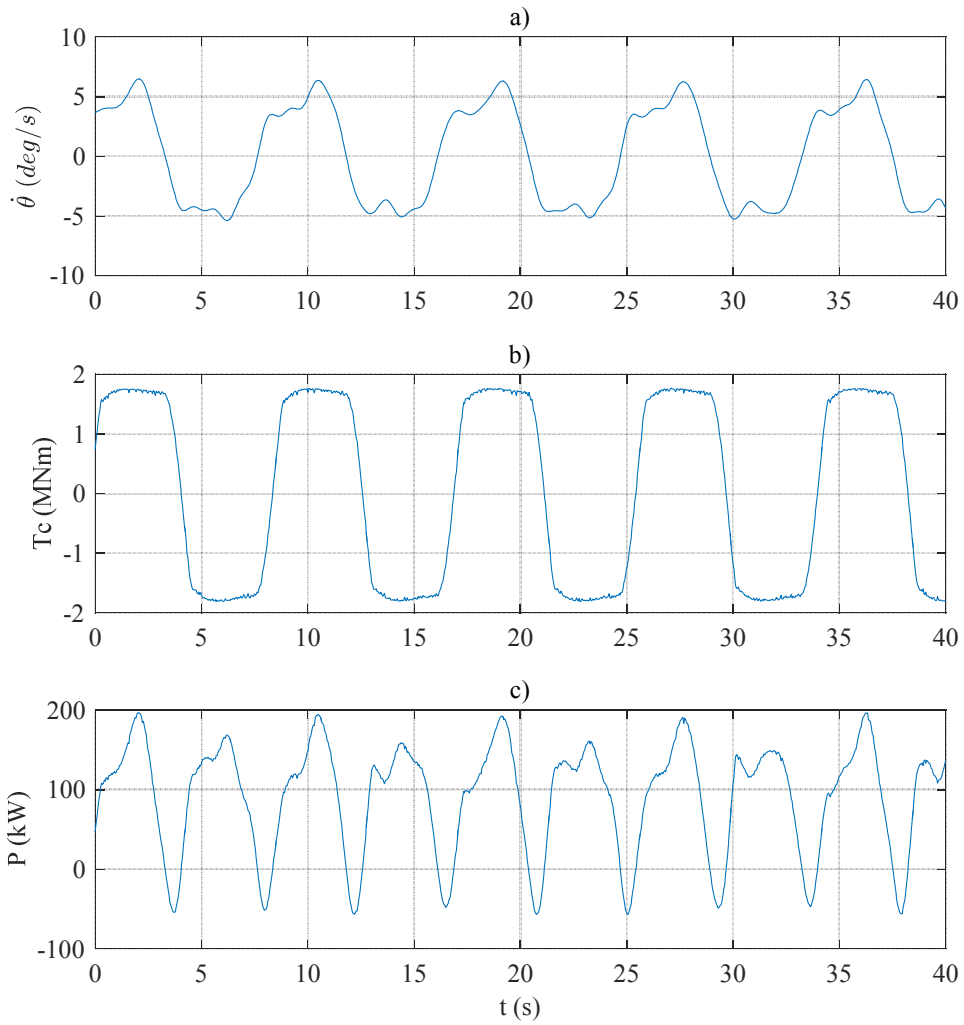


**Figure 88. Graph showing calculation of instantaneous module power, *P*, (c), with angular velocity, $\dot{\theta}$, (a) and damping torque, *Tc*, (b). The results are for the forth module.**

The results shown in Figure 88 generally exhibited the expected characteristics of the signals and hence provided verification of the module physical model system. The angular velocities and damping torques, shown in subplots a) and

b), for example, were broadly sinusoidal and square-wave, respectively, in shape and were generally in phase with each other; the magnitudes of all of the signals were in the same region as results shown in previous works, hence providing independent verification (Henry, 2008; van ’t Hoff, 2009; Clabby, 2013); finally, the signal noise levels were insignificant, hence raising no concern of grounding issues.

One unusual feature of the results, however, was the presence of a short period of negative power, shown in subplot c). For an ideal passive damper, applied torque is always in phase with angular velocity, resulting in continuous non-negative power. One of the aims of this study was to assess the potential of the power-capture of a modular flap-type WEC using an ideal passive damper. This was desired so that the modular characteristic of the device could be studied, independent of damping control strategy. Figure 88, however, indicates that the damping torque was not always in phase with the angular velocity, resulting in negative power. One of these periods is highlighted in Figure 89 to allow further investigation.

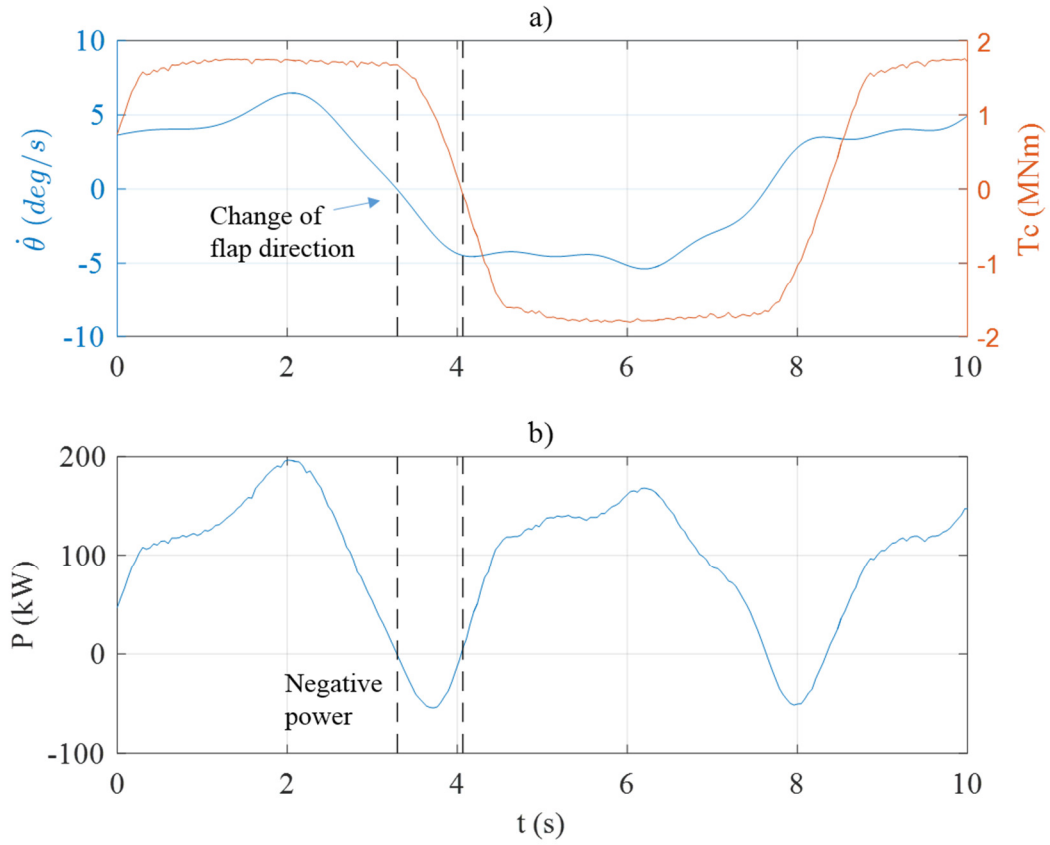


**Figure 89. Short sections of time-series of module a) angular velocity, $\dot{\theta}$, and damping torque, Tc, b) and power, *P*, highlighting negative power period.**

It can be seen from Figure 89 that the negative power period began when the flap changed direction, i.e. when the angular velocity changed sign. An ideal damper, at this point, would instantly reverse its sign of applied torque. However, the torque here changed sign gradually. The result of this was that, for a period, the torque was working with the flap motion, until the brake started resisting motion again. Therefore, initially no work was done against the damper and hence no positive power extracted.

The negative power characteristic was thought to have arisen due a spring effect resulting from compliance in the magnetic couplings. This may have resulted in potential energy storage as the flap moved in one direction, which was then released as kinetic energy when the flap changed direction. With no energy losses, the kinetic energy would be converted purely into flap kinetic energy. In this case, the positive power would equal the negative power.

Hence, ignoring small differences due to phase changes, the mean power would be the same as if a perfect passive damper had been used. In a real fluid, however, hydrodynamic viscous and radiation damping result in energy losses. However, the spring effect was only present for the relatively low velocities that occurred when the flap changed direction. For these velocities, the hydrodynamic damping would have been low and hence it is expected that so were the losses. Hence, it was assumed that the effect of the negative power period on the mean power was insignificant and no data analysis methods were applied to correct for it.

To verify the operation of the load cells, Figure 90 shows example foundation load results.

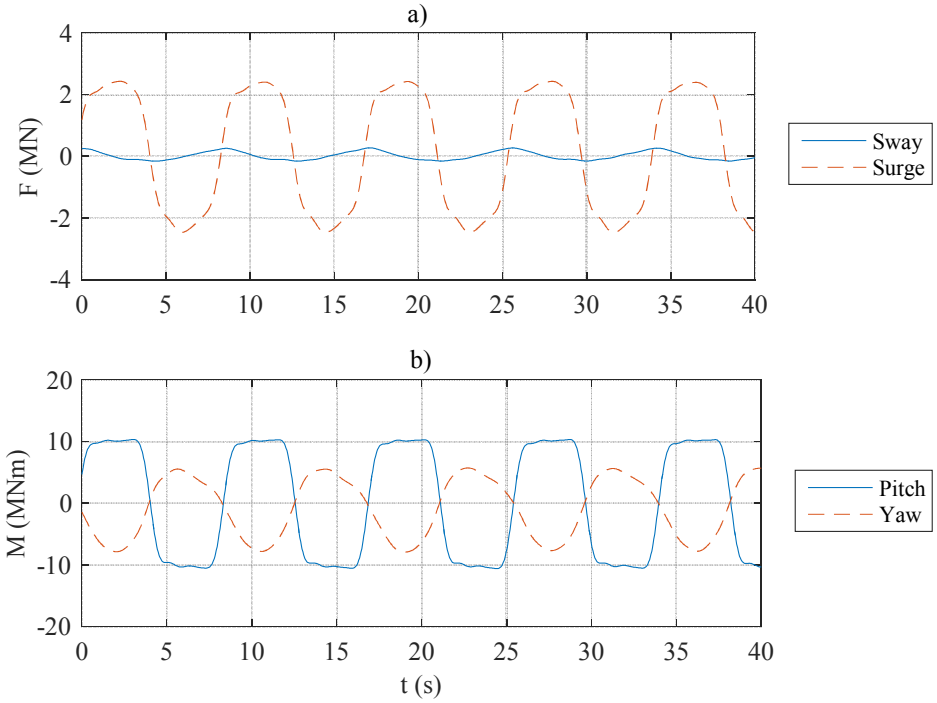


**Figure 90. Example of instantaneous foundation load results, showing forces, F, (a) and moments, M, (b) against time, t.**

Again, these results illustrate that the characteristics of the recorded signals were as expected. The surge forces, in subplot a), were of similar magnitude to previous work (Howard, Whittaker and Doherty, 2009); the relative proportions of surge and sway were as expected, the sway being significantly

smaller due to the side cross-sectional area of the device being similarly smaller than the frontal area; the yaw load was approximately equal to the product of half the surge load and a quarter of the flap width, 8 m; the pitch load was approximately equal to the product of the surge load and half of the distance from the hinge to the mean water level, 5 m.

The shapes of the foundation load signals were sinusoidal for the surge, sway and yaw loads. This was expected as this is the profile generated by the wave excitation torque acting on a device in regular waves (Crooks *et al.*, 2014). The pitch load, conversely, is the measure of the torque that is resistive to the motion of the flap and acting around the hinge. The only source of this was the dampers. Hence, this explains why the pitch profile was square-wave in shape. This also leads on to the point that further verification of the pitch load could be achieved by comparison of it to the total damping torque, as carried out in Figure 91. This shows that there was very good agreement between the two signals, both in magnitude and phase.

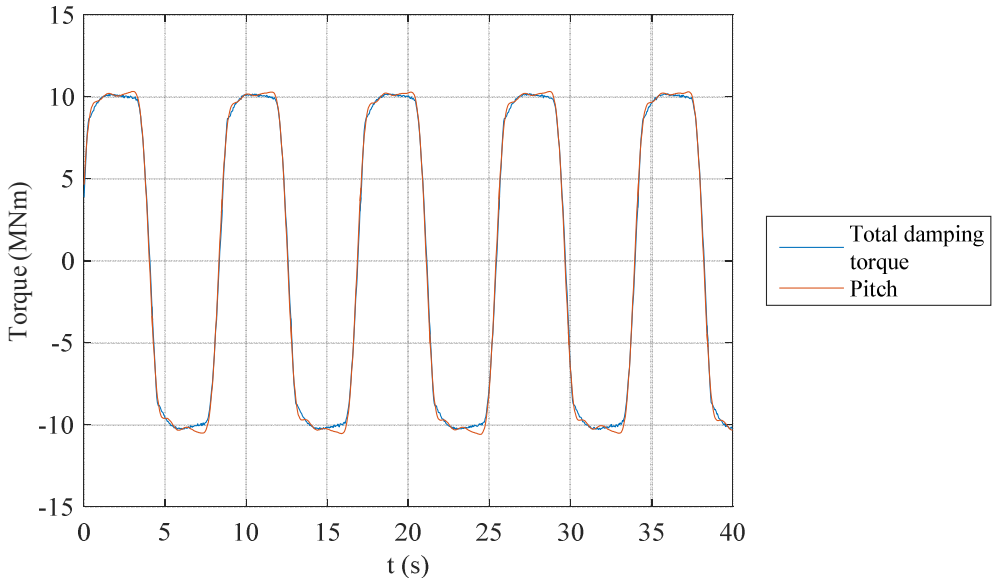


**Figure 91. Example showing agreement of instantaneous total damping torque and pitch foundation load, over time, *t*.**

Based on the above analysis, the physical model system was deemed adequate for the generation of instantaneous results for further statistical analysis.

## 5.4 Angular Velocity Statistics

The device motions were summarised through quantification of the mean absolute angular velocities of the modules and of the devices. The absolute values were used in order to produce non-zero results, given the oscillating motion of the flaps. The mean absolute angular velocity of a given module, $\overline{|\dot{\theta}|}$, was calculated using Equation 42.

$$\overline{|\dot{\theta}|} = \frac{\sum_{i=1}^{N} |\dot{\theta}_i|}{N} \qquad \text{Equation 42}$$

Where *N* and *i* were the number of samples and the sample index, respectively, in the time series.

The mean absolute angular velocity of the devices, $\overline{|\dot{\theta}|}_T$, was then the mean of the values associated with each module, as shown in Equation 43.

$$\overline{|\dot{\theta}|}_T = \frac{\sum_{n=1}^{M} \overline{|\dot{\theta}|}_n}{M} \qquad \text{Equation 43}$$

Where, *M* was the number of modules, six, *n* the module number and $\overline{|\dot{\theta}|}_n$ the mean absolute angular velocity of the *n*th module.

## 5.5 Damping Statistics

The statistic for the magnitude of the damping level applied to a given module was evaluated as the root-mean-square (RMS) damping torque, $Tc_{RMS}$, in Nm, as shown in Equation 44.

$$Tc_{RMS} = \sqrt{\frac{\sum_{i=1}^{N} {Tc_i}^2}{N}} \qquad \text{Equation 44}$$

The statistic for the total RMS damping torque applied to the whole device, $Tc_{RMS,T}$, was calculated using Equation 45.

$$Tc_{RMS,T} = \sum_{n=1}^{M} Tc_{n,RMS} \quad \text{Equation 45}$$

Where $Tc_{n,RMS}$ was the RMS damping torque applied to the *n*th module.

## 5.6 Power Capture Statistics

### 5.6.1 Mean Module Power Capture

The mean power-capture for each module $\bar{P}$, in kW, was generated using Equation 46.

$$\bar{P} = \frac{\sum_{i=1}^{N} P_i}{N} \quad \text{Equation 46}$$

Where $P_i$ was the instantaneous power of a module at timestep *i* and *N* was the number of timesteps.

### 5.6.2 Device Mean Power Capture

The total power generated by the devices was a sum of that generated by the flap modules. Hence, the total mean power, $\bar{P}_T$, was calculated using Equation 47.

$$\bar{P}_T = \sum_{n=1}^{M} \bar{P}_n \quad \text{Equation 47}$$

Where *M* was the number of constituent modules, 6, and $\bar{P}_n$ was the mean power capture by the *n*th module.

### 5.6.3 Maximum Mean Device Power Capture

The maximum mean device power capture was found by first measuring the mean device power capture, $\bar{P}_T$, at each damping level, defined by the RMS device damping torque, $Tc_{RMS,T}$.

The maximum mean device power capture for each wave condition, $\bar{P}_{T,max}$, was then estimated by fitting a quadratic curve to the $Tc_{RMS,T}$, $\bar{P}_T$ pairs and finding the peak. The reason for a quadratic curve being used for the fit requires some theory on wave power absorption. A body oscillating due to wave action has mechanical power, otherwise known as *excitation power*, $P_e$. This is, for a pitching body, the product of the magnitudes of the wave excitation torque and the body's angular velocity. As the wave excitation torque is, for small amplitudes of motion, independent of the body's rotation, the relationship between the excitation power and angular velocity is linear. The oscillating body also radiates waves. The power in these waves is called the *radiated power*, $P_r$, which is equal to the radiation resistance multiplied by the angular velocity squared and hence has a quadratic relationship. The *absorbed power*, $P$ is the excitation power minus the radiated power. The relationship between the absorbed power and angular velocity is hence described by a parabola, which is defined by a quadratic function, as shown in Figure 92 (Falnes, 2014).

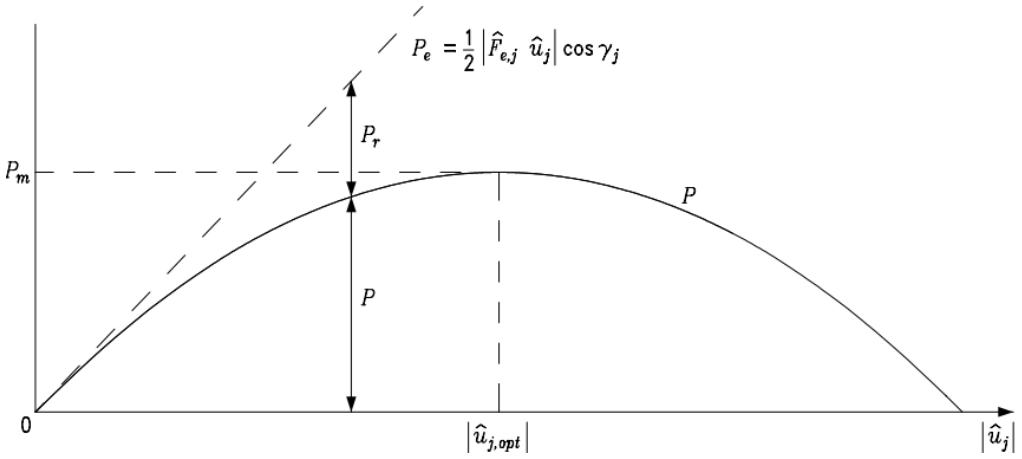


**Figure 92. Graph showing quadratic relationship between absorbed power, $P$, and velocity amplitude in the $j$th axis, $|\hat{u}_j|$. $P_r$ is the radiated power, $P_e$ the excitation power, $\hat{F}_{e,j}$ the excitation force and $\gamma_j$ the phase difference between $\hat{F}_{e,j}$ and $\hat{u}_j$. It can be seen that radiated power is the difference between absorbed and excitation powers. Graph from Falnes (2014).**

The absorbed power is also equal to the angular velocity multiplied by the applied PTO damping torque. Hence, the angular velocity is inversely proportional to the PTO damping torque, for a given absorbed power.

Therefore, the absorbed power should also have a quadratic relationship with the PTO damping torque. The x-axis value of the peak on the quadratic curve then corresponds to the optimum PTO damping torque level for power production. An example power curve is provided in Figure 93.

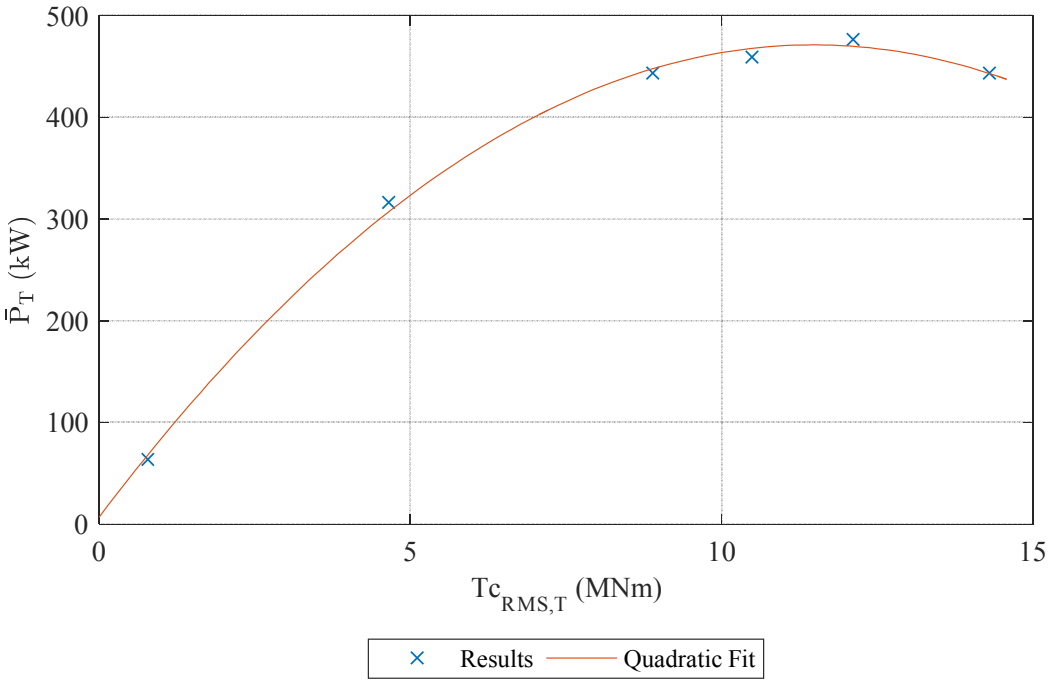


**Figure 93. Example of power curve, showing total mean power, $\bar{P}_T$, against total RMS damping torque, $Tc_{RMS,T}$, with quadratic curve fit.**

### 5.6.4 Capture Factor

The capture factor, *CF*, is a useful measure of the efficiency of a device (Folley, Whittaker and van't Hoff, 2007). The capture factor is the ratio of generated power, in this case the maximum mean device power capture, $\bar{P}_{T,max}$, to incident power, and was calculated using Equation 48.

$$CF = \frac{\bar{P}_{T,max}}{P_{inc}\cos(D)\,W} \qquad \text{Equation 48}$$

Where, $P_{inc}$ was the incident power per metre of crest, in kW/m; $D$ was the wave direction in rad.; $W$ was the device width, 33.3, in m. $P_{inc}$ was calculated for each wave condition, with the results presented in Table 11 and Table 12.

To compare the power capture of the Modular Flap to the Rigid Flap, the relative differences in capture factors, *ΔCF'*, were computed using Equation 49.

$$\Delta CF' = \frac{CF_{Mod} - CF_{Rig}}{CF_{Rig}} \qquad \text{Equation 49}$$

Where, $CF_{Mod}$ and $CF_{Rig}$ were, for a given wave condition, the capture factors achieved by the Modular Flap and Rigid Flap, respectively. This method of computing relative differences for statistics was carried out for many variables, as described in section 5.9.

Finally, the relative capture factors were weighted with the available wave power. The 'available' power here is the power flux moving in the direction perpendicular to the device hinge axis. This process was carried out to account for the fact that different wave conditions have different levels of available power and hence the importance of performing well in them varies. The weighted relative differences in capture factors, $\Delta CF'_w$, were computed using Equation 50.

$$\Delta CF'_w = \frac{\Delta CF' P_{inc} \cos(D)}{P_{inc_{max}} \cos(D)_{max}} \qquad \text{Equation 50}$$

Where, $P_{inc_{max}}$ was the maximum incident wave power for a set of conditions and $\cos(D)_{max}$ was the cosine of the wave direction angle for the maximum available power condition.

### 5.6.5 Smoothness of Power Capture

Another point of interest was how smooth the generated power was. A smoother delivery of power to the electrical grid is less problematic for the

network (Molinas, Sorby and Lundberg, 2007). The metric for 'smoothness', $S_P$, was calculated using Equation 51, which is the inverse of the standard measure of dispersion, the coefficient of variation. A higher $S_P$ value indicated a greater level of smoothing.

$$S_P = \frac{P_{\bar{T}}}{P_{T,std}} \qquad \text{Equation 51}$$

Where $\bar{P}_T$ was the mean value of the instantaneous total power, $P_T$, and $P_{T,std}$ was the sample standard deviation of $P_T$, calculated using Equation 52 and Equation 53, respectively.

$$P_{\bar{T}} = \frac{\sum_{i=1}^{N} P_{T,i}}{N} \qquad \text{Equation 52}$$

$$P_{T,std} = \sqrt{\frac{1}{N-1}\sum_{i=1}^{N}(P_{T,i} - P_{\bar{T}})^2} \qquad \text{Equation 53}$$

## 5.7 Uncertainty of Power Capture

Statistical significance of the calculated power capture was determined through the completion of an uncertainty analysis on the obtained results. This section contains some background information on this type of analysis, discussion of the uncertainty sources and a description of the calculation method for the dominant source. Details of all of the calculation methods are provided in the appendix in section 14.1.

Uncertainties arise from random or systematic errors. Random errors arise due to fluctuations in conditions that have an approximately random effect. These could be, for example, variation in water temperature; systematic errors are those that are associated with a constant absolute or relative inaccuracy, for example due to calibration of sensors (Coleman, H. and Steele, 2009).

The outcome of an uncertainty analysis is an estimation of a value range, +/- $U_X$, around the 'best' measurement of a result, $X_{best}$, such as the mean. $U_X$ may

not be symmetric around the $X_{best}$ but it will be assumed to be here for simplicity. It is believed that the true value, $X_{true}$, lies within this range, to a certain degree of confidence (Coleman, H. and Steele, 2009; Lamont-Kane, Folley and Whittaker, 2013). In this study, the 95 % confidence limit was used, which is standard for engineering applications (Coleman, H. and Steele, 2009; International Towing Tank Conference, 2014). The aim of the uncertainty analysis in this thesis was to estimate the uncertainty $U_{\overline{\Delta CF'}}$ for the mean relative differences in capture factor, $\overline{\Delta CF'}$ between the Rigid Flap and various configurations of the Modular Flap. The formula for the mean relative difference, for a generic variable, will be defined in Equation 57.

The uncertainties in the measured variables were propagated to the results through the use of the Taylor Series Method, a standard technique (Coleman, H. and Steele, 2009).

Both random and systematic uncertainties were considered. There were many sources of uncertainty in the physical modelling. However, some sources, such as the uncertainty due to calibration of the wave probes resulting from sensor inaccuracy, was assumed to be negligible. For this example, this because the sensor accuracy was 0.1 %, as stated in section 3.4.2. Only those sources of uncertainty which were deemed of significant magnitude were accounted for. These are listed below, with the category of the source provided in brackets:

1. Torque sensor calibration slopes (systematic)
2. Rotation sensor calibration accuracy (systematic)
3. Variation of wave conditions and model behaviour (random)
4. Model angle orientation (systematic)

The dominant source of uncertainties was found to be number 2, the ‘rotation sensor calibration accuracy’. These uncertainties were made apparent when the modules were fixed together as the Rigid Flap. The measurements of angular velocity should have been the same for this configuration due to the rigid nature of the body. However, it was noted that there were appreciable

differences in the recorded values. This issue is thought to have arisen as a result of the sensor calibration method. As described in section 4.2.3, the six sensors were calibrated simultaneously by first fixing the modules together with an aluminium bar on each face of the model. For practical reasons, this was conducted outside of the wave tank. The modules were then separated, installed in the wave tank and fixed together with PVC sheets to form the Rigid Flap. The deviations in the rotation and velocity may have therefore resulted from the slight differences in constraint, between that supplied by the bars and the PVC sheets.

An example that indicates the typical velocity differences is provided in Figure 94. The results presented are for the sensors that displayed the largest differences when compared to the mean results, which are also provided.

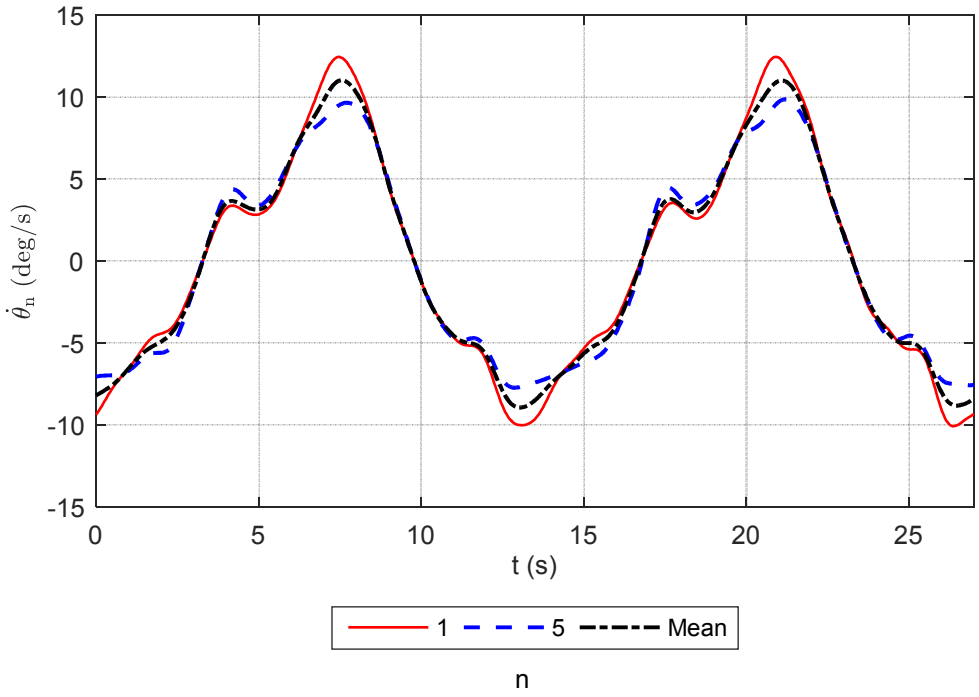


**Figure 94. Example of variation in angular velocity, $\dot{\theta}_n$, with time, *t*, for the *n*th module, and mean values for all modules. The modules were fixed together in the Rigid Flap configuration.**

Figure 94 shows that the rotation sensors, when compared to the mean results, under or overestimated the magnitudes of the angular velocities. These deviations were summarised by comparing the mean velocity of each module

to the combined mean of the modules. This was carried out across the range of wave conditions, for the tests where the maximum mean device power capture was recorded. The means of these results, as well as the variation around these results, are presented for the individual modules in Figure 95.

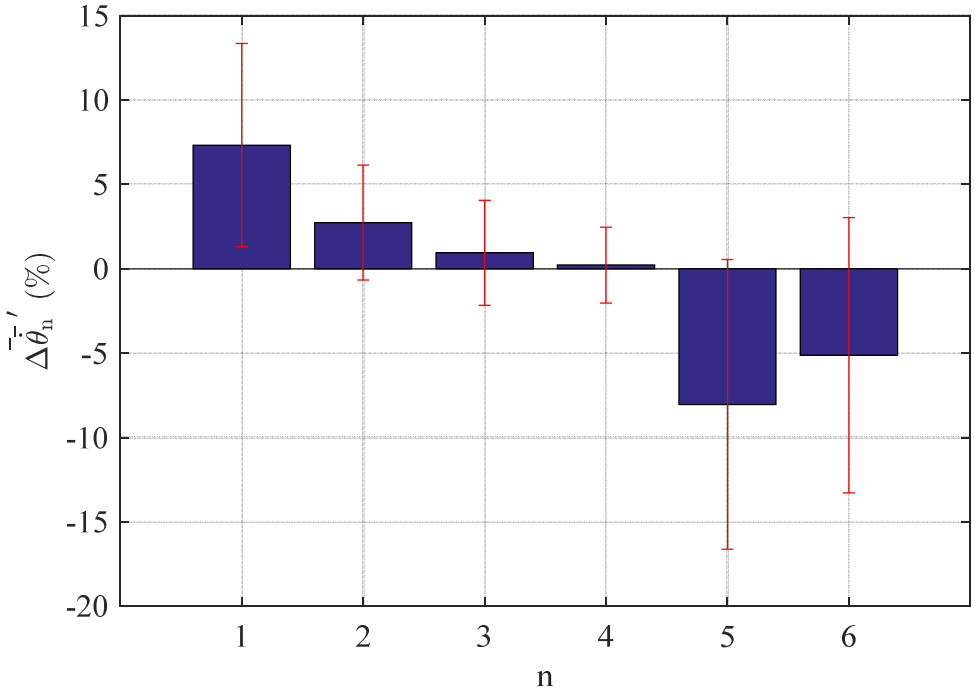


**Figure 95. Means of relative angular velocity differences to the mean across the full range of wave conditions for Rigid Flap tests where the maximum mean power capture was recorded, $\bar{\Delta}\dot{\theta}'_n$, for the *n*th module. The error bars were twice the standard deviation, a standard technique for evaluating uncertainty (Coleman, H. and Steele, 2009).**

Figure 95 shows that the variation in the relative differences in the mean angular velocities were, in most cases, greater than the magnitudes of the means. This suggests that there was no statistical significance in the results. However, the trend was that the angular velocities for some modules were, for the majority, greater or smaller than 0 %. This suggests that these velocity differences were systematic in nature. Thus, the differences in the module and mean velocities were used to estimate the *systematic* uncertainties on the velocity measurements. For the Rigid Flap, direct comparison to the instantaneous mean of the module velocities was used to calculate these. For the Modular Flap, however, there were natural differences in the velocities of

the modules because of the hydrodynamics. This meant that a different method had to be applied. This was to multiply the mean relative differences in the velocities, shown in Figure 95, by the instantaneous velocities for each module.

The other sources of uncertainty were significantly smaller than that attributed to the angular velocity measurements, with relative magnitudes of less than 1 %. Hence, as mentioned, the dominant source was the angular velocity measurements. Nevertheless, the experimental system was still able to show statistically significant differences in the capture factors achieved by the Rigid and Modular Flaps for individual wave conditions.

## 5.8 Foundation Loads Statistics

The design loads for an offshore structure are typically assessed in common and extreme wave conditions (Wilkinson *et al.*, 2014). The common conditions are the waves that occur for the majority of the lifetime of the structure. As discussed previously, these are the types of waves that were used for this thesis. For a lifetime of 25 years, for example, if the mean wave period was 8 s, these conditions would result in around 100 million waves and hence load cycles. These loads cause an accumulation of structural damage and hence can result in failure due to fatigue. A fatigue assessment is therefore usually carried out to design for these loads. This type of assessment is typically conducted for irregular waves, as these are the conditions that the structure will experience in the field. The waves used in this study were mostly regular. However, to maximise the practical use of the regular wave results, it was sensible to present them in a way that could be used for fatigue assessment. The use of a common method also allowed comparison between the regular and irregular wave results. Hence, a fatigue load metric was used to assess the foundation loads in both the regular and irregular wave tests.

A simple metric was used for the fatigue load assessment. The metric, referred to as the 'Effective Load Range' (ELR) represented the long term average range of a random load oscillation.

To calculate the Effective Load Range from the recorded load time-series in each sea state, a Rainflow method was used to first count the load amplitudes, *F*, and numbers of load reversals, *N* (Nieslony, 2010). The 'damage' contribution of each reversal was found by raising its amplitude to a fatigue damage exponent, *m*, and then multiplying this by the number of reversals. The *m* value used here, from typical stress-number of cycles to failure curves for the assumed foundation material, 'steel with corrosion protection', was 5. This was because the overall number of load cycles, over the life time of the structure, was assumed to be greater than 1 million (Norwegian Technology Standards Institution, 1998). The damage contribution of the single sea state, *DC*, was then the sum of these products, as shown in Equation 54.

$$DC = \sum N * F^m \qquad \text{Equation 54}$$

The effective load range for each sea state, *ELR*, was then found. The damage contribution was first divided by the number of waves in the test time-series, $n_{test}$. $n_{test}$ was calculated by dividing the duration of the test by the mean wave period. This quotient was then raised to the power of the inverse of *m*, as shown in Equation 55.

$$ELR = \left(\frac{DC}{n_{test}}\right)^{\frac{1}{m}} \qquad \text{Equation 55}$$

For the results shown in Chapter 7, the ELR results for each of the degrees of freedom will be subscripted with '*ELR*', for example, '$Su_{ELR}$' for the surge loads.

## 5.9 Relative Differences of Statistics

To compare the statistics between the device configurations, the relative differences were computed. Comparisons were always made between a modular device and a rigid device. As the rigid device was the benchmark, it was used as the reference point in the calculation of relative differences. For a

generic variable, $y$, the relative difference, $\Delta y'$, was hence calculated using Equation 56.

$$\Delta y' = \frac{y_{Mod} - y_{Rig}}{y_{Rig}} \qquad \text{Equation 56}$$

Where, $y_{Mod}$ and $y_{Rig}$ were the results for the Modular and Rigid Flaps, respectively.

For a set of wave conditions, the mean relative difference, $\overline{\Delta y'}$, for a variable was given by Equation 57.

$$\overline{\Delta y'} = \frac{\sum_{j=1}^{P} \Delta y_j'}{P} \qquad \text{Equation 57}$$

Where $P$ was the number of wave conditions, for example 8 for the head-on regular waves, and, for the $j$th wave condition, $\Delta y_j'$ was the relative difference in $y$ values.

## 5.10 Summary

This chapter has presented the key methodologies that have been applied for generating the results presented in Chapters 6 and 7. This involved converting the recorded time-series into statistics, for motions, damping torque, power capture and foundation loads. An uncertainty analysis was also applied to the power capture results. Finally, the method for calculating the relative differences between these statistics for the Modular and Rigid Flaps was shown.

# 6. Power Capture

## 6.1 Introduction

This chapter presents power capture results obtained during physical modelling assessment of the Modular Flap WEC concept. Benchmarking is attained through comparison to the equivalent width Rigid Flap. Where differences arise from comparisons, the results are accompanied with their suggested explanations.

Section 6.2 shows how the mean power captures compared at module level, for only the fundamental conditions, the head-on regular waves. Section 6.3 then provides a broader assessment of the power capture of the different device configurations, in the full range of wave conditions. In section 6.4, the smoothness of the power capture is then assessed. The chapter is then summarised in section 6.5.

## 6.2 Module Mean Power Captures

Results were generated for all six modules in the Modular Flap. For head-on wave conditions, however, there may not have been a significant need to show results for all of the modules. This is because, theoretically, the results were symmetrical around the centre of the device. This would mean that the results for module 1 would be the same as those for module 6, for example. In real physical modelling, however, this is not always the case, for example due to differences in the amplitude of the wave crest across the model. However, if the relative differences between the results within pairs of modules are smaller than the relative differences between the pairs, then the level of symmetry is arguably acceptable. This was generally the case for the tests conducted here, with an example for mean module power capture results shown in Figure 96 to demonstrate this. The uncertainty limits on the results are also shown, indicating that the ‘true’ results, i.e. those without uncertainty, may have also had greater levels of symmetry than the measured results indicated.

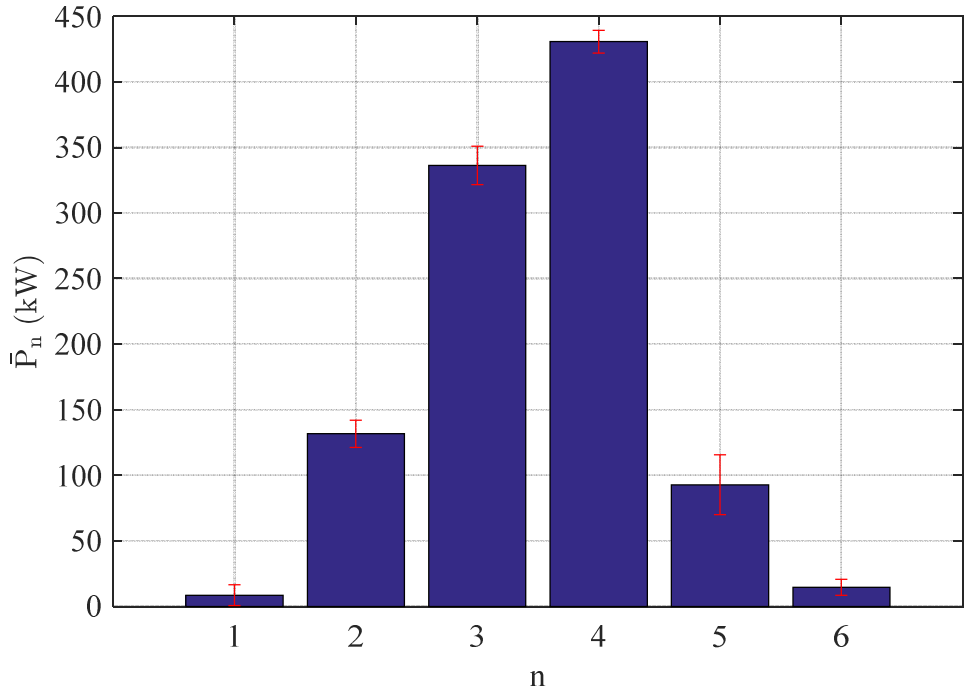


**Figure 96. Mean module power capture for *n*th module, $\bar{\bar{P}}_n$, against module number, n, for the Modular Flap for a typical case. Expanded uncertainty bars are shown in red. The wave was regular, with a period of 9.5 s, an amplitude of 1 m and a direction of 0 degrees.**

Given the observed level of symmetry shown in Figure 96, to simplify the analysis and associated graphics, the module results are henceforth presented in the following way: for the time-series, the results are shown for the modules on one side of the device, arbitrarily chosen as the left side, consisting of modules 1, 2 and 3 (see Figure 82 for further reference); for the statistics, the means of the results for the pairs of modules are used.

To first gauge the relative magnitudes and phases of module power capture, a typical, mid-wave period range, example of time-series is shown in Figure 97. Also illustrated to aid explanation are the constituent factors of power capture, angular velocity and damping torque.

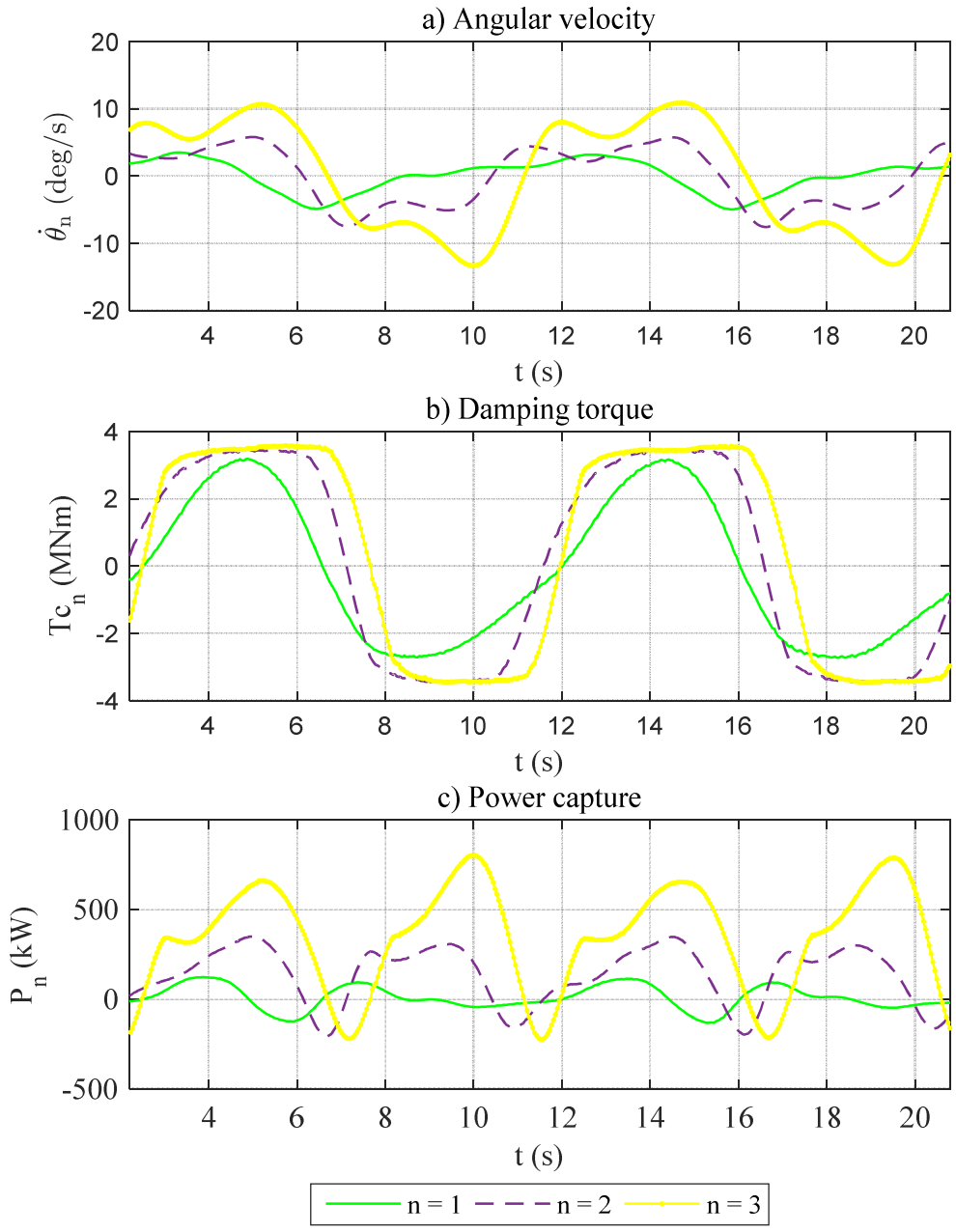


**Figure 97. Example of variation of individual module angular velocities, $\dot{\theta}_n$, a) damping torques, $Tc_n$, (b), and power captures, $P_n$, (c) for the $n$th module, with time, $t$ (Wilkinson *et al.*, 2017). The wave was regular, with a period of 9.5 s, an amplitude of 1 m and a direction of 0 degrees.**

As shown in subplots a) and b) of Figure 97, the magnitudes of angular velocity and damping torque, respectively, increased towards the central modules. The consequence of this was that the power capture was significantly larger for the central modules.

For the outermost module (n = 1), subplot a) shows that its angular velocity was close to 0 deg/s for the majority of the time-series. This suggests that the resultant torque acting on the module was close to 0 Nm. This was because the maximum torque that the damper could deliver was equal to the wave excitation torque, meaning that the module was overdamped. This is also suggested by the sinusoidal shape of its damping torque profile shown in subplot b). As a result, the power-capture was virtually 0 kW. This relationship between wave excitation torque, damping torque and power is explored further when the results for all of the wave periods are considered shortly. More sophisticated damper control could also alleviate the issue of the outer modules being overdamped and this is discussed further in Chapters 8 and 9.

Another feature of Figure 97 is the phase differences between the signals. This is especially apparent in subplot c) for the power capture signals of modules 1 and 3. In that case, the phase difference of the peaks was around one quarter of the oscillation period. These phase differences will have likely been caused by diffracted and radiated waves meeting the different modules at different points in time. As will be shown later, this has implications for the total power capture of the Modular Flap device.

To summarise the module results, Figure 98 shows the statistics for the angular velocities, damping torques and power captures across the wave period range. These were generated from the tests where maximum mean total power capture was recorded for each wave period.

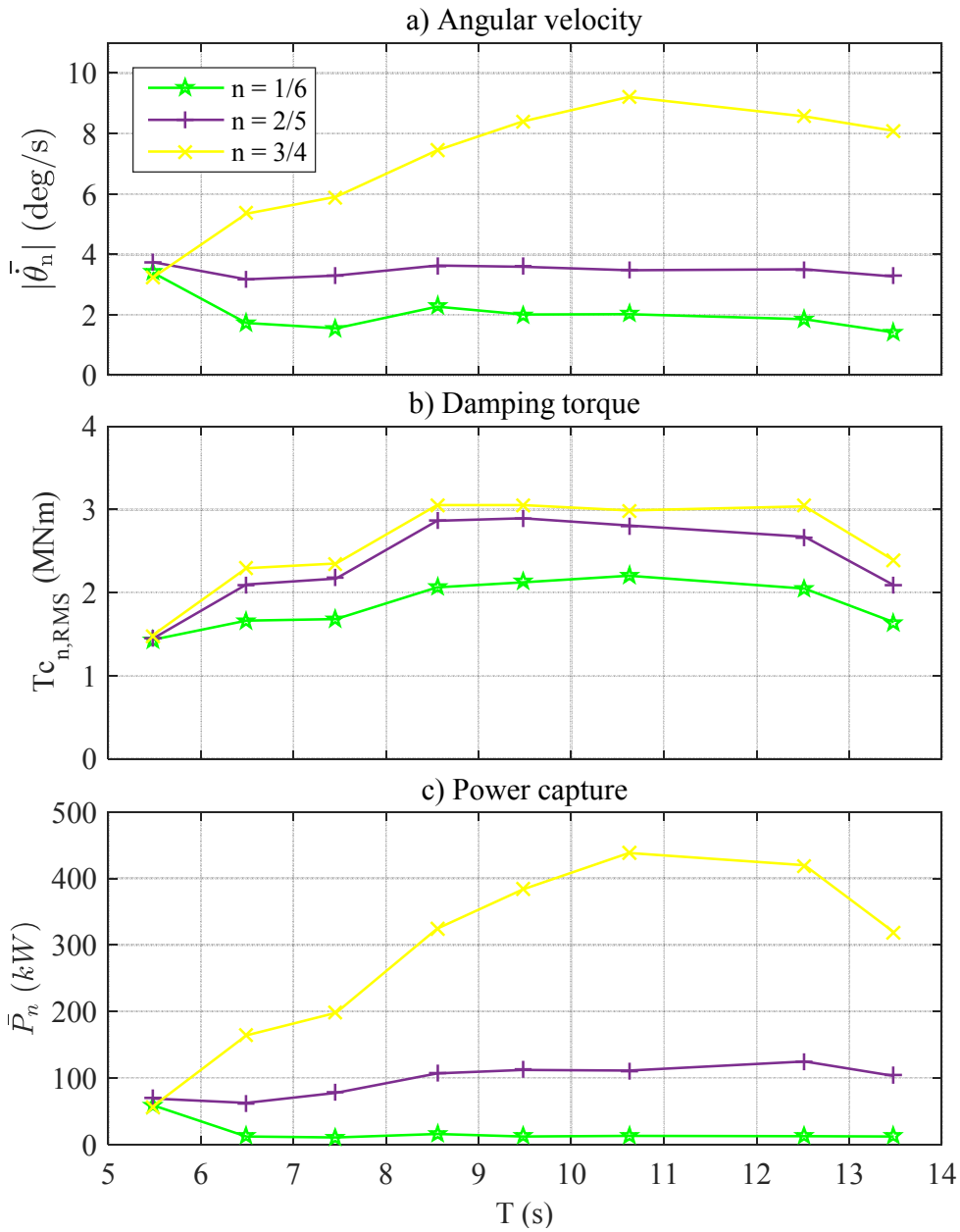


**Figure 98. Mean absolute angular velocity, $\overline{|\dot{\theta}_n|}$, root-mean-square damping torque, $Tc_{n,RMS}$, and mean power capture, $\overline{P_n}$, for the nth modules, against wave period, $T$. Note that the results are for the means of the results for the pairs of symmetrical modules (1/6, 2/5 and 3/4). The waves were regular, with an amplitude of 1 m and a direction of 0 degrees.**

Subplot a) of Figure 98 shows, at the shorter wave periods, the flap modules had approximately equal angular velocities. At increasing periods, however, the velocities diverged. This was particularly so for the central modules (n = 3/4). They experienced a large acceleration, peaking at around 10 s wave

period. In contrast, the outer (n = 1/6) and inner (n = 2/5) modules travelled at largely constant and significantly lower velocities across the wave period range. The velocities for the outer modules, for example, were on average 280 % lower than for the central units.

As one would expect, the trend of the mean power captures of the modules, shown in subplot c) of Figure 98, was to compound the results for the angular velocities and damping torques. The power capture for the central modules was by far the highest, with values then decreasing towards the outer modules. This agrees with the findings by Sarkar et al. (2016). Averaging the contributions to the total mean power-capture across the wave periods, the central modules produced 68 %, the inner modules 25 % and the outer modules only 7 %. This trend of increasing power towards the central modules is likely due to a combination of viscous losses and the balance between applied damping and wave excitation torque.

Flow separation at the edge of a body oscillating in a viscous fluid causes eddies to be generated and shed. This results in a resistive torque acting on the body and hence a reduction in resultant torque, leading to reduced motion and power capture (Henry, 2008). The fact that the modules were mechanically, but not hydrodynamically, separate from each other suggests that the outer modules experienced the greatest losses in power due to eddie generation. This therefore provides some explanation for their lower power capture.

For flap-type devices that were similar in geometry to those studied in this thesis, wave excitation torque has been shown to have a more dominant influence over power capture than viscous losses (Henry, 2008). Hence, it is likely that the principal driver of the module power capture differences was the wave excitation torque.

Wave excitation torque is the moment that drives flap motion. It occurs due to differences in hydrostatic and hydrodynamic pressure across the front and back

face of a flap. This results from a combination of differences in water surface elevation and water particle motion, respectively (Renzi *et al.*, 2014).

For devices that are driven by the diffraction process, like flap-type WECs, the magnitudes of the wave excitation torque and power capture are strongly linked (Henry, 2008). The magnitude of the wave excitation torque also limits the maximum damping torque that can be applied to a device. Hence, the wave excitation torque on each flap module was evaluated to aid this explanation.

The wave excitation torque was measured by applying the maximum torques that the dampers could supply to the modules and exciting them with regular head-on waves. Application of the maximum damping minimised the motions of the modules and hence the majority of the wave excitation torque was absorbed by the dampers. This torque was measured using the torque sensors.

In some cases, the wave excitation torque exceeded the applied damping torque. This was partly inferred through study of the profiles of the measured damping torque signals. A sinusoidal signal indicated that the full extent of the wave excitation torque was being measured (Crooks *et al.*, 2014); a square-wave, on the other hand, indicated that not all of the wave excitation torque was being measured because all of the damping torque from the damper was being supplied. Some signals were not completely sinusoidal in profile, meaning that the wave excitation torques were not completely measured. Nevertheless, the results demonstrate the relative differences in the magnitudes of module wave excitation torque well. Example time-series results for the flap modules are shown in Figure 99.

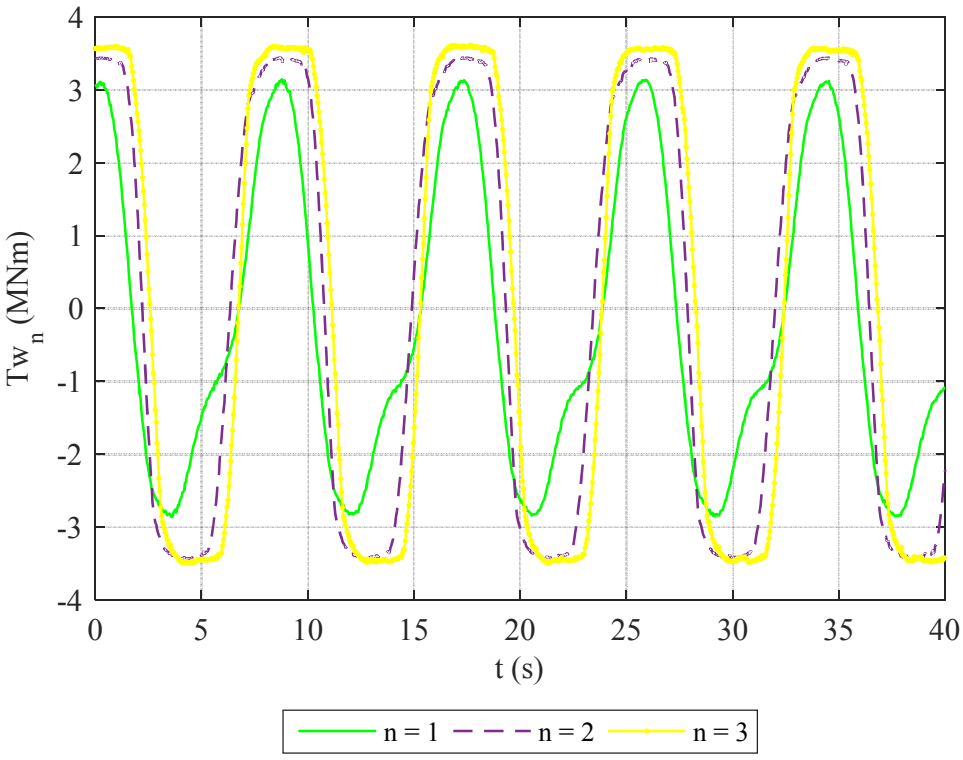


**Figure 99. Example of measured wave excitation torque on the *n*th module, $Tw_n$, against time, t. The wave was regular, with a period of 8.5 s, an amplitude of 1 m and a direction of 0 degrees.**

Figure 99 shows that the magnitude of the wave excitation increased towards the central modules. The plateauing of the signals for these modules, numbers 2 and 3, also suggests that the peak wave torques were, in fact, even greater than that measured.

To present the general picture for the head-on regular waves, the mean RMS wave excitation torques, for each pair of modules, across the wave period range are shown in Figure 100.

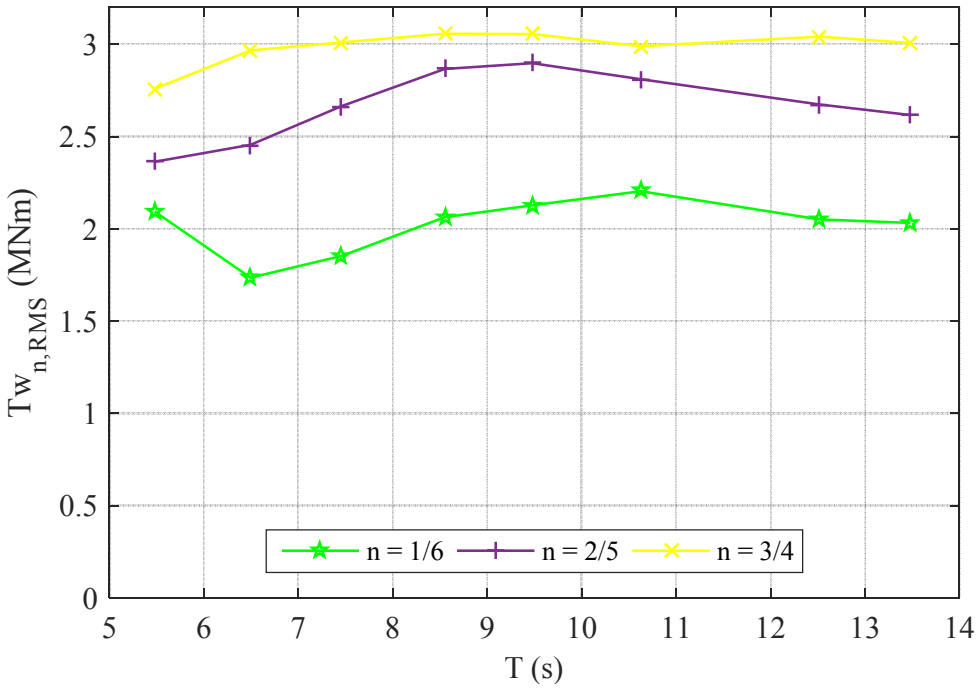


**Figure 100. Root-mean-square of measured wave excitation torque on the *n*th module pair, $Tw_{n,RMS}$, against wave period, *T*. The waves were regular, with an amplitude of 1 m and a direction of 0 degrees.**

Figure 100 shows a peaking of the wave excitation torque around a wave period of 10 s, which explains the greater angular velocities, especially for the central modules, shown in Figure 98 a). Figure 100 also shows that, in all cases, the measured wave torque increased towards the central modules. To quantify this, the module torques were compared to the total device values. The latter were determined by summing the module values at each wave period. On average, the proportions of the total wave excitation torque experienced by the outer (n = 1/6), inner (n = 2/5) and central (n = 3/4) pairs of modules was 26, 35 and 39 %, respectively. Assuming linearity between wave amplitude and wave excitation torque, these magnitudes and the trend of increase towards the central modules agree with previous work (Sarkar, Doherty and Dias, 2016). The heightened wave excitation torque was likely due to the greater pressure difference, between the front and back of the flaps, in the centre of the device (Renzi *et al.*, 2014).

The heightened wave excitation torque acting on the central modules resulted in higher angular velocities and allowed greater damping torque to be applied. The outer modules, on the other hand, were typically damped to their highest magnitude of wave excitation torque, i.e. approximately 2 MNm. This meant that the resultant torque was small, resulting in the angular velocities and power capture being minimal. This finding may only apply if the achievable damping level on each module was set to be the same value. However, this is the simplest damping strategy and is hence a realistic option. Further discussion on the implications of the applied damping strategy is provided in Chapter 8.

## 6.3 Device Capture Factors

### 6.3.1 Introduction

The power captures for the Modular and Rigid Flaps were assessed using the capture factor, the ratio of absorbed to incident wave power, as defined in Equation 48. This section presents these results, split between those for the head-on regular and irregular waves and off-angle regular waves, in sub-sections 6.3.2, 6.3.3 and 6.3.4, respectively.

### 6.3.2 Head-On Regular Waves

Presented first, in Figure 101, are comparisons of the capture factors achieved by the two devices across the range of regular wave periods (Wilkinson *et al.*, 2017).

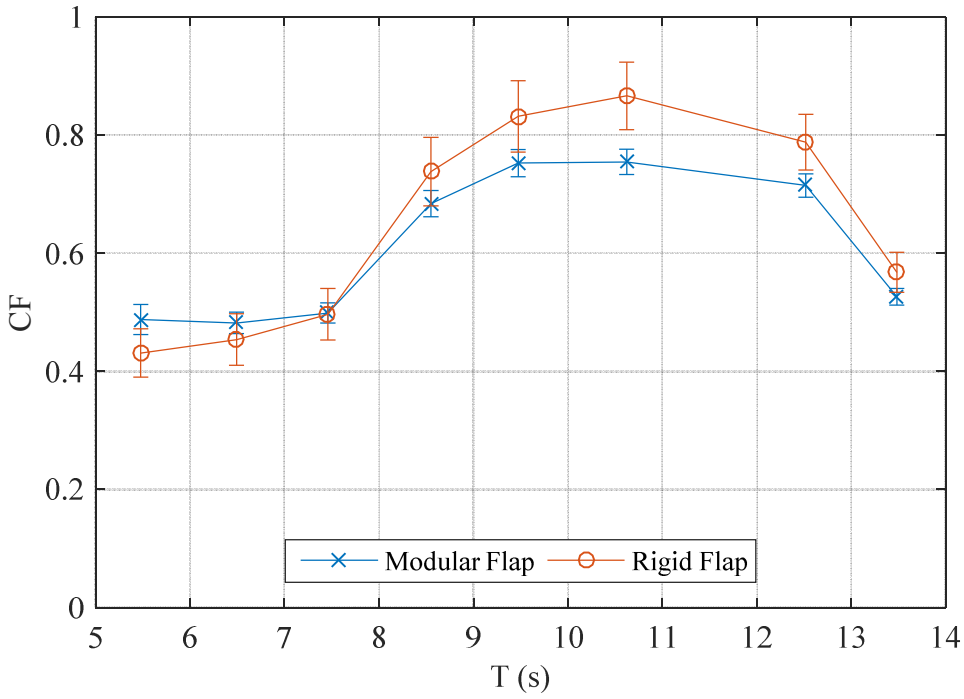


**Figure 101. Capture factors, *CF*, with associated expanded combined uncertainties, $\overline{U_{CF}}$, against wave period, *T*, for the six-module Modular and Rigid Flaps (Wilkinson *et al.*, 2017). The waves were regular, with an amplitude of 1 m and a direction of 0 degrees.**

Figure 101 shows that both devices achieved relatively high capture factors, compared to a range of other WEC concepts that have been shown to have capture factors predominately in the range of 0.05-0.40 (Babarit, 2015). This was achieved across the range of wave periods, indicating a broad bandwidth. Though not well defined, the capture factors of both devices peaked around the wave period of 10.6 s, with a capture factor of approximately 0.8.

Figure 101 also indicates that there was variation in the relative differences in the capture factors achieved by the two devices. Figure 102 shows this in more detail by presenting the computed relative differences, using the Rigid Flap as the reference device, for each wave period.

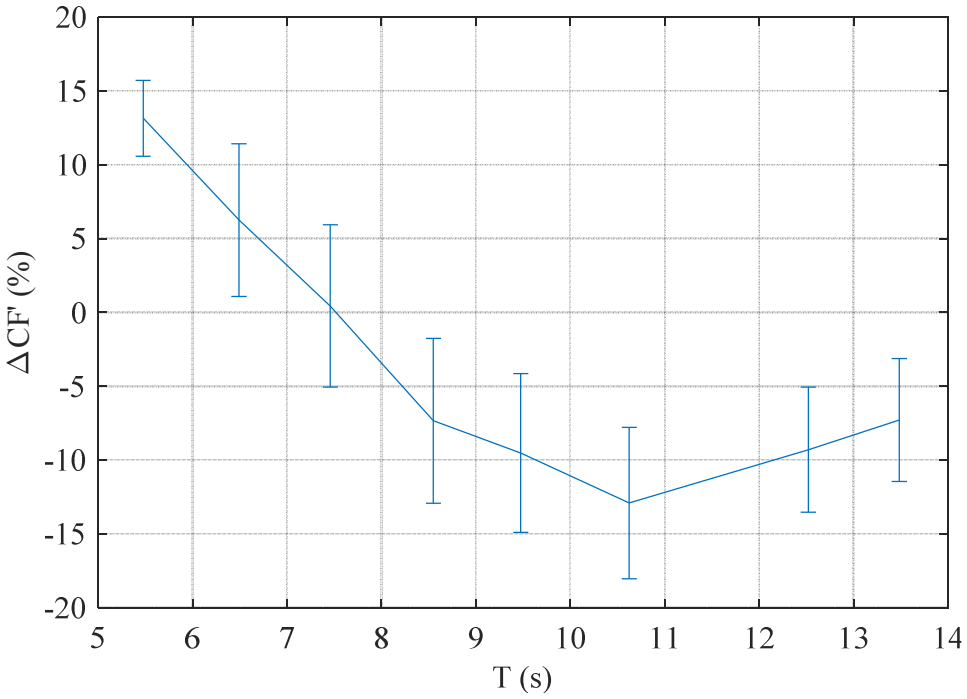


**Figure 102. Relative differences in the capture factors, *CF*, achieved by the Modular and Rigid Flaps, *ΔCF'*, with associated expanded combined uncertainties, $\overline{U_{CF}}'$, against wave period, *T* (Wilkinson *et al.*, 2017). The waves were regular, with an amplitude of 1 m and a direction of 0 degrees.**

For most of the results shown in Figure 102, the uncertainty limits were lower than the relative differences in the capture factors. This indicates that there were statistically significant differences in the power capture performances of the modular and rigid devices.

For the shorter wave periods, between 5 and 6 s, the Modular Flap outperformed the Rigid Flap, by up to 13 %. It is unclear why this occurred. The natural period of the Modular Flap was approximately 20 s, as indicated by the free decay tests described in appendix section 13.4. In previous works, amplification of motions of a modular device occurred at wave periods equal to half of the natural period of the device, i.e. 10 s for this case (Mei *et al.*, 1994). This suggests that the effect shown in the tests in this thesis was not related to resonance. One alternative explanation could be that it was actually that the Rigid Flap performance was lessened at these wave periods. This could have been due to the 'terminator effect'. This is where the capture factor of a device

is lowered and limited to 0.5 when its width is similar to the wavelength of the incident wave (Henry, 2008; Renzi *et al.*, 2014). For a wave period of 5.5 s, the lowest in the studied range, in a water depth of 13.9 m, the wavelength is 45 m (United States Naval Academy, no date). The device width, 33 m, was therefore similar to the wavelength. The Modular Flap, whilst possessing the same total width, consisted of modules each with a width of only 5.5 m. Hence, each flap module will have been impacted by the terminator effect to a lesser degree.

For the higher wave periods, i.e. those greater than 8 s, the Rigid Flap outperformed the Modular Flap, also by up to 13 %. The lower power capture of the Modular Flap may have resulted from an increase in the mean size of the gaps between the modules. A gap here is the cross-sectional area of the opening between the modules when viewing the device from the side. An increase in the size of the gaps would likely result in power reduction due to water leaking between the modules. The relative magnitude of the mean gap size over time can be inferred from the variation of the magnitudes of the mean module angular velocities, shown in Figure 98. The variation was measured using the standard metric, the 'coefficient of variation'. This is the ratio of the standard deviation and the mean. The relative differences in the capture factors were then correlated against the variations of mean angular velocity. The resulting correlation coefficient was -0.83, indicating a fairly strongly inverse correlation (MathWorks, 2017).

Summarising across the wave period range, the mean value of the relative differences between the capture factors achieved by the two devices, was -3 %, with an expanded combined uncertainty of +/-5 %.

The relative differences in capture factor were also weighted with the available incident wave power. The weighting was achieved by first normalising the incident powers with the maximum value, 48.4 kW/m in the 13.5 s sea state. The relative differences in capture factor were then multiplied by these normalised incident powers, with the results shown in Figure 103.

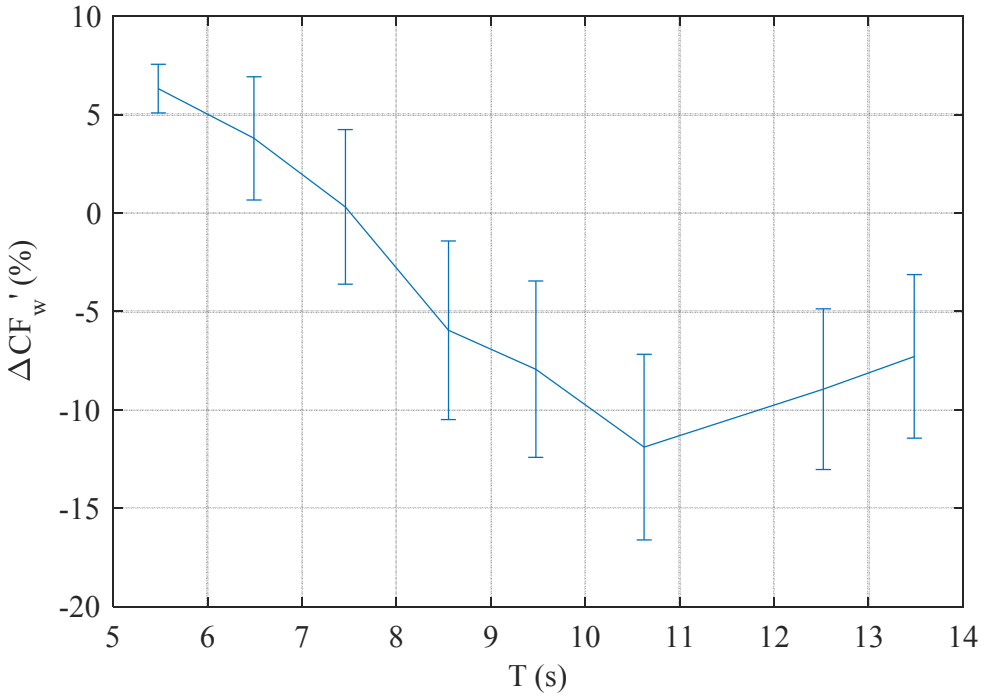


**Figure 103. Relative differences in the capture factors, *CF*, achieved by the Modular and Rigid Flaps weighted with the available incident wave power, $\Delta CF'_w$ against wave period, *T*. Error bars are the expanded uncertainties, $U_{\Delta CF'_w}$. The waves were regular, with an amplitude of 1 m and a direction of 0 degrees.**

The relationship shown in Figure 103 was, in fact, very similar to that for the unweighted relative differences in capture factors, shown in Figure 102. The effect of weighting the differences with the available power was that the enhanced power capture of the Modular Flap in the shorter wave periods was lessened, due to their lower available power. The result of this was that the mean reduction in power was slightly higher, with a mean weighted relative difference of -4 %, with uncertainty of +/-4 %.

These analyses have shown that there was not a statistically significant reduction in efficiency when comparing the Modular Flap to the Rigid Flap. It does suggest, however, that a small decrease in power capture would be shown if the uncertainty limits were lower. Reasoning for this small decrease in power capture are provided by first assessing the constituent components of the power capture – the angular velocity and damping torque. Figure 104 achieves this by

presenting results for device angular velocity, damping torque and, for reference, power capture, respectively, across the wave period range.

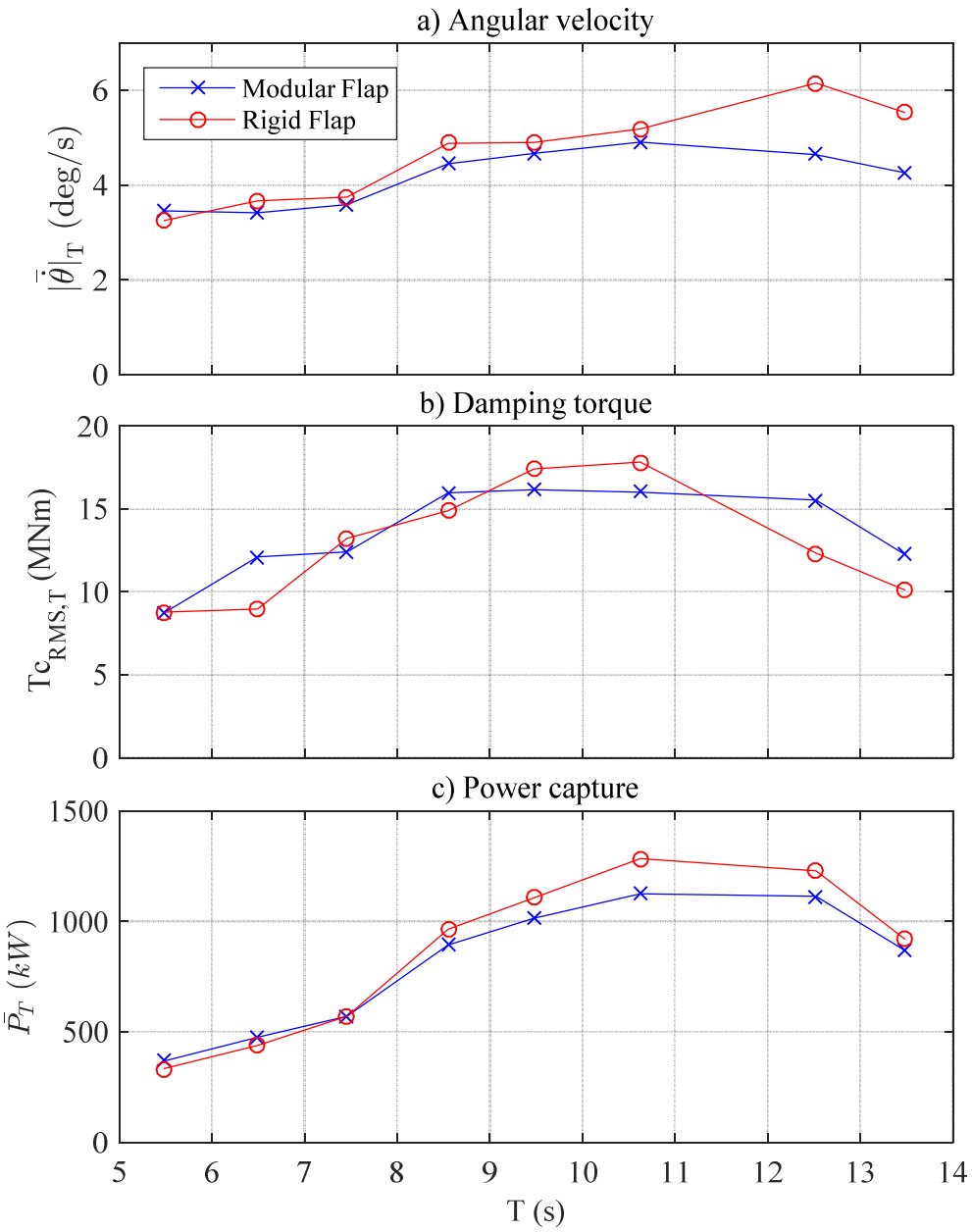


**Figure 104. Device mean absolute angular velocities, $\overline{|\dot{\theta}|}_T$, root-mean-square damping torque, $Tc_{T,RMS}$, and mean power capture, $\overline{P_T}$, against wave period, $T$. The waves were regular, with an amplitude of 1 m and a direction of 0 degrees.**

Subplot a) of Figure 104 shows that the mean absolute angular velocities of the Modular Flap were generally slightly lower than for the Rigid Flap. The mean

relative difference over the wave periods, compared to the Rigid Flap, was -9 %.

For the damping torques, presented in subplot b), the trend was not as clear as for the angular velocities. The differences in the magnitudes for the two devices fluctuated across the wave period range. The mean relative difference, however, was +8 %, indicating that the Modular Flap required slightly higher damping torque. This may have been because the application of higher damping torque reduced the size of the gaps that opened up between the modules.

The culmination of the trends for the angular velocity and damping torques was that, as stated previously, the power captures for the two devices were similar across the wave period range, with a mean relative difference of -3 %, indicating a slight decrease in power capture for the Modular Flap. The reduction was likely due to the wave excitation torque experienced by the Modular Flap being almost consistently lower, as illustrated in Figure 105.

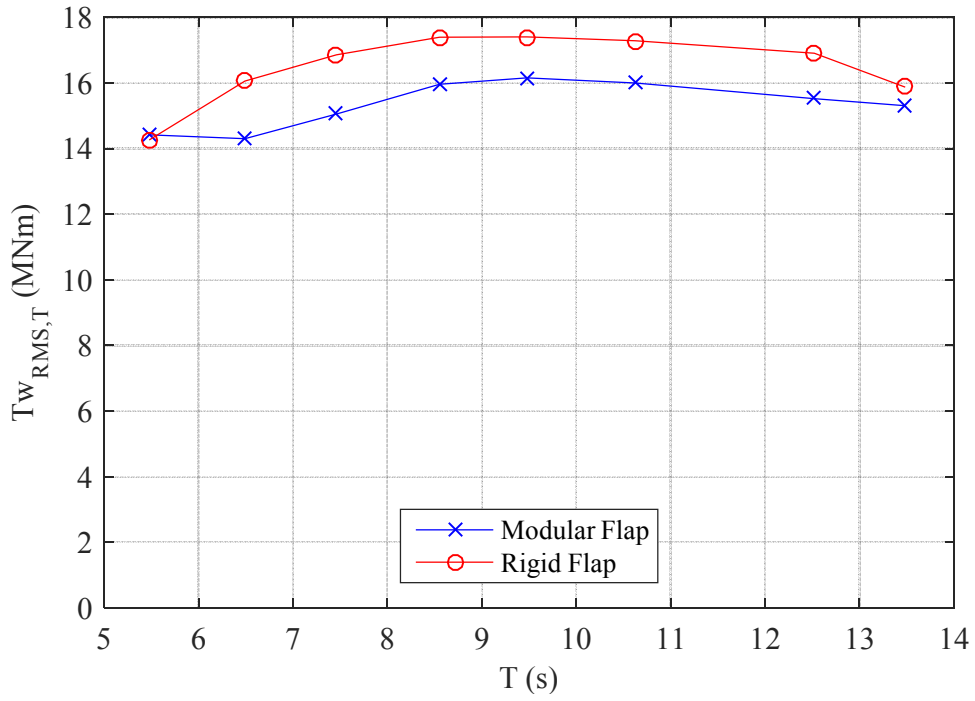


**Figure 105. Root-mean-square of measured wave excitation torque on the Modular and Rigid Flaps, $Tw_{RMS,T}$, against wave period, $T$. The waves were regular, with an amplitude of 1 m and a direction of 0 degrees.**

The general reduction in wave excitation torque for the Modular Flap, compared to the Rigid Flap, is likely a result of water leaking through the gaps in between the modules and thus decreasing the force exerted by the water.

The mean relative difference between the measured wave excitation acting on the two devices across the wave periods was -10 %. Henry (2008) showed that, for a flap not tuned to the incident wave period, the power capture is proportional to the square of the wave excitation torque. If this was completely correct for the Modular-Rigid Flap comparison, it would be expected that the power capture of the former would be 81 % of the latter. The fact that the unweighted capture factor reduction was instead only 3 % suggests that the average decrease in wave excitation torque was a contributing factor, but that the Modular Flap compensated for it through a focusing of power capture in the central modules and perhaps partial enhancement by the resonance phenomenon discussed in Sarkar et al. (2016).

### 6.3.3 Head-on Irregular Waves

As discussed in section 4.4.2, the Modular and Rigid Flaps were tested in several irregular sea states, to assess their relative performance in more realistic conditions than regular waves. For these irregular waves, the nominal mean wave period, $T_{01}$, varied between 6.5 and 8.5 s, while the nominal significant wave height, $H_{m0}$, was held at 2.75 m. The resulting capture factors are presented in Figure 106.

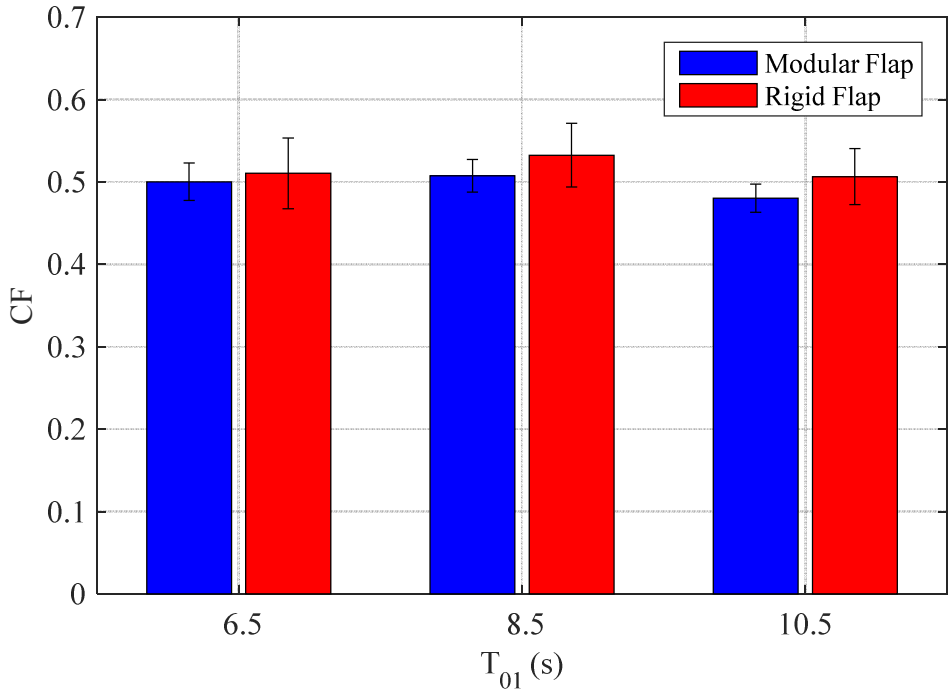


**Figure 106. Capture factor, *CF*, against mean wave period, $T_{01}$. For the Rigid Flap and 6 module Modular Flaps. Error bars are the expanded uncertainties, $U_{CF}$. The waves were irregular, with a significant wave height, Hs, of 2.75 m and a direction of 0 degrees.**

Figure 106 shows that both devices achieved a reasonably constant capture factor, of approximately 0.5 across the wave periods. Compared to the regular conditions with the same wave period and direction, there was lower variation in the capture factors achieved in the irregular waves.

For testing in irregular waves using a single PTO damping level, it would be usually expected that the capture factor would be lower than that achieved in regular waves with the same parameters, i.e. wave period and incident power. This is because one cannot apply PTO damping that is optimum, for power production, across all of the frequencies in an irregular sea state. Hence, as expected, the capture factors were lower than in the regular waves, especially so for the higher wave periods.

The overlapping uncertainty limits in Figure 106 suggested no difference between the performances of the two devices. However, the Modular Flap capture factors were consistently lower, 4 % on average. This was a similar

outcome to that for the regular wave tests and was hence likely caused by the same combination of reduced wave excitation torque, compensated for by power-enhancing module interaction.

### 6.3.4 Off-Angle Regular Waves

For the head-on regular wave with an 8.5 s period, it was shown in Figure 102 that the six-module Modular Flap had 7 % lower efficiency than the Rigid Flap. The uncertainty on this result was +/-6 %. This shows that there was a statistically significant reduction in efficiency when employing the Modular Flap for this wave condition. This reduction may be offset, however, by a superior performance in off-angle waves. This hypothesis was tested by carrying out an equivalent evaluation of the capture factors achieved in the off-angle regular waves. First shown, in Figure 107, are the capture factors achieved at different wave direction angles by the two devices.

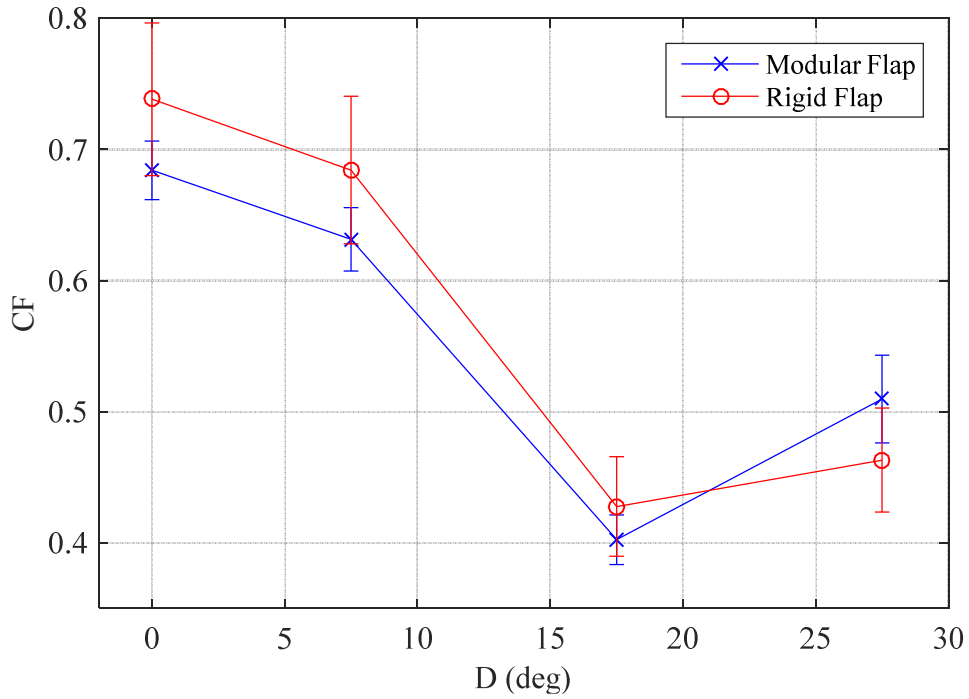


**Figure 107. Capture factor, *CF*, against wave direction, *D*, for the Modular and Rigid Flaps. Error bars are the expanded uncertainties, $U_{CF}$. The waves were regular, with a period of 8.5 s and an amplitude of 1 m.**

The first point to note on Figure 107 is the unexpected increase in capture factor between the wave direction angles of 17.5 and 27.5 degrees. Previous work has shown the power capture of a similar device, a 24 m wide flap-type WEC, to be proportional to the cosine of the wave direction angle raised to an exponent of 2.5 (Henry, 2008). The available incident power that is aligned with the axis of flap rotation reduces with the cosine of the wave direction angle. Hence, the capture factor of a similar device would be expected to decrease with the cosine of the angle raised to an exponent of 1.5. The values shown in Figure 107 broadly follow this relationship, apart from the results at an angle of 17.5 degrees, on average approximately 0.42, which are significantly below the expected power capture, which was in the region of 0.64.

The fact that the power captures of both devices were unexpectedly low at the 17.5 degrees wave direction suggests that the occurrence was likely due to a tank effect and not the devices themselves. The tank effect could have been a standing wave being created. A standing wave is the superposition of reflected and incident waves, creating nodes and anti-nodes in a wave tank. Maximum surge and heave particle motion occur at nodes and anti-nodes, respectively (Henry, 2008). Due to the hydrodynamics of a flap-type device being dominated by the surge particle motion, it can be expected that a device would experience a reduction in power capture if located at an anti-node. The changing of the direction of the wave generation may have hence moved the position of or created an anti-node at the model position for the 17.5-degree angle wave, resulting in an artificially reduced power capture.

Returning to the matter of relative device performance, Figure 107 shows that the difference in the capture factors achieved by the two devices reduced as the wave direction angle increased. This is better shown by plotting the relative differences in capture factors, as carried out in Figure 108.

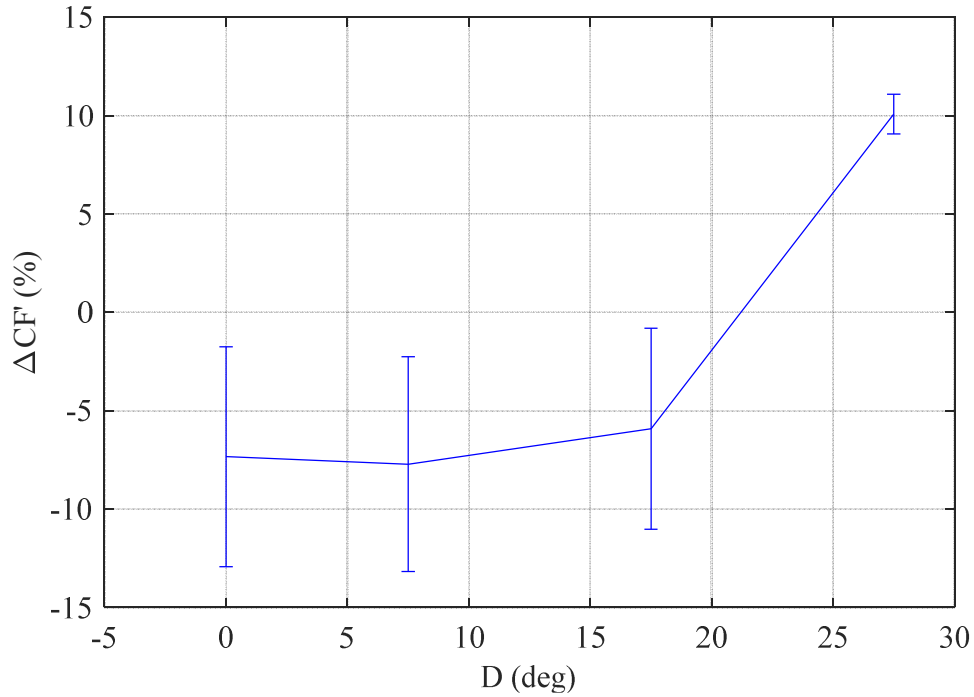


**Figure 108. Capture factor achieved by the Modular Flap relative to that achieved by the Rigid Flap, *ΔCF'*, against wave direction, *D*. Error bars are the expanded uncertainties, $U_{\Delta CF'}$. The waves were regular, with a period of 8.5 s and an amplitude of 1 m.**

Figure 108 shows that, between the directions of 17.5 and 27.5 degrees, the Modular Flap surpassed the Rigid Flap in efficiency, eventually achieving a 10 % higher capture factor.

The lower rate of capture factor reduction with wave direction angle for the Modular Flap can be explained by comparison of the input wave excitation torque to the resisting torques. The wave excitation torque drives the device motion, while the resistive torques, such as inertia and restoring buoyancy, lower the magnitude of motions.

For a head-on wave, the wave excitation torque acts upon the whole flap, or flap modules, approximately simultaneously. Phase differences do occur, but the magnitudes of these differences are lower than for highly angled waves. The available torque that can overcome the resistive torque is hence large and so too is the net torque acting on the flaps. This results in large amplitudes of motion and hence, with suitable applied damping torque, high levels of power

capture. For an off-angle wave, however, there exists an angle between the wave crest and the flap hinge. This leads to phase differences in the wave excitation torque acting at different points along the device hinge axis. Additionally, the wave direction angle means that the magnitude of the component of the driving force that acts perpendicular to the hinge is lowered. This combination results in a lowering of the net torque acting on the whole device at any moment in time.

Lowering of the net torque occurs for both the Rigid and Modular Flaps. However, the difference is how the resistive torques change with wave direction angle. For the Rigid Flap, the inertia and restoring buoyancy torques are the same, regardless of wave direction angle, because the flap is a single body. This means that the reduced wave excitation torque is having to overcome the same level of resistance. Hence, the motions, and so power, significantly reduce with flap direction angle. For the Modular Flap, however, as the wave direction angle increases, the resistance torques can actually reduce. This is because, for large wave direction angles, the flap modules are excited independently. As a result, the motions and power capture are not as heavily reduced. This explanation is aided though the free body diagrams shown in Figure 109.

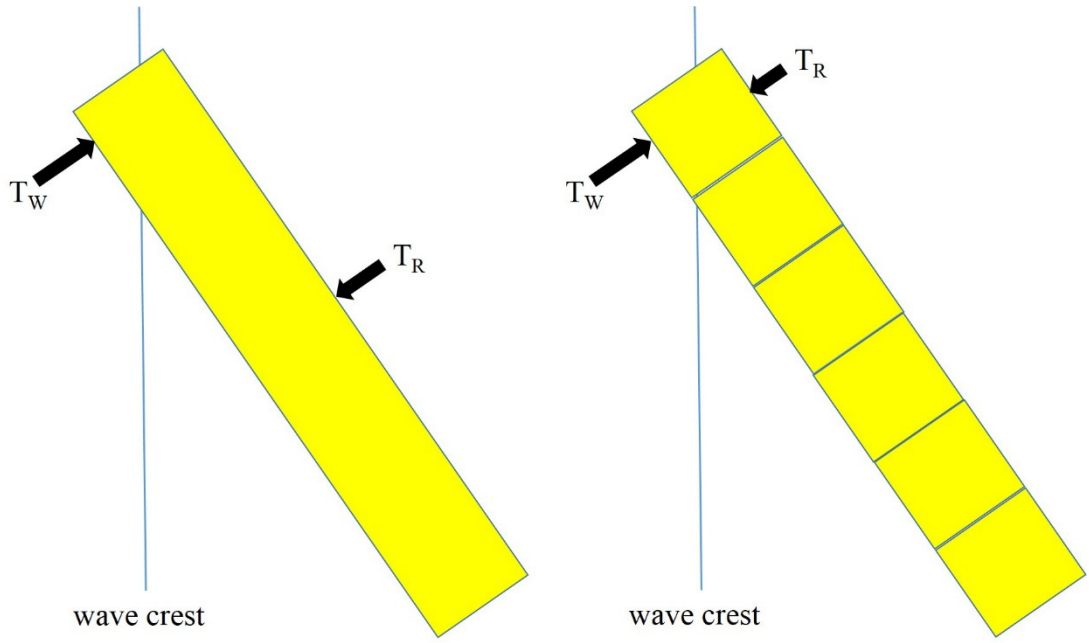


**Figure 109. Free body diagrams of torques acting on Rigid Flap (left) and six-module Modular Flap (right) when met by off-angle wave. $T_W$ and $T_R$ are the wave excitation and resistive torques, respectively.**

In terms of overall performance, the mean relative difference in capture factors across the conditions was –3 %, with an uncertainty of +/-4 %. This shows that, although the Modular Flap outperformed the Rigid Flap at the largest wave direction angle, the lower power at the smaller angles diminished the overall relative performance. Nonetheless, the uncertainty limits were at least as large as the mean difference and hence the result was statistically significant.

As with the head-on regular waves, a further analysis was carried out in order to assess the effect of weighting the relative differences in capture factor with the available wave power. In this case, the available power in the wave front was constant between each condition. However, the power incident to the device axis changed due to the variation in wave direction. Hence, the available wave power reduced as the wave direction angle increased. The resulting weighted relative differences in capture factor are presented in Figure 110

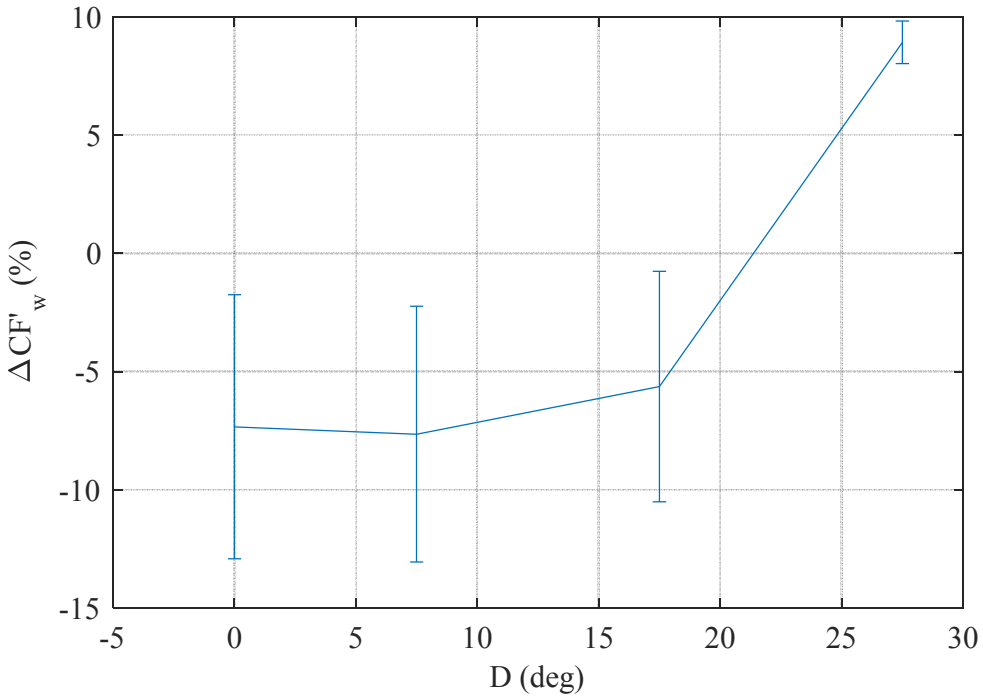


**Figure 110. Capture factors achieved by the six-module Modular Flap relative to that achieved by the Rigid Flap weighted with the available incident wave power, $\Delta CF'_w$, against wave direction, $D$. Error bars are the expanded uncertainties, $U_{\Delta CF'_w}$. The waves were regular, with a period of 8.5 s and an amplitude of 1 m.**

The relationship shown in Figure 110 was similar to that for the unweighted relative differences in capture factors shown in Figure 108. The only noticeable difference in the results was that the increase in power capture by the Modular Flap at the greatest wave direction angle was slightly lessened, from 9 to 10 %. This does elude to the fact though that the impact of increased power capture for a less energetic wave condition is decreased. Hence, it is important to weight the wave conditions with some regard to their available energy. In this case, however, the weighting was not strong enough to change the mean relative difference in capture factor, which was –3 %, with uncertainty of +/-4 %.

## 6.4 Device Smoothness of Power-Capture

The 'smoothness' of the device power capture is the degree to which it varies over time. A power output of greater smoothness lowers requirements for

electrical energy storage and hence the cost of energy produced (Molinas, Sorby and Lundberg, 2007).

In Figure 97, subplot c), it was shown that there were phase differences between the instantaneous power capture produced by each flap module in the Modular Flap; for the Rigid Flap, the flap modules are locked together and so the power capture is synchronous. From this, it can be predicted that the total instantaneous power capture by the Modular Flap would exhibit lower levels of variation due to the phase differences between the modules causing a smoothing of the total power. To illustrate this for a single example, time-series of total power capture for the Modular and Rigid Flaps are shown in Figure 111. Note that, to allow direct comparison, this graph is for the same test example as was used in Figure 97.

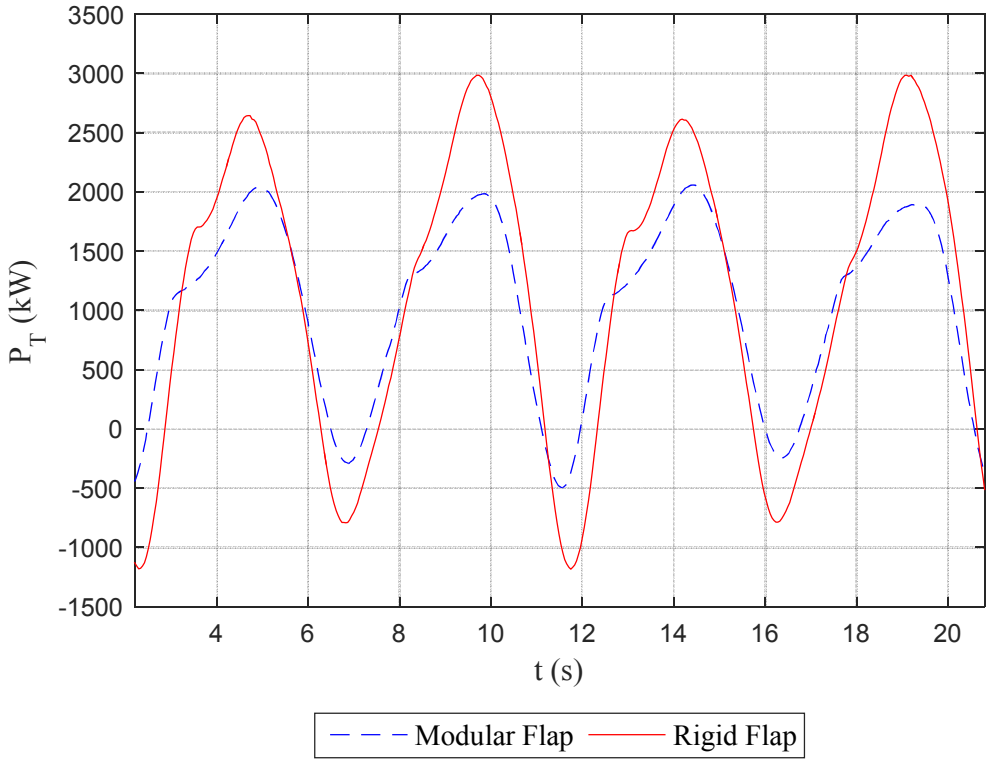


**Figure 111. Variation of total power, $P_T$, with time, $t$, for the Modular and Rigid Flaps. Both devices had the same total damping torque level applied to them. Note that the time has been adjusted so that the time-series approximately overlay (Wilkinson *et al.*, 2017). The wave was regular, with a period of 9.5 s, an amplitude of 1 m and a direction of 0 degrees.**

Figure 111 shows that the total power capture signal for the Modular Flap, when compared to the individual module powers in Figure 97 c), combined into a single oscillation. It is also apparent that the variation in the Modular Flap power signal was lower than that associated with the Rigid Flap power. This is indicated by the lower range and broader base of the oscillation. This was confirmed by calculation of the smoothness metric, $S_P$, as defined in Equation 51 as the ratio of the mean to the standard deviation, as 1.30 and 0.89 for the Modular and Rigid Flaps, respectively. To then gauge the general trend, a comparison of the smoothness metrics across the head-on regular wave conditions is provided in Figure 112.

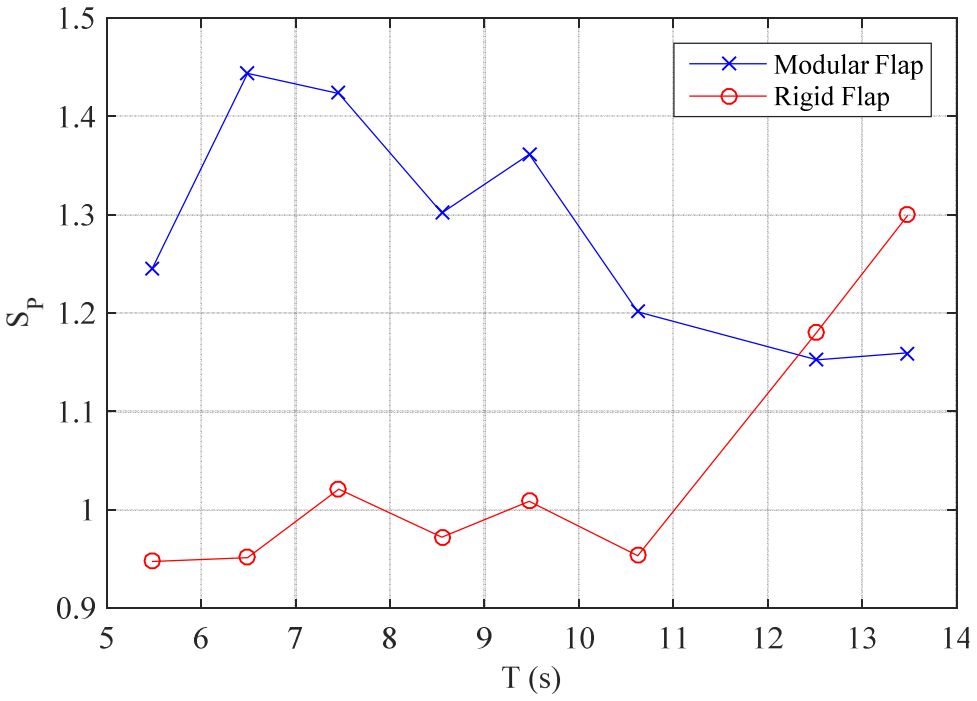


**Figure 112. Power smoothness metric, $S_P$, against wave period, $T$ for the Modular and Rigid Flaps. The waves were regular, with an amplitude of 1 m and a direction of 0 degrees.**

Figure 112 shows that, for most of the wave periods, the smoothness metric was higher for the Modular Flap. On average, the total power produced by the Modular Flap was 23 % smoother, as a result of the phase differences between the power produced by the modules.

## 6.5 Summary

This chapter has presented the key power capture results generated in the physical modelling campaign. The results were studied at both the flap module and whole device level. Most of the wave conditions were regular, with an amplitude of 1 m and a range of wave periods, 5.5-13.5 s, and directions, 0-27.5 degrees, supplemented with a small set of head-on, irregular waves.

It was shown that the mean angular velocities, achievable damping torques and mean power captures were concentrated in the centre of the modules making up the Modular Flap. On average, the central pair of modules produced 68 % of the total power, the inner modules 25 % and the outer modules only 7 %. This was likely because of a similar trend in wave excitation torque and the outer modules being overdamped.

The device power captures were assessed using the standard metric, the capture factor, which is the ratio of generated to available power. The results were presented with and without weighting applied to account for the wave power available in the sea states. The uncertainty on the results was also assessed, to determine the statistical significance of the results.

For the head-on waves, without weighting, the mean relative difference in capture factors was –3 %, with uncertainty of +/-5; with weighting, the mean relative difference was -4 %, with uncertainty of +/-4 %. A similar outcome was found for the irregular waves. It was suggested that the slight consistent reduction in power capture for the Modular Flap could be explained by a lower wave excitation torque acting on it.

For the off-angle waves, the mean relative difference in capture factors was -3 %, with +/-4 % uncertainty, for both the unweighted and weighted cases. Thus, again there was no statistically significant change in power capture by adopting the modular form. However, the rate of power reduction with wave direction angle was lower for the Modular Flap than for the Rigid Flap. This meant that, for the largest wave direction of 27.5 degrees, the Modular Flap outperformed

the Rigid Flap by 9-10 %, depending on weighting, with uncertainty of +/-1 %. The lower sensitivity of the Modular Flap to the wave direction was a result of the independent modules being excited separately, thus lowering the level of resistive torque generated by the body.

A further difference between the power capture of the two devices was in the variation of the instantaneous results. Due to phase differences in the power produced by each module, the total power capture of the Modular Flap was shown to be, on average, 23 % smoother for the head-on waves.

# 7. Foundation Loads

## 7.1 Introduction

This chapter presents the key foundation load results generated during the physical modelling campaign. The loads acting on the Modular Flap are evaluated and compared to those experienced by the Rigid Flap.

The loads are assessed for the degrees of freedom, surge and yaw, in sections 7.2 and 7.3, respectively. The surge loads were focused on because they are typically the largest forces acting on a flap-type device (Howard, Whittaker and Doherty, 2009; Wilkinson *et al.*, 2014); the yaw loads were partly chosen because, unlike in the surge axis, no power capture is generated in this degree of freedom and it hence represents a 'parasitic' load (Wilkinson *et al.*, 2014; Álvarez, 2015). Significant differences between modular and rigid device yaw loading were also shown in previous work but without applied damping (Wilkinson *et al.*, 2014). Hence, it was desirable to ascertain if this was still the case with damping applied and hence power being generated.

The assessment is carried out for the head-on and off-angle regular waves. A structure must be designed to withstand the highest loads that are expected to act on it. Hence, in this foundation load assessment, only the results where the highest loads occurred are presented. Thus, the surge loads are presented only for the head-on waves and the yaw loads for the off-angle waves.

Foundation load results are typically presented at the PTO damping level that is associated with the maximum mean power capture (Álvarez, 2015). However, it is also interesting to assess the loads at different damping levels. Justification for this is provided by first discussing the relationship between foundation loads and damping torque.

The surge foundation force is a function of the surge wave force and flap motion. Increased applied damping torque elevates the reaction torque that the flap generates against the wave action and hence results in a rise in the surge

foundation load (Folley, 2007). This is illustrated in Figure 113, which shows examples of surge foundation loads for different damping levels.

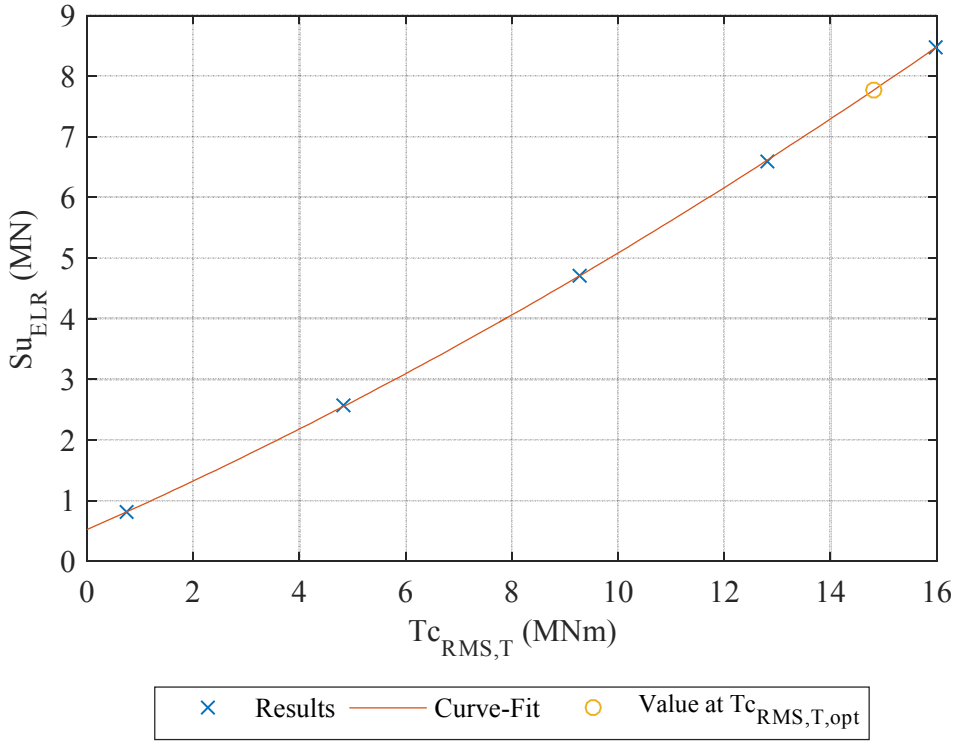


**Figure 113. Surge foundation effective load range, $Su_{ELR}$, against total RMS damping torque, $Tc_{RMS,T}$, example, showing increase in loads with damping torque. Quadratic curve has been fit to data. Value at optimum damping for power production also indicated. Example for Modular Flap, in regular wave with a period of 8.5 s and an amplitude of 1 m.**

Figure 113 shows that the surge foundation load increased quadratically with the damping torque. This was generally true for both of the devices and across the wave condition test range.

The yaw foundation load is a product of the surge foundation load and the distance from the resultant point of application to the centre of the device. Hence, the yaw foundation load was also a function of the applied damping torque.

The surge and yaw foundation loads can be used as metrics for the *cost* of the structures of the devices. This is because the material requirement of a structure is proportional to the load that it must withstand. The cost is then

approximately proportional to the material requirement (Álvarez, 2015). This does not account for non-linearities, such as machining costs not being necessarily directly proportional to the material requirements. Using the foundation load as a cost metric also ignores other costs such as for operations and maintenance of the devices. However, use of the foundation load is sufficient for this study, highlighting the relationships between loads and damping torques for the devices.

As shown in Figure 93, the power capture, like the foundation loads, was also a function of the applied damping torque, with the relationship also being approximately quadratic. In contrast to the foundation loads, the power capture is a metric for the *revenue* generated from the sale of the electricity produced by a WEC. Hence, while increased damping torque may result in greater power capture and therefore revenue, it may also lead to higher costs due to elevated foundation loads.

It is desirable to apply a damping strategy that results in the most *economical* power production. This can be achieved by maximising the power generated per unit of cost. Whilst a detailed study on the economy of power production is out of the scope of this thesis, the power produced per unit of foundation load provides a useful approximation of it (Folley, Whittaker and van't Hoff, 2007). In this thesis, this ratio is referred to as the 'Value of Power'. The numerator of the ratio is the device mean power capture at each damping level, while the denominator is the foundation load cost metric, for example the surge effective load range. The formula for the surge value of power metric, $V_{Su}$, for example, is provided in Equation 58.

$$V_{Su} = \frac{\bar{P}_T}{Su_{ELR}} \qquad \text{Equation 58}$$

Where $Su_{ELR}$, is the surge effective load range and $\bar{P}_T$ is the total mean power capture.

Referring back to Figure 93 and Figure 113, respectively, the power capture and surge load can increase at different rates with the applied damping torque. Hence, the value of power metric sometimes changed with damping torque. This meant that the power production had to rise at a greater rate than the surge loads for the applied damping strategy to be 'economical'. This is illustrated in Figure 114, which shows the range of value of power results for the different damping levels applied for a single sea state.

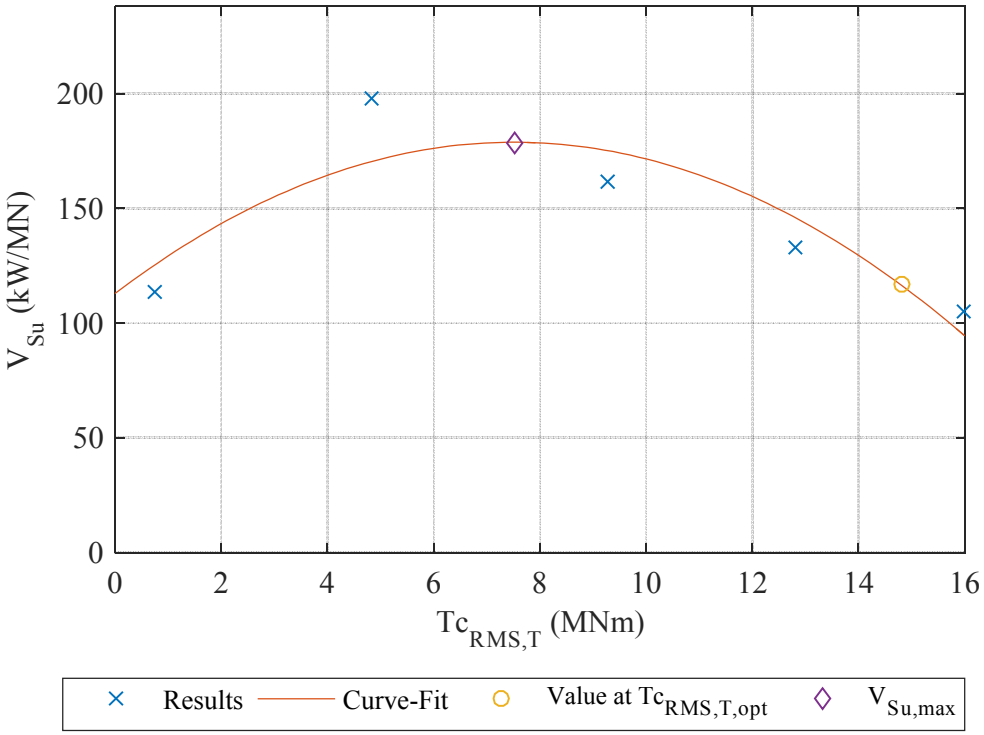


**Figure 114. Value of power using surge effective load range as cost, $V_{Su}$, against total RMS damping torque, $Tc_{RMS,T}$, example. Results at optimum damping for power production and maximisation of the value metric also indicted. Example for six-module Modular Flap, regular wave with a period of 8.5 s, an amplitude of 1 m and a direction of 0 degrees.**

As Figure 114 shows, the value of power metric had an approximately quadratic relationship with the applied damping torque. Hence, there were damping torques that maximised the value of power. The damping torque that resulted in the maximum mean power capture for this example is also shown in Figure 114. This indicates that this damping level was approximately twice the level that resulted in maximisation of the value of power.

Given the presented relationship between foundation loads and damping torque, it is hence fair to assess the foundation loads in this chapter for both the cases of maximum power capture, referred to as 'max power', and maximum value of power, referred to as 'max value'. For the surge load results, the surge loads are used exclusively for determining the 'max value' cases, with the equivalent true for the yaw load results.

## 7.2 Surge Loads

This section presents the surge foundation effective load ranges for the head-on regular waves. The results for each wave period are presented in Figure 115.

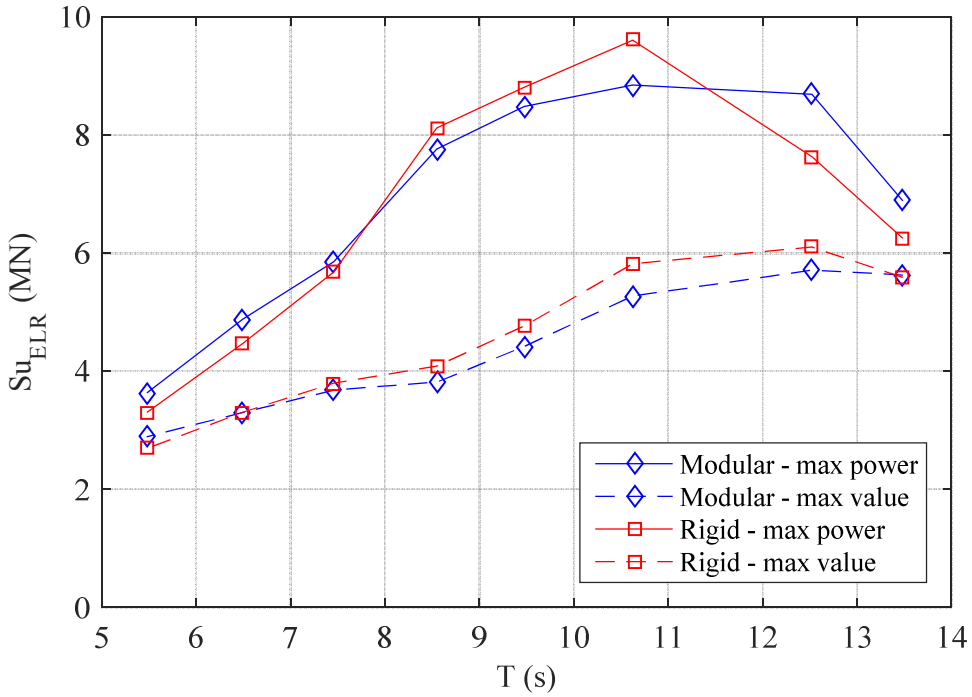


**Figure 115. Surge Effective Load Range, $Su_{ELR}$, against wave period, $T$, for the Modular and Rigid Flaps. Results are shown at maximum power and maximum value of power. The waves were regular, with an amplitude of 1 m and a direction of 0 degrees.**

Figure 115 includes several key features. Firstly, for both damping strategies, the surge loads experienced by the Modular Flap were very similar to those exerted on the Rigid Flap. This shows that, even though the modules in the Modular Flap were independent, the global surge loads added up to the same as

those experienced by the Rigid Flap. To quantify this, the mean relative differences between the Modular Flap and Rigid Flap surge loads were +2 % and -4 % for the 'max power' and 'max value' cases, respectively.

The trends of the 'max power' lines were also like those for the capture factors, shown in Figure 101. This shows that high power capture efficiency can come at the price of high surge foundation loads. Although the 'max value' results followed a similar trend, the peak in surge loads, around the 10.6 s wave period, was less pronounced. In fact, the max value surge loads were significantly lower than those experienced for the max power damping levels. To indicate this, the mean relative difference between the Modular Flap results for the two damping strategies was -36 %, with the maximum power result as the reference. This suggests that optimising the damping strategy for the ratio of power to load, instead of just power, could result in a considerable reduction in the foundation loads experienced by a WEC structure.

## 7.3 Yaw Loads

This section presents the key yaw foundation load results for the off-angle regular waves. Figure 116 first shows results for the different damping levels applied for a single wave condition. This is shown to contrast the relationships that the modular and rigid device yaw loads had with damping level.

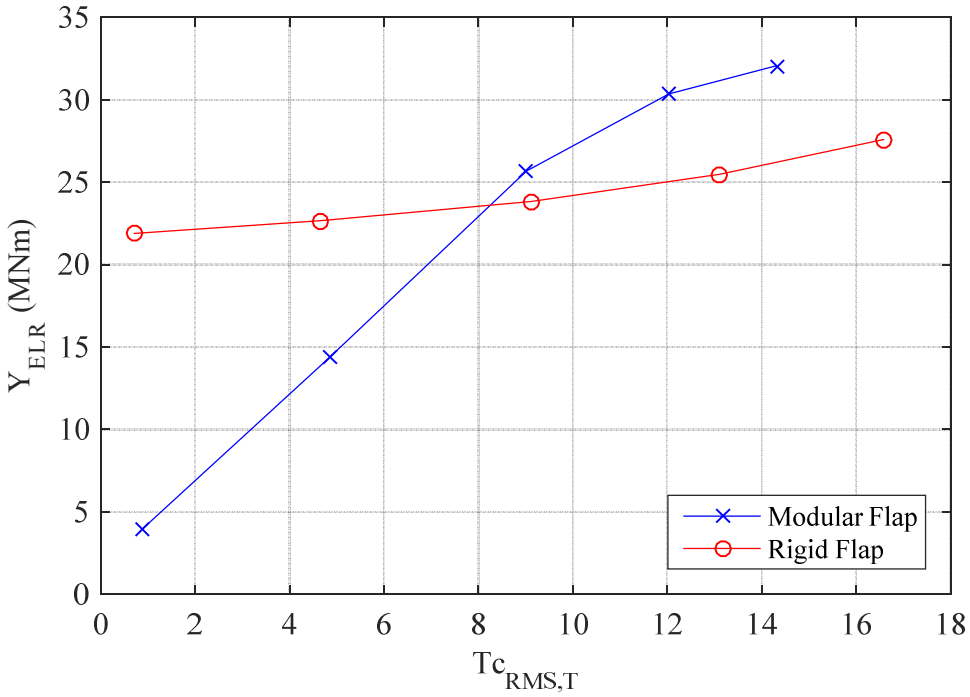


**Figure 116. Example results showing differing relationships between yaw effective load range, $Y_{ELR}$, and total RMS damping torque, $Tc_{RMS,T}$, for the Modular and Rigid Flaps. The wave was regular, with a period of 8.5 s, an amplitude of 1 m and a direction of 27.5 degrees.**

For the lowest damping level in Figure 116, the yaw load experienced by the Modular Flap was 80 % lower than for the Rigid Flap. This explains why previous results for undamped tests on modular and rigid devices showed the modular flap experiencing significantly lower yaw loads than the rigid device (Wilkinson *et al.*, 2014). As the damping lever increased, however, the greater rate of load increase for the Modular Flap meant that the loads that it experienced were eventually similar to the Rigid Flap. The difference in the relationships between yaw load and damping for the two devices is explored further shortly.

To provide a broader picture, the yaw foundation effective load ranges were evaluated at each of the wave directions, with the results presented in Figure 117.

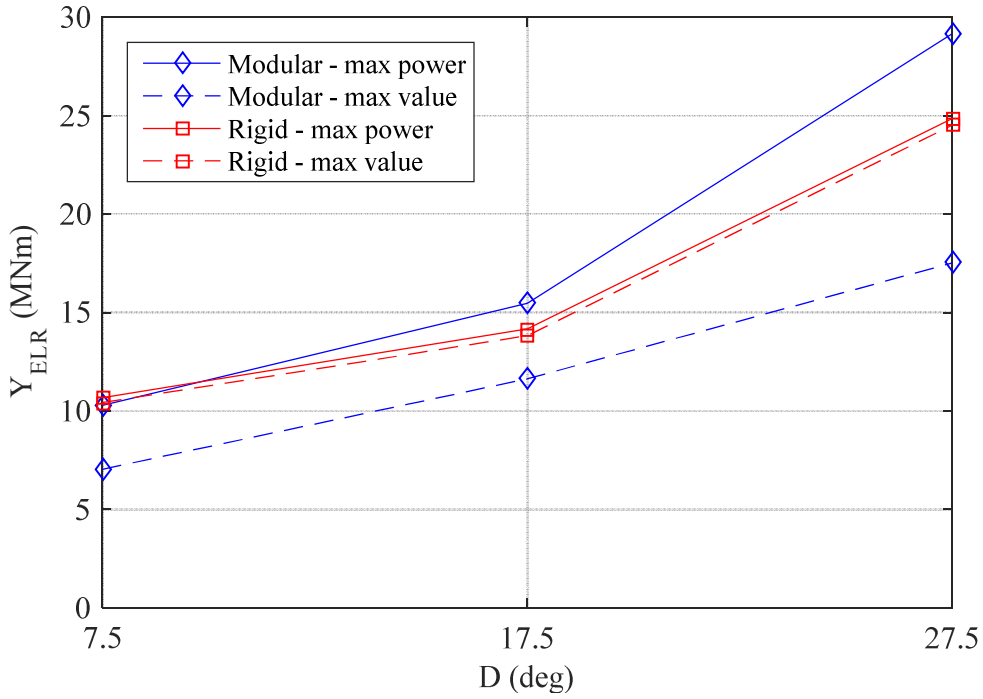


**Figure 117. Yaw Effective Load Range, $Y_{ELR}$, against wave direction, $D$. Results are shown at maximum power and maximum value of power. The waves were regular, with a period of 8.5 s and an amplitude of 1 m.**

Figure 117 shows that, as one would expect, the yaw loads increased as the wave direction angle grew. From the range of values shown, the employment of the different devices and damping strategies resulted in a range of yaw foundation loads.

For the base case damping strategy, i.e. of maximising power capture, the Modular Flap experienced a mean increase of loads over the Rigid Flap of 10 %. In contrast, for the damping strategy which maximised the value of power, the Modular Flap was subjected to 26 % lower loads, on average.

A further contrast in the results was between those for the two damping strategies for the Modular Flap. The mean relative difference, using the 'max power' case as the reference, was –34 %; for the Rigid Flap, the difference was negligible. This shows that, echoing the results shown in Figure 116, the magnitude of the yaw loads acting on the Modular Flap are highly dependent

on the applied damping strategy. This significant result can be explained by consideration of the differing ways that the two devices respond to yaw loads.

The yaw load is the surge force multiplied by the distance, or 'lever arm', between the resultant point of application and the central vertical axis of the device. A lever arm exists when there is asymmetry in the pressure acting on the flap face. This can result from, for example, an angle between the wave crest and flap hinge. Due to their mechanical composition, the Rigid Flap and Modular Flap respond differently to this situation and hence experience different yaw loads.

A resultant load acting on the Rigid Flap away from its centre results in torsion of the flap body. This is then transferred to the foundation as a yaw load. When the body has no notable external damping applied by the PTO systems, it is free to yield slightly, thus reducing the magnitude of the load that is transmitted to the foundation; when there is damping, however, the flap becomes more rigid and hence transmits more of the load. This behaviour is indicated by Figure 116, which shows the relatively gentle, but apparent, gradient between yaw load and damping level for the Rigid Flap.

Due to the mechanical independence of its modules, the flexibility of the Modular Flap can be assumed to be significantly larger than that of the Rigid Flap. However, the device still experiences yaw loads but the dependence on the applied damping level is much stronger. The yaw load is instead caused by a surge load acting on an individual module that has its centre away from the device centre. For low damping levels, as Figure 113 showed, the surge load on this module would also be low. Thus, the yaw load on the device would also be low. For these damping levels, the yaw loads on the Modular Flap were significantly lower than those acting on the Rigid Flap, as illustrated in Figure 116. When the damping is high on a module, however, the surge load and hence yaw load are also high. For the case of high damping, the yaw loads were similar to, but in fact greater than those experienced by the Rigid Flap. The larger loads were likely caused by overdamping the outer modules, which

have the greatest lever arm and so likely contribute significantly to the device yaw load.

## 7.4 Summary

This chapter has presented the key surge and yaw foundation load results. This was for the Modular Flap and the Rigid Flap. The results were from tests conducted in head-on and off-angle regular waves, with an amplitude of 1 m and a range of wave periods, 5.5-13.5 s, and directions, 0-27.5 degrees. Only the highest loads were shown, with the surge and yaw loads presented separately for the head-on and off-angle wave results, respectively. Results were also presented for damping levels where the power capture and the ratio of power capture to foundation loads were individually maximised.

Surge results were generally similar for the Modular and Rigid Flaps, with -4-+2 % mean relative differences. There were, however, significant reductions in the surge loads for both devices when the power capture to load ratio was maximised, instead of just the power capture. For the Modular Flap, for example, the mean reduction was 36 %.

The comparison of the yaw loads acting on the two devices was shown to be heavily dependent on the damping strategy employed. This was because the yaw loads acting on the Modular Flap were highly sensitive to the damping level, whereas this was not the case for the Rigid Flap. This meant that, for the maximum power damping case, the yaw loads on the Modular Flap were, on average, 10 % higher. This was likely caused by the outer modules being over-damped. In contrast, for the maximum power capture to loads ratio damping, the loads were 26 % lower for the Modular Flap. This was explained by the higher material flexibility of the system due to the independence of the modules.

# 8. Discussion

## 8.1 Introduction

This chapter provides a discussion of the key results and the impact of the work in the wider context. The majority of results were from testing in regular head-on waves of varying period and off-angle waves up to a direction of 27.5 degrees and hence this discussion focuses on these results.

In sections 8.2 and 8.3, the key power capture and foundation load results, respectively, are first discussed. Section 8.4 then uses these results to estimate the economy of the power production of the modular and rigid devices using different damping strategies.

## 8.2 Power Capture

### 8.2.1 Module Results

The key result related to the power capture of the flap modules that made up the Modular Flap was the increase in power towards the centre of the device, as shown in section 6.2. It was shown that, on average, for regular head-on waves, the central modules produced 68 %, the inner modules 25 % and the outer modules only 7 % of the total power. This was using a damping strategy whereby the modules had the same achievable damping level applied to them. This meant that the outer modules were often damped to a level that was equal to the wave excitation torque acting on them. This resulted in them having negligible angular velocity and hence producing the equivalent level of power capture. Using this damping strategy, the outer modules were therefore individually contributing very little to the device power capture. However, their presence likely enhanced the power capture of the device through funnelling of the waves to the central modules. Hence, if this damping strategy is applied, for sites with low wave directional variation, it may be more economical to remove the PTO from the outer modules. However, if this results in a

significant reduction in wave torque for the central modules, it may be better to completely replace the outer modules with rigid structures, if the loading on them is not too significant in extreme waves. On the other hand, where the damping level applied to each module can vary, as in previous analytical work, the outer modules may make a notable contribution to the device power capture (Sarkar, Doherty and Dias, 2016). This could result in the Modular Flap closing the gap with, or even outperforming the Rigid Flap, for example by inducing the resonant behaviour shown in other works (Dias, F. and Sammarco, 2013; Sammarco, Michele and D'Errico, 2013; Sarkar, Doherty and Dias, 2016).

Variation in the damping torque requirements across the modular device in this work suggests that it could be more economical to vary the rating of the module PTOs. This is because the cost of a PTO is approximately linearly proportional to its rating and hence cost savings may be made by lowering the ratings of the modules with lower torque requirements (Murtagh, C. and Walsh, 2015). However, specifying each module with a different PTO rating could increase the costs of design and assembly, due to the heightened complexity. Furthermore, modular devices of different geometries or with different applied damping strategies may have constituent modules with lower variation in their damping torque requirements and hence PTO ratings.

### 8.2.2 Device Results

#### 8.2.2.1 Head-On Waves

In section 6.3.2, it was shown that in head-on waves, the mean relative difference in power capture between the Modular and Rigid Flaps, was -3 %, with an expanded combined uncertainty of +/-5 %. It was hence shown that there was no statistically significant difference between the power capture of the two devices. This finding was derived from testing in wave conditions with energy levels typical of common sea states for wave power production. For larger waves, non-linearities may have occurred, such as angular differences

between the modules increasing, resulting in potentially disproportionately lower efficiency for the Modular Flap. Testing was, in fact, carried out by the author to investigate this. The results have not been shown, to keep the work focused on common wave conditions. However, it is useful to know that at the largest wave amplitude that was tested in, 2 m at a period of 8.5 s, the reduction in power production by the Modular Flap was increased. However, the reduction only rose from 7 % at 1 m amplitude to 10 %. Hence, while the relationship was non-linear, the Modular Flap maintained comparable power capture.

The flap-type WEC is one of the most efficient devices at converting incident wave power into mechanical power (Babarit *et al.*, 2012; Babarit, 2015). Hence, the similar power capture between the rigid and modular devices shown in these results shows that adoption of a modular form to a flap-type WEC would likely not jeopardise one of the key advantages of the flap-type concept.

The power capture comparison of the modular and rigid devices in head-on waves was carried out using a damping strategy whereby each module had the same achievable torque applied by its PTO. The results in previous analytical work, where this strategy was applied, were similar, with the two devices achieving comparable power capture across the same wave period range as used in this thesis (Sarkar, Doherty and Dias, 2016). However, this analytical work also investigated the effects of applying a damping strategy whereby each module was damped differently, using a genetic algorithm to determine the optimum damping coefficients. The result of using this strategy was that the modular device experienced multiple resonances, allowing it to produce greater power than the rigid device at high wave periods (Sarkar, Doherty and Dias, 2016). Hence, the work in this thesis, testing in a real, viscous fluid, partly validates this analytical work and lays the foundation for further physical modelling of the modular device with different damping strategies, discussed in Chapter 9.

In fact, the work in this thesis has already eluded to the dependency of the modular device on the damping strategy through presentation of the correlation of reduction in power capture, compared to the rigid device, and the variation in angular velocity of the flap modules. This suggested that decreasing the power reduction, compared to the Rigid Flap, is achieved by minimising the gaps that open between the modules. This could be achieved by applying different damping levels to each module.

Finally, in section 6.4, the power capture of the Modular Flap was shown to be, on average, 23 % smoother than for the Rigid Flap. This is an advantage for the Modular Flap as smoother, i.e. less variable, power production reduces cost requirements for energy storage for achieving electrical grid compliance (Molinas, Sorby and Lundberg, 2007).

#### 8.2.2.2 Off-Angle Waves

In previous work, it was shown that the power capture of a rigid flap-type WEC was sensitive to the direction of a wave. The typical minimum rate of power-capture reduction was equal to the cosine squared of the wave direction angle (Henry, 2008). Although for sites with low wave directionality this sensitivity is a minor issue, other sites have their energy spread well across the wave direction range (Wilkinson *et al.*, 2014). Hence, to increase the number of viable sites for flap-type WECs, it is desirable to reduce the sensitivity of the power capture of the device to the wave direction.

Work in this thesis has, for the first time, compared the power capture of a modular device to a rigid one in off-angle waves. The results in section 6.3.4 suggested that adoption of the modular form could reduce the sensitivity of the flap-type device because it was shown that the rate of power capture reduction was lower for the Modular Flap than the Rigid Flap. By the largest angle, 27.5 degrees, the former outperformed the latter by 10 %, with +/-1 % uncertainty. Gains like this would mitigate any reduction in power capture experienced by the Modular Flap in head-on waves.

## 8.3 Foundation Loads

Chapter 7 presented the key foundation load results for the six-module Modular Flap and compared them to the Rigid Flap. The surge loads were presented for the head-on waves and the yaw loads for the off-angle waves.

It was shown that there was no significant difference in the surge loads acting on the two devices. However, the surge load is the driving force for power production and so, given the similar power capture of the two devices, this result was expected.

No power production is gained due to the yaw load and it can therefore be seen as 'parasitic'. It was hence an important result that there were significant differences in the yaw loads experienced by the two devices. These differences were a function of both the wave direction angle and the applied damping strategy.

For the case where damping was applied to maximise the power capture, the Modular Flap, on average, experienced 10 % higher loads. As was mentioned, this was likely caused by overdamping the outer modules as they had the greatest lever arm. The maximum damping torque applied to the outer modules could be set lower than the levels of the inner modules, for example. This would likely lower the yaw load acting on the device. This highlights the point that the application of a modular system allows some degree of load control through the use of an advanced PTO damping strategy. Similar to numerical work, an optimisation function could be used to control the damping on the modules to maximise the ratio of power capture to foundation loads (Sarkar et al. 2016).

The opportunity for load reduction through control of the damping of the modular system was shown in the results where the damping was applied to maximise the ratio of power capture to foundation loads. Here, the Modular Flap, on average, experienced 26 % lower loads than the Rigid Flap. This was because the Modular Flap was more responsive in terms of having reduced yaw

loads when the applied damping was lowered. If this decrease in loads resulted in a reduction in the material requirements of the foundation of a flap-type device, there would be cost saving.

## 8.4 Value of Power

The aim of this section is to provide an evaluation of the 'value' of the power capture production of the devices. As touched upon in section 7.1, this is defined in this thesis as the ratio of device mean power capture to a cost metric, the foundation loads. As also discussed, this cost metric does not account for other costs such as machining and operations and maintenance, but effectively captures the interdependency of power production and foundation loads.

This section elaborates on this approach by quantifying these ratios for the devices under various wave and damping torque conditions. In doing so, the section brings together some of the key results from Chapters 6 and 7, the device mean power captures and the surge and yaw foundation effective load ranges, respectively. The wave conditions of interest were the regular head-on and off-angle waves.

This analysis is helpful because results were presented previously as independent results, for different damping strategies. By quantifying the value of power ratios, however, this instead provides a general picture.

The analysis was carried out by calculating the values of power for the surge and yaw foundation loads, $V_{Su}$ and $V_Y$ as presented in Equation 59 (repeat of Equation 58 for ease of access) and Equation 60, respectively.

$$V_{Su} = \frac{\bar{P}_T}{Su_{ELR}} \qquad \text{Equation 59}$$

$$V_Y = \frac{\bar{P}_T}{Y_{ELR}} \qquad \text{Equation 60}$$

Where, for a given damping level, $\bar{P}_T$ was the device mean power capture and $Su_{ELR}$ and $Y_{ELR}$ were the surge and yaw Effective Load Ranges, respectively.

The $V_{Su}$ and $V_Y$ results were generated for each damping level for each of the wave conditions of interest. Results were calculated for both cases of maximising the value and, the benchmark case, of maximising power capture.

As with the foundation load results in Chapter 7, the surge loads were analysed for the head-on waves and the yaw loads for the off-angle waves. Presented first, in Figure 118, are the value of powers using the surge loads, $V_{Su}$, for the head-on waves.

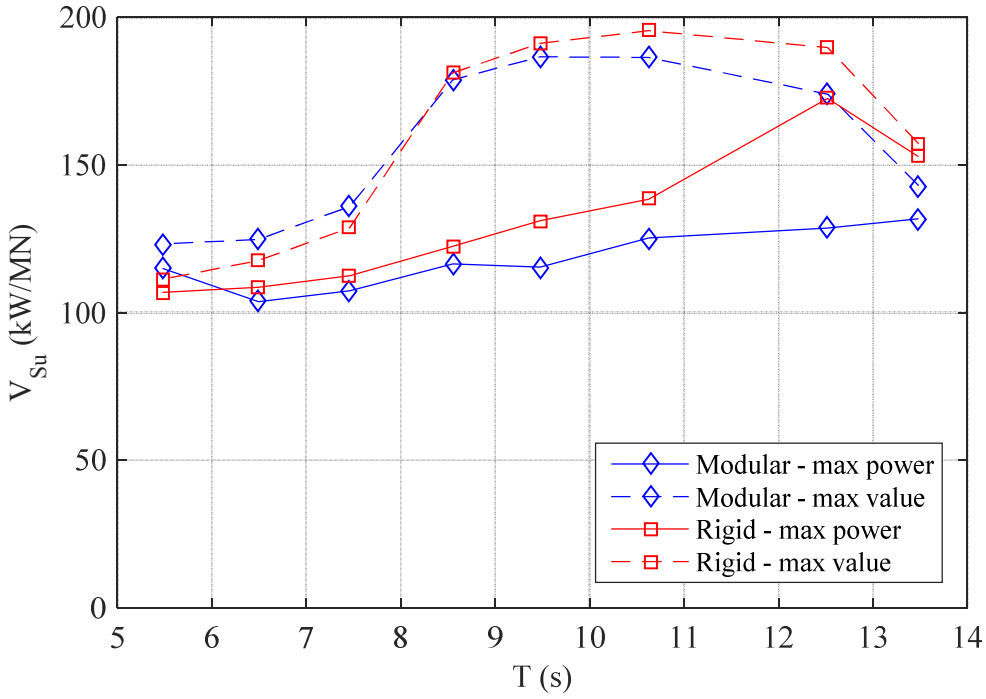


**Figure 118. Value of power using surge foundation loads, $V_{Su}$, against wave period, $T$, for different device configurations and damping strategies. The waves were regular, with an amplitude of 1 m and a direction of 0 degrees.**

Figure 118 shows that there was not a significant difference in the value of power results between the devices for the head-on waves. This is because the same was shown for the power captures and surge foundation loads in Chapters 6 and 7, respectively. Using the 'max power' results, the mean relative difference between the devices was –8 %, showing that the Modular Flap had a

slightly lower economy of power capture; using the 'max value' results, however, the mean relative difference was –0.4 %.

The significant differences in the results, however, were between the 'max value' and 'max power' datasets. For both devices, there were significant increases in the value of power results for the former damping strategy. The mean relative difference between the datasets, using the Modular Flap results and the 'max power' results as the reference, was +33 %, indicating a markedly improved economy of power capture, using this simplified analysis.

The same analysis was carried out for the off-angle waves, using the yaw foundation loads as the cost metric, with the results shown in Figure 119.

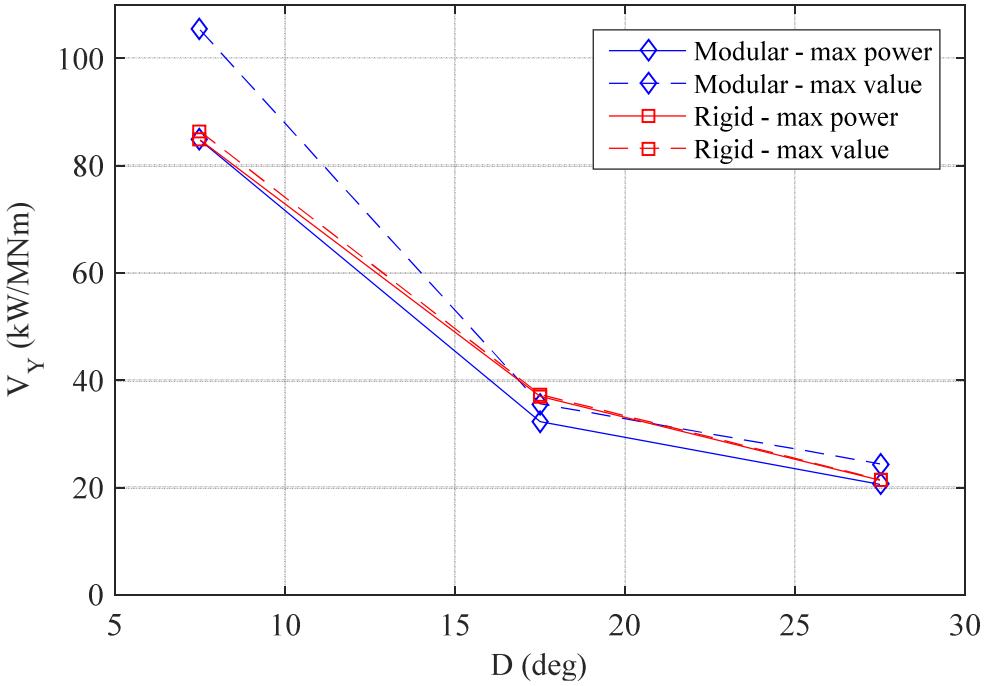


**Figure 119. Value of power using yaw foundation loads, $V_Y$, against wave direction, $D$, for different device configurations and damping strategies. The waves were regular, with a period of 8.5 s and an amplitude of 1 m.**

Figure 119 shows that, as the wave direction increased, the value of power rapidly reduced. This was as a result of the simultaneous reduction in power-capture and increase in yaw foundation loads. What is also shown is that there were lower relative differences in the value of power results between the devices and damping strategies across the wave directions. Using the same

analysis as used for the head-on waves, the mean relative differences between the devices and damping strategies were –6 % and +18 %, respectively. Interestingly, the mean relative difference between the ‘max value’ results was +10 %, indicating an improved power production per foundation load for the Modular Flap using this damping strategy.

# 9. Further Work

The physical model, the modelling methodology and the subsequent data analysis techniques were robust and generally yielded results with acceptable levels of uncertainty. However, although they do not severely undermine the presented results, the work had several limitations. These are summarised in this chapter and were related to the model design, employed methodology and the testing program used. The chapter also suggests further work to both address these limitations and expand the research, for example with numerical modelling and carrying out economic assessments.

For the physical model design, it is believed that the most significant limitation was the way in which the modules were fastened to the base structure. Applying bolts from underneath the model was practical for attaching the module plates to the housings. However, for attaching the modules to the cross-beam on the base structure, this proved to be inconvenient. An alternative solution would have been to have the bolts coming from the top, with threaded holes in the cross-beam instead of the housings. Although it may not be viable to alter the design now, this limitation should be noted for design of further physical models.

The primary limitation in the methodology was related to the measurement of the foundation loads. As discussed in section 4.2.5, for an unknown reason, the heave signal on the AMTI 2000B load cell did not record during the testing campaign. While this had little effect on the degrees of freedom of primary interest in this study, surge and yaw, it meant that the heave and roll loads could not be measured with confidence. Hence, in further work, the issue with the AMTI load cell should be resolved.

Due to time limitations, the uncertainty limits were also not evaluated for the foundation loads. Based on the maximum mean calibration error of 0.7 %, shown in Table 8, however, it is likely that the uncertainty limits of the

foundation loads will have been acceptable. However, further work should assess the uncertainties to make the analysis more robust.

The testing program was partly limited through the range of waves that it used. The majority of the waves were regular and head-on. This is a necessary first step for the assessment of a new concept like the modular flap-type WEC. However, the practical significance of the results was limited by the number of irregular sea states, which are more realistic than regular waves, that were used.

Equally so, the limitation in the maximum wave direction angle, 27.5 degrees, potentially capped the benefits of the application of the modular form that could be shown. Hence, the level of wave directionality should also be increased. This should be firstly for uni-directional waves, increasing the range and number of directions to levels present at sites of interest for development (Subsea World News, 2012; Wilkinson *et al.*, 2014). Beyond this, multi-directional waves should be employed, which would assess the impact of employing the modular design in non-uniform pressure.

A final point related to the wave conditions is that the irregular waves that are tested in should be assigned occurrences for several sites of interest for wave energy deployment. Use of these conditions would allow accurate assessment of the annual energy production of the modular device (Babarit *et al.*, 2012).

The damping strategy employed in the test program was also limited. The simplest strategy, of setting the achievable damping to be equal on each module, was employed. This was essential for the first assessment of the modular concept. However, literature has shown that enhanced power production for a modular system, relative to a rigid one, can only be achieved by applying different damping to each module, resulting in resonant behaviour (Sarkar, Doherty and Dias, 2016). Hence, further physical modelling should also vary the damping levels, partly to see if the resonant behaviour occurs in real, viscous fluid. This would also complement physical modelling that did

show this behaviour but for an undamped, continuous flap-type device (Mei *et al.*, 1994; Dias, F. and Sammarco, 2013). The damping type that was applied was also limited to Coulomb damping and hence further physical modelling should use other types, such as linear and quadratic. This is especially true given the high level of controllability of the physical model developed for this thesis.

Beyond addressing the highlighted physical modelling limitations, there is scope for further work using numerical modelling. During this project, a numerical model was developed for the modular flap, based on previous array work (Folley, 2007; Wilkinson *et al.*, 2015). Due to time restraints, this model was not used for this thesis. However, there is huge potential for development, calibration, validation and application of this model. A component that could also be developed is one that would allow prediction of foundation loads. Further work could also be carried out to improve the capability of the model to better account for viscous effects (Crooks, 2016). For reference, brief information on the existing model is provided in the appendix in section 15.1.

Once validated, the numerical model could be used to relatively quickly explore the modular flap design space. Devices of different total widths, made up of varying numbers of modules, could be studied to determine the optimum configuration for a wave site. An example configuration of interest could be a very wide device, for example 100 m in width, as shown in Figure 120. If the gaps between devices were relatively small, such as 20 m, this would result in increased packing density and power capacity per wave farm. Through economies of scale, this could increase the economic viability of the flap-type device significantly. It would achieve this by sharing costs, such as site consenting and maintenance vessel hire, over a larger power output. Such continuous devices could also be used as sea defences, as used in the Venice Lagoon flap barrier (Windsor, 2015b).

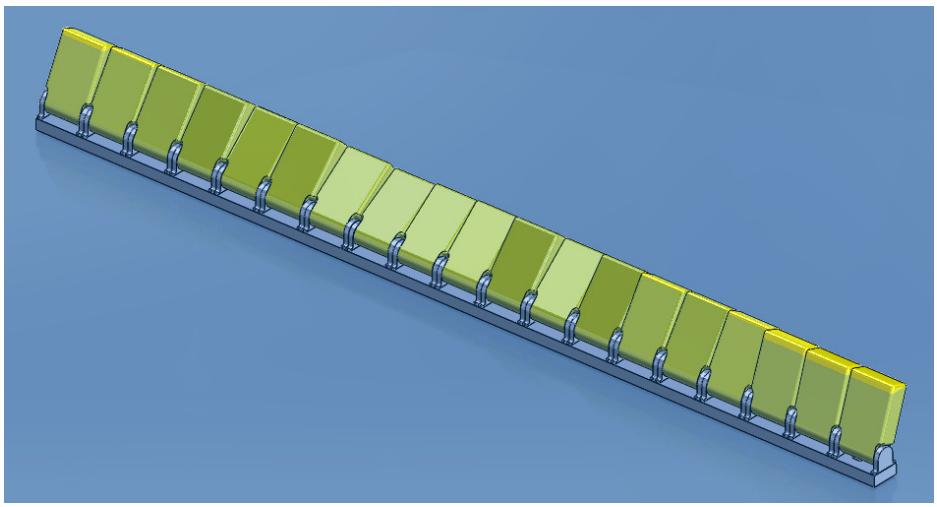

**Figure 120. Approximately 100 m wide modular flap-type WEC.**

If using numerical or physical modelling, the cost of the energy production of a modular flap-type WEC should be assessed. The costs should include reasonably accurate estimates for capital and operations and maintenance expenditure. This would address the limitations of the cost metric used in this thesis, the foundation loads, as discussed in section 8.4. Cost evaluation would allow estimation of the industry standard levelised cost of energy (de Andres *et al.*, 2016). This would allow comparison of the modular flap-type WEC with other energy sources and hence determination of economic viability. This would permit one to ascertain if the device was a viable concept for developing to prototype scale and beyond.

# 10. Conclusions

This thesis presents an assessment of a nearshore modular flap-type WEC. Comparisons were made to an equivalent width rigid device. All quoted relative differences between the device results use the rigid flap as the reference point. The variables that were evaluated were the power capture and surge and yaw foundation loads. The power capture was evaluated at both module and device level, while the foundation loads were evaluated only at device level. The assessment was carried out through testing of a $30^{th}$ scale physical model in the QUB Portaferry Wave Tank. The primary outputs from this research have been the production of the physical model and the insights provided by the testing results.

The physical model consisted of six flap modules, mounted on a common base structure. The total width of the model was approximately 33 m at full scale. Testing of the rigid device was allowed by connection of the modules. The primary research advancement related to the physical model was in the design of the flap modules. For each unit, a highly controllable and compact Coulomb damping PTO system was developed. The system consisted of a magnetic particle brake housed in a waterproof box. Damping torque was then transferred from the brake to the module hinge via an air gap between magnetic couplings. The use of magnetic couplings minimised additional parasitic losses due to friction and significantly increased durability, compared to shaft seals. The damping was controlled using a multi-port power supply and software program. This allowed the damping to be controlled to such a degree that, when using the rigid device, the mean difference in the root-mean-square torques applied to the modules was only 3 % across the test range. This meant that the desired simplest damping strategy could be applied, which was to set the achievable damping level on each module to be the same.

The model was used to generate results for an initial assessment of the viability of the modular flap-type WEC. The model configurations were tested at a depth of 14 m at full scale. Testing was in a range of conditions, primarily

consisting of regular waves, with energy levels typical of commonly occurring conditions at sites of development interest. The variables of the regular waves were the wave period and direction, using full scale ranges of 5.5-13.5 s and 0-27.5 degrees, respectively. The 0-degree waves are referred to as 'head-on', while the set of conditions where the direction angle varied was called 'off-angle'. The wave amplitude was held constant at 1 m at full scale.

The head-on wave results showed that the power capture increased significantly moving from the outer to the central modules. On average, the central pair of modules produced 68 % of the total mean power, the inner modules 25 % and the outer modules only 7 %. The significantly reduced power capture by the outer modules was explained by their lower experienced wave excitation torque and, as a result, them being overdamped. This suggested that, for sites with low wave directional variation, it may be more economical to not use PTOs in the outer modules, thus reducing the overall cost of the device.

The device power captures were assessed using the standard metric, the capture factor, which is the ratio of generated to available power. The results were presented with and without weighting applied to account for the wave power available in the sea states. The uncertainty on the results was also assessed, to determine the statistical significance of the results.

For the head-on waves, without weighting, the mean relative difference in capture factors was –3 %, with uncertainty of +/-5; with weighting, the mean relative difference was -4 %, with uncertainty of +/-4 %. The slight consistent reduction in power capture for the modular device could be explained by a lower wave excitation torque acting on it. Nevertheless, these results showed that there was no statistically significant mean relative difference in power capture between the devices. This indicates that adoption of the modular form would not compromise the high conversion efficiency of the flap-type WEC in head-on waves.

For the off-angle waves, the mean relative difference in capture factors was -3 %, with +/-4 % uncertainty, for both the unweighted and weighted cases. Thus, again there was no statistically significant change in power capture by adopting the modular form. However, the rate of power reduction with wave direction angle was lower for the modular device than for the rigid device. This meant that, for the largest wave direction of 27.5 degrees, the modular device outperformed the rigid flap by 9-10 %, depending on the weighting, with uncertainty of +/-1 %. This suggests that a modular flap-type WEC could outperform a rigid device in sites with large wave directional variation.

A further difference between the power capture of the two devices was in the variation of the instantaneous results. Due to phase differences in the power produced by each module, the total power capture of the modular device was shown to be smoother. For the head-on waves, it was on average 23 % smoother. This is an advantage for the modular device as less variable power production offers the opportunity to reduce the costs associated with energy storage required for achieving electrical grid compliance.

A strong correlation between the foundation loads acting on the devices and the applied PTO damping torque was found. The foundation loads were hence assessed for the damping levels that resulted in the maximising of the power capture and the ratio of power capture to foundation loads. The surge and yaw foundation loads were assessed for the head-on and off-angle waves, respectively. The surge foundation loads were shown to be very similar for the two devices, with the mean relative difference being +2/-4 % depending on damping strategy. However, significant differences in the yaw foundation load were found for the devices. The yaw loading on the modular device was found to be highly dependent on the magnitude of the total PTO damping applied to it. Using damping where the power capture was maximised, the yaw loads were increased by a mean of 10 % compared to the rigid flap. This suggests that the outer modules were overdamped and hence the issue may be resolved through more sophisticated damper control. Using damping where the power to

foundation loads ratio was instead maximised, however, the modular yaw load was 26 % lower. This reduction was explained by the higher mechanical flexibility of the modular device and could represent significant opportunities for structural cost savings.

Finally, the economy of the power production was estimated using the ratio of device mean power capture to a cost metric, the foundation loads. This hence expanded the analysis carried out solely for the foundation loads. Using the foundation loads to represent device cost neglected non-linearities in their relationship with capital costs and ignored other device expenses, such as for operations and maintenance. However, it effectively demonstrated the interdependency of power production and foundation loads for the devices. Again, the results were generated for the cases of maximising power capture and the ratio of power to loads.

The mean relative differences in the economy of power production were found to be small between the devices across the wave conditions. In the head-on waves, the differences were between –8 and –0.4 %, depending on damping strategy, indicating a slight reduction in economy for the modular flap; in the off-angle waves, the differences were between –6 and +10 %. For both sets of wave conditions, the modular flap performed better when the damping was set to maximise the ratio of power capture to foundation loads, most apparent in the off-angle waves.

This assessment has shown that some benefits can be achieved through adoption of the modular WEC system, notably in improved power capture and reduced yaw foundation loads in off-angle waves. However, overall the differences in the economy of the power capture between the two devices, in waves of small-medium directional ranges, were relatively low. Given the high power capture efficiency, nearshore location, simple mode of operation and high survivability of the flap-type WEC, this shows though that the modular device is a viable stand-alone concept. Clear advancements for the flap-type concept could be seen in waves of higher directionality and using different

damping on modules. There may also be cost savings for manufacture, transport and installation using a modular system. It may, on the other hand, be that the greater complexity and likely higher maintenance costs of the modular device make it a less attractive option for the geometry of device considered in this thesis. There may, however, be economies of scale achieved by increasing the power rating of each machine, as has occurred in offshore wind, by expanding the width of a flap-type device, also using wider flap modules. This work has indicated that the susceptibility to power reduction and increased yaw loads in off-angle waves for devices of greater width would be lessened by an appropriately damped modular device.

Given the results shown and discussions presented, there is large scope for further work. One effort should increase the ranges of irregular and directional waves that the modular flap is tested in. This would allow the estimation of annual energy productions for a range of viable wave energy sites. The effect of applying different damping strategies and types, such as linear and quadratic, on the power capture and foundation loads of a modular flap should be assessed. This will allow one to determine if the device can produce greater power capture than the rigid device in head-on waves through more sophisticated PTO control. It could also allow the shedding of yaw loads by reducing the damping on the outer modules. Finally, the design space for the modular flap should be explored, ideally through the use of a numerical model for fast assessment. This model should include estimates for the life-time cost of energy production of the system. This would allow the viability of the concept to be shown, before prototype development is commenced.

# 11. References

van 't Hoff, J. (2009) *Hydrodynamic Modelling of the Oscillating Wave Surge Converter - PhD thesis*. The Queen's University of Belfast.

Aalborg University (2013) 'Exercise 1: Hands-on experimental work with point absorbers - handout for Modelling & Control of Wave Energy Converters PhD Course 2013'. Aalborg, Denmark.

Abadie, T. & Dias, F. (2016) 'Numerical Study of Wave Interaction with a Modular Oscillating Wave Surge Converter', in *Proceedings of the Twenty-sixth International Ocean and Polar Engineering Conference*. Rhodes, Greece.

Adamo, A. and Mei, C. (2005) 'Linear response of Venice storm gates to incident waves', *Proceedings of the Royal Society A: Mathematical, Physical and Engineering Sciences*, 461(2058), pp. 1711–1734. doi: 10.1098/rspa.2004.1432.

Advanced Mechanical Technology Inc (2011) 'SP2.5D General Transducer Outline Drawing 13I-33186, located on Queen's University Belfast server'. Watertown.

Advanced Mechanical Technology Inc (2012) *Transducer Instructions Single Element Multi-Component Transducer Model: SP2.5D-XX, located on Queen's University Belfast server*. Watertown, Massachusetts.

Álvarez (2015) *Evaluation of Concepts to Reduce Structural Loading on The Wave Energy Converter Oyster, Masters Thesis*. Technical University of Hamburg-Harburg.

de Andres, A., Maillet, J., Todalshaug, J. H., Moller, P., Bould, D. and Jeffrey, H. (2016) 'Techno-economic related metrics for a wave energy converters feasibility assessment', *Sustainability (Switzerland)*, 8(11). doi: 10.3390/su8111109.

Aquamarine Power Ltd (2009) *Oyster generates £1m for Orkney economy*.

Available at: http://www.aquamarinepower.com/news/oyster-generates-£1m-for-orkney-economy.aspx (Accessed: 18 July 2016).

Aquamarine Power Ltd (2011) '110721 EMEC Directional Occurrence Matrices APL-RD.RA.05-CAL-0010 A4 - interal Aquamarine Power Ltd Excel spreadsheet'.

Aquamarine Power Ltd (2012) '120814 Lewis - Level B - Met Ocean - A9 - internal Aquamarine Power Ltd Excel spreadsheet'.

AW-Energy (2012) *WaveRoller Concept*. Available at: http://aw-energy.com/about-waveroller/waveroller-concept (Accessed: 18 July 2016).

AW-Energy (2015) *Home*. Available at: http://aw-energy.com/ (Accessed: 5 October 2016).

Azo Materials (2001) *Stainless Steel - Grade 316 (UNS S31600)*. Available at: https://www.azom.com/properties.aspx?ArticleID=863 (Accessed: 26 February 2018).

AZO Materials (2017) *Stainless Steel - Grade 304 (UNS S30400)*. Available at: http://www.azom.com/properties.aspx?ArticleID=965 (Accessed: 30 April 2017).

Babarit, A. (2015) 'A database of capture width ratio of wave energy converters', *Renewable Energy*. Elsevier Ltd, 80, pp. 610–628. doi: 10.1016/j.renene.2015.02.049.

Babarit, A., Hals, J., Muliawan, M., Kurniawan, A., Moan, T. and Krokstad, J. (2012) 'Numerical benchmarking study of a selection of wave energy converters', *Renewable Energy*, 41, pp. 44–63. doi: 10.1016/j.renene.2011.10.002.

Banks, D. and van 't Hoff, J. (2013) 'The Development of an Experimental Force Feedback Dynamometer to Investigate the Real Time Control of an Oscillating Wave Surge Converter', in *32nd International Conference on*

*Ocean, Offshore and Arctic Engineering*. Nantes, France.

Bourdier, S., Abdulla, K., Henry, A. and Whittaker, T. (2013) 'Derivation of Wave Loads for the Design of Oscillating Wave Surge Converters', in *Proceedings of the Tenth European Wave and Tidal Energy Conference*. Aalborg, Denmark.

Brown, A and Paasch, R. (2014) 'Fatigue Life Distribution for a Simple Wave Energy Converter', in *Proceedings of the Second Marine Energy Technology Symposium*. Seattle, United States of America.

Budar, K. and Falnes, J. (1975) 'A resonant point absorber of ocean-wave power', *Nature*, 256, pp. 478–479.

Child, B. (2011) *On the configuration of arrays of floating wave energy converters - PhD thesis*. The University of Edinburgh. Available at: http://hdl.handle.net/1842/5792.

Clabby, D. and Lamont-Kane, P. (2013) 'spectrum_from_trace_PLK - Queen's University Belfast internal MATLAB script'. Belfast.

Clabby, D. (2012) 'Jonswap_Tm - Queen's University Belfast internal MATLAB script'. Belfast.

Clabby, D. (2013) *Wave Energy Conversion at Prototype and Model Scales - PhD thesis*. Queen's University Belfast.

Clabby, D. (2014) *130822 Sea Calibration using Spectral Amplitude & Phase Control - APL-RD.FDR.03-MAN-0003, internal document*. Belfast.

Clabby, D., Henry, A., Folley, M. and Whittaker, T. (2012) 'The Effect of the Spectral Distribution of Wave Energy on the Performance of a Bottom Hinged Flap Type Wave Energy Converter', in *Proceedings of the ASME 2012 31st International Conference on Ocean, Offshore and Arctic Engineering*. Rio de Janeiro, Brazil.

Coastal Wiki (2008) *Wave transformation*. Available at: http://www.coastalwiki.org/wiki/Wave_transformation (Accessed: 17 April 2017).

Coleman, H. and Steele, W. (2009) *Experimentation, Validation, and Uncertainty Analysis for Engineers*. John Wiley & Sons.

Crooks, D. (2016) *Nonlinear Hydrodynamic Modelling of an Oscillating Wave Surge Converter - PhD thesis*. Queen's University Belfast.

Crooks, D., Whittaker, T., Hoff, J. van't and Cummins, C. (2014) 'Experimental validation of numerically generated wave excitation torque on an OWSC', in *1st International Conference on Renewable Energies Offshore*. Lisbon, Portugal.

Day, A. H., Babarit, A., Fontaine, A., He, Y. P., Kraskowski, M., Murai, M., Penesis, I., Salvatore, F. and Shin, H. K. (2015) 'Hydrodynamic modelling of marine renewable energy devices: A state of the art review', *Ocean Engineering*, 108, pp. 46–69. doi: 10.1016/j.oceaneng.2015.05.036.

Dias, F. and Sammarco, P. (2013) *A Review of All Research Done on Modular Flap Structures, report commissioned by Aquamarine Power Ltd*. Gentilly, France.

Doherty, K. (2013) 'Personal communication with Aquamarine Power Ltd colleague.' Belfast.

Edinburgh Designs Ltd (2016a) *Piston Coastal Wave Generators*. Available at: http://www.edesign.co.uk/product/piston-wave-generators/ (Accessed: 17 October 2016).

Edinburgh Designs Ltd (2016b) *Wave Gauges*. Available at: http://www.edesign.co.uk/product/wavegauges/ (Accessed: 19 October 2016).

eFunda (2017) *Square Channel*. Available at: http://www.efunda.com/designstandards/beams/SquareChannel.cfm (Accessed:

30 April 2017).

European Commission (2016a) *2050 Energy strategy*. Available at: http://ec.europa.eu/energy/en/topics/energy-strategy/2050-energy-strategy (Accessed: 19 September 2016).

European Commission (2016b) *2050 low-carbon economy*. Available at: http://ec.europa.eu/clima/policies/strategies/2050/index_en.htm (Accessed: 19 September 2016).

European Marine Energy Centre (2009) *Tank Testing of Wave Energy Conversion Systems*. Available at: http://www.emec.org.uk/tank-testing-of-wave-energy-conversion-systems/.

European Marine Energy Centre (2016a) *Marine Energy*. Available at: http://www.emec.org.uk/marine-energy/ (Accessed: 19 September 2016).

European Marine Energy Centre (2016b) *Wave Devices*. Available at: http://www.emec.org.uk/marine-energy/wave-devices/ (Accessed: 19 September 2016).

Falcão, A. (2014) 'Modelling of oscillating-water-column wave energy converters', in. Available at: https://fenix.tecnico.ulisboa.pt/downloadFile/3779580627113/Chapter 4 2014.pdf.

Falcão, A. F. O. and Henriques, J. C. C. (2016) 'Oscillating-water-column wave energy converters and air turbines: A review', *Renewable Energy*, 85(January), pp. 1391–1424. doi: 10.1016/j.renene.2015.07.086.

Falnes, J. (2014) *Ocean Waves and Oscillating Systems*. Cambridge University Press. doi: 10.1007/s13398-014-0173-7.2.

Folley, M. (2007) *Numerical Modelling of Oyster Clusters - internal Queen's University Belfast report*. doi: 10.1002/ejoc.201200111.

Folley, M. (2010) *Physical model testing of OWCs - internal Queen's University Belfast report*.

Folley, M., Clabby, D. and Crooks, D. (2015) 'threeproberef_DJC- Queen's University Belfast internal MATLAB script'. Belfast.

Folley, M., Whittaker, T. W. T. and van't Hoff, J. (2007) 'The design of small seabed-mounted bottom-hinged wave energy converters', in *Proceedings of the 7th European Wave and Tidal Energy Conference*. Porto, Lisbon.

fugro (2011) *Successful completion of the Oyster 2 foundations*. Available at: http://www.seacore.com/News/archivenews2011/Excalibur (Accessed: 28 September 2016).

Gill Sensors and Controls (2016) *1498 Blade 360 Rotary Position Sensor*. Available at: https://www.gillsc.com/products/position-sensors/1498-blade-360/ (Accessed: 8 July 2016).

Gill Sensors and Controls Ltd (2015) 'Blade360 Rotary Non-Contact Position Sensor Datasheet'. Available at: https://www.gillsc.com/products/position-sensors/1498-rotary-position-sensor/.

Gunn, K. and Stock-Williams, C. (2012) 'Quantifying the Potential Global Market for Wave Power', in *Proceedings of the 4th International Conference on Ocean Engineering*. Dublin, Ireland.

Heller, V. (2012) *Model-Prototype Similarity*. Available at: http://www.drvalentinheller.com/Dr Valentin Heller_files/Heller_Model-Prototype Similarity.pdf (Accessed: 4 February 2017).

Henry, A. (2008) *The hydrodynamics of small seabed mounted bottom hinged wave energy converters in shallow water - PhD thesis*. Queen's University Belfast.

Henry, A., Rafiee, A., Schmitt, P., Dias, F. and Whittaker, T. (2014) 'The Characteristics of Wave Impacts on an Oscillating Wave Surge Converter',

*Journal of Ocean and Wind Energy*, 1(2), pp. 101–110. doi: 10.1115/OMAE2013-10189.

Henry et al. (2010) 'Advances in the Design of the Oyster Wave Energy Converter', in *Royal Institution of Naval Architect's Marine and Offshore Renewable Energy Conference*.

Herbers, T. H. C., Elgar, S. and Guza, R. T. (1999) 'Directional spreading of waves in the nearshore zone', *Journal of Geophysical Research*, 104, pp. 7683–7693. doi: 10.1029/1998JC900092.

Hiles, C. E., Beatty, S. J. and de Andres, A. (2016) 'Wave Energy Converter Annual Energy Production Uncertainty Using Simulations', *Journal of Marine Science and Engineering*, 4(3), p. 53. doi: 10.3390/jmse4030053.

Howard, D., Whittaker, T. and Doherty, K. (2009) 'Foundation load analysis of Oyster ® using a five degree of freedom load transducer', in *Proceedings of the 8th European Wave and Tidal Energy Conference, Uppsala, Sweden*.

Hydroworld (2015) *Aquamarine Power, MHK energy developer, falls into administration*. Available at: http://www.hydroworld.com/articles/2015/10/aquamarine-power-mhk-energy-developer-falls-into-administration.html (Accessed: 30 September 2016).

IBD Wickeltechnik GmbH (no date) *Electromagnetic powder brakes/clutches*. Available at: http://www.ibd-wt.de/en/products/brakes/electromaganetic-powder-brakes.html (Accessed: 18 March 2018).

Institute for Fluid Power Drives and Controls (2016) *Home*. Available at: http://www.ifas.rwth-aachen.de/html/00_general/main.php?lang=en (Accessed: 21 October 2016).

Intergovernmental Panel on Climate Change (2013a) *Climate Change 2013: The Physical Science Basis. Contribution of Working Group I to the Fifth Assessment Report of the Intergovernmental Panel on Climate Change*,

*Intergovernmental Panel on Climate Change, Working Group I Contribution to the IPCC Fifth Assessment Report (AR5)(Cambridge Univ Press, New York)*. doi: 10.1029/2000JD000115.

Intergovernmental Panel on Climate Change (2013b) *Climate Change 2013: The Physical Science Basis. Contribution of Working Group I to the Fifth Assessment Report of the Intergovernmental Panel on Climate Change Technical Summary*. doi: 10.1017/ CBO9781107415324.005.

International Energy Agency (2015a) *CO2 Emissions From Fuel Combustion Highlights*, *IEA Statistics*. doi: 10.1787/co2-table-2011-1-en.

International Energy Agency (2015b) *Key Electricity Trends Excerpt from: Electricity Information*. Available at: https://www.iea.org/publications/freepublications/publication/Electricitytrends.pdf.

International Renewable Energy Agency (2014) *Wave Energy Technology Brief*. Available at: http://www.irena.org/documentdownloads/publications/wave-energy_v4_web.pdf.

International Towing Tank Conference (2014) *ITTC – Recommended Procedures - General guideline for uncertainty analysis in resistance tests. 7.5-02-02-02 (Revision 02).*

Journée, J. and Massie, W. (2001) 'Wave forces on slender cylinders', in *Offshore Hydromechanics*. 1st edn. Available at: https://ocw.tudelft.nl/wp-content/uploads/Part_4.pdf.

Lamont-Kane, P. (2015) 'Personal communication with Queen's University Belfast colleague'. Belfast.

Lamont-Kane, P. (2015a) *Physical and Numerical Modelling of Wave Energy Converter Arrays - PhD thesis*. Queen's University Belfast.

Lamont-Kane, P. (2015b) ‘QUB PLK 150609 - 01B - One-Two Load Cell Calibration and Comparison - PLK June 2015, Queen’s University Belfast internal report’.

Lamont-Kane, P., Folley, M. and Whittaker, T. (2013) ‘Investigating Uncertainties in Physical Testing of Wave Energy Converter Arrays’, in *Proceedings of 10th European Wave and Tidal Energy Conference*. Aalborg, Denmark.

Lamont-Kane, P., McKinley, A., Henry, A., Nicholson, J., Folley, M. and Elsaesser, B. (2015) ‘Investigating Extreme Loads on an Oscillating Wave Surge Converter’, in *Proceedings of the 11th European Wave and Tidal Energy Conference*. Nantes, France.

Lamont-Kane P. and Moore, R. (2015) *General Use of the Portaferry Wave Paddles - Queen’s University Belfast internal health and safety guide*.

LinMot (2018) *LinMot*. Available at: http://www.linmot.com/ (Accessed: 3 March 2018).

Magnetic Technologies Ltd (2015a) *Magnetic Couplings Co-Axial Type*. Available at: http://www.magnetictech.com/magnetic-couplings-co-axial-type/ (Accessed: 21 October 2016).

Magnetic Technologies Ltd (2015b) *Magnetic Disk Couplings*. Available at: http://www.magnetictech.com/magnetic-disc-couplings/ (Accessed: 21 October 2016).

Mäki, T., Vuorinen, M. and Mucha, T. (2014) ‘WaveRoller – One of the Leading Technologies for Wave Energy Conversion’, in *5th International Conference on Ocean Energy*. Halifax, Canada, pp. 4–6.

Mansard, E. and Funke, E. (1980) ‘The Measurement of Incident and Reflected Spectra Using a Least Squares Method’, *Coastal Engineering*, pp. 154–172. Available at: http://journals.tdl.org/icce/index.php/icce/article/view/3432/3112.

Massel, S. (1996) *Ocean Surface Waves: Their Physics and Prediction*. 2nd edn. World Scientific.

MathWorks (2016) *idealfilter - MATLAB function*. Available at: http://uk.mathworks.com/help/matlab/ref/timeseries.idealfilter.html (Accessed: 3 September 2016).

MathWorks (2017) *corr2 - MATLAB function*. Available at: https://uk.mathworks.com/help/images/ref/corr2.html (Accessed: 27 May 2017).

Mckinley, A., Elsaesser, B., Nicholson, J., Windt, C. and Henry, A. (2014) 'The Structural Response of an Oscillating Wave Surge Converter to Wave Slamming', in *Proceedings of the First International Conference on Offshore Renewable Energy*. Glasgow, United Kingdom.

Mei, C. C., Sammarco, P., Chan, E. S. and Procaccini, C. (1994) 'Subharmonic resonance of proposed storm gates for Venice Lagoon', in *Proceedings: Mathematical and Physical Sciences*. doi: 10.1098/rspa.1983.0054.

Michele, S., Sammarco, P., d'Errico, M., Renzi, E., Abdolali, A., Bellotti, G. and Dias, F. (2015) 'Flap gate farm: From Venice lagoon defense to resonating wave energy production. Part 2: Synchronous response to incident waves in open sea', *Applied Ocean Research*, 52, pp. 43–61. doi: 10.1016/j.apor.2015.05.002.

Mitutoyo (2012) *Digimatic Protractor Pro 360*. Available at: http://www.mitutoyo.co.uk/small-tool-instruments-and-data-management/protractors/950-317#prettyPhoto (Accessed: 2 November 2016).

Mobac GmbH (no date) *Home*. Available at: http://www.mobac.de/englisch/index-d.html (Accessed: 21 October 2016).

Molinas, M., Sorby, B. and Lundberg, S. (2007) 'Power Smoothing by Aggregation of Wave Energy Converters for Minimizing Electrical Energy

Storage Requirements', in *Proceedings of the 7th European Wave and Tidal Energy Conference*. Porto, Portugal. doi: 10.1016/j.tree.2005.11.022.

Munson, B. R., Young, D. F. and Okiishi, T. H. (1998) *Fundamentals of Fluid Mechanics*. 3rd edn. John Wiley & Sons, Inc., Hoboken, NJ.

Murtagh, C. and Walsh, P. (2015) 'Wave Energy Conversion : Linear vs . Coulomb PTO Damping Strategies', in *Proceedings of the 11th European Wave and Tidal Energy Conference 6-11th Sept 2015, Nantes, France*.

National Instruments (2009) *Operating Instructions and Specifications NI 9264 16-Channel, ±10 V, 16-Bit Analog Voltage Output Module*. Available at: http://www.juxingyiqi.com/download/dailichanpin/chanpinguige/IO/9264_E.pdf.

National Instruments (2016a) *LabVIEW System Design Software*. Available at: http://www.ni.com/labview/ (Accessed: 11 July 2016).

National Instruments (2016b) *NI 9205 C Series Voltage Input Module*. Available at: http://sine.ni.com/nips/cds/view/p/lang/en/nid/208800 (Accessed: 25 October 2016).

National Instruments (2016c) *NI cDAQ-9188 CompactDAQ Chassis*. Available at: http://sine.ni.com/nips/cds/view/p/lang/en/nid/208990 (Accessed: 25 October 2016).

Newman, J. N. (1976) 'The interaction of stationary vessels with regular waves', in *The Proceedings of the 11th Symposium of Naval Hydrodynamics*. London, United Kingdom.

Nieslony, A. (2010) *Rainflow Counting Algorithm, MathWorks File Exchange*. Available at: http://www.mathworks.co.uk/matlabcentral%0A/fileexchange/3030-rainflow-counting-algorithm (Accessed: 22 July 2014).

Norwegian Technology Standards Institution (1998) *NORSOK N-004 Design*

*of Steel Structures*. Available at: http://www.standard.no/pagefiles/1140/n-004.pdf.

Norwegian University of Science and Technology (no date) 'General Modelling and Scaling Laws - lecture notes from TMR7 Experimental Methods in Marine Hydrodynamics'. Available at: http://www.ivt.ntnu.no/imt/courses/tmr7/lecture/Scaling_Laws.pdf.

O'Boyle, L. (2013) *Wave Fields around Wave Energy Converter Arrays - PhD thesis*. Queen's University Belfast.

O'Boyle, L., Doherty, K., Hoff, J. van't and Skelton, J. (2015) 'The Value of Full Scale Prototype Data - Testing Oyster 800 at EMEC , Orkney', in *11th European Wave and Tidal Energy Conference*. Nantes, France.

passyworldofmathematics.com (2013) *Passy's World of Mathematics*. Available at: http://passyworldofmathematics.com/mathematics-of-ocean-waves-and-surfing/ (Accessed: 15 April 2017).

Perrin, A. (2012) *Tank Performance Uncertainty Analysis, APL-RD.FRD.03-REP-0016 - Aquamarine Power Ltd internal document*. Edinburgh.

Placid Industries (2014) 'Drawing for magnetic particle brake B35-24-1M-AQUA, modified by manufacturer, received in personal communication'. Available at: http://www.placidindustries.com/spec.b35.pdf.

Placid Industries (no date a) *How Magnetic Particle Brakes Work*. Available at: http://www.placidindustries.com/crossection-br.html (Accessed: 21 October 2016).

Placid Industries (no date b) *magnetic particle brake B15 data sheet*. Available at: http://www.placidindustries.com/spec.b15.pdf.

Placid Industries (no date c) *magnetic particle brake B35 data sheet*. Available at: www.placidindustries.com/spec.b35.pdf.

Queen's University Belfast (2013) 'QUB_040613_2521 typical wave probe array in PF, marketing photo, on Queen's University Belfast server'.

Queen's University Belfast (2015) 'QUB Equipment List - Queen's University Belfast internal Excel spreadsheet'.

Queen's University Belfast (2016) *Portaferry Wave Tank*. Available at: http://www.qub.ac.uk/research-centres/cerc/Facilities/MarineFacilities/PortaferryWaveTank/ (Accessed: 8 July 2016).

Renzi, E. and Dias, F. (2012) 'Resonant behaviour of an oscillating wave energy converter in a channel', *Journal of Fluid Mechanics*, 701(2007), pp. 482–510. doi: 10.1017/jfm.2012.194.

Renzi, E. and Dias, F. (2013) 'Hydrodynamics of the oscillating wave surge converter in the open ocean', *European Journal of Mechanics, B/Fluids*. Elsevier Masson SAS, 41, pp. 1–10. doi: 10.1016/j.euromechflu.2013.01.007.

Renzi, E., Doherty, K., Henry, A. and Dias, F. (2014) 'How does Oyster work? the simple interpretation of Oyster mathematics', *European Journal of Mechanics, B/Fluids*, 47, pp. 124–131. doi: 10.1016/j.euromechflu.2014.03.007.

Rhode Island College (no date) *Seawater Properties that Control Density*. Available at: http://www.ric.edu/faculty/PSCI103/Seawater/Seawater_notes.htm.

Rogers, D. and King, G. B. (1997) *Wave generation using Ocean and wave, Version 3.62*.

Roymech (2013) *Coefficients Of Friction*. Available at: http://www.roymech.co.uk/Useful_Tables/Tribology/co_of_frict.htm (Accessed: 28 February 2018).

Sammarco, P., Michele, S. and D'Errico, M. (2013) 'Flap gate farm: From

Venice lagoon defense to resonating wave energy production. Part 1: Natural modes', *Applied Ocean Research*. Elsevier Ltd., 43, pp. 206–213. doi: 10.1016/j.apor.2013.10.001.

Sarkar, D., Doherty, K. and Dias, F. (2016) 'The modular concept of the Oscillating Wave Surge Converter', *Renewable Energy*. Elsevier Ltd, 85, pp. 484–497. doi: 10.1016/j.renene.2015.06.012.

Sarkar, D., Renzi, E. and Dias, F. (2014) 'Wave farm modelling of oscillating wave surge converters', in *Proceedings of the Royal Society A: Mathematical, Physical and Engineering Sciences*, pp. 20140118–20140118. doi: 10.1098/rspa.2014.0118.

Scher, R. (1985) *A Study of Flap-Type Wave Absorbing Devices - PhD thesis*. The University of Michigan.

Schmitt, P. (2013) *Investigation of the near flow field of bottom hinged flap type wave energy converters - PhD thesis*. Queen's University Belfast.

Schmitt, P., Bourdier, S., Sarkar, D., Renzi, E., Dias, F., Doherty, K., Whittaker, T. and Hoff, J. van't (2012) 'Hydrodynamic Loading on a Bottom Hinged Oscillating Wave Surge Converter', in *Proceedings of the Twenty-second International Offshore and Polar Engineering Conference*. Rhodes, Greece.

Sheng, W., Raymond, A. and Lewis, T. (2014) 'Physical modelling of wave energy converters', *Ocean Engineering*, 84, pp. 29–36. doi: 10.1016/j.oceaneng.2014.03.019.

Silver Spray (no date) *Cold water tap temperature*. Available at: http://www.silverspray.co.uk/2012/12/13/cold-water-tap-temperature/ (Accessed: 6 February 2017).

Stanford University (no date) 'Lecture 3: Temperature, salinity, density and ocean circulation - notes from Biological Oceanography/Marine Chemistry

course', pp. 1–17. Available at: http://ocean.stanford.edu/courses/bomc/chem/lecture_03.pdf.

Subsea World News (2012) *UK: Aquamarine Power Unveils Proposals for Lewis Wave Energy Project*. Available at: http://subseaworldnews.com/2012/03/05/uk-aquamarine-power-unveils-proposals-for-lewis-wave-energy-project/ (Accessed: 19 September 2016).

Synectic Electronics (2016) *Home*. Available at: http://www.synectic.co.uk/ (Accessed: 20 October 2016).

Talkchannels (2017) *Beam Deflection Equations*. Available at: http://www.talkchannels.com/beam-deflection-equations/ (Accessed: 30 April 2017).

Techet, A. (2004) 'Morrison's Equation - lecture notes from course 13.42 Design Principles for Ocean Vehicles'. Massachusetts Institute of Technology, pp. 191–197. Available at: http://web.mit.edu/13.42/www/handouts/reading-morrison.pdf.

Techet, A. (2005) '13.42 Design Principles for Ocean Vehicles - Massachusetts Institute of Technology lecture notes, course 2.22'. Massachusetts Institute of Technology.

Tom, N., Lawson, M., Yu, Y. and Wright, A. (2016) 'Spectral modeling of an oscillating surge wave energy converter with control surfaces', *Applied Ocean Research*. Elsevier B.V., 56, pp. 143–156. doi: 10.1016/j.apor.2016.01.006.

Trident Foams Ltd (no date) *Tancast*. Available at: http://www.tridentfoams.co.uk/tancast.html (Accessed: 31 October 2016).

Truong, H. V. P. (2012) 'Natural Frequencies of Oscillations of Oceans Frequencies of Tsunamis', in *15th World Conference on Earthquake Engineering (15WCEE)*. Lisbon, Portugal.

UK National Annex (2014) 'NA to BS EN 1993-1-1:2005+A1:2014, UK

National Annex to Eurocode 3: Design of steel structures General rules and rules for buildings, BSI'. Available at: http://www.steelconstruction.info/Design_codes_and_standards#cite_note-NAtoBSEN1993-1-1-20.

United States Naval Academy (no date) 'EN475 - Ocean Engineering Mechanics - Equation Sheet 1: Linear Wave Properties'. Available at: https://www.usna.edu/NAOE/academics/en475.php.

University College London (2009) 'Drag Forces on Circular Cylinders - lecture notes from Civil/Environmental Engineering undergraduate course'.

University of Florida (2009) 'EML4500 Finite Element Analysis and Design - lecture notes'. Available at: http://web.mae.ufl.edu/nkim/eas4200c/VonMisesCriterion.pdf.

University of Sydney (2005) *Aerodynamics for students*. Available at: http://www-mdp.eng.cam.ac.uk/web/library/enginfo/aerothermal_dvd_only/aero/fprops/introvisc/node8.html (Accessed: 28 January 2017).

University of Washington (2007) 'Thick Walled Cylinders - lecture notes from ME354 Mechanics of Materials Laboratory'. Available at: http://courses.washington.edu/me354a/Thick Walled Cylinders.pdf.

Vicon (no date) *Bonita*. Available at: https://www.vicon.com/products/camera-systems/bonita (Accessed: 19 October 2016).

Vishay (no date) *Home*. Available at: http://www.vishay.com/ (Accessed: 20 October 2016).

Vishay Precision Group Inc (2015) *General Purpose Strain Gauges-Shear/Torque Pattern*. Available at: http://www.vishaypg.com/docs/11122/062tv.pdf.

WAMIT (2016) *Home*. Available at: http://www.wamit.com/ (Accessed: 23

September 2016).

Wei, Y., Rafiee, A., Henry, A. and Dias, F. (2015) 'Wave interaction with an oscillating wave surge converter , Part I : Viscous effects', *Ocean Engineering*, 104, pp. 185–203. doi: 10.1016/j.oceaneng.2015.05.002.

Weisz, A. (2012) *111215 New 40th Scale Model Design - APL-RD FDR 04-MAN-0001 - A2 - Aquamarine Power Ltd internal report*.

Whittaker, T. and Folley, M. (2012) 'Nearshore oscillating wave surge converters and the development of Oyster.', *Philosophical transactions. Series A, Mathematical, physical, and engineering sciences*, 370(1959), pp. 345–64. doi: 10.1098/rsta.2011.0152.

Whittaker, W. and Folley, M. (2005) 'Optimisation of Wave Power Devices Towards Economic Wave Power Systems', in *World renewable energy congress, Aberdeen, United Kingdom*, pp. 1–6. Available at: http://www.aquamarinepower.com/sites/resources/published papers/2476/optimisation of wave power devices towards economic wave power systems.pdf.

Wilkinson, L. and Lamont-Kane, P. (2013) *Review of QUB-APL PTO Dampers A2 - Aquamarine Power Ltd/Queen's University Belfast internal report*.

Wilkinson, L. and Nicholson, J. (2013) *131111 LW IFAS Testing in Waves A3 - Aquamarine Power Ltd/Queen's University Belfast internal report*.

Wilkinson, L. and Pernod, L. (2014) *140414_LP_LW_Rotation_Testing-A2 - Aquamarine Power Ltd/Queen's University Belfast internal report*.

Wilkinson, L. (2013) *131120 LW LinMot Linear Motor Testing A2 - Aquamarine Power Ltd/Queen's University Belfast internal report*.

Wilkinson, L. (2014a) *140122 LW Magnetic Particle Brake Testing - A2 - Aquamarine Power Ltd/Queen's University Belfast internal report*.

Wilkinson, L. (2014b) *140211 LW Magnetic Particle Brake and Magnetic Couplings Testing A1 - Aquamarine Power Ltd/Queen's University Belfast internal report*.

Wilkinson, L. (2014c) *140212 LW Electrical Hysteresis Brake Testing A1 - Aquamarine Power Ltd/Queen's University Belfast internal report*.

Wilkinson, L. (2016a) '160329 Two AMTI2000 Load Cell Calibration Data for Modular Flap without LC4, different excitation voltages and removed Heave - Aquamarine Power Ltd/Queen's University Belfast internal Excel spreadsheet'. Belfast.

Wilkinson, L. (2016b) '161026 LW Physical Model Costs - Aquamarine Power Ltd/Queen's University Belfast internal Excel spreadsheet'.

Wilkinson, L., Doherty, K., Nicholson, J., Whittaker, T. and Sandy, D. (2015) 'Modelling the performance of a modular flap-type wave energy converter', in *Proceedings of the 11th European Wave and Tidal Energy Conference*. Nantes, France.

Wilkinson, L., Russo, V., Doherty, K., Henry, A., Whittaker, T. and Day, S. (2014) 'Wave Loads on the Foundation of a Bottom-Hinged Modular Flap Structure', in *Proceedings of the First International Conference on Offshore Renewable EnergyOffshore Renewable Energy*. Glasgow, United Kingdom.

Wilkinson, L., Whittaker, T. J. T., Thies, P. R., Day, A. and Ingram, D. (2017) 'The power-capture of a nearshore, modular, flap-type wave energy converter in regular waves', *Ocean Engineering*, 137, pp. 394–403. doi: 10.1016/j.oceaneng.2017.04.016.

Windsor, A. (2015a) *Inside Venice's bid to hold back the tide*. Available at: https://www.theguardian.com/cities/2015/jun/16/inside-venice-bid-hold-back-tide-sea-level-rise (Accessed: 6 April 2017).

Windsor, A. (2015b) *Inside Venice's bid to hold back the tide*. Available at:

https://www.theguardian.com/cities/2015/jun/16/inside-venice-bid-hold-back-tide-sea-level-rise (Accessed: 4 October 2016).

World sea temperature (2017) *World Sea Temperatures*. Available at: https://www.seatemperature.org/ (Accessed: 6 February 2017).

# 12. Appendix 3 – Physical Model System

## 12.1 Damper Review Table

**Table 15. Full version of damper review table (Wilkinson and Lamont-Kane, 2013).**

1. Key

| Situation | Level/Answer | | |
|---|---|---|---|
| | low/N | medium | high/Y |
| Where low/medium/high is bad/average/good: | | | |
| Where low/medium/high is good/average/bad: | | | |
| Where N/Y is bad/good: | | n/a | |
| Unknown or n/a answer | | | |
| Answer is theoretically true but unproven | | | |

2. Table

| Damper | | | | | | | | | | | | | |
|---|---|---|---|---|---|---|---|---|---|---|---|---|---|
| Damping Specifications | Braking clutch | Closed hydraulic system | Open hydraulic system | Disc brakes | Hydraulic (oil) | Force Feedback Dynamometer/actuator | Hydraulic Rotary | Magnetic Particle Brake | Electrom. clutch | Electrical hysteresis brake | Linear motor |
| Damping Type | direct friction | hydraulic (water) | hydraulic (water) | direct friction | hydraulic (oil) | electric motor | hydraulic (water) | friction | direct friction | electromagnetic | electromagnetic |
| Damping Application (rotary/linear) | rotary | linear | linear | rotary | rotary | rotary | rotary | rotary | rotary | rotary | linear |
| Damping Profile | square | approx. quadratic and square | approx. square | square | square | any, theoretically | quadratic | square | square | square | square (theoretically) |
| Type of Control (physical/electrical) | physical | physical | physical | physical | electrical | electrical | physical | electrical | electrical | electrical | electrical |
| Maximum Damping (Nm) | 1.32 | unknown | unknown | unknown | 10.4 | 66 | 1 | 3.95 | 5.5 | 3.6 | 5.2 |
| Minimum Damping (Nm) | unknown | unknown | unknown | unknown | 1.7 | unknown | unknown | 0.05 | unknown | 0.02 | 0.2 |
| Damping Range Suitability to 30th Scale Testing (low/medium/high) | | | | | | | | | | | |
| Repeatability (low/medium/high) | | | | | | | | | | | |
| Ease of Use (low/medium/high) | | | | | | | | | | | |
| Control from Outside the Tank Possible? (Y/N) | | | | | | | | | | | |
| Dynamic Control Possible? (Y/N) | | | | | | | | | | | |
| Speed of Dynamic Control (low/medium/high) | | | | | | | | | | | |
| Possible to Use Underwater? (Y/N) | | | | | | | | | | | |
| Relative Size of Unit (low/medium/high) | | | | | | | | | | | |
| Relative Cost of Unit (low/medium/high) | | | | | | | | | | | |
| Actual Cost of Unit (€) | 10 | unknown | unknown | 115 | 17000 for first unit, 4500 after | 20000 (cost 1 | unknown | 360 (+ waterproofing) | 150 (+ waterproofing) | est. 650 (+ waterproofing) | 3000 (motor, drive and power supply) |

## 12.2 Damper Torque-Voltage Coefficients

**Table 16. Damping torque-voltage polynomial coefficients for the six MPB dampers used in the main experimental campaign. Note that the coefficients shown in Figure 52 are slightly different to those shown here due to the data analysis method being different.**

| Damper | Curve | | | | | | | |
|---|---|---|---|---|---|---|---|---|
| | Increasing Damping | | | | Decreasing Damping | | | |
| | x^0 | x^1 | x^2 | x^3 | x^0 | x^1 | x^2 | x^3 |
| 1 | -0.0751 | 4.2542 | -1.073 | 0.1506 | -0.2319 | 3.5176 | -0.693 | 0.1034 |
| 2 | 0.0637 | 3.8104 | -0.884 | 0.1182 | -0.1204 | 3.1908 | -0.5724 | 0.0812 |
| 3 | -0.1244 | 4.2079 | -1.0235 | 0.1396 | -0.3165 | 3.525 | -0.672 | 0.0968 |
| 4 | -0.1502 | 3.792 | -0.8467 | 0.1054 | -0.3348 | 3.2212 | -0.5871 | 0.0774 |
| 5 | -0.015 | 3.98 | -0.9765 | 0.1379 | -0.2377 | 3.3478 | -0.6464 | 0.0977 |
| 6 | 0.1207 | 3.967 | -0.983 | 0.1369 | -0.0889 | 3.3482 | -0.6814 | 0.1024 |

## 12.3 Physical Model System Costs

**Table 17. Costs of physical model system.**

| Item | Key Components | Total Cost of Component (£) | Total of Each Item (£) | Contribution (%) |
|---|---|---|---|---|
| Physical Model | Machined Parts | 17675 | 76650 | 88 |
| | Dampers | 10375 | | |
| | Sensors | 22799 | | |
| | Design and Development | 25800 | | |
| Damper Control | PCBs (Fabrication) | 70 | 3591 | 4 |
| | Breakout Box | 302 | | |
| | Linear Power Supply | 209 | | |
| | NI 9264 Card | 906 | | |
| | Share of CDAQ Chassis NI 9188 | 348 | | |
| | Design and Development | 1756 | | |
| DAQ | Breakout Box | 379 | 6590 | 8 |
| | Share of CDAQ NI 9188 chassis | 1392 | | |
| | NI 9205 Cards | 2394 | | |
| | NI 9402 Card | 227 | | |
| | PCBs (Fabrication) | 405 | | |
| | Design and development | 1793 | | |
| | | **Total (£)** | 86832 | 100 |

# 13. Appendix 4 – Physical Modelling Methods

## 13.1 Load Cell Gains and Excitation Voltages

**Table 18. Gain values used for load cell calibration and data processing (Wilkinson, 2016a).**

| **Gain, *G*** | **Degree of Freedom** | | | | |
|---|---|---|---|---|---|
| **Load Cell** | **Sway** | **Surge** | **Pitch** | **Roll** | **Yaw** |
| AMTI2000A | 5000 | 5000 | 500 | 2000 | 2000 |
| AMTI2000B | 2000 | 2000 | 2000 | 2000 | 2000 |

**Table 19. Excitation voltage values used for the load cell calibration and data processing (Wilkinson, 2016a).**

| **Excitation Voltage, $V_{ex}$ (V)** | **Degree of Freedom** | | | | |
|---|---|---|---|---|---|
| **Load Cell** | **Sway** | **Surge** | **Pitch** | **Roll** | **Yaw** |
| AMTI2000A | 5 | 5 | 5 | 5 | 5 |
| AMTI2000B | 5 | 5 | 5 | 5 | 5 |

## 13.2 Wave Probe Positions for Reflection Analysis

The reflection analysis used for calibration of the head-on waves used an array of seven probes, placed in-line with the direction of wave propagation, i.e. the x-axis. This number of probes was used to allow a range of wave periods to be accommodated in the reflection analysis. The positions of these probes are provided in Table 9. For each wave period, only three wave probes were used for the reflection analysis. Probe 1 was used for all of the conditions. The

combinations of the two other probes for each wave condition were then set through use of the MATLAB script, 'A_Probe_Spacing', version 4 (Clabby, 2014). The probes chosen for the regular and irregular waves are provided in Table 20 and Table 21, respectively.

**Table 20. Probe numbers used with Probe 1 for reflection analysis for head-on regular waves. Table 9 provides the co-ordinates of the probes.**

| Wave period, T (s) | 5.5 | 6.5 | 7.5 | 8.5 | 9.5 | 10.5 | 12.5 | 13.5 |
|---|---|---|---|---|---|---|---|---|
| First probe from Probe 1 | 2 | 2 | 2 | 3 | 3 | 3 | 4 | 4 |
| Second probe from Probe 2 | 3 | 4 | 4 | 6 | 5 | 6 | 7 | 7 |

**Table 21. Probe numbers used with Probe 1 for reflection analysis for head-on irregular waves. Table 9 provides the co-ordinates of the probes.**

| Mean wave period, $T_{01}$ (s) | 6.5 | 8.5 | 10.5 |
|---|---|---|---|
| First probe from Probe 1 | 3 | 3 | 4 |
| Second probe from Probe 2 | 6 | 6 | 7 |

## 13.3 Analysis Scripts

**Table 22. 'threeproberef_DJC' MATLAB script (Folley, Clabby and Crooks, 2015).**

```
function [frequency, amp, phase] = threeproberef_DC(y1, y2, y3,
d12,d23, h, dt, d1poi)


%
**********Description**********
% Calculates the incident and reflected spectral amplitude &
phase
% components at each probe so that time traces of incident &
reflected
% waves may be calculated at each probe.
%
% Probe1         Probe2                    Probe3
%   |-------d12-----|-------------d23---------|
%   ---> incoming wave direction
%
% Inputs:
%         y1, y2, y3: time series of surface elevation at
probes 1, 2, & 3
%         d12, d13: probe spacings
%         h: water depth
%         dt: time step
%         d1poi: spacing from probe 1 to point of interest (If
not one of
%         the ref analysis probe locations)
% Outputs:
%         frequency: (0:1:0.5*length(yi) - 1) [Hz]
%         amp: spectral amplitude components of the incident
(:, 1) &
%              reflected (:, 2) waves
%         phase: spectral phase components at probes 1 - 3 of
the incident
%                (:, 1:3, 1) and reflected (:, 1:3, 2) waves
%
% Note: Reflection analysis based on
```

```
threeprobereflectionalnalysis.m
%       Requires: wave_number_NR.m
%
% Author: MF with modifications by DC and DJC
% Edited by LW on 04/03/15 to use his 'dispersion' function

%apply fourier transform to signals
y1_fft = fft(y1);
y2_fft = fft(y2);
y3_fft = fft(y3);

N = length(y1);
frequency = [0:1:(N/2) - 1]./(N*dt);

% LW: I used my 'dispersion' function instead because it's in
my Matlab
% folder. This uses rad/s, as opposed to Hz. I added in 'omega'
to change
% frequency units.
omega = 2*pi*frequency;
k = dispersion(omega, h); % Inserted by DJC to speed up script.

% Transpose the wave number
k = k';

d13 = d12 + d23;
kx(1,:) = k.*0;
kx(2,:) = k.*d12;
kx(3,:) = k.*d13;

% wave component amplitudes at each wave probe position
A(:,1) = abs(y1_fft(1:N/2))/(0.5*N);
A(:,2) = abs(y2_fft(1:N/2))/(0.5*N);
A(:,3) = abs(y3_fft(1:N/2))/(0.5*N);

% wave component phases at each wave probe position
```

```
phase(:,1) = angle(y1_fft(1:N/2));
phase(:,2) = angle(y2_fft(1:N/2));
phase(:,3) = angle(y3_fft(1:N/2));

s1 = sum(exp(complex(0,2*kx)),1);
s2 = sum(exp(complex(0,-2*kx)),1);
s3 = sum(A'.*exp(complex(0,phase'+kx)),1);
s4 = sum(A'.*exp(complex(0,phase'-kx)),1);
s5 = (s1 .* s2) - 9;
%Adjusted xi and xr to be in accordance with wave direction as
in documentation
% xr = abs((s2.*s3 - 3*s4) ./ s5);
% xi = abs((s1.*s4 - 3*s3) ./ s5);
xr = ((s2.*s3 - 3*s4) ./ s5); xr(1) = 0; xr(2) = 0; xr = xr';
xi = ((s1.*s4 - 3*s3) ./ s5); xi(1) = 0; xi(2) = 0; xi = xi';

amp(:, 1) = abs(xi);
amp(:, 2) = abs(xr);

kx(4,:) = k.*d1poi; % Added by DJC to get the phase at point of
interest

for probe = 1:4
    phase(:, probe, 1) = -angle(xi) - kx(probe, :)';
    phase(:, probe, 2) = -angle(xr) + kx(probe, :)';
end
```

**Table 23. 'Jonswap_Tm' MATLAB script (Clabby, 2012)**

```
function [J_Spec, Hs_2, Tm_2, Te_2] = Jonswap_Tm(f_vec, Hs, Tm,
gamma)

%
**********Description**********
% Calculates the JONSWAP spectrum for significant wave height
Hs, mean
```

```
% period Tm, and peak enhancement factor gamma over the
frequency
% range defined by f_vec.
% Note:
% - Spectral units are [Hs]^2/[freq]
% - Hs and Tm are calculated for each iteration of Tp and
output as Hs_2 & Tm_2
% - Hs is influenced by gamma and is therefore corrected on
each iteration
% - Equations based on Goda, Coastal Eng. Journal 41(1) 1999
% Author: DC
%
% Hs = 3;
% Tm = 10;
% f_vec = [0:1:1023].*(1/1024);
% gamma = 7;

d = 0.8;
Tm_2 = Tm;
T_p = Tm_2/(1 - 0.532*(gamma + 2.5)^(-0.569)); % Initial
estimation of Tp
H = Hs;

while (abs(d - 1) > 0.00001)

    T_p = d*T_p;
    f_peak = 1/T_p;

    for i = 1:length(f_vec)
        if f_vec(i) <= f_peak,
            sigma(i) = 0.07;
        else sigma(i) = 0.09;
        end
            beta = (1.094-
0.01915*log(gamma))*(0.06238)/(0.23+(0.0336*gamma)-
0.185/(1.9+gamma));
            A(i) = beta*(H^2)*(T_p^(-4))*(f_vec(i)^(-5));
```

```
            E(i) = exp(-1.25*(T_p*f_vec(i))^(-4));
            P(i) = gamma^(exp(-(T_p*f_vec(i) -
1)^2/(2*sigma(i)^2)));
            J_Spec(i) = A(i)*E(i)*P(i);
    end

    m0 = trapz(f_vec(2:i), J_Spec(2:i));
    m1 = trapz(f_vec(2:i), f_vec(2:i).*J_Spec(2:i));
    m_1 = trapz(f_vec(2:i), J_Spec(2:i)./f_vec(2:i));

    Hs_2 = 4.*(m0.^0.5);
    Tm_2 = (m0/m1);
    Te_2 = (m_1/m0);

    d = Tm/Tm_2;
    e = Hs/Hs_2;
    H = e*H;

end
```

**Table 24. 'spectrum_from_trace_PLK' MATLAB script (Clabby, D. and Lamont-Kane, 2013).**

```
%%%%%%%%%%%%%%%%%%%%%%%%%%%%%%%%%%%%%%%%%%%%%%%%%%%%%%%%%%%%%%%%%%%%%%%%
%%%%%%%%%%%
% OVERVIEW
% spectrum_from_trace_PLK.m is a function called to perform an
FFT on a
% read in time trace. The code is based on
spectrum_from_trace.m obtained
% from DC and has been modified to V1.2 by PLK.
%
%
%%%%%%%%%%%%%%%%%%%%%%%%%%%%%%%%%%%%%%%%%%%%%%%%%%%%%%%%%%%%%%%%%%%%%%%%
%%%%%%%%%%%
% VERSION HISTORY
```

```
%
% Author: Darragh Clabby
%
% V 1.1 - Paul Lamont-Kane on 31/1/2013
%         modified to include df as an output
% V 1.2 - PLK (7/10/2013)
%         modified to auto zero a trace using trace_zero
function written
%         by PLK
%
%%%%%%%%%%%%%%%%%%%%%%%%%%%%%%%%%%%%%%%%%%%%%%%%%%%%%%%%%%%%%%%%%%%%%%%%
%%%%%%%%%%%%

function [freq, amp, var, phase, df] =
spectrum_from_trace_PLK(time_trace, dt)

%
**********Description**********
% Calculates the amplitude and energy density spectra (amp &
var respectively)
% for the input time trace signal sampled at dt seconds.
% Note:
% - time_trace should have a mean value of 0 to avoid severe
low frequency
%   contamination
% - [amp] = [time_trace]
% - [var] = [time_trace]^2/[freq]
% Author: DC

% dt = 0.1;
% time = [0:1:99].*0.1;
% time_trace = 14*sin(2*pi*0.2.*time);

% First zero the time trace using trace_zero
% [tr_zero] = trace_zero(time_trace); %LW: I changed this
because I don't
% have 'trace_zero' function
```

```
%LW: I generated the 'tr_zero' below:
tr_zero = time_trace-mean(time_trace);


L = length(tr_zero);
Y = fft(tr_zero);
amp = abs(Y(1:(L/2)))./(L/2);
freq = [0:1:L/2 - 1]./(L*dt);
phase = angle(Y(1:(L/2)));
df = freq(2) - freq(1);
var = (amp.^2)./(2*df);
```

## 13.4 Free Decay Tests

Free decay tests were performed to measure the natural frequencies of the Modular and Rigid Flap models. These were carried out in still water, by releasing a single flap body away from its point of equilibrium. The resulting rotations of the modules were then measured. The frequencies of the motions were then taken as the natural frequencies. The full scale results from these tests and analyses, for the six-module Modular Flap, are presented in Figure 121 and Figure 122. The natural frequency of the modular system, from Figure 122, was taken as the mean of the frequencies where reasonable values were determined. Hence, a value of 0.05 Hz was used for the natural frequency. Using the same analysis, the Rigid Flap natural frequency was determined to be 0.04 Hz.

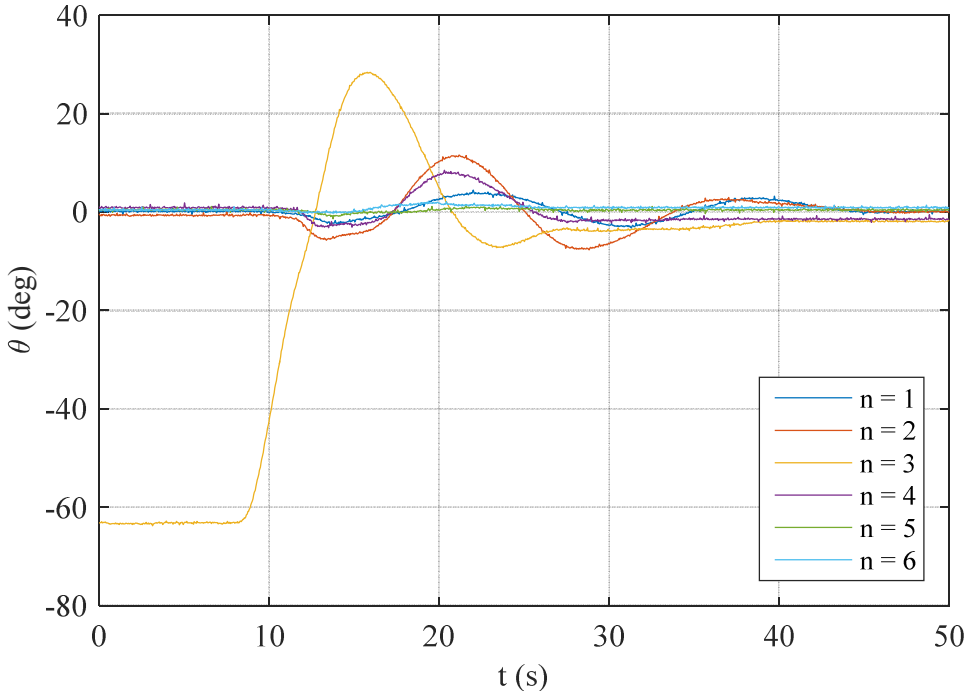


**Figure 121. Rotation results from free decay test for six-module Modular Flap.**

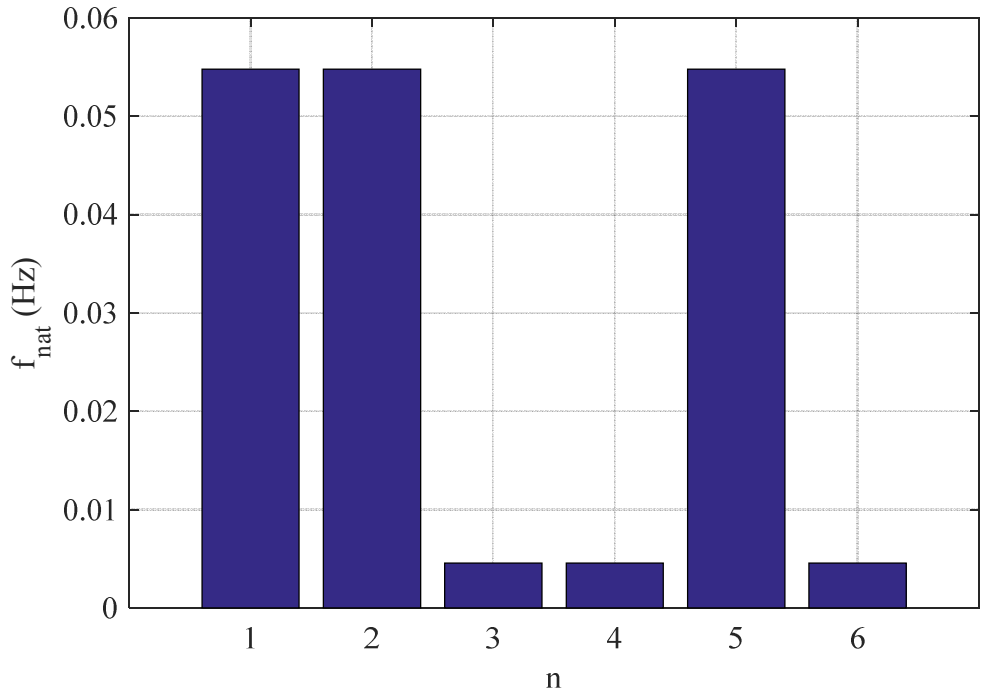


**Figure 122. Natural frequencies for flap modules.**

# 14. Appendix 5 – Data Analysis

## 14.1 Uncertainty Analysis Calculation Method

This section provides details on how the uncertainties on the power capture results were calculated. As mentioned in section 5.7, the ultimate aim of the analysis was to calculate the expanded uncertainty on the mean relative difference in capture factors achieved by the Modular and Rigid Flaps, $U_{\overline{\Delta CF}}$. Formulae were used and adapted from Coleman and Steele (2009) and publications by the ITTC (2014a, 2014b). The uncertainties in the measured variables were propagated to the results through the use of the Taylor Series Method (TSM). For a general function of independent variables, $q = f(x_1, \dots, x_n)$, the uncertainty $\delta q$ can be estimated using TSM as presented in Equation 61 (Lamont-Kane, Folley and Whittaker, 2013).

$$\delta q^2 = \sum_{i=1}^{n} \left(\frac{\partial q}{\partial x_i}\right)^2 \delta {x_i}^2 \qquad \text{Equation 61}$$

The uncertainty analysis was started at the instantaneous level, instead of using the mean values, as carried out in ITTC (2014a). This was because of the phase-dependence of the constituent variables of power capture, damping torque and angular velocity.

Only the systematic uncertainties were considered at the instantaneous level. This was because it was assumed that the random instantaneous fluctuations in the signals would have a negligible impact on the uncertainties of the generated statistics, e.g. the mean module powers.

The systematic uncertainties on the instantaneous damping torque signals, $b_{Tc_n}$, in MNm, were calculated using Equation 62.

$$b_{Tc_n} = V_n b_{m_{Tc,n}} \qquad \text{Equation 62}$$

Where, for the *n*th torque sensor, $V_n$ was the instantaneous recorded voltage, in V, and $b_{m_{Tc,n}}$ was the systematic uncertainty on the calibration slope, in MNm/V. The $b_{m_{Tc,n}}$ values were quantified using the method provided in ITTC (2014b). The absolute and relative $b_{m_{Tc,n}}$ values are provided in Table 25.

**Table 25. Absolute and relative torque sensor calibration slope uncertainties.**

| **Torque Sensor No., *n*** | **Calibration Slope Uncertainty (Model Scale) $b_{m_{Tc,n}}$ (Nm/V)** | **Calibration Slope Uncertainty (Full Scale) $b_{m_{Tc,n}}$ (MNm/V)** | **Relative Calibration Slope Uncertainty, $b_{m_{Tc,n}}$' (%)** |
|---|---|---|---|
| 1 | 0.0014 | 0.0011 | -0.15 |
| 2 | 0.0004 | 0.0003 | -0.04 |
| 3 | 0.0019 | 0.0015 | -0.21 |
| 4 | 0.0009 | 0.0007 | -0.10 |
| 5 | 0.0010 | 0.0008 | -0.11 |
| 6 | 0.0037 | 0.0030 | -0.42 |

The systematic uncertainties on the instantaneous module angular velocity, $b_{\dot{\theta}_n}$, in rad./s, were calculated using Equation 63 and Equation 64 for the Rigid Flap and Modular Flap, respectively.

Equation 63

$$b_{\dot{\theta}_n} = \dot{\theta}_n - \bar{\dot{\theta}}$$

Where, $\bar{\dot{\theta}}$ was the instantaneous mean of the module angular velocity, $\dot{\theta}_n$, values with the model configured as the Rigid Flap.

$$b_{\dot{\theta}_n} = \bar{\Delta}\dot{\theta}_n{}'\dot{\theta}_n \qquad \text{Equation 64}$$

Where, $\bar{\Delta}\dot{\theta}_{a,n}{}'$ was the mean of the relative differences between the mean module angular velocities and the mean of the values, across the range of wave conditions, as illustrated in Figure 95, in rad./s.

The instantaneous systematic uncertainties on the module powers, $b_{P_n}$, in kW, were calculated using a sum of squares approach as given by Equation 79. Note that the uncertainties on module damping torques, $Tc_n$, and angular velocities, $\dot{\theta}_n$, were assumed to be uncorrelated.

$$b_{P_n} = \sqrt{{Tc_n}^2 {b_{\dot{\theta}_n}}^2 + {\dot{\theta}_n}^2 {b_{Tc_n}}^2} \qquad \text{Equation 65}$$

The relative systematic uncertainties on the mean module powers were significantly higher than the equivalent values for the RMS module damping torques. Therefore, only the systematic uncertainties on the mean module powers, $b_{\bar{P}_n}$, were considered and were calculated with Equation 66. This evaluation allowed consideration of the correlation between the values throughout the time-series.

$$b_{\bar{P}_n} = \frac{\sum_{i=1}^{N} b_{P_{n,i}}}{N} \qquad \text{Equation 66}$$

Where *N* was the number of samples in the time series.

The random uncertainties on the power-capture were evaluated using a set of repeat tests for each device. The tests were conducted by leaving the waves running for five test durations and keeping the damping levels the same. A single, mid-range wave condition, of period 8.5 s, amplitude 1 m and direction 0° was used. The key outputs from this set of tests were the total mean power captures. Sample results are provided in Figure 123.

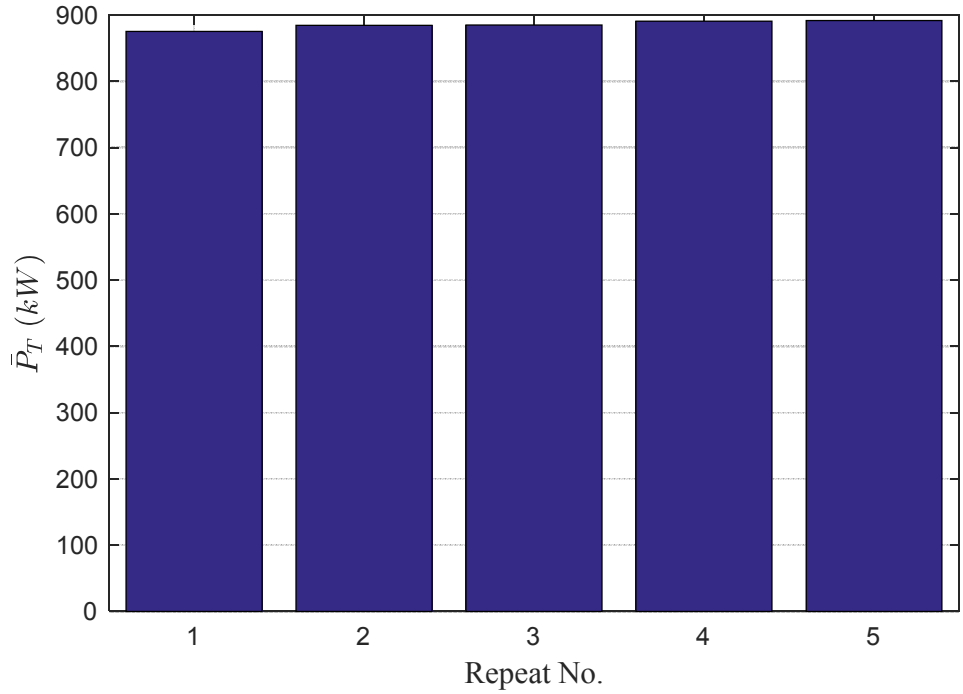


**Figure 123. Total mean power capture, $\bar{P}_T$, for each repeat no. for set of repeats. Results are for the 6 module Modular Flap.**

Figure 123 shows that the level of repeatability was very high. This variation was measured using the coefficient of variation (*CV*), which presents the standard deviation of a dataset as a fraction of the mean. The generic formula for *CV* is provided in Equation 67.

$$CV_X = \frac{s_X}{\bar{X}} \qquad \text{Equation 67}$$

Where, $s_X$ was the standard deviation of the sample of repeat measurements of variable *X* and $\bar{X}$ was the mean of the repeat *X* measurements.

The random uncertainties for the total mean power-capture, $s_{\bar{P}_T}$, were then calculated using Equation 68. This assumed that the variation level across the test results was constant, a standard technique in the absence of a larger dataset (International Towing Tank Conference, 2014).

$$s_{\bar{P}_T} = \frac{CV_{\bar{P}_T}\bar{P}_T}{\sqrt{N}} \qquad \text{Equation 68}$$

Where, $CV_{\bar{P}_T}$ was the *CV* value for the total mean power capture and $N$ is the number of repeats, 5. At only 0.7% for the Modular Flap and 0.3% for the Rigid Flap, the *CV* values were low enough to not contribute significantly to the standard combined uncertainties on the total mean power capture.

$b_{\bar{P}_n}$ and $s_{\bar{P}_T}$ were then used to find the standard combined uncertainties on the total mean power capture, $u_{\bar{P}_T}$, using Equation 69.

$$u_{\bar{P}_T} = \sqrt{\left(\sum_{n=1}^{M} {b_{\bar{P}_n}}^2\right) + {s_{\bar{P}_T}}^2} \qquad \text{Equation 69}$$

The standard combined uncertainty on the maximum total mean power, $u_{\bar{P}_{T,max}}$ was then estimated. This involved calculating $u_{\bar{P}_T}$ for each damping level, defined by the total RMS damping torque, $Tc_{RMS,T}$. The $Tc_{RMS,T}$-$u_{\bar{P}_T}$ pairs were then plot, with a quadratic curve subsequently fit through the data. The $u_{\bar{P}_{T,max}}$ value was then the value on the curve that corresponded to the damping level that resulted in maximum power generation.

The expanded combined uncertainties on the capture factors, $U_{CF}$, were then calculated. The $u_{\bar{P}_{T,max}}$ values were first considered as systematic uncertainties, as shown in Equation 70.

$$b_{\bar{P}_{T,max}} = u_{\bar{P}_{T,max}} \qquad \text{Equation 70}$$

The standard combined uncertainty on the capture factors, $u_{CF}$, was then calculated using Equation 85.

$$u_{CF} = \sqrt{\frac{{b_{\bar{P}_{T,max}}}^2 + {\bar{P}_{T,max}}^2 {b_{\cos(D)}}^2 \cos D^{-2}}{\cos D^2 \, {P_{inc}}^2 W^2}} \qquad \text{Equation 71}$$

Where, $b_{\cos(D)}$ was the systematic uncertainty on the cosine of the angle of the model relative to the wave crest, $D$. $b_{\cos(D)}$ was calculated using Equation 72.

$$b_{\cos(D)} = 1 - \cos(b_D)$$ Equation 72

Where, $b_D$, was the systematic uncertainty on $D$, which was estimated to be, quite conservatively, 5 deg. $U_{CF}$ was then calculated using Equation 73.

$$U_{CF} = k_p u_{CF}$$ Equation 73

Where, $k_p$ is the coverage factor, 2, for a 95% confidence level (International Towing Tank Conference, 2014).

The standard combined uncertainty on the differences in capture factors achieved by the two devices, $u_{\Delta CF}$, were then calculated using Equation 74.

$$u_{\Delta CF} = \sqrt{\frac{b_{\bar{P}_{T,max,Rig}}{}^2 + \cos D^{-2}\, \bar{P}_{T,max,Rig}{}^2 b_{\cos(A)}{}^2 + b_{\bar{P}_{T,max,Mod}}{}^2 + \cos D^{-2}\, \bar{P}_{T,max,Mod}{}^2 b_{\cos(A)}{}^2}{\cos D^2\, P_{inc}{}^2 W^2}}$$ Equation 74

Where terms with 'Rig' or 'Mod' in their subscripts refer to values associated with the Rigid and Modular Flaps, respectively.

The standard combined uncertainties on the relative differences of the capture factors, $u_{\Delta CF}{}'$, were then calculated using Equation 75.

$$u_{\Delta CF\prime} = \sqrt{\frac{u_{\Delta CF}{}^2}{CF_{Rig}{}^2} + \frac{\Delta CF^2}{CF_{Rig}{}^4} u_{CF,Rig}{}^2 - 2\frac{\Delta CF}{CF_{Rig}{}^3} u_{\Delta CF} u_{CF,Rig}}$$ Equation 75

The expanded combined uncertainties on the relative differences of the capture factors, $U_{\Delta CF\prime}$, were then calculated using Equation 76.

$$U_{\Delta CF\prime} = k_p u_{\Delta CF\prime}$$ Equation 76

The expanded combined uncertainty on the mean of the relative differences of the capture factors, $U_{\overline{\Delta CF'}}$, was then calculated using Equation 77.

$$U_{\overline{\Delta CF'}} = \frac{\sum_{j=1}^{P} U_{\Delta CF'_j}}{P} \quad \text{Equation 77}$$

Where, $P$ is the number of wave conditions, for example 8 for the head-on, regular, constant amplitude waves, and $U'_{\Delta CF_j}$ is the expanded combined uncertainty on the relative difference of the capture factors for the *j*th wave condition.

The expanded combined uncertainty on the relative differences in capture factor weighted with the incident wave power was calculated in much the same way as for the unweighted case that culminated in Equation 77. Hence, only the formula for the standard combined uncertainty, for a given wave condition, $u_{\Delta CF'_w}$, is provided in Equation 78.

$$u_{\Delta CF'_w} = \sqrt{\begin{matrix} {P_{inc}}^2 {P_{inc_{max}}}^2 \cos(D)_{max}^{-2} (\cos(D)^2 {b_{\Delta CF'}}^2 + \\ \Delta CF'^2 {b_{\cos(D)}}^2 + \\ \Delta CF^2 \cos(D)^2 \cos(D)_{max}^{-2} {b_{\cos(D)_{max}}}^2) \end{matrix}} \quad \text{Equation 78}$$

Where, $P_{inc_{max}}$ was the maximum available wave power across a given range of wave conditions, in kW/m, $\cos(D)_{max}$ was the cosine of the wave direction for the wave condition with maximum incident power and $b_{\Delta CF'}$ was the standard combined uncertainty on the relative difference in capture factors, defined as $u_{\Delta CF'}$ in Equation 75.

## 14.2 Analysis Scripts

**Table 26. 'fivepointfirstderivative' MATLAB script.**

```
function [derivative] = fivepointfirstderivative(signal,dt)


derivative=0*signal;
```

```
n=length(signal);


derivative(1)=(signal(2)-signal(1))/dt;
derivative(2)=(signal(3)-signal(1))/2./dt;
derivative(n-1)=(signal(n)-signal(n-2))/2./dt;
derivative(n)=(signal(n)-signal(n-1))/dt;


for i=3:length(signal)-2
derivative(i)=(signal(i-2)-8.*signal(i-1)+8.*signal(i+1)-
signal(i+2))/(12.*dt);
end
```

## 14.3 Discussion of Scaling Viscous Forces for the Modular Flap

This section provides a discussion and analysis of the issue of scaling the viscous forces that the Modular Flap is subjected to. Scale effects arise due to the inability to preserve force ratios between the model and the full-scale experiments. The significance of the scale effects depends on the relative importance of the forces involved. In physical modelling, it is hence highly important to understand which forces need to be correctly scaled and which ones can be neglected. In fluid dynamics, there are a number of relevant force types, for example inertial, gravitational and viscous. The ratios of these forces are some of the key parameters, such as the Froude and Reynolds numbers. The former is the ratio of inertial to gravitational forces, while the latter is the ratio of inertial to viscous forces. In order to appropriately scale results, the most relevant force ratio is selected. The remaining ratios, which are not preserved between the scales, result in scale effects. Froude similarity, i.e. when the Froude number is preserved across the scales, is assumed when gravitational and inertial forces are dominant and the remaining forces, such as viscous ones, are small (Heller, 2012) or that they scale in the same way that an inertial/gravitational force does (Clabby, 2013). In this thesis, the discussion is limited to viscous forces, as these, outside of the inertial and gravitational forces, are deemed the potentially most significant.

The particular viscous force that is discussed here is the drag force. This has two components – the 'skin friction' and 'pressure drag'. The skin friction is due to the integration of the tangential viscous shear force around the surface of the body. The pressure drag is the integration of the local fluid pressure force normal to the surface and resolved in the relative flow direction. For bluff bodies, such as circular cylinders, flow separation occurs. In these cases, the skin friction component of the drag force is typically negligible (University College London, 2009). Nevertheless, both components are discussed in this section.

In section 2.2.2, a strong argument was put forward that the scaling of viscous forces using Froude laws for the Rigid Flap would not represent a significant issue. The assumption was made that the device could be modelled as a flat plate, due to its high ratio of width and height to thickness. This resulted in a constant drag coefficient and hence a pressure drag force that scaled in the same way that other forces did with Froude laws. The viscous shear force was also neglected, based on CFD work showing that it represented an insignificant part of the overall driving surge force (Schmitt *et al.*, 2012).

For the Modular Flap, especially for the six module configuration, the arguments applied to the Rigid Flap break down. The width of the modules is no longer large compared to the thickness. Firstly, this undermines the assumption that the device can be modelled as a flat plate. Instead, each module in the 6-unit configuration, the most important device, could be modelled as a cuboid or cylinder. This is because the width and thickness are similar, at 5.5 m and 3.6 m, respectively, at full scale. Literature is readily available on the drag properties of cylinders so the modules will be modelled as these. This assumption has been applied in analytical modelling of a Modular Flap with reasonable results (Sarkar, Doherty and Dias, 2016). For a cylinder and a number of body shapes, the drag coefficient is a function of the Reynolds number, as shown in Figure 124.

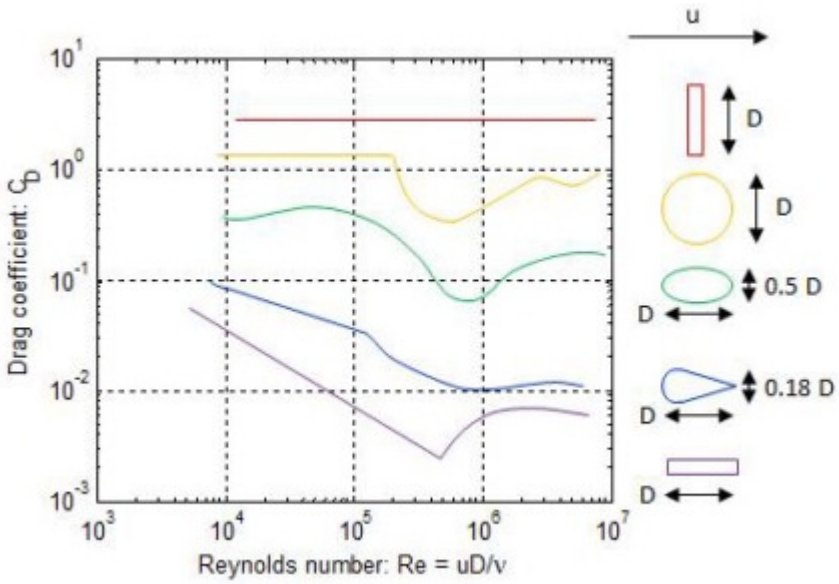


**Figure 124. Drag coefficient, $C_D$, against Reynolds number, *Re*, for flat plate perpendicular to flow, circular cylinder, elliptical cylinder, aerofoil, and flat plate parallel to flow, respectively (Munson, Young and Okiishi, 1998).**

The Reynolds number, *Re*, as indicated in Figure 124, can be calculated using Equation 79.

$$Re = \frac{uD}{v} \qquad \text{Equation 79}$$

Where, $u$ is the body speed relative to the flow, $D$ is the characteristic length and $v$ is the kinematic viscosity (Munson, Young and Okiishi, 1998). The application of Equation 79 to this problem requires a number of assumptions, for example that $u$ is the body speed, without consideration of the fluid speed and that $v$ is constant across the testing conditions. These assumptions introduce a large degree of uncertainty into the calculated values. However, the main aim of this analysis is to determine the order of magnitude of the contribution of the viscous forces at different scales and so the exact figures are not important. For $u$, the average speed of a typical oscillation can be used. Using the example shown in Figure 88, the amplitude of the rotation, $\theta$, was 15 degrees or 0.26 radians, with an oscillation period, T, of 8.5 s at full scale and 1.6 s at model scale. The speed can be taken half way up the flap from the

hinge. As shown in Figure 64, the distance from the hinge to the top of each module was 12.2 m, at full scale. Hence, the distance from the hinge to the middle, $r$, was 6.1 m at full scale and 0.2 m at model scale. The average speed can be calculated with this information, as shown in Equation 80.

$$u = \frac{4r\theta}{T} \qquad \text{Equation 80}$$

The values of $u$ were calculated as 0.14 m/s and 0.75 m/s at model and full scales, respectively. The characteristic length, $D$, can be taken as the average of the width and thickness of each module. This is 0.15 m and 4.5 m, at model and full scales, respectively. Finally, the value of the kinematic viscosity, $v$, must be decided. $v$ is a function of temperature (Norwegian University of Science and Technology, no date). An estimate for the typical temperature of the water in both the wave tank and the ocean where the full scale device would be deployed is 10°C (Silver Spray, no date; World sea temperature, 2017). At this temperature, $v$ is an estimated $1.5 \times 10^{-6}$ $m^2/s$ (Norwegian University of Science and Technology, no date). This results in Reynolds numbers of $1.4 \times 10^4$ and $2.3 \times 10^6$ at model and full scale, respectively. From Figure 124, the equivalent drag coefficient, $C_D$, values for a cylinder are estimated to be 1.5 and 0.9, respectively. This suggests that the drag force experienced by the model scale module is disproportionately larger than it would be subjected to at full scale, by a factor of 1.7. The degree to which this would likely affect the results, for example the power capture, can be estimated by comparing the drag force to the driving surge force. The drag force, $F_D$, can be estimated using the classic Morrison's equation, provided in Equation 2.

$$F_D = \frac{1}{2}\rho(u-q)|u-q|A_f C_D \qquad \text{Equation 81}$$

Where, with model and full scale values provided respectively, $\rho$ is the density of water, 1000 $kgm^{-3}$ and 1030 $kgm^{-3}$ for fresh and saline water, respectively, $u$ is the velocity of the module, 0.14 m/s and 0.75 m/s, $q$ is the free stream

velocity, $A_f$ is the frontal area of the module, 0.05 $m^2$ and 42.6 $m^2$, and $C_D$ is the drag coefficient, 1.5 and 0.9.

The application of the Morrison's equation requires that the local flow be assumed uniform. In a wave, the water particle motion is orbital. Hence, the wavelength of the wave, λ, must be must be much larger than the diameter of the body for the flow to be assumed locally uniform. For this comparison, the characteristic diameter of the body, $D_c$, is taken as the average of the width and thickness, i.e. 4.5 m at full scale. λ can be calculated using Equation 82.

$$\lambda = \frac{gT^2}{2\pi}\tanh(kd) \qquad \text{Equation 82}$$

Where, $g$ is the acceleration due to gravity, 9.81 $m/s^2$, $T$ is the wave period, $k$ is the wave number and $d$ is the water depth, 13.9 m at full scale (United States Naval Academy, no date). $k$ is found iteratively using the dispersion theorem, provided in Equation 83.

$$k = \frac{2\pi}{\lambda_0 \tanh(kd)} \qquad \text{Equation 83}$$

Where $\lambda_0$ is the wavelength calculated for deep water, using Equation 64.

$$\lambda_0 = \frac{gT^2}{2\pi} \qquad \text{Equation 84}$$

For the regular waves used in the 30th scale testing campaign, the range of ratios of $D_c$ to λ were calculated, with the results shown in Figure 125.

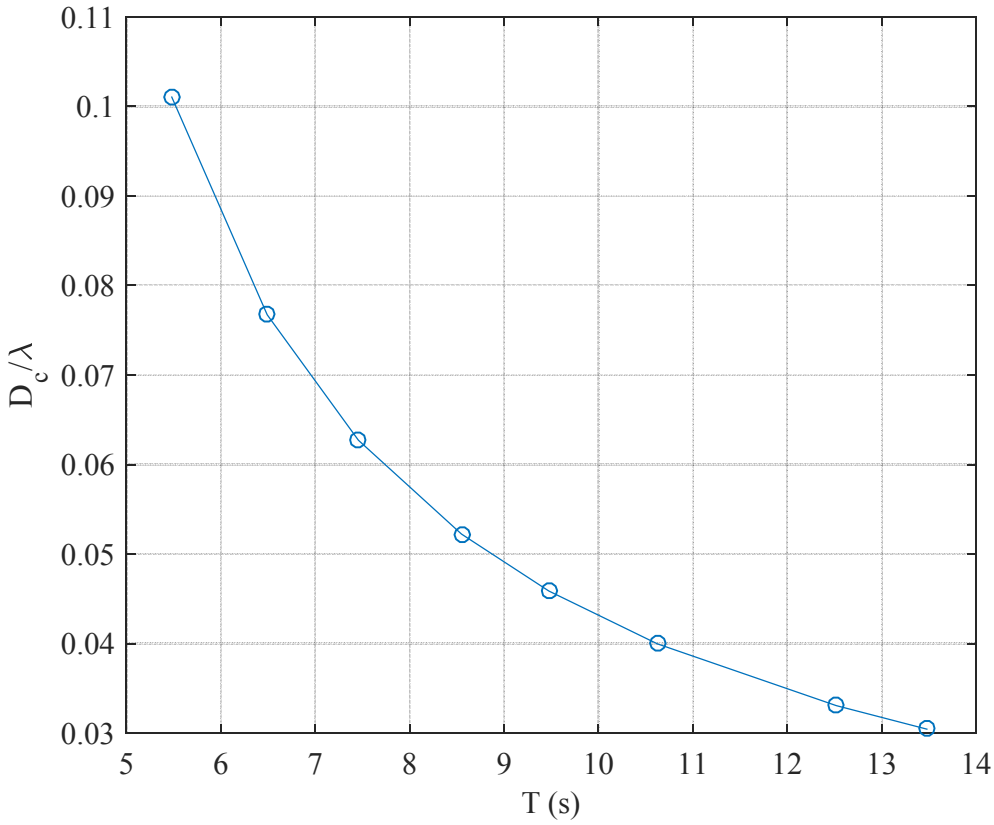


**Figure 125. Ratio of characteristic diameter, $D_c$, to wavelength, $\lambda$ for range of wave periods $T$ for regular waves used in 30th scale testing. $T$ given at full scale.**

Figure 125 shows the maximum ratio of the characteristic diameter to the wavelength was just above 0.1. The maximum range for the assumption that the diameter is much smaller than the wavelength is typically taken to be 0.1-0.2 (Journée, J. and Massie, 2001). Hence, Morison's equation is applicable for this application.

The free stream velocity, $q$, is taken as the average horizontal particle velocity at mid-way up the water column. The value is multiplied by 0.5 as well. This latter step was taken to approximate the effect of a phase difference between the velocity of the flap and the water particles. A phase difference can be present due to the forces involved, for example, the damping torque, changing the phase of the motion of the flap. A phase difference would result in either an increase or decrease in the drag pressure force, $D_F$. Hence, multiplying the average velocity magnitude accounts for this phase difference in a conservative

way. The equation for $q$, modified from standard formula (United States Naval Academy, no date), is provided in Equation 85.

$$q = 0.5 \sum_{i}^{N} \frac{\pi H \cosh(k(z+d))}{T \sinh(kd)} \cos(kx - \sigma t) \qquad \text{Equation 85}$$

Where, $N$ is the number of samples over a wave period, $T$, 8.5 s, $i$ is the sample number $H$ is the wave height, 2 m, $k$ is the wave number 0.073 $m^{-1}$, $z$ is the position in the z-axis, -6.9 m, $d$ is the water depth, 13.9 m, $x$ is the position in the x-axis, 0 m, $\sigma$ is the phase, arbitrarily taken as $\pi$ and $t$ is time, in s (United States Naval Academy, no date). From Equation 64, $q$ was calculated as 0.04 m/s and 0.22 m/s, at model and full scales, respectively.

From the calculation of the components in Equation 2, the typical pressure drag force, $F_D$, was evaluated as 0.34 N and 5600 N, at model and full scales, respectively.

The division of the Rigid Flap into separate modules also means that the areas of the sides of each flap become much greater per width of device. The likely result of this is that the viscous shear force acting on the sides of each flap becomes a larger proportion of the overall force. The shear force, $S$, acting on a solid boundary moving relative to water, can be calculated using Equation 86.

$$S = \mu A \frac{u}{y} \qquad \text{Equation 86}$$

Where, $\mu$ is the dynamic viscosity of water, $A$ is the area that the shear force is acting over, $u$ is the body speed and $y$ is the boundary layer thickness. $\mu$ is a function of the water temperature. The difference in temperature, between the water in the wave tank and the ocean water that the full scale machine would be deployed in, is likely relatively small. $\mu$ can therefore be assumed to be constant between the testing locations and scales. $A$ will scale with the length factor squared. $u$ would scale with the square root of the length factor. $y$ can be estimated with theory for a flat plate. The choice of the equation for y depends

on the type of flow. Due to the close proximity of the modules and the complex wave structure interaction, it is likely that there is a high level of mixing in the gaps between the modules. Hence, the flow can be assumed to be 'turbulent'. For a flat plate moving through turbulent water, y is calculated using Equation 87.

$$y = \frac{0.385x}{Re_x{}^{0.2}} \qquad \text{Equation 87}$$

Where $x$ is the distance from the leading edge of the plate and $Re_x$ is the Reynold's number along a line at $x$ (University of Sydney, 2005). To obtain the typical value for $y$, $x$ can be set as the distance from the front face of the module to the centre, i.e. half the thickness. This provides values for $x$ of 0.06 m and 1.8 m at model and full scales, respectively. Using the same values for the Reynolds numbers as used previously, this results in values for $y$ of 0.003 m and 0.037 m at model and full scale, respectively. The area, $A$ of each side of a module can be calculated from the rectangle between the mean water level and the bottom of the box section, as 0.031 $m^2$ and 27.9 $m^2$ at model and full scales, respectively. The dynamic viscosity, $\mu$, was calculated using Equation 88.

$$\mu = v\rho \qquad \text{Equation 88}$$

Where $\rho$ is the water density and $v$ is the kinematic viscosity. Using the same figures calculated earlier for $v$, this provides values for $\mu$ of 0.00150 Pa s and 0.00155 Pa s for the fresh water and seawater, respectively. The values for the body speed, $u$, can be taken as before. This results in shear forces, $S$, of 0.002 N and 0.9 N at model and full scale, respectively. For each module, i.e. with S acting on both sides, this results in values of 0.004 N and 2 N, respectively.

To gauge the significance of the calculated viscous forces, the values can be compared to a typical wave force. It has been shown that the power capture of a flap-type WEC is proportional to the square of the wave force (Henry, 2008).

The surge wave force is typically the largest that a flap experiences and so the viscous forces are compared to it. Figure 113 provides a value for the driving surge force. The driving force is measured when the damping level becomes so large that the device is no longer moving. Although this condition was not actually reached in this case, it provides an indication of the order of magnitude of a typical value. The maximum measured surge effective load range was 8.5 MN at full scale. Hence, the amplitude was 4.25 MN. Over a full cycle for a regular wave, this results in an average load of 2.7 MN. Divided between the six modules, to provide an indication of the individual driving force, the load is 0.45 MN, or $4.5 \times 10^5$ N. The equivalent value at model scale was 16 N. The typical relative magnitudes of the drag pressure force were hence 2.0 % and 1.3 %, at model and full scales, respectively. The equivalent values for the viscous shear forces were 0.02 % and 0.0002 %. Therefore, the ratios of forces for both viscous components were not maintained across the scales. However, the lower contribution of pressure drag force at full scale suggests that the model scale power results are a slight underestimation of the full scale values. On the other hand, it also implies that the surge foundation loads will be slightly increased at full scale (Folley, 2007). For the shear forces, the contributions are negligible in both cases. Hence, the incorrect scaling of viscous shear forces will have no significant effect on the key results, such as the capture factors. There is a high level of uncertainty in the magnitudes of the calculated viscous forces. However, it is suggested that the power capture and foundation loads, that are affected by the flap dynamics, will slightly increase at full scale.

# 15. Appendix 9 – Further Work

## 15.1 Numerical Model

This sub-section provides some brief information on the numerical model of the modular flap-type WEC, for those wishing to use it for further work. A time-domain model was developed based on previous work on flap arrays (Folley, 2007). The model solved equations of motion for each module, based on the input wave torque, hydrodynamic damping, buoyancy restoring torque, inertia and applied PTO damping. Further details on the mathematics and simulation of the model can be found in Wilkinson et al (2015). The model originally used the wave-structure interaction software, Wamit, to determine the wave torque, added inertia and radiation damping coefficients. Subsequently, the model was adopted by an Aquamarine Power Ltd engineer, Jos van 't Hoff, and developed further. These advancements included making it simpler to model a large number of modular flap configurations and using the free software, Nemoh (Crooks *et al.*, 2014). All significant model iterations can be accessed from the QUB Belfast Wave server, at 'Laurie\Numerical Modelling'. The latest model can be found in the same location, in the folder 'OysterM'.

# 16. Appendix 11 - Papers

The following papers were published during the time that this research was completed and, in part, contributed to this work. Thank you also to the co-authors of these papers. The papers are presented in the following chronological order:

- Wave Loads on The Foundation of a Bottom-Hinged Modular Flap Structure (Wilkinson *et al.*, 2014)
- Modelling of a Modular Flap Type Wave Energy Converter (Wilkinson *et al.*, 2015)
- The Power-Capture of a Nearshore, Modular, Flap-Type Wave Energy Converter in Regular Waves (Wilkinson *et al.*, 2017)

# WAVE LOADS ON THE FOUNDATION OF A BOTTOM-HINGED MODULAR FLAP STRUCTURE

**L. Wilkinson**, *Industrial Doctoral Centre for Offshore Renewable Energy (IDCORE) & Aquamarine Power Ltd, UK*
**V. Russo**, *Queen's University Belfast, UK*
**K. Doherty**, *Aquamarine Power Ltd, UK*
**A. Henry**, *Aquamarine Power Ltd, UK*
**T. Whittaker**, *Queen's University Belfast, UK*
**S. Day**, *University of Strathclyde, UK*

## ABSTRACT

Large loads result in expensive foundations which are a substantial proportion of the capital cost of flap-type Wave Energy Converters (WECs). Devices such as Oyster 800, currently deployed at the European Marine Energy Centre (EMEC), comprise a single flap for the full width of the machine. Splitting a flap-type device into smaller vertical flap modules, to make a 'modular-flap', might reduce the total foundation loads, whilst still providing acceptable performance in terms of energy conversion.

This paper investigates the foundation loads of an undamped modular-flap device, comparing them to those for a rigid flap of an equivalent width. Physical modelling in a wave tank is used, with loads recorded using a six degree of freedom (DoF) load cell. Both fatigue and extreme loading analysis was conducted. The rotations of the flaps were also recorded, using a motion-tracking system.

## NOMENCLATURE

| | |
|---|---|
| $H_s$: | significant wave height |
| $T_m$: | mean wave period |
| F: | load amplitude |
| N: | number of load reversals |
| m: | fatigue damage exponent |
| $DC_{single\ sea}$: | damage contribution of sea state |
| $ELR_{single\ sea}$: | effective load range of sea state |
| $n_{test}$: | number of waves in test |
| $n_{single\ sea}$: | number of waves in sea state |
| $D_{single\ sea}$: | damage in sea state |
| TYD: | total yearly damage |
| $n_{year}$: | number of cycles in a year |
| TELR: | total effective load range |
| $98^{th}$ percentile: | 98% exceedance value |

## 1. INTRODUCTION

Bottom-hinged flap-type Wave Energy Converters (WECs) are designed to absorb energy contained in the horizontal motion of water within ocean waves [1]. They are typically sited in the intermediate water depths of the nearshore region in order to take advantage of the amplification of horizontal water particle motion due to shoaling effects [2].

Aquamarine Power Ltd is a developer of one such flap-type WEC called Oyster, [3], [4], [5]. Oyster consists of a large buoyant flap which is hinged at the seabed and pierces the water surface. Wave action forces the flap to pitch back and forth and this mechanical energy is used to pump high pressure water ashore where it is used to produce electricity. Aquamarine Power's second full scale prototype, labelled Oyster 800, is currently in operation at the European Marine Energy Centre (EMEC), Orkney, Scotland. Several studies have shown that the Oyster concept has many advantageous characteristics in terms of energy yield and survivability and is one of the leading WEC technologies currently under development, [6], [7], [8].

Flap-type WECs are, by their nature, predominately force driven devices [3], [5]. This fundamental operating principle intrinsically links the power extraction capacity and loading characteristics. Splitting a flap-type WEC into multiple smaller vertical modules, which share a common foundation, is one possible way of reducing the global loading whilst still maintaining a high power capture capacity.

The concept of a modular flap structure in the ocean environment is not necessarily a novel idea. The Venice Gates, currently under construction, is a 1.6km barrier system comprising of 78 closely spaced modules designed to protect the Venice lagoon from flooding, and is probably the most well know example of such a structure. Extensive experimental and numerical research has been conducted on this concept, [9], [10], [11], [12], which has revealed several unique and interesting characteristics. The most notable of these is a strong sub-harmonic out-of-phase motion between neighbouring gates or modules in the barrier and has been the focus of much of the research since its discovery.

Due to the origin of this research, the majority of the investigations have focused predominantly on application to flood defences. Only more recently has attention been given to a modular flap-type structure for the purpose of wave energy extraction [13], [14] and [15]. To date, research efforts have focused predominantly on trying to exploit the sub-harmonic resonance characteristics of a modular flap-type WEC to increase its potential power extraction capacity above its rigid equivalent counterpart. However, the excitation of sub-harmonic resonance depends on a delicate balance between the WEC's inertia and geometric characteristics and the incident wave conditions, in particular, the wave frequencies and bandwidth. In practise, real coastal sites will have a broad spectrum of incident wave frequencies and so the contribution of sub-harmonic resonances to the overall performance of the WEC is likely to be diminished in such scenarios. Nevertheless, this does not mean that a modular flap-type WEC could not have distinct advantages over a rigid equivalent flap, but rather research efforts should focus more on assessing the feasibility of the concept in more real world conditions.

There has been little research on the foundation loading of a modular flap-type WEC. The costs of foundations represent a large proportion of the capital expenditure for flap-type WECs. Therefore, reductions in foundation loads would likely result in significant savings.

The pitching motion of a flap-type WEC is largely driven by the dominant surge forces [4], and to a lesser extent heave forces. Thus these loading degrees of freedom (DoF) contribute to the power extraction of the device. However, the sway, roll and yaw loads can be considered parasitic as power cannot be extracted from them. Therefore, reductions in these loads would be beneficial. Due to the independence of the flap modules, it is particularly likely that there would be reductions in the yaw DoF. For a rigid flap, yaw loading results in a racking force across the structure; for both concepts, yaw loading also causes torsion of the foundation. Therefore, reducing the yaw load would decrease the demands of the whole structure and hence the cost of power.

The work presented in this paper assesses the behaviour of a modular flap-type WEC in real ocean wave conditions typical of energetic sites along the North Atlantic coast. In particular, the scope of the research is focused on the foundation loading characteristics of the concept which are quantified and compared to those of a rigid flap of equivalent width. Both fatigue and extreme loading regimes are considered which are of paramount importance to the design of any WEC concept. The rotational responses of the devices are also evaluated, to compare their average motions and to show the fundamental behaviour of the modular flap.

## 2. METHODOLOGY

### 2.1 EXPERIMENTAL SETUP

A $40^{th}$ scale model was used in physical experiments in a wave tank at Queen's University Belfast. The tank is approximately 18 m long, from the wave paddles to an absorbing beach, 4.6 m wide and has a maximum operating depth of 0.8 m.

The model that was used could be interchangeably tested as a modular flap or a rigid flap. This was done by using PVC sheets to attach adjacent flap modules together. In its modular form, the model was made up of six individual flap modules. The flap model was 0.66 m wide and 0.09 m thick. The height from the flap hinge to the top was 0.31 m.

The modules were made of high-density closed cell foam and supported with aluminium uprights. Each module had its own bearings and shaft. The

bearing blocks were attached to a structural beam. The connection to the wave tank floor was then via a single load cell. Renderings of both configurations of the model are shown in Figure 1.

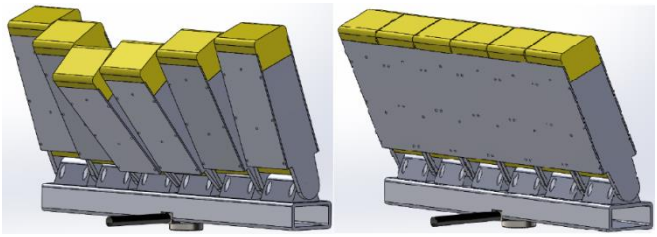

Figure 1. Renderings of modular flap (left) and rigid flap (right) model configurations, with load cell at base of model

The load cell was used to measure foundation loads in six DoF – heave, surge, sway, pitch, roll and yaw. The reference system and sign conventions are shown in Figure 2.

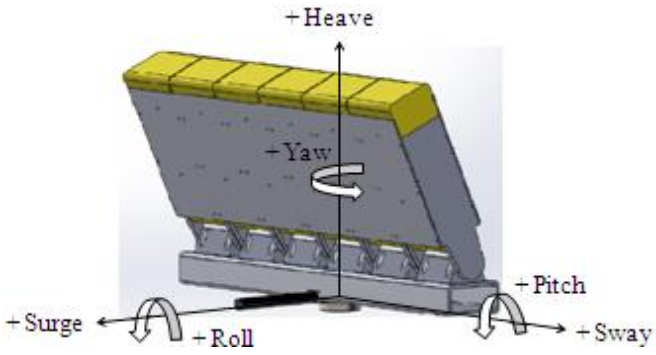


Figure 2. DoF for load cell and sign conventions; positive surge is towards the beach

The rotation angles of the flaps were measured using a motion-tracking system. This uses three infra-red cameras to track the positions of reflective balls on each flap module. The balls were mounted above the tops of the model to better avoid overtopping waves which would obstruct them from the view of the camera. The experimental setup is shown in Figure 3.

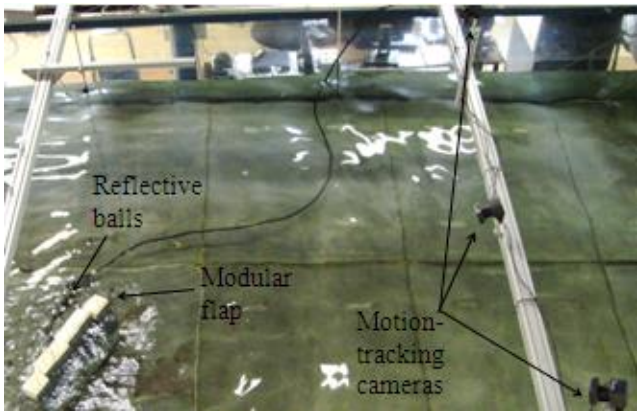


Figure 3. Motion-tracking system and modular flap in the wave tank, with the wave paddles to the right and the beach to the left

## 2.2 TEST SEA STATES

The models were tested in a range of irregular wave conditions, based on data from the wave testing birth at EMEC. This data was taken from long time history numerical modelling results, validated with in-situ Acoustic Doppler Current Profiler measurements, by Aquamarine Power Ltd. The waves that were selected included both regularly occurring sea states, for fatigue testing, and extreme storm conditions. All tests were run for 128 seconds at model scale.

To obtain results of the highest accuracy when estimating fatigue, it would be necessary to use the full range of sea states that are likely to occur at the site over the lifetime of the device. However, for concept comparison, as was being done in this investigation, sufficient accuracy can be achieved with a smaller set of sea states. When the results are interpolated across the full wave resource scatter table of sea states, global metrics, such as the annual fatigue, can be achieved that are within a few percent of those from testing across a much larger range. In this case, seven sea states were selected, which are shown in full-scale in Table 1.

**Table 1. List of sea states for fatigue testing**

| Sea State | $H_s$ (m) | $T_m$ (s) |
|---|---|---|
| 1 | 0.75 | 5.5 |
| 2 | 1.75 | 5.5 |
| 3 | 1.25 | 8.5 |
| 4 | 3.25 | 8.5 |
| 5 | 0.75 | 9.5 |
| 6 | 2.75 | 11.5 |
| 7 | 4.75 | 13.5 |

For extreme sea testing, wave conditions with a 1 in 100 year return period were used. These are characterised by a significant wave height, $H_s$, of 8.1 m and mean wave period, $T_m$, of 11.2 s. The derivation of this extreme condition was achieved following the procedure outlined in [7].

## 2.3 WAVE DIRECTIONS

As well as different wave conditions, both modular and rigid flap model configurations were tested in a range of wave directions. Alternative wave directions were achieved by rotating the model to create an angle between it and the incident waves. An example of such a case is shown in Figure 3. The models were tested, in all wave conditions, at 0 degrees, i.e. head-on waves, and in off-angle cases of 15, 30 and 45 degrees.

The foundation loads were recorded in all test cases, but the rotations were recorded for the wave direction angles of only 0 and 45 degrees. The intermediate angles were not recorded due to time restrictions and the fact that detailed evaluation of the responses of the models was not a priority.

## 2.4 FATIGUE LOADING ANALYSIS

The primary purpose of this paper is to compare the foundation loading on modular and rigid flap concepts. The focus is not on formulating a complex fatigue analysis procedure. Therefore, a simple metric is used here to evaluate the fatigue loading. The metric, referred to as the 'Total Effective Load Range' (TELR) represents the long term average of a random load oscillation. A lower TELR is desirable as it means that less fatigue damage has been incurred. The metric was calculated for each DoF.

A Rainflow method, using Matlab's free to download toolbox [16], is used to first count the load amplitudes, *F*, and numbers of load reversals, *N*, from the recorded load time-series in each sea state. The 'damage' contribution of each reversal is found by raising its amplitude to a fatigue damage exponent, *m*, and then multiplying this by the number of reversals. The *m* value used here, from typical SN curves for the assumed foundation material, steel with corrosion protection, was 5, because the overall number of load cycles is assumed to be greater than 1 million [17]. The damage contribution of the single sea state, $DC_{single\ sea}$, is then the sum of these products, as shown in Equation 1.

Equation 1:

$$DC_{single\ sea} = \sum N * F^m$$

The effective load range for each sea state, $ELR_{single\ sea}$, is then found, first by dividing its damage contribution by the number of waves in the test time-series, $n_{test}$. This is then raised to the power of the inverse of *m*, as shown in Equation 2.

Equation 2:

$$ELR_{single\ sea} = \left(\frac{DC_{single\ sea}}{n_{test}}\right)^{\frac{1}{m}}$$

The damage from each sea state, $D_{single\ sea}$, over a year is then found by multiplying $ELR_{single\ sea}$, raised to the power *m*, by the number of waves in that sea state in a year, $n_{single\ sea}$, as shown in Equation 3.

Equation 3:

$$D_{single\ sea} = n_{single\ sea} * ELR_{single\ sea}{}^m$$

The damage from each of the tested sea states is then interpolated and extrapolated across the full resource scatter table. The damage in a whole year, *Total Yearly Damage (TYD)*, is then found by summing the damage produced by each sea state, as shown in Equation 4.

Equation 4:

$$TYD = \sum D_{single\ sea}$$

To find the *TELR*, the *TYD* is first divided by the number of cycles in a year, $n_{year}$. This is assumed to be 5 million, which is approximately equal to the number of waves in a year, based on a conservatively low mean period of 6.5 seconds. This quotient is then raised to the inverse of *m*, as shown in Equation 5.

Equation 5:

$$TELR = \left(\frac{TYD}{n_{year}}\right)^{\frac{1}{m}}$$

## 2.5 EXTREME LOADING ANALYSIS

The extreme loading results were analysed to deduce a measure of the maximum loads in each DoF. This was done for each direction, giving four sets of results per model. However, taking purely the maximum value from each time-series could give unrepresentative results. This is because of the inherent limitations in repeatability of an extreme event. Therefore, instead, a percentile of all the load maxima recorded was taken in each case. This is a value under which a percentage of the loads occur. The 98$^{th}$ percentile, which was used for this analysis, is the load that 98% of the loads fall below. The cumulative distribution function (CDF) is the cumulative probability that other loads will fall below the values. Figure 4 shows an example of a CDF for surge loading on the modular flap, indicating the 98$^{th}$ percentile.

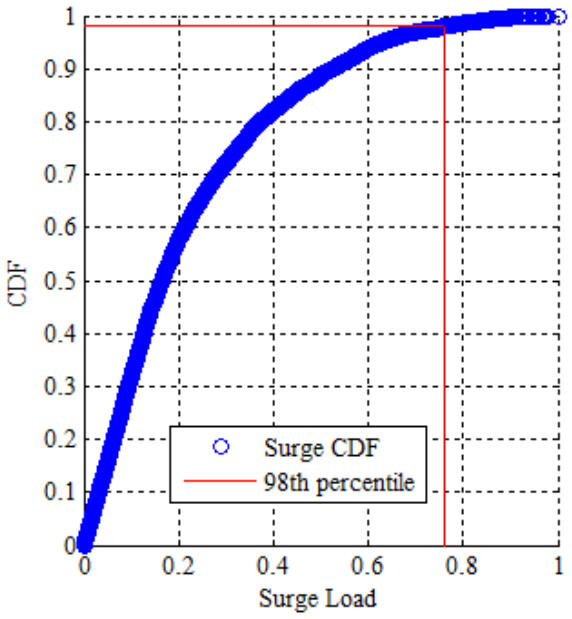


Figure 4. Cumulative Distribution Function (CDF) example showing 98$^{th}$ percentile surge load from extreme wave tests; loads normalised with maximum value from time-series; results from modular flap at 0 degrees

# 3. RESULTS AND ANALYSIS

The results from the fatigue and extreme foundation loading are first presented, followed by those related to the motion responses of the models. All loading results have been normalised and time periods are shown in full-scale.

## 3.1 FOUNDATION LOADING

### 3.1 (a) Fatigue Loading

It is first interesting to look at examples of the foundation loading time-series. Figure 5 shows two of these, for surge and yaw loads in 15 degrees off-angle waves.

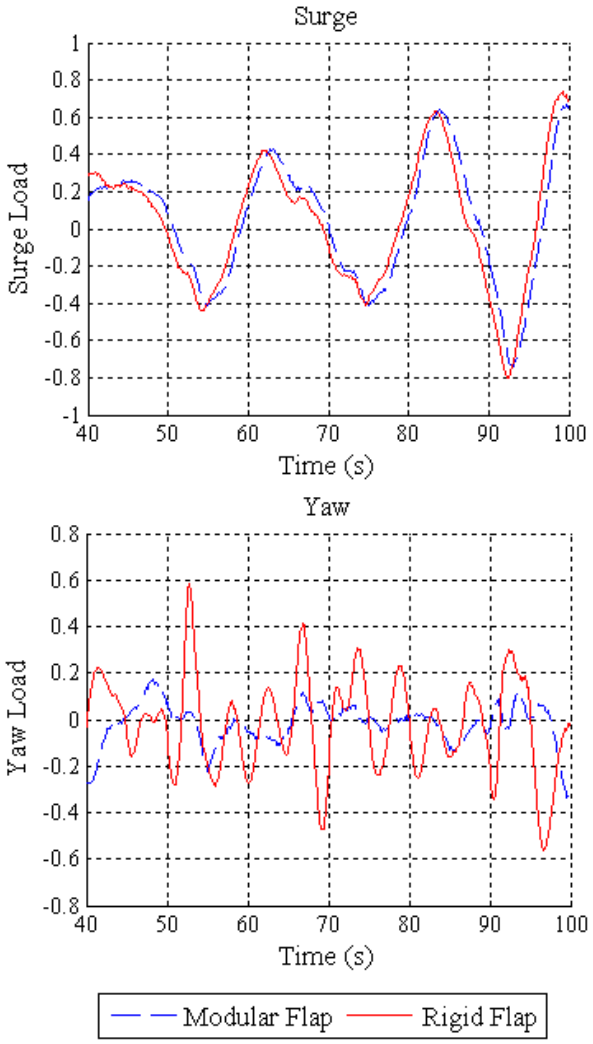


Figure 5. Example time-series of surge and yaw loads for modular and rigid flaps; loads normalised with maximum values from time-series; sea state 2; 15 degrees off-angle

Figure 5 shows that, for this example, the surge loads were very similar for the modular and rigid flap models. The yaw loads were smaller though for the modular flap. These trends were seen across many of the time-series, the latter case being because of the independence of the modular flap modules. Further explanation for this is given in section 3.1 (c).

To summarise the loads, the TELRs were calculated. This was carried out for each DoF and each wave direction and the results are shown in Figure 6.

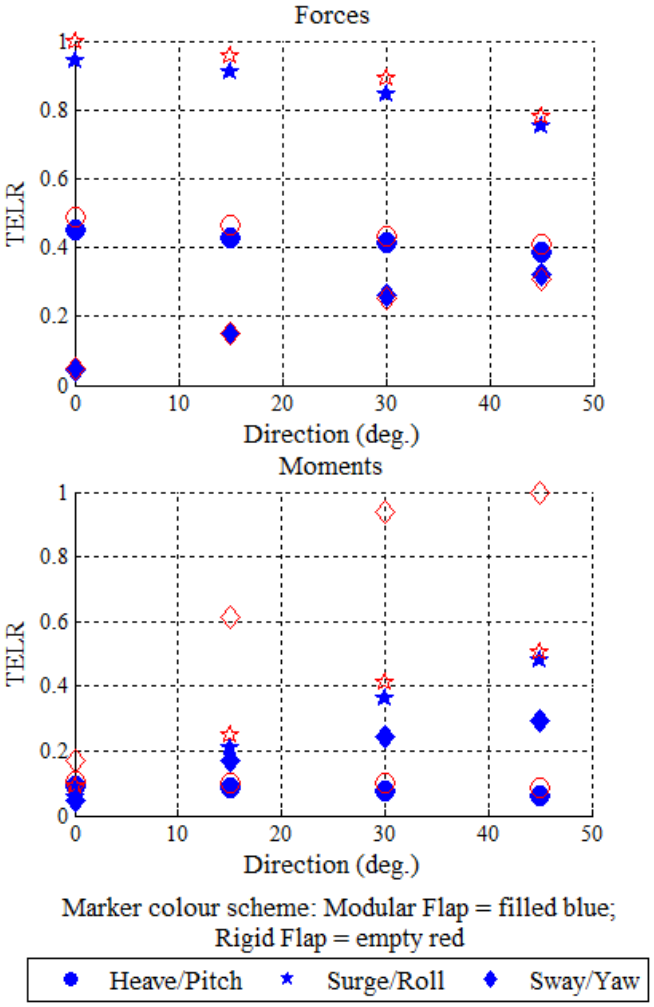


Figure 6. Total Effective Load Ranges (TELRs) for each DoF and each model direction; forces and moments normalised with maximum surge and yaw TELRs, respectively, of rigid flap

Figure 6 shows that for the head-on case, the TELRs were virtually the same for both models. There were small roll, sway and yaw loads due to slight asymmetries in the models and wave front. For off-angle waves though, in virtually all DoF, the TELRs were reduced with the modular flap. The most significant difference, as might be expected, was in yaw. The modular flap incurred about 71% lower yaw fatigue at 45 degrees, for example.

Using the same weighting for different directions gives an unrealistic bias towards off-angle waves. In the nearshore wave environment at EMEC, the directional spread is reduced compared to offshore [4]. It is therefore more realistic to apply different weightings to each of the directions. This was done by using sea state occurrence matrices, split into directional bins. Table 2 presents the directional occurrences and closest fitting results that were used.

**Table 2. Directional bins and corresponding results used for EMEC site**

| Bin (deg.) | Bin Centre (deg.) | +/- Head-On (deg.) | Results Angle Used | Occurrence (%) |
|---|---|---|---|---|
| 280-295 | 288 | 0 | 0 | 56 |
| 295-315 | 305 | 18 | +/- 15 | 29 |
| 260-280 | 270 | -18 | +/- 15 | 16 |

Any differences in loading due to direction would also be likely more significant for a site with greater directional spread. The more energetic site of Lewis, off the west coast of Scotland, represents such a case. Modelled data was used to produce directional occurrence tables. Table 3 presents the directional occurrences and closest fitting results that were used.

**Table 3. Directional bins and corresponding results used for Lewis site**

| Bin (deg.) | Bin Centre (deg.) | +/- Head-On (deg.) | Results Angle Used | Occurrence (%) |
|---|---|---|---|---|
| 292-307 | 299 | 0 | 0 | 18 |
| 307-327 | 317 | +18 | +/- 15 | 11 |
| 272-292 | 282 | -18 | +/- 15 | 35 |
| 327-347 | 337 | +38 | +/- 30 | 11 |
| 252-272 | 262 | -38 | +/- 30 | 5 |
| 232-252 | 242 | +58 | +/- 45 | 10 |
| 347-7 | 357 | -58 | +/- 45 | 10 |

The resulting TELRs, for both the EMEC and Lewis sites, are then shown in Figure 7.

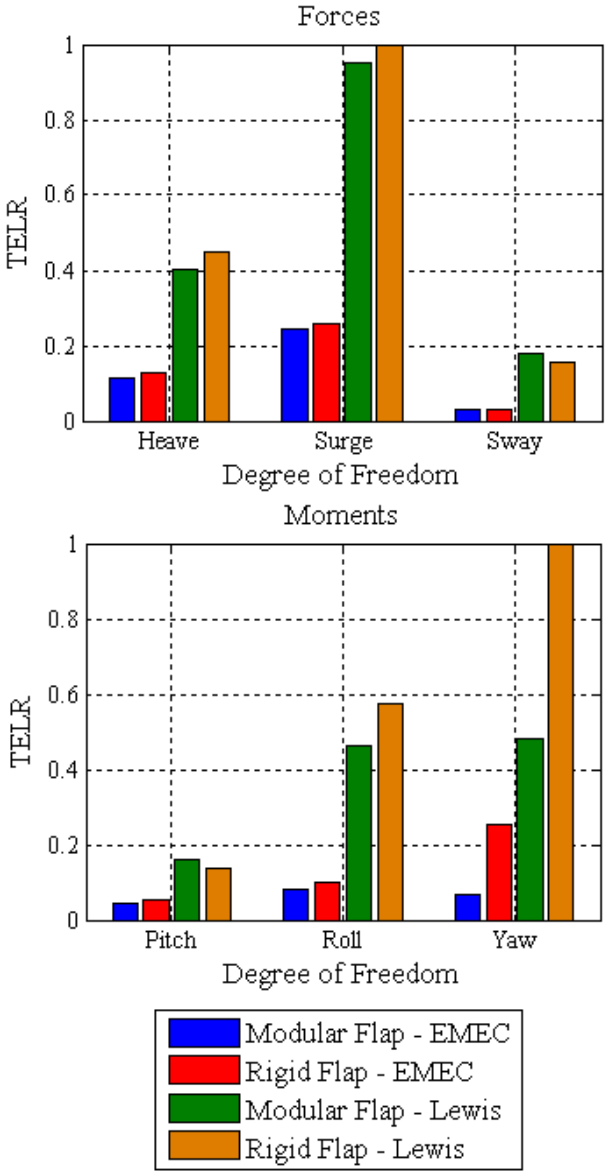


Figure 7. Total Effective Load Ranges (TELRs) for directionally spread waves at EMEC and Lewis sites; forces and moments normalised with surge and yaw TELRs, respectively, of the rigid flap Lewis results

Figure 7 shows that while the forces and the pitch fatigue loading were similar for the modular and rigid flaps, the yaw loads were significantly reduced with the modular flap at both sites. For the EMEC site, even with a relatively narrow directional bandwidth, the yaw loads were reduced by 73%; at Lewis, there was a decrease of 52%.

In all DoF, the loading was significantly greater at the more energetic Lewis site for both flap models. The yaw load on the rigid flap, for example, was almost four times larger. Therefore, while the percentage difference between the yaw loading of the models at EMEC was larger, the absolute load reduction was almost three times larger at Lewis. There were also noticeable reductions in roll loading at Lewis, with the modular flap incurring 19% less fatigue than the rigid flap.

3.1 (b) Extreme Loading

The 98$^{th}$ percentile loads were calculated for both modular and rigid flaps, for all DoF and all model directions. To summarise the values, the mean 98$^{th}$ percentile loads from each set of model directions are presented in Figure 8.

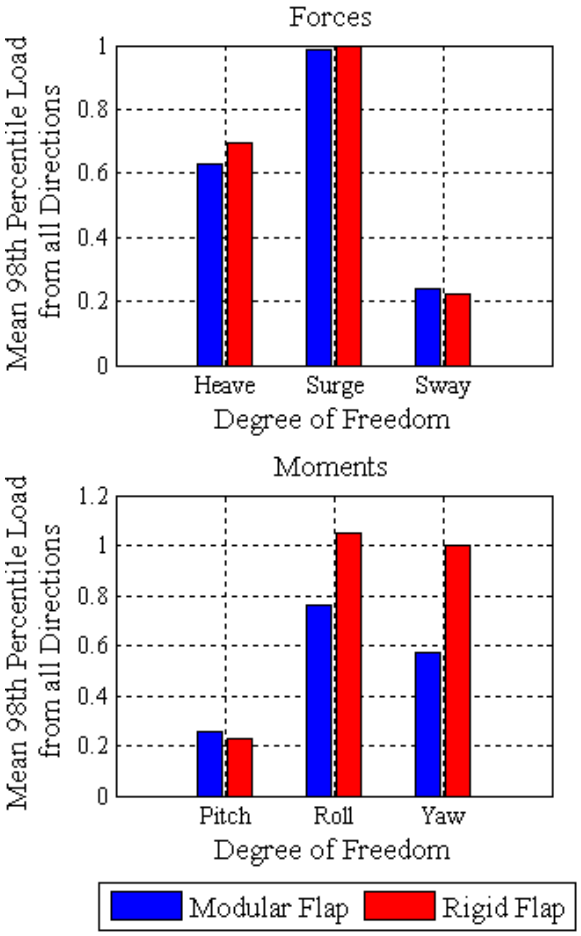


Figure 8. Mean 98$^{th}$ percentile loads from extreme load tests from all directions; forces and moments normalised with surge and yaw values, respectively, of the rigid flap

Figure 8 shows that, similar to the fatigue analysis, the extreme forces and pitch loads were similar for the modular and rigid flaps. Again, the yaw load was significantly smaller for the modular flap, with a reduction of 43%. The difference, when compared to the fatigue tests, was that the roll load case was of much greater relative significance. There was also a 28% reduction in the roll load for the modular flap.

3.1 (c) Loading Summary

In general, the modular flap had significantly reduced fatigue and extreme loading in the yaw DoF. Yaw loads occur for both flaps in off-angle waves because of the resultant surge load acting away from the central axis of the load cell. As shown in all of the loading plots, the surge loads for the modular and rigid flaps were very similar. While the modules in the modular flap move independently, the sharing of a foundation means that it still experiences yaw loading across the device.

The pressures due to the resistance of the water, such as the added mass, act to reduce the surge loads. For the rigid flap, the resultant force of this pressure acts close to the centre of the structure, and therefore provides little resistance to the yaw load. For the modular flap though, the independence of the modules means that the resisting pressure acts at the centre of the module, i.e. away from the load cell axis. This results in a force that acts opposite to the yaw load, reducing the resultant moment.

## 3.2 ROTATIONAL RESPONSES

This section describes and evaluates the rotational responses of the modular and rigid flaps. Particular focus is on the fundamental behaviour of the modular flap. While reductions in foundation loading are desirable, a simultaneous reduction in the modular flap's average response would likely be detrimental to power production. This is because the rotations of an undamped flap give some indication as to how the device will perform as a WEC. Therefore, the average responses of the modular and rigid flaps are also compared. For the following plots, the flap modules have been numbered, as shown in Figure 9.

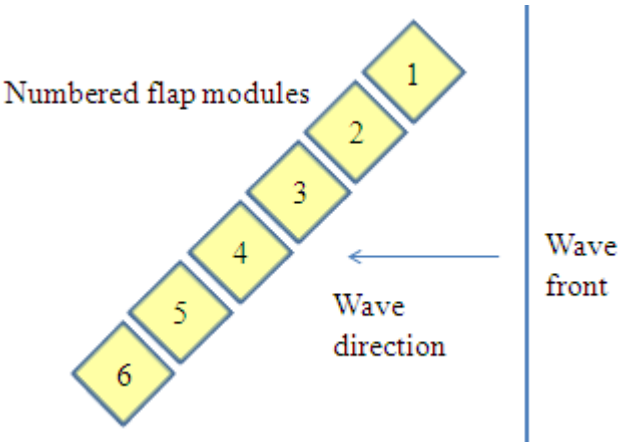


Figure 9. Modular flap module numbering system

For head-on waves, the flap modules were mostly in-phase with each other. Though there was generally a phase difference between adjacent modules, motion was in symmetrical pairs about the central modules, 3 and 4. An example of this is shown in Figure 10.

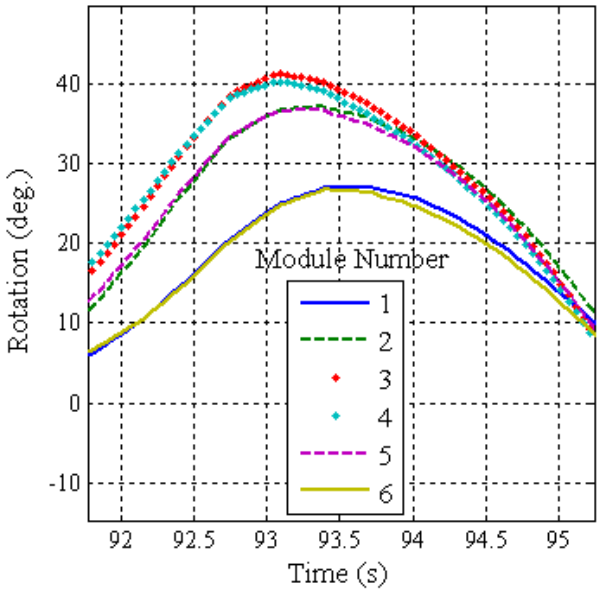


Figure 10. Example of rotations of flap modules, showing symmetrical pairs of modules moving together; head-on waves; Sea State 6

For the off-angle waves though, there was a phase difference of all modules, with an example shown in Figure 11.

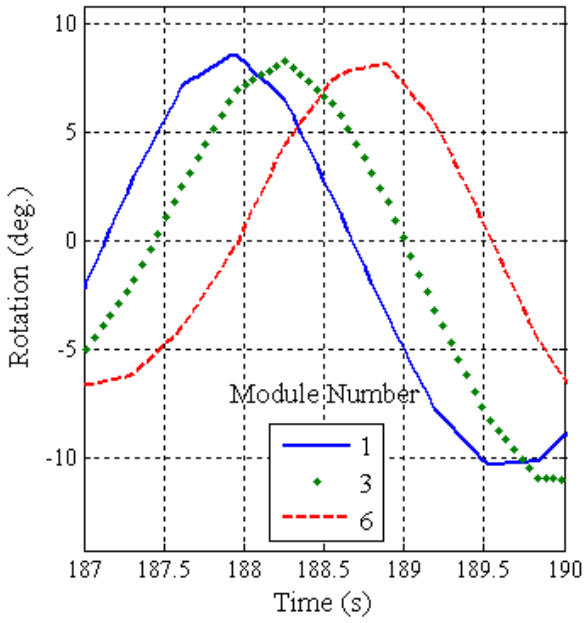


Figure 11. Motion of modules in off-angle waves, showing phase differences; model angled 45 degrees to waves; Sea State 2

The independence of the flap modules, shown in Figure 11, results in the reduction of yaw foundation loads in off-angle waves.

The amplitudes of rotation of individual flap modules of the modular flap were generally different across the device, especially so for the waves of longer period or larger height. Figure 12 shows an example where the middle modules moved more than the others.

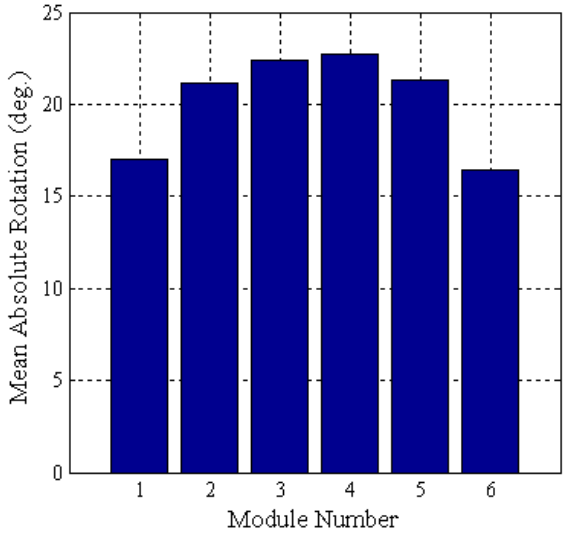


Figure 12. Average rotations of flap modules of modular flap against module number; example from head-on wave tests, Sea State 6

While the individual rotations of the flap modules may have differed to the rigid flap, comparing the average rotations of the two concepts is of more general interest. The average absolute rotations were recorded for six out of seven of the sea states used. The results from Sea State 7 were not used due to the high frequency of instances where the motion-tracking reflective balls were obstructed by large overtopping waves. The mean values from each of the six sea states for the modular and rigid flaps at 0 and 45 degrees were then evaluated. The means of these sets were then taken, giving four results, which are shown in Figure 13.

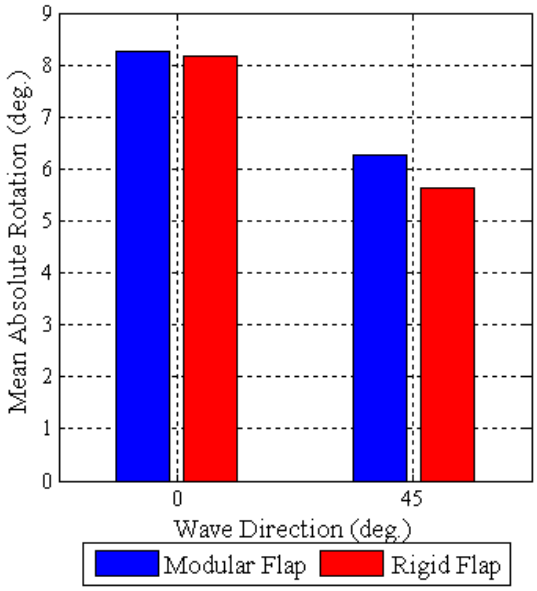


Figure 13. Averages of mean absolute rotations for sea states 1-6, at angles of 0 and 45 degrees

Figure 13 shows that there was little difference between the mean rotations of the modular and rigid flaps. Although applying damping to the models would change their dynamics, this undamped case gives some indication that there will not be a significant loss of power production with a modular flap.

## 5. CONCLUSIONS

The primary goal of this paper was to compare the foundation loads of a modular flap to a rigid flap. Fatigue loading was analysed at the sites of EMEC and Lewis, the latter of which was characterised by more energetic and directionally spread waves. Extreme loading conditions, at the EMEC site, were also tested.

The results showed that fatigue loading, in directionally spread waves, was significantly lower in the yaw DoF for the modular flap. There were reductions of 73% and 52% at EMEC and Lewis, respectively. The absolute reduction was approximately three times larger at the Lewis site.

Extreme yaw loading was also significantly lower for the modular flap, with a maximum reduction of 45%. There was also a 28% reduction in the extreme roll load.

The average rotations across the modular flap, in head-on and off-angle waves, were approximately the same as the rigid flap. This potentially suggests that there will be no significant reduction in power production for a damped device.

These results show that the modular flap is a promising concept for flap-type WECs, with reductions in parasitic foundation loads and no obvious significant loss of hydrodynamic response. Future testing will be of a damped modular flap, to quantify directly if both reduced foundation loading and improved power capture can be achieved.

## ACKNOWLEDGEMENTS

Thank you to Aidan Flaherty, a mechanical technician at Queen's University Belfast, and Jon Nicholson, of Aquamarine Power Ltd. Their skilled design and fabrication of the physical flap model made this investigation possible.

## REFERENCES

1. Folley, M., Whittaker, T., Van 't Hoff, J., 2007 'The Design of Small Seabed-Mounted Bottom Hinged Wave Energy Converters', *7th European Wave & Tidal Energy Conference, Porto*

2. Folley, M., Whittaker, T., Henry, A., 2007 'The Effect of Water Depth on the Performance of a Small Surging Wave Energy Converter', *Ocean Engineering 34, 1265–1274*

3. Whittaker, T., Folley, M., 2012, 'Nearshore oscillating wave surge converters and the development of Oyster', *Philos. T. Roy. Soc. A, 370, 345–364*

4. Henry, A., Doherty, K., Cameron, L., Whittaker, T., Doherty, R., 2010. 'Advances in the Design of the Oyster Wave Energy Converter.' *Marine & Offshore Renewable Energy, RINA, London*

5. Renzi, E., Doherty, K., Henry, A., Dias, F., 2014. 'How does Oyster work? The simple interpretation of Oyster mathematics.' *European Journal of Mechanics B/Fluids. 47, 124-131*

6. Babarit, A., et al, 2012, 'Numerical benchmarking study of a selection of wave energy converters', *Renewable Energy, 41, 44-63*

7. Doherty, K., Folley, M., Doherty, R., Whittaker, T., 2011, 'Extreme Value Analysis of Wave Energy Converters', *Proc 21st Int J Offshore and Polar Eng, Maui, ISOPE*

8. Clabby, D., Henry, A., Folley, M., Whittaker, T., 2012, 'The Effect of the Spectral Distribution of Wave Energy on the Performance of a Bottom Hinged Flap Type Wave Energy Converter' *Proc 31st Int. Ocean Offshore and Arctic Eng., Rio de Janeiro, OMAE*

9. Consorzio Venezia Nuova. 1988, 'Study on the influence of the inclination angle and the gate shape on gate response'. *Technical report studio 2.2.10 by Delft Hydraulic*

10. Sammarco, P., Tran, H., Mei, CC., 1997, Subharmonic resonance of Venice Storm Gates in waves. I. Evolution equation and uniform incident waves', *J. Fluid Mech. 349:295-325*

11. Sammarco, P., Tran, H., Gottlieb, O. & Mei, C.C., 1997 'Subharmonic resonance of Venice Storm Gates in waves. II. Sinusoidally modulated incident waves', *J. Fluid Mech. 349:327-359*

12. Adamo, A., Mei, CC., 2005, 'Linear response of Venice storm gates to incident waves'. *Proceedings of the Royal Society of London A 461: 1711-34*

13. Renzi, E., Dias, F., 'Relations for a Periodic Array of flap-type wave energy converter' 2012, *Applied Ocean Research, 39, 31-9*

14. Sammarco, P., Michele, S., d'Errico, M., 2013, 'Flap gate farm From Venice lagoon defense to resonating wave energy production. Part I: Natural modes'. *Applied Ocean Research, 43, 206-13*

15. Sarkar, D., Doherty, K., Dias, F., 2014, 'The modular concept of the Oscillating Wave Surge Converter', *Submitted*.

16. Nieslony, A., 2010, 'Rainflow Counting Algorithm', available from: *http://www.mathworks.co.uk/matlabcentral /fileexchange/3030-rainflow-counting-algorithm, accessed on 22/07/14*

17. Norwegian Technology Standards Institution, 1998, 'NORSOK N-004 Design of Steel Structures'

# Modelling the Performance of a Modular Flap-Type Wave Energy Converter

Laurie Wilkinson[#1, *], Kenneth Doherty[*2], Jonathan Nicholson*[3], Trevor Whittaker'[4], Sandy Day[~5]

[#]*Industrial Doctoral Centre for Offshore Renewable Energy (IDCORE), University of Edinburgh*
*The King's Buildings, Faraday Building*
*Edinburgh, EH9 3JL, United Kingdom*
[1]l.wilkinson@ed.ac.uk

[*]*Aquamarine Power Ltd*
*Elder House, 24 Elder Street*
*Edinburgh, EH1 3DX, United Kingdom*
[2]kenneth.doherty@aquamarinepower.com
[3]jonathan.nicholson@aquamarinepower.com

*'School of Planning, Architecture and Civil Engineering, Queen's University Belfast*
*David Keir Building, Stranmillis Road*
*Belfast, BT9 5AG*
[4]t.whittaker@qub.ac.uk

[~]*Naval Architecture & Marine Engineering, University of Strathclyde*
*Henry Dyer Building, 100 Montrose Street*
*Glasgow, G4 0LZ, United Kingdom*
[5]sandy.day@strath.ac.uk

***Abstract*— One route to increasing the economic viability of wave energy converters (WECs) would be to improve their energy conversion performance. For flap-type devices, this could be achieved by adopting a modular form. The performance must be evaluated and compared to an equivalent single 'rigid' flap. Two of the most cost-effective methods for assessing the feasibility of a new concept are numerical and laboratory-scale physical modelling. These are often complementary, with the latter being used to calibrate and validate the former.**

**In this paper, the numerical and physical modelling methodologies for assessing the hydrodynamic performance of modular and rigid flaps are shown. For the numerical model, the multi-body equation of motion for the modular flap is presented and discussed. Attempts have been made to model the interactions between the multiple bodies in an appropriate way. For the physical model, a design is presented that allows close control of the damping applied to each flap module, as well as incorporating components with high geometrical constraints.**

**The paper finishes with some preliminary comparisons of numerical to physical results for a single module. This ties in to a process whereby a validated multi-body numerical model will be built up with each flap module.**

***Keywords*— wave energy converter, power performance, modular flap, OWSC, numerical modelling, physical testing.**

## I. INTRODUCTION

There is a drive to increase the energy conversion performance of wave energy converters (WECs). This will increase their economic viability, which will lower the Levelised Cost of Energy (LCOE) associated with their electricity production. Another method of reducing the LCOE is to decrease the material requirements of the structure through design changes that lower the loads on its foundation.

Bottom-hinged flap-type WECs, or Oscillating Wave Surge Converters (OWSCs), are designed to absorb energy contained in the horizontal motion of water within ocean waves [1]. They are typically sited in the intermediate water depths of the nearshore region in order to take advantage of the amplification of horizontal water particle motion due to shoaling effects [2]. Aquamarine Power is a developer of one such OWSC called Oyster [3], [4], [5]. Oyster consists of a large buoyant flap which is hinged at the seabed and pierces the water surface. Wave action forces the flap to pitch back and forth and this mechanical energy is used to pump high pressure water ashore where it is used to produce electricity. Aquamarine Power's second full scale prototype, labelled Oyster 800, is currently deployed at the European Marine Energy Centre (EMEC) in Orkney, Scotland. Several studies have shown that the Oyster concept has many advantageous characteristics in terms of energy yield and survivability and is one of the leading WEC technologies currently under development [6], [7], [8].

The Oyster, like other similar OWSCs, comprises a single flap for the full width of the machine. Splitting a flap-type device into smaller vertical modules, to make a 'modular-flap', might provide improvements, such as in energy conversion performance. Results have already suggested that adopting such a design change will result in desired reductions in fatigue and extreme foundation loading. In the twisting/yaw degree-of-freedom, for example, fatigue loads were reduced by over 70% as shown in [9]. Other benefits may include:

increased ease and cost effectiveness of manufacture and installation, and availability due to greater component redundancy.

In this paper, the methodology for assessing the hydrodynamic performance of a modular-flap, and its rigid flap equivalent (Fig. 1), is presented. This includes numerical and physical modelling. The strategy will be to calibrate and validate the numerical model with the physical test results. The numerical model can then be used to expand the ranges of variables investigated, such as: wave climate, device and module width, power take-off (PTO) strategy, in a time efficient manner.

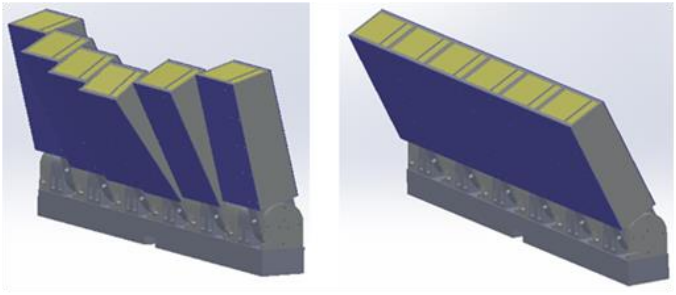

Fig. 1 CAD models of a modular flap (left) and a rigid flap (right)

Details of the numerical and physical modelling methodologies are first presented. These are followed by a short section on numerical model calibration, starting with a single body and then speculating on the multi-body approach. This is followed by some preliminary numerical model validation results for a single flap module. The paper finishes with some conclusions about the current models and, subsequently, a look to future work.

## II. Methodology

### A. Numerical Model

Numerical models have been developed for the rigid and modular flaps. The former uses a time-domain model for a single body moving in pitch, while the latter is an extension of this for multiple bodies. A time-domain, as opposed to frequency-domain, approach is used, in order to better capture non-linear effects, such as applied PTO and non-linear viscous drag damping. The equation of motion for each body is solved to predict the response, in terms of rotation, velocity and acceleration, of the device. This is in reaction to the wave excitation torque, hydrodynamic and hydrostatic effects and applied PTO damping torque. Device performance is assessed by summing the mechanical powers, which is the product of angular velocity and damping torque, of each module. Preliminary tests show that large spatial variation exists in the wave excitation torques, optimum damping torques and power captures across the device, due to the close proximity and strong interactions of the modules. The terms in the equation of motion of the device, shown in Equation 1, come from a combination of mechanical properties of the bodies, such as buoyancy, applied damping torque and hydrodynamic forces. The mechanical properties of the bodies are derived from the physical model design, while the hydrodynamic forces, wave torque, added inertia and radiation damping, are obtained from the Boundary Element Method (BEM) software, Wamit©.

The models use a number of assumptions and simplifications, which currently are:

- The hydrodynamic inputs to the model, such as wave excitation torque, from Wamit©, use the same assumptions, for example that the fluid is ideal, i.e. inviscid [10];
- Viscosity is added to the models through the use of a non-linear damping term for each flap;
- The only degree of freedom allowed by the flaps is rotation around the y-axis, which is defined as parallel with the crest of a head-on wave;
- The majority of amplitudes of motion are relatively small (less than 30°);
- Each flap module has the same mechanical properties, for example body inertia; the rigid flap has approximately the same properties, taking into account the additional mass due to the parts of the PVC sheets spanning the gaps between modules in the physical model;
- The mean water depth is constant across the motion of the flaps;
- The applied PTO control damping torque uses an approximation of a coulomb damping profile;
- There is no restriction on the level of applied PTO control damping torque;
- The restoring buoyancy term for each flap is proportional to the sine of its angular position.

This section discusses the models, with a focus on the multi-body version. For this, the governing equations of motion are shown and the derivation of some of their constituent terms explained.

*1) Single Body*: the modelling of a single flap-type wave energy converter (WEC) is well established, for example in [11], [6]. The equation of motion for the model in this paper is detailed in [11]. Accurate predictions of motion and power, when compared to laboratory results in [11] give confidence that this can be used for the current application.

*2) Multi-Body Model:* There are a number of published numerical models of multi-body wave energy converters, such as [12], [13], [14]. Indeed, multiple bottom-hinged flap-type WECs have been simulated, for example in [15], [16]. However, the application of closely-spaced, narrow flaps has not been numerically modelled before. An analytical model for such a device has been developed [17]. While complementary to this current work, this used different modelling methods and focused on regular waves. The current model uses numerical techniques and will eventually have a greater focus on real ocean, irregular wave conditions.

The single body model, discussed previously, was extended to be applicable to multiple bodies. This was based on [15], which presented a numerical model of arrays of flap-type WECs. The current work was the culmination of using this model for what is effectively a very closely-spaced array. The

equations for each body have also been adapted to incorporate a number of features from [11]. The equations of motion that are in the current model, presented in matrix form, are shown in Equation 1.

The cross-coupling interactions between the modules currently come from extensions of the added inertia and radiation damping terms to multiple values for each body. The interaction terms are the off-diagonal terms of the matrices of these hydrodynamic coefficients. These are the torques experienced by the module in-phase with another module's acceleration and velocity, respectively. The coefficients are used to calculate impulse response functions (IRFs), with one for each body and for all interactions. A convolution of each IRF is used to represent the hydrodynamics. Unlike for a widely spaced array, the off-diagonal infinite frequency added inertia terms make a non-insignificant contribution.

The final term in the equation, for the non-linear drag losses, is currently modelled without considering interactions between the bodies. Further work will be needed to encompass these interactions in a suitable manner.

$$\begin{bmatrix} T_{W_1} \\ \vdots \\ T_{W_n} \end{bmatrix} = \begin{bmatrix} I_{\infty 11} & \cdots & I_{\infty 1n} \\ & \vdots & \\ I_{\infty n1} & \cdots & I_{\infty nn} \end{bmatrix} \begin{bmatrix} \ddot{\theta}_1 \\ \vdots \\ \ddot{\theta}_n \end{bmatrix} + \begin{bmatrix} I_1\ddot{\theta}_1 \\ \vdots \\ I_n\ddot{\theta}_n \end{bmatrix} + \begin{bmatrix} \int_0^t G_{11}(\tau)\dot{\theta}_1(t-\tau)d\tau \cdots + \int_0^t G_{1n}(\tau)\dot{\theta}_n(t-\tau)d\tau \\ \vdots \\ \int_0^t G_{n1}(\tau)\dot{\theta}_1(t-\tau)d\tau \cdots + \int_0^t G_{nn}(\tau)\dot{\theta}_n(t-\tau)d\tau \end{bmatrix} + \begin{bmatrix} B_{nl_1}\dot{\theta}_1|\dot{\theta}_1| \\ \vdots \\ B_{nl_n}\dot{\theta}_n|\dot{\theta}_n| \end{bmatrix} + \begin{bmatrix} k_{P_1}\sin\theta_1 \\ \vdots \\ k_{P_n}\sin\theta_n \end{bmatrix} + \begin{bmatrix} T_{C_1} \\ \vdots \\ T_{C_n} \end{bmatrix} \quad (1)$$

- $n$ body number
- $T_W$ wave torque
- $\ddot{\theta}$ acceleration
- $\dot{\theta}$ velocity
- $\theta$ rotation
- $I_\infty$ infinite frequency added inertia
- $I$ body inertia
- $G(\tau)$ impulse response function
- $t$ time
- $k_p$ net restoring buoyancy pitch stiffness
- $B_{nl}$ non-linear damping coefficient
- $T_C$ PTO control damping torque

The control damping torque term, $T_C$, was simulated using a coulomb damping profile. This was chosen to broadly replicate the power take-off (PTO) characteristics of a typical hydraulic system, such as that used in Aquamarine Power's full scale Oyster machines. The coulomb damping was approximated to better replicate mechanical artefacts such as backlash. This was achieved through the use of the hyperbolic tangent function, as shown in Equation 2.

$$T_C = a_n * tanh(b*\dot{\theta}) \quad (2)$$

- $a_n$ damping coefficient for each body
- $b$ PTO slope coefficient
- $\dot{\theta}$ velocity

The PTO slope coefficient, $b$, sets the gradient of the section of the signal where the sign of the torque is changing direction. This is illustrated with an example in Fig. 2.

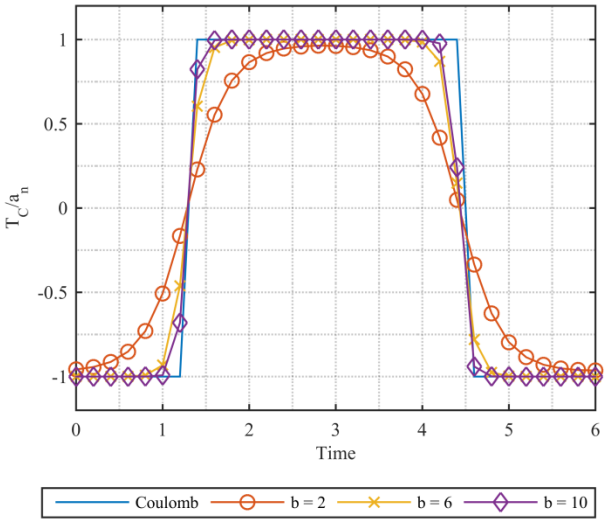


Fig. 2 Theoretical plot comparing idealised Coulomb damping torque against synthetic signals using different values of $b$ coefficient

The coefficients, $a_n$, were used to maximise the power capture of the device. A different $a_n$ value can be used for each module, due to the large differences in the hydrodynamic torques. The values were chosen using a multi-variable optimisation function in Matlab [18].

Drag losses occur due to the formation of a wake behind each body, as a result of flow separation. The flow reversal at the separation point causes vortices to form. This results in the flow in the wake being turbulent, consisting of eddies. Rapid energy dissipation takes place, causing the pressure in the wake to be reduced. This results in a net pressure on the front face of the body in the direction of the relative fluid velocity. This is referred to as the *pressure drag*. The drag contribution due to shear stress at the body surface is called the *friction drag*. The culmination of the two drags is referred to as *profile drag*. The relative contributions of the pressure and friction drags to the profile drag are determined by the shape of the body [19]. For the rigid flap, the width is approximately ten times its thickness. The profile drag will therefore likely be dominated by the pressure drag. For the smallest flap module though, the thickness is approximately two thirds as large as the width. Hence in this case, both forms of drag may have a notable contribution. With either body, from its reference point, the fluid is moving in the opposite direction to the body, and therefore the drag represents a resistive pressure. The summation of this pressure is a force, resulting in a torque. This torque can be theoretically calculated but this requires

knowledge of the pressure and shear stress distribution around the body. For a body moving in waves, this would be especially difficult. This could be laborious and it is therefore usually simpler to infer drag experimentally [19]. A similar approach is taken in this work. According to the Morison equation, drag is proportional to the square of the difference in velocity of the fluid and the body [20]. In the current application, the torque due to drag is assumed to be proportional to the square of the angular velocity of the flap. An alternative assumption, where it was proportional to velocity cubed, as in [21], was also tested. With either approach, the damping due to the drag is non-linear and is approximated using the coefficient $B_{nl}$. This can in theory be estimated from experimental free decay tests [11]. For flaps though, the number of oscillations was found to be insufficient for this approach due to the excessively high added inertia associated with this structure. The best approach to determine $B_{nl}$ was found to be empirical fitting to the measured results. This can be justified by the fact that all other coefficients in the equation of motion are known [11]. This will be the approach taken when calibrating the numerical model in this work. The $B_{nl}$ for each flap module will be indirectly determined for each wave condition.

In the current model, $B_{nl}$, is the same for each body in a single device. With this assumption, the wake of each body does not interact with that of its neighbour. For the case of a head-on wave, the validity of this assumption is reasonable. For off-angle waves though, the interactions will likely need to be considered. Further discussion on this topic is given in section C 2). An example of preliminary results from the model is shown in Fig. 3.

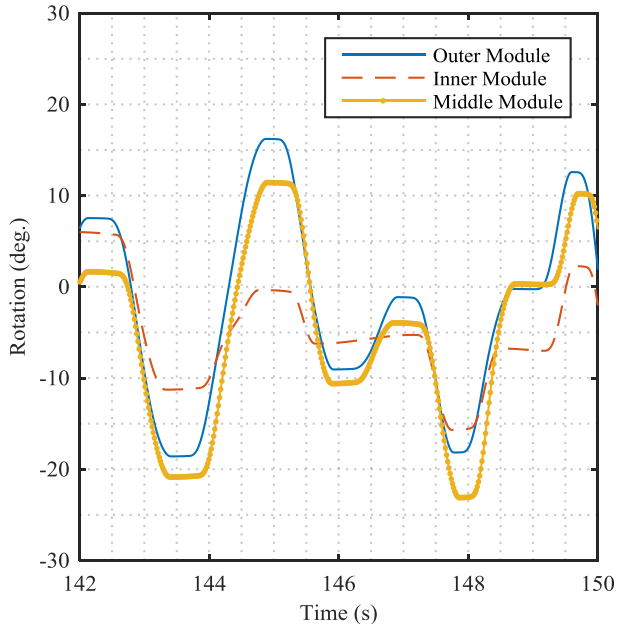


Fig. 3 Output from multi-body numerical model, showing rotations of three flap modules in six module device; irregular waves with an angle of 30° relative to the flaps' rotation axis

As shown in Fig. 3, the model captures well the expected differences in amplitudes and phases of motion of the flap modules.

### *B. Physical Model Design*

A physical model has been designed, with the purpose of providing both a testing tool in itself and a source of numerical model calibration and validation results. As of yet, a single flap module prototype has been fabricated, with the production of the full multi-body device underway. This section provides details of the design process that has been undertaken.

1) *Design Requirements*: The overall design requirement was that modular and rigid flap physical models would be produced. An extension of this was that the devices had the same dimensions and mass properties. A convenient way to satisfy both of these conditions was to create a single model that could be easily interchangeable between all of the configurations. This was achieved by locking flap modules together to change the width of each rotating body.

The required outputs from the physical model were measures of power production and foundation loads. The former was achieved, in part, through the use of a simulated PTO, or 'damper' system. This applies a torque that creates the scaled-down resistance that would be exerted by a full-scale unit, such as a hydraulic cylinder. The other component necessary to measure power production is the angular velocity of the rotating flaps. Foundation loads were measured for the whole device, meaning that the flap modules shared a common base frame.

In terms of device dimensions, the original requirement was that, at full scale, the model would be approximately the same size as Aquamarine Power's Oyster 800 machine. The Oyster 800 has a width of 26 m and operates at a depth of approximately 13 m [22]. The target to achieve the same dimensions was so that the output results from the testing regime would be comparable to those from a relatively established device. This condition also simplified the design space. The subsequent design requirement was to, for a given total width, maximise the number of modules that the modular flap consisted of. Achieving this would create the largest difference in character to the rigid flap. It would also allow a number of module widths to be tested, by locking a different number of constituent modules together. The module number was maximised by minimising the module width. This was set by the lengths of the components, such as the damper.

The final design requirement was that the device had to be at an appropriate scale. This was firstly related to the limitations of the two tanks available where this research is being conducted, at Queen's University Belfast (QUB). Constraints were in terms of water depth, wave generation capability and width, with both tanks offering different advantages over each other. The second factor related to scale was the choice of damper. According to Froude scaling, torque is proportional to the length scale factor to the power of four. Therefore, choosing a larger scale, though it facilitates more space for components, results in a rapid increase in the

required damping torque range. The design process involved a balance between all of these issues. This resulted in 30th scale being selected as the appropriate scale for physical testing.

2) *PTO Damper:* The choice of damper was governed by a number of design requirements. The primary one was that the simulated PTO could achieve approximately constant or 'coulomb' damping. This broadly represents the characteristics of full scale hydraulic systems such as that on the Oyster 800 machine. Further requirements were that the torque would be applied in an easily controlled way, with a suitable torque range, low backlash, high repeatability, relatively low cost, with suitable geometry and the ability to operate under water. Based on previous studies, scale and geometry, a suitable model scale damping range per flap module was estimated at 0.1-4.1 Nm. The constraints related to the geometry were that the damper would be, ideally, rotary and small, for example less than 120 mm in diameter. The desired rotary nature would provide the easiest model integration and would make it simpler to apply a constant torque. A large number of damping options were reviewed and tested in order to make a selection. These included disc brakes, an oil hydraulic system and a magnetic particle brake. The information from this review was collated into a table that compared the dampers against common criteria. A consolidated version of this is shown in Table 1.

TABLE I
DAMPER SELECTION

| **Damper** | **Damper Criteria** | | | |
|---|---|---|---|---|
| | **Torque Range (Nm)** | **Ease of Control** | **Relative Size** | **Relative Cost** |
| Braking clutch | unkn.-1.3 | Low | Low | Low |
| Disc brakes | 0-∞ | Medium | Medium | Low |
| Hydraulic (water) | unkn. | Low | Medium | Medium |
| Hydraulic (oil) | 1.7-10.4 | High | Medium | High |
| Linear motor | 0.7-5.2 | Medium | Medium | High |
| Magnetic particle brake | 0.07-3.95 | High | Medium | Medium |
| Electrical hysteresis brake | 0.01-2.3 | High | Medium /High | Medium /High |

The damper chosen from this selection process was the magnetic particle brake. This was because it provided a good approximation to coulomb damping, was rotary, was relatively compact at 86 mm diameter, offered a suitable damping range and good repeatability, was relatively inexpensive and was easy to control. In regards to the latter, the damping torque of the brake was controlled by changing the electrical current supplied to it. A diagram of a magnetic particle brake used in this research is shown in Fig. 4.

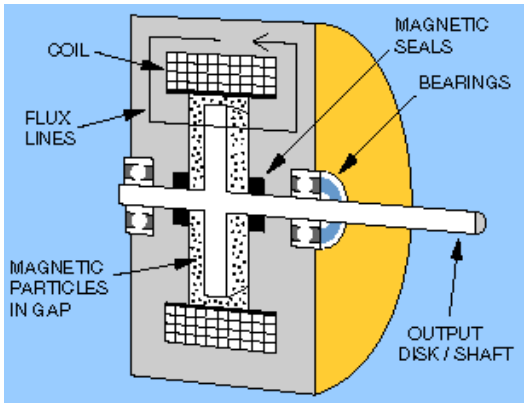


Fig. 4 Cross-section of magnetic particle brake [23]

Based on discussions with the manufacturer, the applications of magnetic particle brakes were usually not for oscillatory motions. If this motion was required, then it was recommended to mount the shaft vertically. However, thorough testing showed that the brake, horizontally mounted with oscillatory motion, was still capable of achieving the required damping characteristics.

A drawback of the brake, as opposed to disc brakes, for example, was that it was inherently not waterproof. It was decided to avoid radial shaft seals as a solution, due to the added friction and limited life associated with these. An alternative was to use magnetic couplings. These are magnetic hubs that transmit torque across an air gap. These can be separated by a non-magnetic containment barrier, allowing isolation from liquids [24], [25]. One hub would be connected to the brake shaft and both components then housed in a waterproof box. Two types of couplings were considered: 'disc' and 'co-axial'. The latter variety was eventually opted for as they avoided exerting a considerable thrust load on the shaft of the magnetic particle brake, and offered a reduced diameter. A diagram of the couplings is shown in Fig. 5.

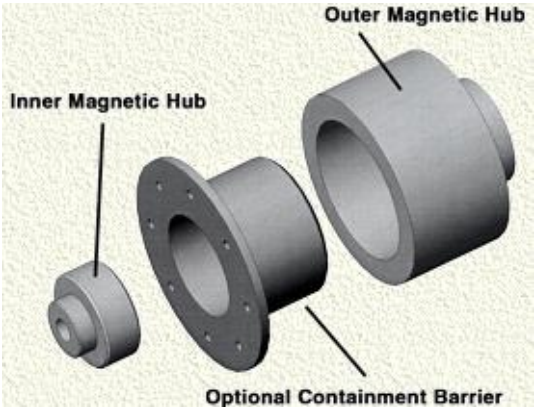


Fig. 5 Magnetic co-axial couplings with containment barrier [26]

3) *Sensors:* The model included three sensors, for measuring applied damping torque, angular velocity and foundation loads. The applied damping torque was measured using a thin-walled, strain-gauged stainless steel tube. The tube was custom designed and fabricated in-house at QUB, with the strain-gauging out-sourced [27]. The angular velocity was indirectly determined by measuring the rotation and differentiating the signal with respect to time. Two rotation sensors were considered for the application. The first was a motion-tracking system that used infra-red cameras to measure the position of reflective balls located on each flap, as used in [9]; the second measured rotation using non-contact magnetic induction to record the position of a metallic activator [28] connected to the shaft of each flap module. While both produced similar results, the latter was opted for due to its greater perceived ease of setup and higher applicability in overtopping waves and for multiple, closely-spaced bodies. Finally, the foundation loads of the whole device were measured using a six degree of freedom load cell, as used in [9]. The sensor represented the sole connection between the model and the wave tank floor.

*4) Design Process:* The design of the flap module was a process that started with a relatively crude model, containing the required components. Refinements were then made in order to reduce the width of each module. One such alteration was to, where possible, overlap parts. An example of this was using the lower diameter section of the outer magnetic coupling as the shaft connection to the torque sensor, as shown in Fig. 7. Other refinements included: requesting bespoke shortened magnetic couplings, minimising the length of the torque sensor and using low-head bolts. The module width went from approximately 270 mm to 183 mm, or 5.49 m at full scale. This transition is shown in Fig. 6. This allowed the modular flap to consist of a maximum of six modules, achieving the target total width of approximately 1 m at model scale.

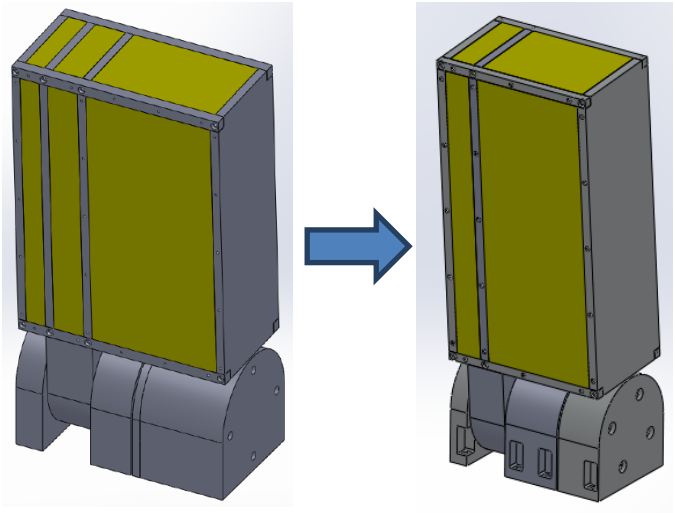

Fig. 6 Reduction in width of flap module, achieved through design refinements

The majority of machined parts were made of aluminium, stainless steel, high-density closed cell foam and PVC sheet. A cross-section of the flap module design, with the key components labelled, is shown in Fig. 7.

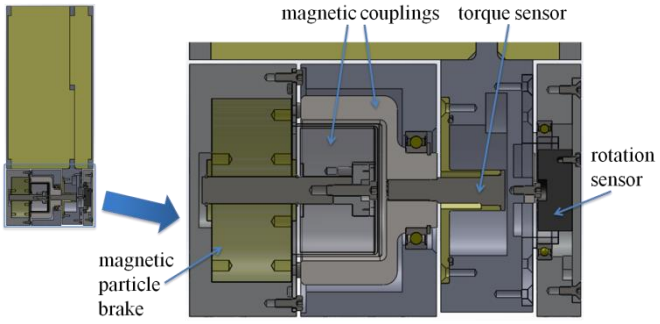


Fig. 7 Cross-section of flap module

From preliminary testing of a single flap module, the model worked to its design requirements. A sample of the damping torque and rotation results are shown in Fig. 8.

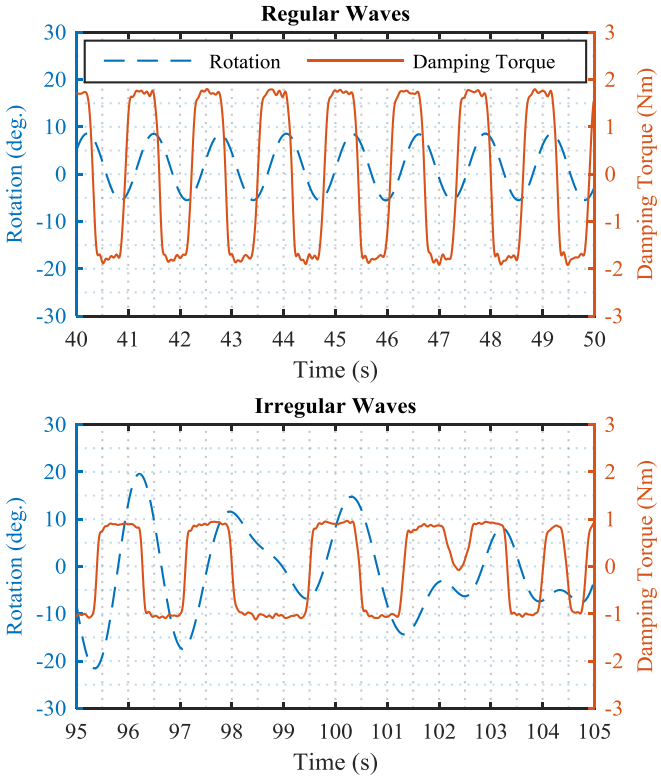


Fig. 8 Damping and rotation signals from physical model of single flap module in regular and irregular waves

5) *Overall Design:* The flap modules will be either in their smallest unit or connected with PVC sheets to change the widths of the rotating bodies. In this way, it will be possible to test the single, rigid flap and then in its modular form, in halves, thirds or sixths. Fig. 9 shows the overall model, with six modules connected to a common cross-beam and load cell.

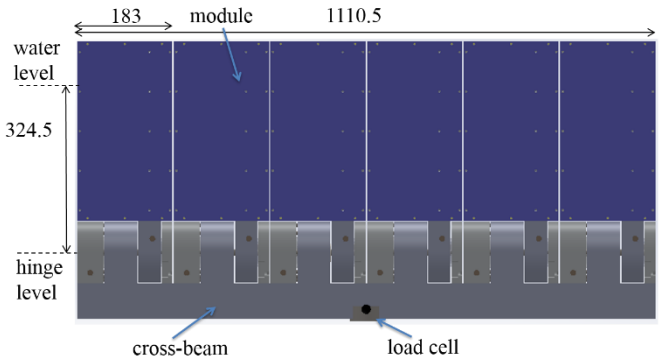


Fig. 9 CAD model of modular flap with six modules, showing dimensions, in millimetres at model scale

The flap thickness, not shown in Fig. 9, was 120 mm, and the gap between modules was 2.5 mm; the model was designed for a mean water depth of 460 mm, or 13.8 m at full scale. All key dimensions, at both model and full scale, are presented in Table 2.

TABLE II
DEVICE DIMENSIONS

| Dimension | Model Scale (m) | Full Scale (m) |
|---|---|---|
| Total device width | 1.1105 | 33.315 |
| Module width | 0.183 | 5.49 |
| Gap between modules | 0.0025 | 0.075 |
| Flap thickness | 0.12 | 3.6 |
| Depth at hinge | 0.3245 | 9.735 |
| Water depth | 0.46 | 13.8 |
| Freeboard | 0.0805 | 2.415 |

### *C. Numerical Model Calibration*

A short test series was conducted in order to test the physical model and the validity of the numerical model for the simplest case of a single module. The tests were carried out in a wave tank facility at QUB. The tank is approximately 18 m long, from the wave paddles to an absorbing beach, 4.6 m wide and has a maximum operating depth of 0.8 m. The flap module being tested is shown in Fig. 10.

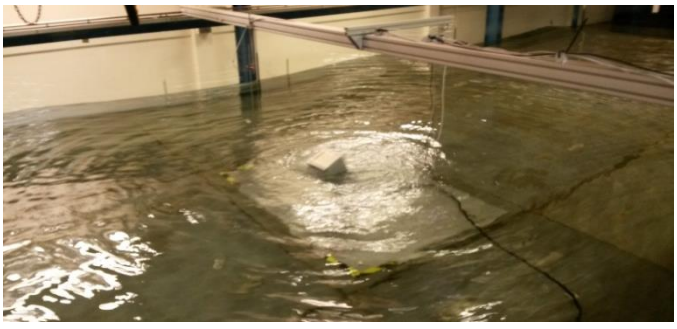

Fig. 10 Single flap module during preliminary tests in QUB wave tank

The waves that were used, presented in Table 3, were regular, of heights 0.033 and 0.067 m, and periods 1.10-2.56 s. They were of relatively small amplitudes and therefore induced small motions. These were chosen so that the terms in the equation of motion were used in the linear realm.

TABLE III
REGULAR WAVE CONDITIONS

| Wave Height | | Wave Period | |
|---|---|---|---|
| **Model Scale (m)** | **Full Scale (m)** | **Model Scale (m)** | **Full Scale (m)** |
| 0.033 | 1 | 1.10 | 6 |
| 0.067 | 2 | 1.28 | 7 |
| | | 1.46 | 8 |
| | | 1.64 | 9 |
| | | 1.83 | 10 |
| | | 2.00 | 11 |
| | | 2.19 | 12 |
| | | 2.37 | 13 |
| | | 2.56 | 14 |

Irregular waves, of a range of mean wave periods and significant wave heights were also used, but the use of the results was deemed to be outside of the scope of the paper.

The model was tested in undamped and damped conditions. The undamped tests were for estimating the non-linear damping coefficient, $B_{nl}$. The damped tests were to determine the optimum damping levels. A number of different damping levels were used for each test. The mean powers were then plotted against the root-mean-square (RMS) values of the damping torque signals. A quadratic curve was then fitted to the points, with the optimum damping level being the RMS damping torque associated with the peak average power. An example of this is shown in Fig. 11.

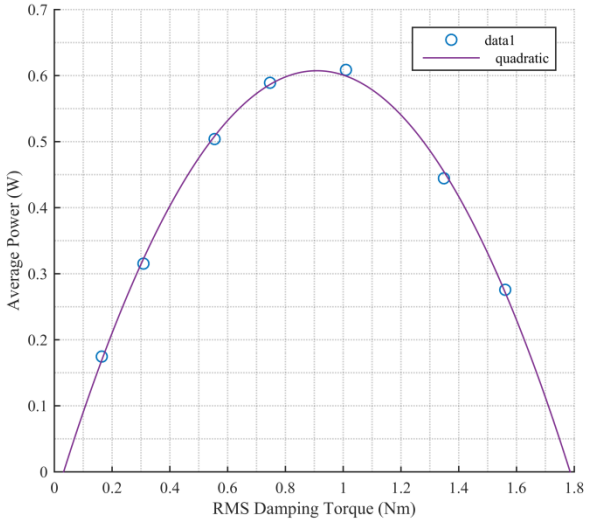


Fig. 11 A power curve with average power plot against root-mean-square (RMS) damping torque; regular waves of height 0.067 m and period 1.83 s

The optimum powers from each test were then used to compare to the numerical results.

The numerical model was first calibrated using the physical model results. The two values to derive were the non-linear damping coefficient, $B_{nl}$, and the PTO slope coefficient, $b$.

1) *Non-linear damping coefficient, $B_{nl}$, for single body:* The non-linear damping coefficient, $B_{nl}$, was estimated via empirical matching of numerical results to those from undamped tests. There was a small residual torque, of approximately 0.2 Nm, from the two bearings and the internal components of the magnetic particle brake. However, these were accounted for in the numerical model. The optimum value of $B_{nl}$ was estimated for each test. This was carried out by searching for the value that resulted in the best agreement between the velocity amplitudes of the numerical and physical results. Fig. 12 shows the resulting $B_{nl}$ value for all cases for each wave period.

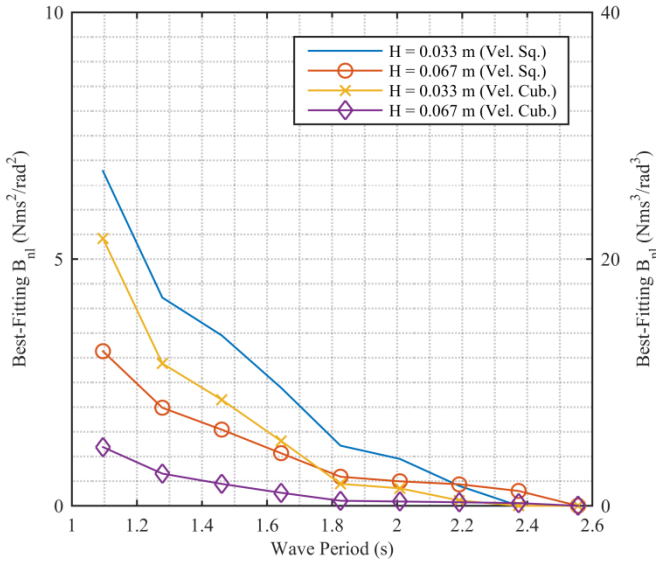


Fig. 12 Graph of non-linear damping coefficients, $B_{nl}$, from empirical matching for assumptions of damping proportional to velocity squared (left axis) and cubed (right axis), for two different wave heights, against wave period

As Fig. 12 shows, the best-fitting $B_{nl}$ values were inversely proportional to the wave periods. This meant that for the smallest periods, the required $B_{nl}$ value had to be large in order to force the numerical model. Fig. 12 also shows that, while there was convergence at the higher periods, there was large divergence between the results for the two wave heights for both data sets at the lower periods. This indicates that the $B_{nl}$ value is, as well as period, dependant on the wave height. This was likely because of the different amplitudes of velocity associated with the varied wave height. A suitable method will be required to apply this dependency for irregular, i.e. multi-period and amplitude, waves. This could be using the value that closely corresponds to the mean wave period and is proportional to the significant wave height. For the damped, wave height 0.067 m tests, the optimum $B_{nl}$ value for each period was used. Both assumptions of drag being proportional to velocity squared and velocity cubed were tested.

*2) Non-linear Damping Coefficient, $B_{nl}$, for multiple bodies:* For multiple, closely-spaced bodies, there will inevitably be interactions of their wakes. This will change the non-linear damping coefficients. To model the physical device that will be fabricated, the method of empirical matching to find the $B_{nl}$ values will still stand. For off-angle waves, the downstream bodies will be in the wakes of the preceding bodies. This could result in a reduction in the drag losses, due to lower experienced wave torque and therefore lower angular velocities. A number of direction angles will be tested with the physical model to calibrate the numerical model. $B_{nl}$ values will then be interpolated across the angles for use in the numerical model. For numerical modelling of devices of greater total width than the physical model, however, a gradual building up of the number of flap modules will be required. This will indirectly show how the drag contributions change with increasing number of bodies in the device, as done in [29]. The $B_{nl}$ values will then be extrapolated from the resulting best-fitting coefficients.

3) *PTO slope coefficient, $b$*: The value for the coefficient, $b$, in the $T_C$ term was estimated using the physical model data. A value for each test was found, using the results that had the highest mean powers for each wave condition. The optimum value for each test was deemed to be the one that gave the highest coefficient of determination (CoD), or $r^2$, between the measured damping torque and a synthetically generated signal that used the $b$ value. The formula for the *CoD* is shown in Equation 3 [11].

$$CoD = \frac{\Sigma(y_i - \bar{y})^2 - \Sigma(y_i - x_i)^2}{\Sigma(y_i - \bar{y})^2} \quad (3)$$

- $y$ measured data
- $\bar{y}$ mean of $y$
- $x$ synthetic data

An example, from the test of wave height 0.067 m and period 2.19 s, is shown in Fig. 13.

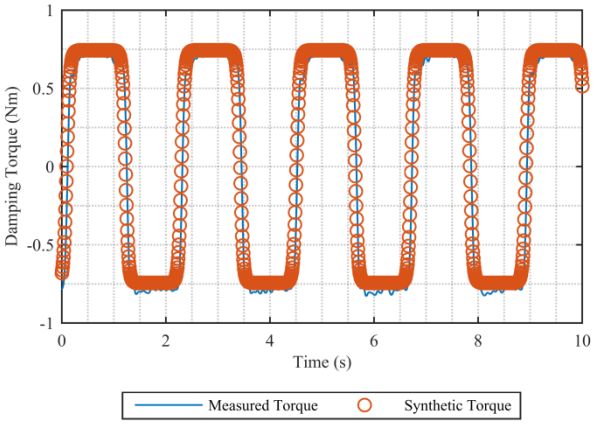


Fig. 13 Time-series of measured and synthetic damping torque signals; damping at close to optimum level for regular wave of period 2.19 s and height 0.067 m

## III. RESULTS

For the waves of height 0.067 m, the numerical model was run for each wave period to find the optimum powers. The $B_{nl}$ values from each of the undamped tests at the same height were used. Both the assumptions of a drag term proportional to the velocity squared and cubed were applied. The capture factors, i.e. the ratios of mean power captured to the mean incident power across the width of the flap, were calculated for each case. The results are presented in Fig. 14.

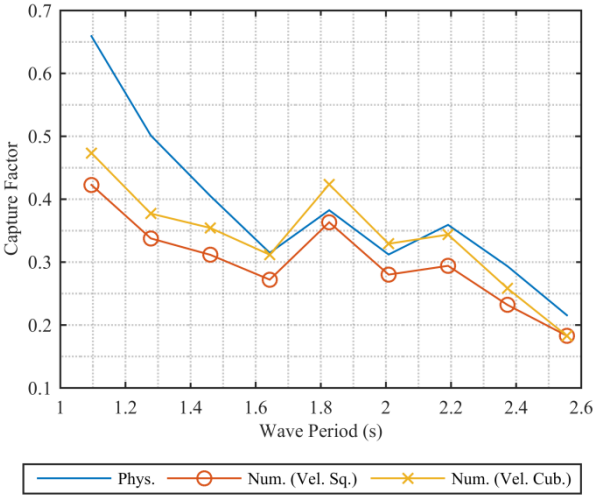


Fig. 14 Capture factors from physical and numerical models of a single flap module, in regular waves of height 0.067 m. The results using assumptions of velocity squared and cubed non-linear damping are both shown. The width of the module was 0.183 m

Fig. 14 shows that all of the models predicted an approximately inversely proportional relationship between capture factor and wave period. However, the numerical model that used an assumption of velocity squared drag estimated lower mean powers than the physical results in all cases, with an average reduction of 19%. For the model that assumed a velocity cubed drag, the error was lower, at 13% mean absolute error and -9% mean error. While the latter configuration of the numerical model achieved better agreement with the physical results, it is clear that further work is needed to improve the accuracy of the numerical model generally. Some consideration could be given, for example, to the water particle velocities and the effects that applied damping torque has on the phase difference between the water surface and the flap.

## IV. CONCLUSIONS

This paper has presented the methodology used for modelling the performance of a modular flap-type WEC. A time-domain numerical model has been described, moving from a single to a multi-body device. A physical model, used to calibrate and validate the numerical model, and its components were then presented.

The procedure used to calibrate the numerical model was shown, followed by some preliminary validation results for a single flap module. Though the general relationship between mean power capture and wave period was reproduced with the numerical model, further work is needed to remove the under-predictions shown. Confidence remains though that the full, multi-body device can be modelled accurately.

Future work will present the numerical model calibration for a multi-body device, and the validated results. This paper has also focused on power production, with [9] presenting results of foundation loading of an un-damped model. Later work will include focus on loading of a device during power production.

## ACKNOWLEDGMENTS

Thank you to Aidan Flaherty, a mechanical technician at QUB. His skilled fabrication and design guidance, for the physical model, were much appreciated. Thank you also to IDCORE, funded by the ETI and the EPSRC RCUK Energy programme, Aquamarine Power Ltd and QUB for financial and research support and the latter for providing experimental testing facilities.

## REFERENCES

[1] M. Folley, T. Whittaker and J. Van 't Hoff, "The Design of Small Seabed-Mounted Bottom Hinged Wave Energy Converters", EWTEC 2007.

[2] M. Folley, T. Whittaker and A. Henry, "The Effect of Water Depth on the Performance of a Small Surging Wave Energy Converter", *Ocean Engineering* , vol. 34, pp. 1265-1274, 2007.

[3] T. Whittaker and M. Folley, "Nearshore oscillating wave surge converters and the development of Oyster", *Philos. T. Roy. Soc. A*, volume 370, pp. 345-364, 2012.

[4] A. Henry, K. Doherty and L. Cameron, "Advances in the Design of the Oyster Wave Energy Converter", Marine & Offshore Renewable Energy, RINA, 2010.

[5] E. Renzi, K. Doherty, A. Henry and F. Dias, "How does Oyster work? The simple interpretation of Oyster mathematics". *European Journal of Mechanics B/Fluids*, volume 47, pp. 124-131, 2014.

[6] A. Babarit, J. Hals, M. J. Muliawan, A. Kurniawan, T. Moan and J. Krokstad, "Numerical benchmarking study of a selection of Wave Energy Converters", *Renewable Energy*, Vol. 41, pp. 44–63, May 2012.

[7] K. Doherty, M. Folley, R. Doherty and T. Whittaker, "Extreme Value Analysis of Wave Energy Converters", ISOPE, 2011.

[8] D. Clabby, A. Henry, M. Folley and T. Whittaker, "The Effect of the Spectral Distribution of Wave Energy on the Performance of a Bottom Hinged Flap Type Wave Energy Converter", OMAE, 2012.

[9] L. Wilkinson, V.Russo, K. Doherty and A. Henry, "Wave Loads on the Foundation of a Bottom-Hinged Modular Flap Structure", ASRANet ICORE, 2014.

[10] Wamit, "Wamit User Manual Versions 6.4, 6.4PC, 6.3S, 6.3S-PC", 1998-2006.

[11] J. Van 't Hoff, "Hydrodynamic modelling of the Oscillating Wave Surge Converter", PhD Thesis, Queen's University Belfast, 2009.

[12] M. O'Cathain et al., "A modelling methodology for multi-body systems with application to wave-energy devices", *Ocean Engineering*, volume 35, 2008.

[13] C. McComb, M. Lawson and Y.-H. Yu, "Combining Multi-Body Dynamics and Potential Flow Simulation Methods to Model a Wave Energy Converter", 1st Marine Energy Technology Symposium, 2013.

[14] OpenEI, WEC-Sim. [Online]. Available: http://en.openei.org/wiki/WEC-Sim

[15] M. Folley, Numerical Modelling of Oyster Clusters. Queen's University Belfast, Internal Tech. Rep., 2007.

[16] D. Forehand, A. Kiprakis, A. Nambiar, and R. Wallace, "Enhancement, Validation and Application of the Wave-to-Wire Array Model", SuperGen UK Centre for Marine Energy Research Annual Assembly, 2013.

[17] D. Sarkar, K. Doherty and F. Dias, “The modular concept of the Oscillating Wave Surge Converter”, *Renewable Energy* (Forthcoming), 2014.
[18] J. D'Errico (2012) fminsearchbnd, fminsearchcon. [Online]. Available: http://uk.mathworks.com/matlabcentral/fileexchange/8277-fminsearchbnd--fminsearchcon
[19] J. F. Douglas, Janusz M. Gasiorek, John A. Swaffield and Lynne B. Jack, *Fluid Mechanics*, 5th ed., J. F. Douglas, Ed. Pearson Hall, 2005.
[20] P. L.-F. Liu, Ed., *Hydrodynamics Around Cylindrical* Structures, Advanced Series on Ocean Engineering, revised ed., World Scientific Publishing Co. Pte. Ltd., 2006, vol. 26.
[21] V. Zatsiorsky, Ed., *Resistive forces in swimming*, The Encyclopedia of Sports Medicine, Blackwell Science Ltd., 2000
[22] Aquamarine Power Ltd., Projects: Oyster 800 project, Orkney. [Online]. Available: http://www.aquamarinepower.com/projects/oyster-800-project-orkney/
[23] Placid Industries, How Magnetic Particle Brakes Work. [Online]. Available: http://www.placidindustries.com/crossection-br.html
[24] Magnetic Technologies Ltd., Magnetic Couplings. [Online]. Available: http://www.magnetictech.com/prod_magcoup.htm
[25] Magnetic Technologies Ltd., Our Products. [Online]. Available: http://www.magnetictech.com/products.htm
[26] Magnetic Technologies Ltd., Co-Axial Couplings. [Online]. Available: http://www.magnetictech.com/prod_magcoup_coax_sae.htm
[27] Vishay, Vishay. [Online]. Available: http://www.vishay.com/
[28] Gill Sensors & Controls Ltd (2015) Non-Contact Rotary Sensor. [Online]. Available: http://gillsc.com/content/rotary.htm
[29] B. Buchner, A. v. Dijk and J. d. Wilde, “Numerical Multiple-Body Simulations of Side-by-Side Mooring to an FPSO”, ISOPE, 2001.

Ocean Engineering 137 (2017) 394–403

Contents lists available at ScienceDirect

Ocean Engineering

journal homepage: www.elsevier.com/locate/oceaneng

# The power-capture of a nearshore, modular, flap-type wave energy converter in regular waves

L. Wilkinson[a,b,*], T.J.T. Whittaker[b], P.R. Thies[c], A. Day[d], D. Ingram[e]

[a] Industrial Doctoral Centre for Offshore Renewable Energy (IDCORE), United Kingdom
[b] Marine Research Group, School of Natural and Built Environment, David Keir Building, Stranmillis Road, Queen's University Belfast, Belfast BT9 5AG, United Kingdom
[c] College of Engineering, Mathematics and Physical Sciences, University of Exeter, Penryn Campus, Penryn, Cornwall TR10 9FE, United Kingdom
[d] Naval Architecture and Marine Engineering, University of Strathclyde, Henry Dyer Building, 100 Montrose St, Glasgow G4 0LZ, United Kingdom
[e] Institute for Energy Systems, The University of Edinburgh, Faraday Building, King's Buildings, Colin Maclaurin Road, Edinburgh EH9 3DW, United Kingdom

ARTICLE INFO

*Keywords:*
Wave energy converter
Power
Modular Flap

ABSTRACT

Bottom-hinged, nearshore flap-type wave energy converters (WECs), have several advantages, such as high power conversion efficiency and survivability. They typically comprise a single flap spanning their full width. However, a potentially beneficial design change would be to split the flap into multiple modules, to make a 'Modular Flap'. This could provide improvements, such as increased power-capture, reduced foundation loads and lower manufacturing and installation costs. Assessed in this work is the hydrodynamic power-capture of this device, based on physical modelling. Comparisons are made to an equivalent 'Rigid Flap'. Tests are conducted in regular, head-on and off-angle waves. The simplest control strategy, of damping each module equally, is employed.

The results show that, for head-on waves, the power increases towards the centre of the device, with the central modules generating 68% of the total power. Phase differences are also present. Consequently, the total power produced by the Modular Flap is, on average, 23% more smooth than that generated by the Rigid Flap.

The Modular Flap has 3% and 1% lower average power-capture than the Rigid Flap in head-on and off-angle waves, respectively. The advantages of the modular concept may therefore be exploited without significantly compromising the power-capture of the flap-type WEC.

## 1. Introduction

There is a need to improve the economic viability of wave energy converters (WECs), for them to compete in the energy market. Design solutions must be found that have high energy yields, whilst offering manageable manufacturing, installation, maintenance and decommissioning costs.

Bottom-hinged flap-type WECs, also known as Oscillating Wave Surge Converters, are designed to absorb energy from the horizontal acceleration of water in ocean waves (Whittaker and Folley, 2012). They usually consist of a buoyant flap, with its hinge mounted on the seabed (Folley et al., 2007). These devices are typically sited in the nearshore region, in water depths of 10–20 m. There is an extensive body of work on this type of device (Henry, 2008; Renzi et al., 2014; van't Hoff, 2009). Through comparative assessments, it has been shown to be one of the most efficient in terms of power conversion (Babarit, 2015; Babarit et al., 2012). It also has cost reduction advantages, such as being located in the relatively accessible nearshore region, being simple in operation and having high survivability (Henry et al., 2010). As a result, the device type has received significant commercial focus, with a number of large scale devices deployed, such as Aquamarine Power Ltd's Oyster machines (Henry et al., 2010; Whittaker and Folley, 2012) and AW-Energy's WaveRoller devices (AW-Energy, 2012).

Most flap-type devices employ a single body for their rotating section (Folley et al., 2007). If this is large, for example 26 m in width like the Oyster 800 device (Aquamarine Power Ltd, 2011), then asymmetric pressure across the flap results in twisting of the structure, including its foundation (Wilkinson et al., 2014). The use of a single wide unit like this can also necessitate the use of large, expensive

* Corresponding author at: Industrial Doctoral Centre for Offshore Renewable Energy (IDCORE), United Kingdom.
*E-mail addresses:* l.wilkinson@ed.ac.uk (L. Wilkinson), t.whittaker@qub.ac.uk (T.J.T. Whittaker), p.r.thies@exeter.ac.uk (P.R. Thies), sandy.day@strath.ac.uk (S. Day), david.ingram@ed.ac.uk (D. Ingram).

http://dx.doi.org/10.1016/j.oceaneng.2017.04.016
Received 7 January 2017; Received in revised form 12 April 2017; Accepted 14 April 2017
Available online 21 April 2017

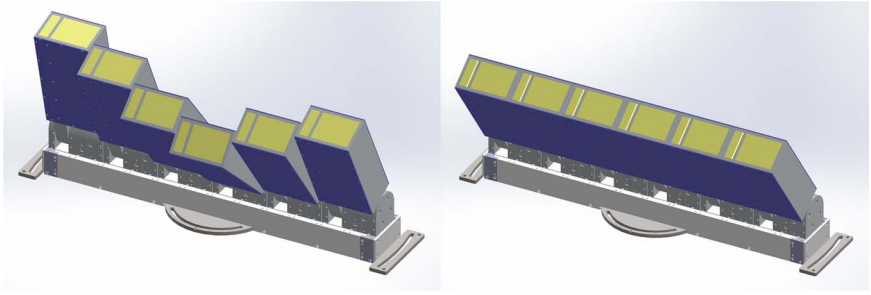

**Fig. 1.** CAD renderings of physical model in Modular Flap (left) and Rigid Flap (right) configurations.

installation vessels (Aquamarine Power Ltd, 2009). Additionally, the power produced by the device is sensitive to the direction of the incident wave (Henry, 2008). A new concept, the 'Modular Flap', formed by splitting the rotating body into a number of narrow, mechanically independent, vertical modules, may reduce the magnitudes of these problems. This could provide improvements, such as increased power production in directional waves, reduced foundation loads, an indicator of capital cost, and lower manufacturing and installation costs. There could also be operational advantages such as increased redundancy in the system, reducing the effect of failure on one module versus a whole flap. Additionally, a modular formation would make the scaling up of devices, in terms of overall width, arguably more feasible.

There are a number of studies on offshore structures comprised of multiple flaps (Mei et al., 1994; Wilkinson et al., 2014). In Wilkinson et al. (2014), it was shown that the foundation loads were reduced for such a device, by up to 73% in the parasitic twisting yaw and roll degrees of freedom. However, the application of such a device for the purpose of wave energy extraction has only recently received attention (Abadie and Dias, 2016; Álvarez, 2015; Sammarco et al., 2013; Sarkar et al., 2016; Wilkinson et al., 2015). These studies investigated the behaviour of the device, in terms of motion amplitudes, and most of them included a power-capture assessment. The latter is a key element of a techno-economic evaluation of a WEC concept. Sarkar et al. (2016), for example, presents a mathematical power-capture assessment of a 24 m wide device, made up of six cylindrical modules. Regular, head-on waves were used in the study. It was found that the power-capture of the modular system was highly dependent on the power take-off (PTO) damping strategy. With each module damped equally, both devices achieved similar levels of power-capture. However, using different damping on each module, the modular flap outperformed the rigid flap, due to the occurrence of multiple resonances. While this study provided an insight into the potential of the device, there were limitations of the modelling that was used, such as not considering nonlinear and viscous effects (Sarkar et al., 2016). The use of scale physical modelling can address these issues by working in a real fluid. It also provides reasonably fast generation of sufficiently long data time-series, compared to, for example computational fluid dynamics (Abadie and Dias, 2016). In this paper, physical modelling in a wave tank is used to assess the hydrodynamic power-capture of the Modular Flap. This is carried out across a range of wave conditions. Comparisons are made to a single device with an equivalent total width, referred to throughout this work as the 'Rigid Flap'. Shown first, in Section 2, are the modelling and analysis methodologies, followed by presentation of the results in Section 3 and finally, in Section 4, some conclusions and suggestions for further work.

## 2. Methodology

This section presents the key information on the physical modelling methodology. This includes details on the physical model, the wave conditions, the wave tank and the modelling and analysis procedures that were used. The physical modelling was conducted at 30th scale. Froude scaling was used to convert the variables and results into full-scale values.

### 2.1. Physical model

The physical model was made up of six box-shaped, surface-piercing modules. The total width of the model was approximately 33 m at full scale, which is similar to the Oyster 800 machine (Aquamarine Power Ltd, 2011). The model could be configured either as the Modular Flap or the Rigid Flap. The Rigid Flap was formed by attaching the modules together with PVC sheets on the front and back faces. The modules, when independent, also had PVC sheets attached to them, to maintain consistent mass and geometric properties. The flap modules were mounted on a base structure, attached to the wave tank floor. 3D CAD renderings of the Modular and Rigid Flaps are provided in Fig. 1; the key dimensions of the model are shown in Fig. 2; the model, installed and operating in the wave tank, is shown in Fig. 3; a diagram illustrating the module numbering system that is used for results presentation is shown in Fig. 4.

At the hinge axis of each module were housings for bearings and instrumentation. The instrumentation included sensors to measure instantaneous rotation and applied damping torque. Each module also contained a magnetic particle brake (MPB), to simulate a Coulomb-

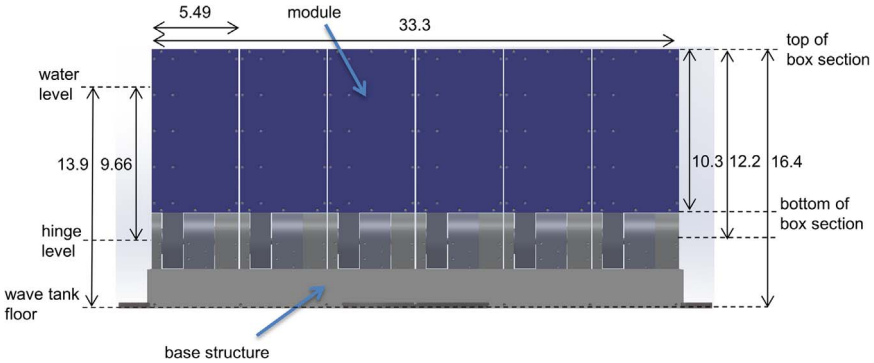


**Fig. 2.** Device dimensions, in full scale, in m. Note that the thickness of the device was 3.6 m.

**Fig. 3.** Photograph of the physical model, in its Modular Flap configuration, operating in the wave tank.

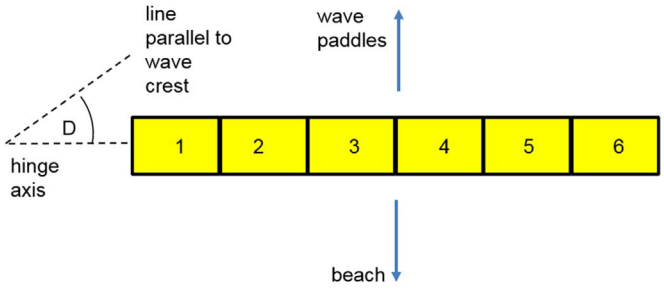


**Fig. 4.** Plan-view diagram illustrating module numbering and wave direction angle, *D*, reference system. Geometry is to scale.

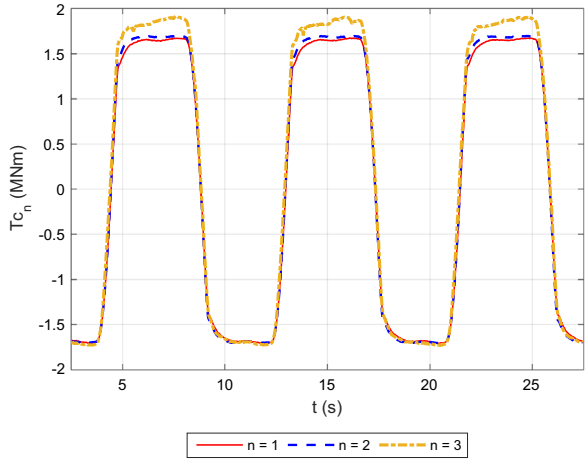


**Fig. 5.** Example of variation in damping torque, $Tc_n$, with time, *t*, for the *n*th modules, fixed together in the Rigid Flap configuration.

damping PTO mechanism. Further model details can be found in (Wilkinson et al., 2015). In this study, the simplest control strategy, of applying damping equally to each module, was applied. This was executed by controlling the supply voltages in a LabVIEW program using damping-voltage conversion equations (National Instruments, 2016). The equations were defined by recording the root-mean-square (RMS) damping levels, calculated using Eq. (3), defined later, at different voltage levels and fitting curves to the results. The MPBs had slightly different damping sensitivities to changes in voltage. This was accounted for, though, by using a different damping-voltage conversion equation for each MPB. To illustrate the resulting high level of control that was achieved, example time-series of damping torques for the modules on one side of the Rigid Flap are shown in Fig. 5.

Fig. 5 shows that there were relatively small differences in the applied damping torque for each MPB, notably in the positive direction. These were present partly because the damping was not controlled dynamically and was not completely constant. The RMS damping torques were acceptably close though, with typical variation between the modules within the Rigid Flap only 2%. The consistency and repeatability was sufficiently high too. Hence, the damping system was adequate for use in the study.

### 2.2. Wave conditions

Regular, head-on waves were used, to generate a fundamental understanding of the Modular Flap. The response of a WEC is generally dependent on the wave period, even for a fairly broad-banded device like a flap-type WEC (Clabby et al., 2012; Whittaker and Folley, 2012). Therefore, one of the chosen variables for this investigation was the wave period. Eight wave periods were used, approximately evenly spaced between 5.5 s and 13.5 s at full scale. These limits represent the typical range for peak periods at a wave energy site (Babarit et al., 2012). Variation in wave amplitude was not considered as it was not thought to be the most significant parameter relating to power capture. A nominal wave amplitude, of 1 m, at full scale, was selected, with maximum variation of only 2%.

The power-capture of a flap-type WEC is sensitive to direction (Henry, 2008). It is hence desirable to mitigate the detrimental effects of increasing wave direction. It is likely that, due to the independence of the modules, the Modular Flap would provide such a solution. Hence, for a small test subset, the wave direction was varied too. Note that for the following sections, the terms ‘head-on’ and ‘off-angle’ are used for cases where the wave direction is 0 and non-0 degrees, respectively. The full range of wave conditions are presented in Table 1.

### 2.3. Wave tank

The Queen’s University Belfast (QUB) Portaferry Wave Tank (QUB, 2016) was selected for testing due to its suitability for shallow water studies, high wave homogeneity (O’Boyle, 2013) and low blockage ratio. A layout of the wave tank, with the model position indicated, is provided in Fig. 6.

### 2.4. Modelling and analysis procedures

The aim of the study, as discussed, was to determine the hydrodynamic power-capture achieved by the two devices for a range of wave conditions. To achieve this, the total average powers were recorded for a range of damping levels, for each wave condition. The maximum average powers were then determined by fitting a curve through the damping-power pairs, with the peak providing the maximum power. The power-capture was then evaluated using the metric, capture factor. The mean difference in the capture factor values achieved by the two devices, relative to those associated with the Rigid Flap, was then the

**Table 1**
List of measured wave conditions that were used.

| Wave Identifier | Wave Amplitude, $a$ (m) | Wave Period, $T$ (s) | Incident Wave Power, $P_{inc}$ (kW/m) | Wave Direction, $D$ (deg) |
|---|---|---|---|---|
| 1 | 0.99 | 13.5 | 48.4 | 0 |
| 2 | 0.99 | 12.5 | 46.5 | 0 |
| 3 | 1.00 | 10.6 | 44.6 | 0 |
| 4 | 0.98 | 9.5 | 40.3 | 0 |
| 5 | 1.01 | 8.5 | 39.3 | 0 |
| 6 | 1.00 | 7.5 | 34.6 | 0 |
| 7 | 1.00 | 6.5 | 29.3 | 0 |
| 8 | 1.00 | 5.5 | 23.3 | 0 |
| 9 | 1.01 | 8.6 | 39.5 | 7.5 |
| 10 | 0.99 | 8.6 | 36.2 | 17.5 |
| 11 | 1.00 | 8.6 | 34.1 | 27.5 |

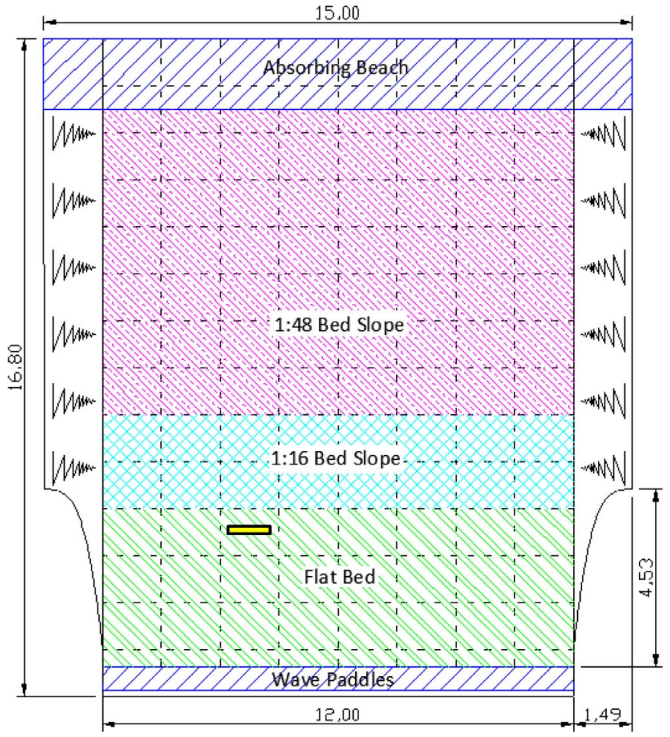


**Fig. 6.** Portaferry Wave Tank layout, to scale, with model scale dimensions in m (O'Boyle, 2013). Model position is indicated by yellow rectangle. Model geometry is approximately to scale.

ultimate metric that was computed. This analysis process started with evaluation of the instantaneous results and is summarised here.

The two instantaneous measurements that were made were damping torque, $Tc_n$, in MNm, and rotation, $\theta_n$, in radians (rad.). Data were recorded at 128 Hz, at model scale. $\theta_n$ was differentiated with respect to time, to find the angular velocity, $\dot{\theta}_n$, in rad/s. These signals were post-processed using a low-pass filter (MathWorks, 2016), with a cut-off frequency of up to 10 Hz, at model scale. The instantaneous power, $P_n$, in kW, was then calculated using Eq. (1).

$$P_n = Tc_n \dot{\theta}_n \tag{1}$$

The instantaneous total power, $P_T$, was then calculated using Eq. (2).

$$P_T = \sum_{n=1}^{M} P_n \tag{2}$$

where $M$ is the number of modules, six.

Each damping level was applied for a duration of 351 s at full scale. The magnitude of each damping level was evaluated as the root-mean-square (RMS) damping torque, $Tc_{n,RMS}$; the equivalent value for the power-capture was the mean power, $\overline{P}_n$. These statistics were generated using Eqs. (3) and (4), respectively.

$$Tc_{n,RMS} = \sqrt{\frac{\sum_{i=1}^{N} Tc_{n,i}{}^2}{N}} \tag{3}$$

$$\overline{P}_n = \frac{\sum_{i=1}^{N} P_{n,i}}{N} \tag{4}$$

where $N$ is the number of samples in the time series.

The device statistics were the total RMS damping torque, $Tc_{RMS,T}$, and total mean power, $\overline{P}_T$, which were calculated using Eqs. (5) and (6), respectively.

$$Tc_{RMS,T} = \sum_{n=1}^{M} Tc_{n,RMS} \tag{5}$$

$$\overline{P}_T = \sum_{n=1}^{M} \overline{P}_n \tag{6}$$

Another point of interest was how smooth the generated power was. A smoother delivery of power to the electrical grid reduces the requirements for energy storage and hence cost (Molinas et al., 2007). The metric for 'smoothness', $S_P$, was calculated using Eq. (7). Note that a higher $S_P$ value indicates a greater level of smoothing.

$$S_P = \frac{\overline{P}_T}{\sigma_T} \tag{7}$$

Where $\sigma_T$ is the standard deviation of the instantaneous total power, $P_T$, defined in Eq. (8).

$$\sigma_T = \sqrt{\frac{1}{N-1} \sum_{i=1}^{N} |P_i - \overline{P}_T|^2} \tag{8}$$

The maximum mean power for each wave condition, for each device, $\overline{P}_{T,max}$, was estimated by fitting a quadratic curve to the $Tc_{RMS,T}$, $\overline{P}_T$ pairs and finding the peak. The x-axis value of this peak corresponded to the optimum damping level. An example power curve is provided in Fig. 7.

The capture factor, $CF$, is a useful measure of the efficiency of a device (Folley et al., 2007). $CF$ is the ratio of generated power, in this case $\overline{P}_{T,max}$, to incident power and was calculated using Eq. (9).

$$CF = \frac{\overline{P}_T}{P_{inc} \cos(D) W} \tag{9}$$

where, $P_{inc}$ is the incident power per metre of crest, in kW/m; $D$ is the wave direction angle, in rad.; $W$ is the device width, 33.3, in m. $P_{inc}$ was calculated for each wave condition, using standard formulae (United States Naval Academy, n.d.), with the results presented in Table 1.

The relative differences in the $CF$ values achieved by the two devices, using the Rigid Flap as the reference point, $\Delta CF'$, were then computed using Eq. (10).

$$\Delta CF' = \frac{CF_{Mod} - CF_{Rig}}{CF_{Rig}} \tag{10}$$

where $CF_{Mod}$ and $CF_{Rig}$ are the $CF$ values achieved by the Modular and Rigid Flaps, respectively.

The mean relative difference in the $CF$ values, $\overline{\Delta CF'}$, was then computed using Eq. (11).

$$\overline{\Delta CF'} = \frac{\sum_{j=1}^{P} \Delta CF_j{}'}{P} \tag{11}$$

where, for the $j$th wave condition, $\Delta CF_j{}'$ is the relative difference in $CF$ values and $P$ is the number of wave conditions, for example 8 for the head-on waves.

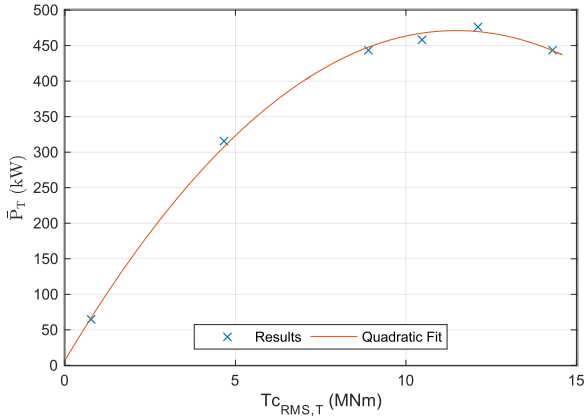


**Fig. 7.** Example of power curve, showing total mean power, $\overline{P}_T$, against total RMS damping torque, $Tc_{RMS,T}$, with quadratic curve fit.

### 2.5. Uncertainty analysis

An uncertainty analysis was completed to ascertain the usability of the results for statistical significance of the conclusions that were drawn. This section contains some background information, discussion of the uncertainty sources and a description of the calculation method for the dominant source.

Uncertainties arise from random or systematic errors (Coleman and Steele, 2009), for example due to temperature variation or calibration of sensors, respectively. The outcome of an uncertainty analysis is an estimation of a range, +/- $U_X$, around the best measurement of a result, $X_{best}$. It is believed that the true value, $X_{true}$, lies within this range, to a certain degree of confidence (Coleman and Steele, 2009; Lamont-Kane et al., 2013). In this study, the 95% confidence limit was used, which is standard for engineering applications (Coleman and Steele, 2009; ITTC, 2014). The aim of the uncertainty analysis in this paper was to estimate $U_X$ for the mean relative differences in *CF* between the two devices, $\overline{\Delta CF}$, as defined in Eq. (10), $U_{\overline{\Delta CF}}$.

The uncertainties in the measured variables were propagated to the results through the use of the Taylor Series Method (TSM), a standard technique (Coleman and Steele, 2009). Both random and systematic uncertainties were considered. Only those sources of uncertainty which were deemed significant were accounted for. These are listed below, with the category of the source provided in brackets:

1. Torque sensor calibration slopes (systematic)
2. Rotation sensor calibration accuracy (systematic)
3. Variation of wave conditions and model behaviour (random)
4. Model orientation (systematic)

The dominant source of uncertainties was number 2, the 'rotation sensor calibration accuracy'. These uncertainties were made apparent when the modules were fixed together as the Rigid Flap. The measurements of rotation and angular velocity should have been the same for this configuration. However, it was noticed that there were appreciable differences. This issue was thought to have arisen due to the way in which the sensors were calibrated. The sensors were calibrated simultaneously by first fixing the modules together with an aluminium bar on the front and back faces. For practical reasons, this was conducted outside of the wave tank. The bars were then removed and the modules installed in the wave tank and fixed together with PVC sheets to form the Rigid Flap. The deviations in velocity may have therefore resulted from the slight differences in constraint, between that supplied by the bars and the PVC sheets. A typical example of the velocity differences is shown in Fig. 8. The results presented are for the sensors that displayed the largest differences when compared to the mean results, which are also provided.

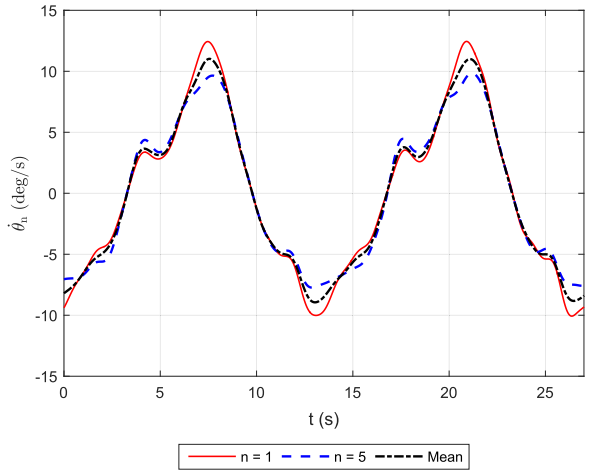


**Fig. 8.** Example of variation in angular velocity, $\dot{\theta}_n$, with time, *t*, for the *n*th modules, and mean values for all modules. Note that the modules were fixed together in the Rigid Flap configuration.

Fig. 8 shows that the sensors, when compared to the mean results, under or overestimated the magnitudes of the velocities. These deviations resulted in fairly consistent relative percentage differences in the mean absolute angular velocities, between −8 and +7% and, on average, 4%. These disparities were greater than any differences in the applied damping torques and the relative uncertainties associated with these. Hence, it is very likely that the dominant contributions to the velocity differences were rotation sensor uncertainties. As the velocity differences were consistent, they were used to estimate the *systematic* uncertainties on the velocity measurements. For the Rigid Flap, direct comparison to the instantaneous mean of the module velocities was used to calculate these. For the Modular Flap though, as a result of the hydrodynamics, there were natural differences in the velocities of the modules. This meant that a different method had to be applied, which was to use the aforementioned mean relative differences in velocities for each module.

The other sources of uncertainty were significantly smaller than that attributed to the angular velocity measurements, with relative magnitudes of less than 1%. Hence, as mentioned, the dominant source was the angular velocity measurements. Nevertheless, the device power uncertainties were reasonable. As a result, the experimental system was still able to show statistically significant differences in the capture factors achieved by the two devices at certain wave conditions.

## 3. Results

This section presents the key results from the study. First shown are results for the individual modules with the model configured as the Modular Flap, in Section 3.1, followed by those for the whole devices, in Section 3.2. Within each of these, compared first are the power time-series. Inspection of these allows one to gauge their relative magnitudes and phases. This is followed by presentation of the mean power results. The focus of the section is the head-on wave results because they are the conditions that a flap-type device should be first tested in. Results for the off-angle waves are provided only in the device section.

### 3.1. Modular Flap modules

Fig. 9 shows an example of power time-series for modules 1–3, which occupied one side of the model. Also shown are time-series of damping torques and velocities, to allow further understanding of the results.

Firstly, subplot c) of Fig. 9 shows that there was a short period of each oscillation where the power was negative. This is thought to have resulted from a spring effect in the dampers when the modules changed direction. This will have injected some torque into the system. For this short period, the damper acted like a motor. The negative power values were included in the calculation of mean power. It is likely though that the effect on the mean power values will have been small. This is because the effect of the negative power phase will likely have been cancelled out by an increase in the positive power due to an increased velocity.

There were also double-peaks present in the velocity and power signals. This may have been due to waves radiated by each flap module interacting with adjacent units. The difference in magnitudes in the maximum values of power for alternate strokes, especially prominent for module 3, were likely due to asymmetry in the surge forces.

The key features of Fig. 9 though are the differences in magnitudes and phases of the signals. Subplot a) of Fig. 9 shows that the damping torque applied to the outer module (n =1) was approximately sinusoidal in shape. This suggests that the allowable damping torque was greater than the wave excitation torque. This resulted in the module velocities and powers being virtually 0, as shown in subplots b and c, respectively. Moving towards the centre modules, the damping torque

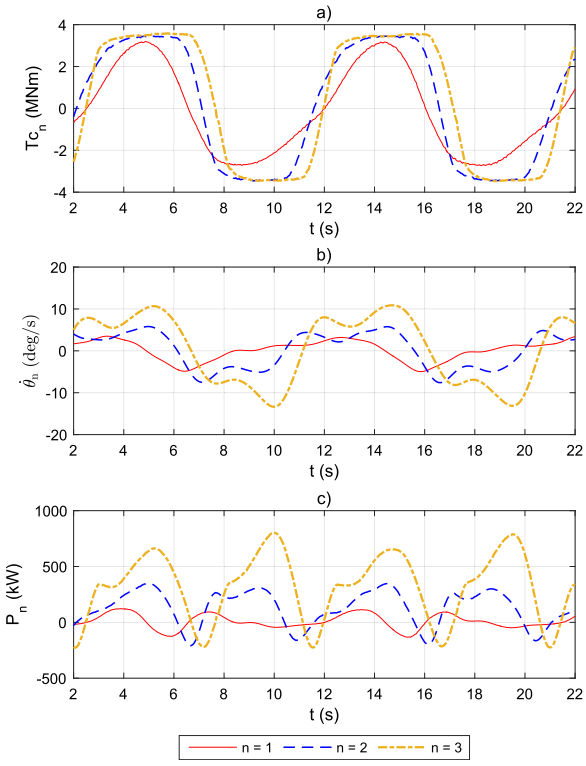


**Fig. 9.** Example of variation of individual module damping torques, $Tc_n$, (a), velocities, $\dot{\theta}_n$, (b) and powers, $P_n$, (c) for the $n$th modules, with time, $t$.

signals bared greater resemblance to Coulomb damping profiles. The magnitudes of the velocities and powers also increased.

The phase differences in the signals shown in Fig. 9 will have been caused by diffracted and radiated waves meeting the different modules at different points in time. The signals for symmetrical pairs, for example modules 3 and 4, were generally in phase. For adjacent modules on one half of the device though, phase differences were present. The greatest difference was between the outer and centre modules, for example numbers 1 and 3. From Fig. 9, differences of approximately 1/3 of the wave cycle were present in the velocity and power signals. Across the range of wave periods, there were phase differences in the velocities and powers, though no distinct relationship was shown. This means that the device was displaying similar behaviour to the out-of-phase motions shown by closely-spaced flap units in works such as Adamo and Mei (2005).

The instantaneous module power values were then averaged to find the mean module powers. Fig. 10 shows an example of results for the

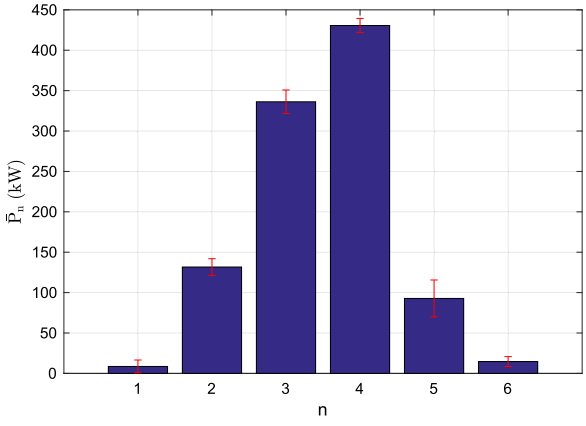


**Fig. 10.** Example of mean module powers, $\overline{P_n}$, for the $n$th modules, with combined expanded uncertainties shown as the error bars.

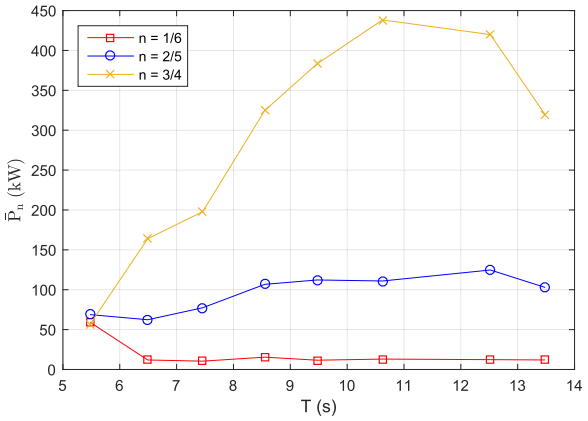


**Fig. 11.** Average mean powers per module for the $n$th symmetrical pairs of modules, $\overline{P_n}$, against wave period, $T$. The values are from tests that corresponded to the optimum recorded damping level.

same conditions as used for producing Fig. 9c). For this graph, though, the results for all modules are provided, to allow the reader to evaluate the level of symmetry present in the power measurements. Also shown are the uncertainties on the results.

Fig. 10 shows that there were some differences in the powers within modules paired around the centre of the device. The differences were due to a combination of tank effects, such as differences in amplitude across the wave crest, variations in module mass properties, imperfect damping control and sensor uncertainty. However, as also seen in Fig. 10, the absolute differences within the module pairs were far smaller than the differences between the pairs of results. This was generally true for the head-on waves. Hence, there was a reasonable level of symmetry in the results and so, for conciseness, the mean results for the pairs are subsequently used. The module pair mean power results are then compared in Fig. 11 across the range of wave periods.

Fig. 11 shows that the mean powers generally increased towards the centre of the device, with the outer most modules generating least power and the inner most modules generating most. This agrees with the findings by Sarkar et al. (2016). Averaging across the wave periods, the central modules (3/4) produced 68% of the total power, the inner modules (2/5) 25% and the outer modules (1/6) only 7%. It is likely that this was due to wave excitation torques increasing towards the centre, as shown in Sarkar et al. (2016).

As also indicated in Fig. 11, the variation of mean module powers changed with wave period. The 'coefficient of variation', a standard metric, was used for evaluating this. Variation was lowest, at 10%, for the shortest wave periods, and highest for the longer periods, maximising at 119% for a period of 10.6 s.

### 3.2. Modular Flap vs Rigid Flap

It is interesting to assess how the phase differences in the individual instantaneous module powers, shown in Fig. 9c, affected the total power produced by the Modular Flap. The same example as used in Fig. 9 was employed to explore this, in Fig. 12. Shown for comparison are also the equivalent results for the Rigid Flap.

Fig. 12 shows that the total power signal for the Modular Flap, when compared to the individual module powers in Fig. 9c, did not have the same relative magnitude of oscillations. While phase differences were shown in the module power values, the total power signal also combined into a single oscillation. However, it is also apparent that the variation in the Modular Flap power signal is lower than that associated with the Rigid Flap power. This was confirmed by calculation of the smoothness metric, $S_P$, as defined in Eq. (7), as 1.30 and 0.89 for the Modular and Rigid Flaps, respectively. To then gauge the general trend, a comparison of the smoothness metrics across the head-on wave conditions is provided in Fig. 13.

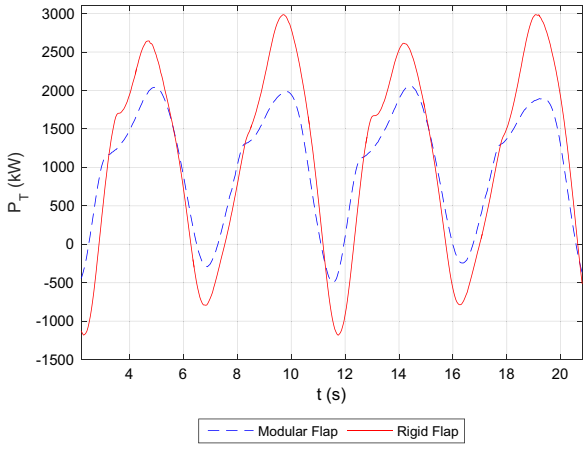


**Fig. 12.** Variation of total power, $P_T$, with time, $t$, for Modular and Rigid Flaps. Both devices had the same allowable total damping torque level applied to them. Note that the time has been adjusted so that the time-series approximately overlay.

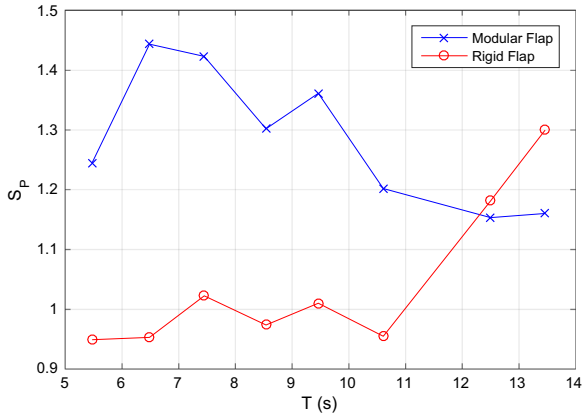


**Fig. 13.** Power smoothness metric, $S_P$, against wave period, $T$, for Modular and Rigid Flaps for head-on waves. Results are for damping level corresponding to maximum total mean power.

Fig. 13 shows that, for most of the wave periods, the smoothness metric was higher for the Modular Flap. On average, the total power produced by the Modular Flap was 23% more smooth. This was due to the out-of-phase power production by the individual modules, illustrated in Fig. 9c. This is an advantage for the Modular Flap as smoother, i.e. less variable, power production reduces cost requirements for energy storage for achieving electrical grid compliance (Molinas et al., 2007).

The capture factors, computed using Eq. (9), for the damping levels that resulted in maximum mean power capture were then computed. Presented first, in Fig. 14, are comparisons of the capture factors achieved by the two devices across the range of periods for the head-on waves.

Fig. 14 shows that both devices achieved relatively high capture factors across the range of wave periods, indicating a broad bandwidth. Though not well defined, both devices peaked at around a period of 10.6 s, with a capture factor of approximately 0.8. Fig. 14 also indicates that there was variation in the relative differences in the capture factors achieved by the two devices. Fig. 15 shows this in more detail by presenting the computed relative differences, using the Rigid Flap as the reference device, calculated with Eq. (10), for each wave period.

Fig. 15 shows that there was generally an inverse relationship between the relative differences in capture factor and the wave periods. For the lower wave periods, the Modular Flap outperformed the Rigid Flap, by up to 13%. This may have been due to a near-excitation of a natural mode of the system, such as shown for a similar device in Adamo and Mei (2005). For the higher periods though, the Rigid Flap

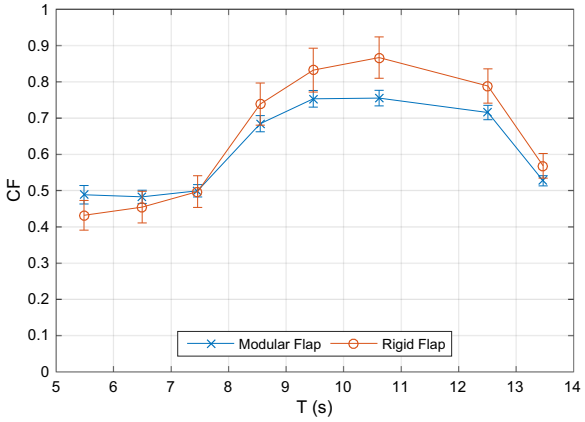


**Fig. 14.** Capture factors, *CF*, with associated expanded combined uncertainties, against wave period, $T$, for the Modular and Rigid Flaps in head-on waves.

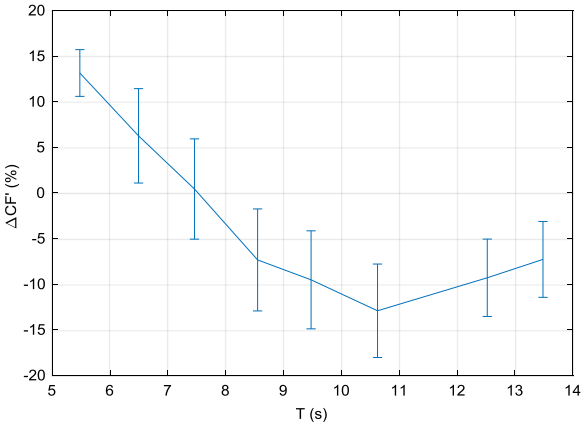


**Fig. 15.** Relative differences in the capture factors, *CF*, achieved by the two devices, using the Rigid Flap as the reference, $\Delta CF$, with associated expanded combined uncertainties, against wave period, $T$, in head-on waves.

outperformed the Modular Flap, also by up to 13%. As one would imagine, the variation in the module power captures, shown in Fig. 11, was strongly correlated with the variation in the rotation amplitudes. Hence, there was an inverse correlation between the relative power production, shown in Fig. 15, and the level of variation in the module rotation amplitudes. This suggests that, with opening of larger gaps between the modules, greater water leakage occurred through the gaps, resulting in reduced power production. This suggests that higher power production is achieved by minimising the level of variation of the rotation of the modules. This could be realised by applying different damping levels to each module, as done in previous mathematical work (Sarkar et al., 2016). The effects of damping strategy on the power-capture of the Modular Flap is an area for further work.

The mean value of the relative differences in the capture factor across the wave periods, shown in Fig. 15, was then recorded. This was −3%, with an expanded combined uncertainty of +/- 5%. This shows that there was not a statistically significant reduction in efficiency when comparing the Modular Flap to the Rigid Flap.

For the head-on wave with an 8.5 s period, it was shown in Fig. 15 that the Modular Flap had 7% lower efficiency, with an uncertainty of +/- 6%. This shows that there was a statistically significant reduction in efficiency. This reduction may be offset by a superior performance in off-angle waves though. This hypothesis was tested by carrying out an equivalent evaluation on the off-angle results. First shown, in Fig. 16, are the capture factors achieved at different wave direction angles by the two devices.

Fig. 16 shows that the absolute deficit in the efficiency achieved by the Modular Flap compared to the Rigid Flap reduced as the wave

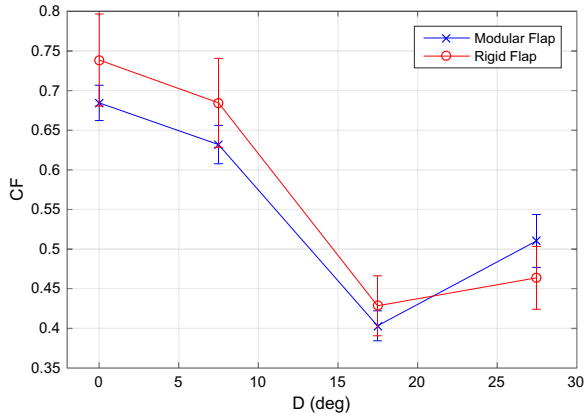


**Fig. 16.** Capture factors, *CF*, with associated expanded combined uncertainties, against wave direction, *D*, for the Modular and Rigid Flaps in off-angle waves.

direction angle grew. For both devices, the efficiency reduced due to a decrease in the net wave excitation torque acting on them. There is a difference though in the rate of this decrease and in the resistive torques applied by the devices. These differences, explored now, result in the distinctions between the rates of capture factor reduction with wave direction angle.

For rigid flaps that are narrow relative to the wavelength, the water particle motion that drives the flap can be approximated as being in phase across the flap width. The results of this is that the wave force acting on the flap simply decays with the cosine of the wave direction angle. The power capture is proportional to the wave force squared. Hence, for a narrow flap, the power capture reduces with the square of the cosine of the angle (Henry, 2008). The available power reduces with the cosine of the angle. Hence, the capture factor reduces with the cosine of the angle.

For flaps that are wider relative to the wave length though, the reduction is faster. This is because of two reasons. Firstly, the angle results in a phase difference in the wave torque across the flap. For the extreme case, the crest and trough of the flap would be at different ends of the flap, resulting in the wave torque being cancelled out (Henry, 2008). The hydrodynamic and body resistance to the wave torque, such as the added inertia, are independent of the wave angle. Hence, the reduced wave torque at any moment in time is having to overcome the same resistance. This results in reduced motions and hence power capture. The reduction in wave torque and hence power capture with wave angle is experienced by the Modular Flap too, but the rate is lower. This is because of the independence of the modules. Apart from at extreme wave angles, it is unlikely that there is any significant reduction in the wave torque due to the phase difference causing opposing forces across an individual module. Also, the increase of wave angle has the effect of reducing the body resistive forces for the Modular Flap. This is because the modules become decoupled and the wave torque must only overcome the added inertia, for example, of an individual module. The differences in the torques acting on the two devices are partly illustrated in the diagram provided in Fig. 17.

The combined effect of the two differences in the way that the devices respond to the changing wave direction is that the wave torque and power capture do not reduce as rapidly with the wave direction angle for the Modular Flap. As a result, it can be seen from Fig. 16 that the Modular Flap eventually outperforms the Rigid Flap. This comparison of the performances of the two devices is perhaps better illustrated in Fig. 18, which shows the relative differences in capture factors with wave direction angle.

Fig. 18 shows that the deficit in efficiency for the Modular Flap gradually reduces with increasing wave direction angle. At the largest angle of 27.5 degrees though, the Modular Flap performance was 10% greater. Although the quantity of results was limited, this shows that there was a point where the gains outweighed the losses for the Modular Flap. Hence, in a wave climate characterised by large directional variation, such as the Isle of Lewis in the Outer Hebrides (Wilkinson et al., 2014), a modular system could yield higher energy.

## 4. Conclusions

This paper has presented a power-capture assessment of a modular flap-type WEC, referred to here as the 'Modular Flap'. The device was made up of six modules, with a total width, at full-scale, of 33 m. Comparisons were made to a single equivalent unit, named the 'Rigid Flap'. The assessment was carried out with 30th scale physical modelling in a wave tank. The waves that were used were regular, with the period and direction varied and the amplitude held constant. The simplest damping strategy was employed, which was to damp each module equally. Results were generated both at module and device levels.

The power produced by the individual flap modules was very different, with power increasing significantly towards the centre. On average, the central pair of modules produced 68% of the total power, the inner modules 25% and the outer modules only 7%. This focusing of the power capture away from the outer modules was particularly prominent at longer wave periods. For sites characterised by these conditions, it may in fact therefore be most economical to have inexpensive structures, without PTOs, in place of the outer modules.

Phase differences were also shown between the powers produced by the modules. These caused a smoothing effect in the total instantaneous power. Using the inverse of the coefficient of variation as a metric, the Modular Flap produced power that was, on average, 23% more smooth. This could result in reductions in the costs associated with the energy storage that is needed for electrical grid compliance (Molinas et al., 2007).

For head-on waves, the average power-capture, measured using a capture factor, of the Modular Flap was 3% lower than the Rigid Flap. This difference had expanded combined uncertainty limits of +/− 5%. This shows that there was not a statistically significant reduction in power when using the Modular Flap. In previous literature (Sarkar et al., 2016), a range of damping strategies were applied. For the cases where equal damping coefficients were used on the flap modules, the total power capture was similar to that produced by the rigid flap used for comparison. The experimental work in this paper therefore provides some validation for this mathematical work. The paper also showed that superior power capture could be achieved by the modular system, even in head-on waves, by allowing the damping coefficients to vary across the modules (Sarkar et al., 2016). Hence, future complementary experimental work should focus on validating this case.

For off-angle waves, the Modular Flap experienced a lower rate of reduction in power-capture, with the wave direction angle, than the Rigid Flap. As a result, the deficit between the two devices reduced with increasing wave direction angle. Across the direction range, 7.5–27.5 degrees, the Modular Flap had average power capture that was 1% lower, with +/- 4% uncertainty, than that produced by the Rigid Flap. For the largest angle, though, the Modular Flap outperformed the Rigid Flap, by 10%, with +/- 1% uncertainty. This suggests that the Modular Flap would perform better in sites with large wave directional variation.

Combining the results for the head-on and off-angle wave conditions, it is likely that the average power captures across a range of sites would be similar for the Modular and Rigid Flaps. Along with previous literature (Sarkar et al., 2016), this work shows that it is unlikely that the adoption of the modular design would compromise the high conversion efficiency of the flap-type WEC (Babarit, 2015; Babarit et al., 2012). The Modular Flap has a number of techno-economic advantages, such as reduced parasitic foundation loads (Wilkinson et al., 2014), the possibility of less expensive installation, and, shown in this study, smoother power generation. These benefits can therefore be

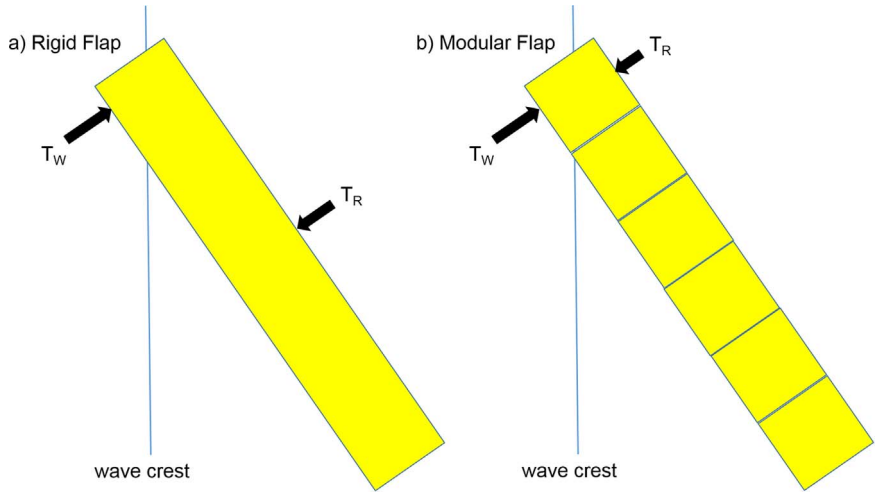


**Fig. 17.** Free body diagrams of torques acting on Rigid Flap (left) and Modular Flap (right) when met by an off-angle wave. $T_W$ and $T_R$ are the wave excitation and body resistance torques, respectively.

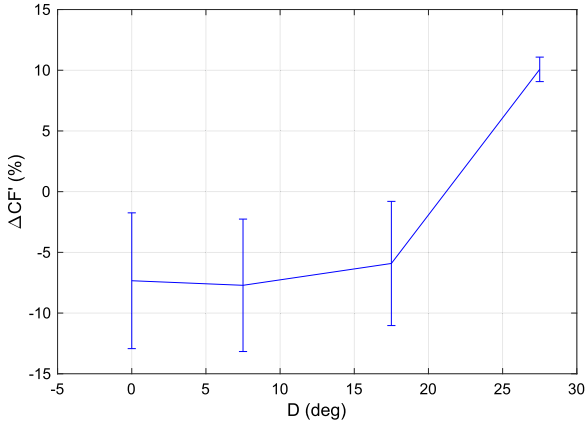


**Fig. 18.** Relative differences in the capture factors, *CF*, achieved by the two devices, using the Rigid Flap as the reference, Δ*CF*', with associated expanded combined uncertainties, against wave direction, D.

exploited without significantly compromising one of the flap-type WEC's greatest advantages, its efficiency.

Further work should evaluate the effects of the use of irregular and multi-directional waves. These, combined with resource occurrence tables, would allow for the estimation of annual energy productions. As discussed, the potential benefits of employing different damping control strategies should also be investigated. Optimisation of the modular concept, for example in terms of geometry, should also be carried out. This could investigate the effects of parameters such as the size of modules, the spacing between the modules and the total device width. Finally, an economic evaluation of the modular concept should be carried out, including estimated operational, maintenance and capital costs, to allow comparison to other energy sources (de Andres et al., 2016).

## Acknowledgements

Thank you to the technicians at QUB, for design guidance and model fabrication, and to the QUB Marine Research Group, for support during the experimental campaign and writing of this paper. This work was supported by the Energy Technologies Institute (ETI) and the RCUK Energy Programme for the Industrial Doctoral Centre for Offshore Renewable Energy (grant number EP/J500847/1). Thank you also to the sponsors of this research, Aquamarine Power Ltd and QUB for financial support and the latter for provision of experimental testing facilities.

## References

Abadie & Dias, 2016. Numerical Study of Wave Interaction with a Modular Oscillating Wave Surge Converter. In: Proceedings of the Twenty-Sixth (2016) International Ocean and Polar Engineering Conference.

Álvarez, 2015. Evaluation of Concepts to Reduce Structural Loading on The Wave Energy Converter Oyster. Technical University of Hamburg-Harburg.

de Andres, A., Maillet, J., Todalshaug, J.H., M??ller, P., Bould, D., Jeffrey, H., 2016. Techno-economic related metrics for a wave energy converters feasibility assessment. Sustain, 8. http://dx.doi.org/10.3390/su8111109.

Aquamarine Power Ltd, 2009. Oyster generates £1m for Orkney economy [WWW Document]. URL http://www.aquamarinepower.com/news/oyster-generates-£1m-for-orkney-economy.aspx (accessed 18.07.16).

Aquamarine Power Ltd, 2011. Projects: Oyster 800 project, Orkney [WWW Document]. URL ⟨http://www.aquamarinepower.com/projects/oyster-800-project-orkney.aspx⟩ (accessed 19.07.16).

AW-Energy, 2012. WaveRoller Concept [WWW Document]. URL ⟨http://aw-energy.com/about-waveroller/waveroller-concept⟩ (accessed 18.07.16).

Babarit, et al., 2012. Numerical benchmarking study of a selection of wave energy converters. Renew. Energy 41, 44–63. http://dx.doi.org/10.1016/j.renene.2011.10.002.

Babarit, 2015. A database of capture width ratio of wave energy converters. Renew. Energy 80, 610–628. http://dx.doi.org/10.1016/j.renene.2015.02.049.

Clabby, et al., 2012. The Effect of the Spectral Distribution of Wave Energy on the Performance of a Bottom Hinged Flap Type Wave Energy Converter. Rio de Janeiro.

Coleman, Steele, 2009. Experimentation, Validation, and Uncertainty Analysis for Engineers. John Wiley & Sons.

Folley, et al.2007. The design of small seabed-mounted bottom-hinged wave energy converters. In: Proceedings of the 7th European Wave and Tidal Energy Conference.

Henry, 2008. The Hydrodynamics of Small Seabed Mounted Bottom Hinged Wave Energy Converters in Shallow Water. Queen's University Belfast.

Henry, et al.2010. Advances in the Design of the Oyster Wave Energy Converter. In: Royal Institution of Naval Architect's Marine and Offshore Renewable Energy Conference. Royal Institution of Naval Architect's Marine and Offshore Renewable Energy Conference.

ITTC, 2014. ITTC – Recommended Procedures - General guideline for uncertainty analysis in resistance tests, (7.5-02-02-02 )(Revision 02).

Lamont-Kane, et al.2013. In: vestigating Uncertainties in Physical Testing of Wave Energy Converter Arrays. In: Proceedings of the 10th European Wave and Tidal Energy Conference.

MathWorks, 2016. idealfilter [WWW Document]. URL ⟨http://uk.mathworks.com/help/matlab/ref/timeseries.idealfilter.html⟩ (accessed 09.03.16).

Mei, et al.1994. Subharmonic resonance of proposed storm gates for Venice Lagoon. In: Proceedings: Mathematical and Physical Sciences. doi:http://dx.doi.org/10.1098/rspa.1983.0054.

Molinas, et al.2007. Power Smoothing by Aggregation of Wave Energy Converters for Minimizing Electrical Energy Storage Requirements. In: Proceedings of the 7th European Wave and Tidal Energy Conference. doi:http://dx.doi.org/10.1016/j.tree.2005.11.022.

National Instruments, 2016. LabVIEW System Design Software [WWW Document]. URL ⟨http://www.ni.com/labview/⟩ (accessed 07.11.16).

O'Boyle, 2013. Wave Fields around Wave Energy Converter Arrays. Queen's University Belfast.

QUB, 2016. Portaferry Wave Tank [WWW Document]. URL ⟨http://www.qub.ac.uk/research-centres/cerc/Facilities/MarineFacilities/PortaferryWaveTank/⟩ (accessed 0708.16).

Renzi, et al., 2014. Wave-power absorption from a finite array of oscillating wave surge converters. Renew. Energy 63, 55–68. http://dx.doi.org/10.1016/

j.renene.2013.08.046.
Sammarco, et al., 2013. Flap gate farm: from Venice lagoon defense to resonating wave energy production. Part 1: natural modes. Appl. Ocean Res. 43, 206–213. http://dx.doi.org/10.1016/j.apor.2013.10.001.
Sarkar, et al., 2016. The modular concept of the Oscillating Wave Surge Converter. Renew. Energy 85, 484–497. http://dx.doi.org/10.1016/j.renene.2015.06.012.
United States Naval Academy, n.d. EN475 - Ocean Engineering Mechanics - Equation Sheet 1: Linear Wave Properties.
van 't Hoff, 2009. Hydrodynamic Modelling of the Oscillating Wave Surge Converter. Queen's Univ. Belfast.
Whittaker, Folley,, 2012. Nearshore oscillating wave surge converters and the development of Oyster. Philos. Trans. A. Math. Phys. Eng. Sci. 370, 345–364. http://dx.doi.org/10.1098/rsta.2011.0152.
Wilkinson, et al., 2014. Wave Loads on the Foundation of a Bottom-Hinged Modular Flap Structure. In: . Offshore Renewable Energy ORE.
Wilkinson, et al.2015. Modelling the performance of a modular flap-type wave energy converter. In: Proceedings of the 11th European Wave and Tidal Energy Conference.